Carbonate factories in the early Archean and their geobiological impacts

Dissertation
for the award of the degree

'Doctor rerum naturalium'

at the Georg-August-Universität Göttingen

within the doctoral degree programme ‘Geoscience’

of the Georg-August University School of Science (GAUSS)

submitted by

Wanli Xiang

from Leshan, China

Göttingen, 2023

Thesis advisory committee

Prof. Dr. Joachim Reitner, Abteilung Geobiologie, Geowissenschaftliches Zentrum, Georg-August-Universität Göttingen

Prof. Dr. Jan-Peter Duda, Abteilung Geobiologie, Geowissenschaftliches Zentrum, Georg-August-Universität Göttingen

Prof. Dr. Andreas Pack, Abteilung Geochemie und Isotopengeologie, Geowissenschaftliches Zentrum, Georg-August-Universität Göttingen

Members of the examination board:

Referee: Prof. Dr. Joachim Reitner, Abteilung Geobiologie, Geowissenschaftliches Zentrum, Georg-August-Universität Göttingen

Co-referee: Prof. Dr. Jan-Peter Duda, Abteilung Geobiologie, Geowissenschaftliches Zentrum, Georg-August-Universität Göttingen

Other members of the Examination Board:

Prof. Dr. Andreas Pack, Abteilung Geochemie und Isotopengeologie, Geowissenschaftliches Zentrum, Georg-August-Universität Göttingen

Prof. Dr. Matthias Willbold, Abteilung Geochemie und Isotopengeologie, Geowissenschaftliches Zentrum, Georg-August-Universität Göttingen

PD. Dr. Michael Hoppert, Abteilung für Allgemeine Mikrobiologie, Georg-August-Universität Göttingen

Dr. Mark van Zuilen, CNRS-UMR6538 Laboratoire Geo-Ocean, Institut Universitaire Européen de la Mer (IUEM), France

Dr. Jan Schönig, Abteilung Sedimentologie/Umweltgeologie, Geowissenschaftliches Zentrum, Georg-August-Universität Göttingen

Day of the oral examination: June 30th, 2023

Preface

The following manuscripts are part of this dissertation (*corresponding author) and in submission:

Xiang, W., Duda, J.-P., Pack, A., van Zuilen, M., Reitner, J.*. Are the early Archean carbonate factories major carbon sinks on the Juvenile Earth? (Chapter 2, submitted to Biogeosciences)

Xiang, W.*, Duda, J.-P., Pack, A., Willbold, M., Bach, W., Karius, V., Reitner, J., Characteristics of REE+Y and radiogenic Sr isotopic compositions of 3.5-3.3 Ga carbonate from the East Pilbara Terrane, Western Australia, and their variations during diagenesis. (Chapter 3)

Xiang, W.*, Duda, J.-P., Pack, A., Willbold, M., Bach, W., Reitner, J., Element mobility during carbonatization of 3.46 Ga Apex Basalt and its geobiological significances. (Chapter 4)

TABLE OF CONTENTS

Chapter-1 Introduction

1. General overview

1.1 Rocks preserving the earliest life on Earth

When did life emerge on Earth? This question has interested researchers for generations but has still not been convincingly answered. The signs of the earliest life were reported to be preserved in the 4.0-3.6 Ga Isua supracrustal belt (ISB) of southern West Greenland with evidence of geochemical signatures (Schidlowski et al., 1979; Mojzsis et al., 1996; Rosing, 1999; Dauphas et al., 2004; Nutman et al., 2010; Craddock and Dauphas, 2011; Yoshiya et al., 2015), graphite microstructures (Ohtomo et al., 2014), and ~3.6 Ga stromatolites (Nutman et al., 2016). However, debates on their biogenicity have never ceased, especially that of the stromatolites (Nutman et al., 2016, 2019, 2021; Allwood et al., 2018; van Zuilen, 2018; Zawaski et al., 2020, 2021), due to the unsatisfactory preservation conditions of regional metamorphism during 3.7-2.7 Ga from lower amphibolite (500-550°C; Nutman et al., 2016) to middle amphibolite facies (up to 650°C; Rollinson, 2003; Nutman et al., 2013).

Compared to the highly metamorphosed ISB rocks, the 3.53-3.17 Ga East Pilbara Terrane (EPT) of the Pilbara Craton, Western Australia, and the 3.55-3.2 Ga Barberton Greenstone belt (BGB) of southern Africa, are favored for searching for traces of early life due to their relatively lower metamorphic degree, from prehnite-pumpellyite (100-250°C) to greenschist facies (300-350°C) (Hickman, 1983; Van Kranendonk et al., 2002; Tice et al., 2004; van Zuilen et al., 2007). Both consist of dominantly mafic-ultramafic volcanic rocks with minor subordinate felsic rocks and sedimentary rocks (including shale, sandstone, conglomerate, chert, and carbonate) and preserve tell-tale signs of the diverse ancient biosphere supported by morphological, geochemical, and mineral biosignatures (Van Kranendonk et al., 2019a; Hickman-Lewis et al., 2019).

As a window into the rich diversity of early life, the EPT has consistently been a hotspot for research with great findings. The EPT contains a 20 km thick succession of predominantly volcanic rocks known as the Pilbara Supergroup (Van Kranendonk et al., 2006). This supergroup is composed of four distinct groups, from the base to the top: the 3.53–3.43 Ga Warrawoona Group, the 3.42–3.32 Ga Kelly Group, the 3.27–3.23 Ga Sulphur Springs Group, and the ca. 3.19 Ga Soanesville Group (Van Kranendonk et al., 2002, 2007b; Rasmussen et al., 2007). The lower two groups have received relatively more attention since Lambert et al. (1978) first introduced stromatolite-like edgewise conglomerates from sedimentary rocks of the Warrawoona Group, although it was soon rejected as evidence of great antiquity (Pidgeon, 1978). Since then, more claims for early life have been made with evidence of distinct types, including diverse macroscopic stromatolites from the 3.48 Ga Dresser Formation and 3.41 Ga Strelley Pool Formation (SPF) (Walter et al., 1980; Buick and Dunlop, 1990; Van Kranendonk, 2006, 2007; Allwood et al., 2006, 2007, 2009; Van Kranendonk et al., 2008,

2019b; Oehler et al., 2009; Wacey et al., 2011, 2018; Lepot et al., 2013; Brasier et al., 2015; Schopf et al., 2017; Kozawa et al., 2019; Delarue et al., 2020). There are also putative microfossils and/or microstructures of carbonaceous materials (CM) in (silicified) sedimentary rocks (Awramik et al., 1983; Schopf, 1992, 1993; Ueno et al., 2001; Sugitani et al., 2010, 2013, 2015a, b, 2018; Duda et al., 2016, 2018), ichnofossils in the chilled margin of pillow basalts (Furnes et al., 2004; Banerjee et al., 2007), characteristic isotopic compositions like the highly negative $\delta^{13}C$ values of CM and methane (Ueno et al., 2001, 2006; Marshall et al., 2007; Morag et al., 2016; Flannery et al., 2018; Baumgartner et al., 2019), and highly fractionated $\delta^{34}S$ values of pyrite crystals (Shen et al., 2001, 2009; Wacey et al., 2010; Bontognali et al., 2012; Baumgartner et al., 2020a, b, c). These findings not only date the debut of early life before ~3.5 Ga, but also indicate the emergence of some important metabolisms in biological history, for example, microbial sulfate reduction, anoxygenic photosynthesis, and methanogenesis (Moore et al., 2017; Lepot, 2020). Therefore, the EPT rocks from ca. 3.5 to 3.3 Ga are of vital significance for understanding the co-evolution of life and environments during the early Archean.

Which rocks generally preserve traces of early life? Currently, the aforementioned traces of early life in the EPT are predominantly preserved in metasedimentary rocks, cherty rocks, and minor metamorphosed pillow basalts (ichnofossils). The original stromatolites in this area may be carbonate rocks that were partly silicified or sulfidized during later alteration. For example, the SPF stromatolites consist of up to 20 m of millimeter-laminated and bedded stromatolitic dolomite and chert, identified as Member 2 of the four members (Allwood et al., 2006, 2009, 2010). The Dresser stromatolites in unweathered drill core material PDP2b and c are mainly laminated pyrite with minor sphalerite, which are the overprint remnants of Mn-rich carbonate, and occur as black and red-weathering iron oxyhydroxide minerals (limonite, goethite) cut by later hydrothermal chert and barite in surface exposures (Van Kranendonk et al., 2008, 2019b). However, putative microfossils, carbonaceous materials and microstructures are commonly preserved in chert (Awramik et al., 1983; Duda et al., 2016; Sugitani et al., 2010, 2013), that some are either in chert dikes/veins (Schopf, 1992, 1993; Ueno et al., 2001; Schopf et al., 2002, 2018; Brasier et al., 2002, 2005; Duda et al., 2018) or stratiform chert (Van Kranendonk, 2006; Sforna et al., 2014; Hickman-Lewis et al., 2016; Rouillard et al., 2021), or quartz-rich sandstone (Sugitani et al., 2015a,b, 2018). The ichnofossils found in the pillow basalts of Euro Basalt (Furnes et al., 2004; Banerjee et al., 2007) have recently been recognized as artifacts called Ambient Inclusions Trails (AITs) (McLoughlin et al., 2020; Lepot, 2020). Pyrite crystals with highly fractionated $\delta^{34}S$ values are preserved in large barite crystals (Shen et al., 2001, 2009) and strongly sulfidized stromatolites (Baumgartner et al., 2019, 2020a, b, c) from the Dresser Formation, as well as in black bedded sandstone at the base of the Strelley Pool Formation (Wacey et al., 2010) and the SPF stromatolite (Bontognali et al., 2012). Although carbonate rocks play a subordinate role in preserving evidence of early life, they are of great significance in reconstructing the geochemical conditions of the early Archean.

1.2 Carbonate as archives for various depositional environments

Carbonate is a unique sediment. One difference between carbonate and siliciclastic sediments was highlighted by James and Ginsburg (1979), who stated that "carbonates are born", originating as skeletal grains or precipitates within the depositional environment (Flügel and Munnecke, 2010). Carbonate sediments are specifically divided into allogenic (or allochthonous), which refers to constituents that were transported to the site of deposition (i.e., detrital/clastic sediments and biogenic/skeletal components), and authigenic (or autochthonous), which refers to features/minerals formed in situ during or after deposition (Pettijohn, 1957; Folk, 1964; Berner, 1980).

Generally, primary (or original) geochemical signals of authigenic carbonates are assumed to reflect the fluids in which they precipitated, offset by a known isotopic fractionation factor or elemental partition coefficient, and thus represent the secular geochemical evolution of seawater (Fantle et al., 2020). In contrast to the strange Archean world, well over 90% of the carbonates found in modern marine environments are biological in origin, biotically induced (by an organic trigger) or biotically controlled (by skeletal carbonate-producing organisms that determine the composition, location, and timing of carbonate production) (Flügel and Munnecke, 2010). Three major depositional environments have been identified as continental (various non-marine terrestrial areas, e.g., caves, glacial, lakes, rivers), transitional (shorelines, coastal lagoons, tidal flats), and marine (shallow marine, e.g., carbonate platforms and reefs, and deep marine) (Flügel and Munnecke, 2010). Therefore, sedimentology, microfacies, and paleontology of carbonate rocks can assist in reconstructing their depositional and burial history, which have been widely adopted in the past years.

Carbonate factory, a notion for carbonate production systems, has been proposed and developed fast over the past couple of years (Reitner and Neuweiler, 1995; Schlager, 2000, 2003, 2005; Pomar and Hallock, 2008; Reijmer, 2021; Pei et al, 2021; Wang et al., 2023). It refers to a conceptual model encompassing carbonate production and associated processes at various scales, from local precipitation to global sedimentation (Reitner and Neuweiler, 1995; Schlager, 2000; Schrag et al., 2013; Reijmer, 2021). Reijmer (2021) reviewed carbonate factories in modern ocean and suggested that each carbonate factory has its unique depositional setting, mineralogy, and pathway, enabling predictions away from known data points. Pei (2022) reported the carbonate factories across the Permian–Triassic boundary. However, the carbonate factories in the early Archean ocean are still unknown.

In addition, applications of carbonate geochemistry have developed rapidly in recent decades. Carbonates can record the trace elemental and isotopic compositions of ambient solutions from which they precipitated, making them good proxies for ancient seawater or seawater-derived fluids (Veizer and Hoefs, 1976; Veizer et al., 1982, 1989a, b, 1999; Webb and Kamber, 2000; Kamber and Webb, 2001; Shields and Veizer, 2002; Yamamoto et al., 2004; Nakamura and Kato, 2004; Coggon et al., 2010; Coogan and Dosso, 2015; Shields, 2019; Zhao et al., 2021). The Mg/Ca and Sr/Ca ratios of carbonates have been used to

reconstruct past seawater Mg/Ca and Sr/Ca ratios, which are important for understanding dynamic exchanges of elements between the solid Earth, atmosphere, hydrosphere, and the evolution of life (Coggon et al., 2010; Zhang et al., 2020). Rare Earth Elements plus Yttrium (REE+Y) can enter carbonate lattices by replacing cations and are commonly used in environmental reconstruction using ancient carbonates, with consideration of their good resistance to later alteration (Webb and Kamber, 2000; Kamber and Webb, 2001; Allwood et al., 2010; Zhao et al., 2021).

As for isotopic compositions, in addition to classic isotopes like C, O, and Sr, which have been used for tracing the carbon source of carbonate (Shields, 2019), calculating formation temperature (Shackleton and Kennett, 1975; Anderson and Arthur, 1983; Hays and Grossman, 1991), and reconstructing seawater Sr strontium isotopic compositions (Shields and Veizer, 2002; Satkoski et al., 2017; Chen et al., 2022), stable Ca and Mg isotopic compositions are recently becoming popular for quantifying early diagenesis (Ahm et al., 2018; Wei et al., 2019) and testing Urey's carbonate–silicate cycle (Blättler and Higgins, 2017) and the global biogeochemical Ca cycle (Fantle and Tipper, 2014; Gussone et al., 2020).

However, in contrast to chert and barite, carbonate is more susceptible to depositional alteration. For example, hydrothermal overprint can affect certain element concentrations of carbonate, such as Mn and Sr (Veizer et al., 1989a), and O and Sr isotopic compositions (Veizer and Compston, 1974; Burke et al., 1982; Shields and Veizer, 2002). Nonetheless, this weakness can sometimes be advantageous. Diagenesis leaves evident traces on carbonate microfacies. For instance, post-depositional alterations occur in freshwater (meteoric), marine, and burial environments and are recorded in thin sections by criteria related to pore-filling cementation, compaction, pressure solution, recrystallization, and dolomitization (Flügel and Munnecke, 2010). Additionally, carbonates may be less ambiguous than chert in some respects because Sr and C isotope studies on the same samples can confirm signatures of their depositional environment and potential hydrothermal overprint (Shields, 2019). Hence, the combination of petrography and geochemistry, as well as sedimentology, can help to distinguish signals of depositional and burial environments and assist in reconstructing environmental conditions and possible biological activities.

1.3 The early Archean carbonates from the East Pilbara Terrane, Western Australia

Chemical carbonate sediments are relatively rare in the EPT, where volcanic sequences are predominantly preserved. Only the SPF dolomitic stromatolites (Hoffman et al., 1999; Van Kranendonk et al., 2003; Allwood et al., 2006; Hickman et al., 2011) and laminated silicified carbonate rocks of the Dresser Formation (Van Kranendonk et al., 2003, 2019b; Hickman and Van Kranendonk, 2012; Runge et al., 2022) have been reported in previous works. However, secondary carbonate minerals are ubiquitous, not only in the EPT greenstone belt but also in all Archean greenstone belts (Roberts, 1987; Veizer et al., 1989a, b; Kitajima et al., 2001; Nakamura and Kato, 2004). Unlike most sedimentary carbonates of marine origin, the carbonates associated with greenstones are described as "hydrothermal"

carbonates by Veizer et al. (1989a). In the EPT, it is common for carbonate minerals to fill the interspaces of pillow basalts. At the beginning of the century, some studies interpreted the pillow basalts as having formed at mid-ocean ridges, and thus, the carbonatization of them due to interaction with CO_2-rich seawater could be regarded as seafloor hydrothermal alteration (Kitajima et al., 2001; Nakamura and Kato, 2002; Yamamoto et al., 2004). Although the mid-ocean ridge model has been replaced by the model of a thick oceanic plateau in subsequent studies (Smithies et al., 2003, 2005, 2007; Van Kranendonk, 2006; Van Kranendonk et al., 2007a, b), carbonates within those settings may still provide a unique window into the hydrothermal alteration of oceanic crust, helping to decipher the early Archean ocean that was fed by hydrothermal fluids.

2. Aims and scope of this work

Research on the EPT carbonates of various facies is limited, with many still in the preliminary stage and focusing on macro- and micro-morphologies or whole-rock geochemistry. Previous works have extensively studied the SPF stromatolites, which are not the primary focus of this research. Instead, this work focuses on two types of carbonates that have been rarely studied before: interstitial carbonates within the interspaces between pillow basalts and sedimentary carbonates. To better understand the diverse EPT carbonates, distinguish primary and secondary signatures, and further decode their depositional environments, several methods were employed, including detailed microfacies analysis using a microscope and Raman spectrometer, in-situ geochemical analysis using micro-XRF based on thin sections, high spatial-resolution geochemical analysis via micro-drilling (ICP-OES, ICP-MS) to determine elemental concentrations and isotopic compositions (stable C and O, radiogenic Sr isotopes), as well as numerical modeling. The results and analyses are presented in three manuscripts along with two chapters of several application cases. The following provides brief introductions to each of the manuscripts.

Chapter 2 aims to determine the mineral constituents of the three types of EPT carbonates, understand mineral transformations during later alteration, identify pristine information from diagenetic overprints, and deduce the formation pathways and environments. In this section, more than 100 thin sections were observed to study protolith and secondary mineral assemblages, and any ambiguous opaque minerals were checked via Raman spectra analysis. Subsequently, in-situ geochemical analysis was conducted on typical thin sections, especially those of interstitial carbonates which are thought to be good proxies for basalt-seawater interaction. Many intriguing findings from the in-situ geochemical analysis prompted me to study the carbon isotopic compositions not only of the targeted carbonates but also of some carbonates in syngenetic and later tectonic vein systems, to trace the carbon source of carbonates. Based on the results, three important carbonate factories in the early Archean have been proposed, with descriptions of mineralogy, characteristic carbon isotopic composition, formation pathway, and depositional environment. Some primary and secondary carbonate samples were further drilled to obtain small columns and were digested by acid to measure precise geochemical compositions (Chapter 3). Additionally, some pillow basalts from the 3.46 Ga Apex Basalt were found to preserve pristine interstitial carbonate and

to show clear and unaltered volcanic concentric structures. Hence, they were chosen to study their geochemical compositions via acid digestion (Chapter 4). Therefore, Chapter 2 is of great significance as the foundation for the following chapters.

Chapter 3 aims to study the geochemical signatures of pristine and secondary carbonates, and investigate the impact of diagenesis on elemental concentrations, REE+Y patterns, and $^{87}Sr/^{86}Sr$ values. Two major findings are briefly introduced here: (1) the pristine signatures of seawater and the seawater-derived low-temperature hydrothermal fluid at 3.5 Ga are recorded in the interstitial carbonates from the Dresser Formation and Apex Basalt, respectively. These can be used as endmembers in future work. (2) Most EPT carbonates are partly altered, and deviations in geochemical compositions between them and the two fluid endmembers show that the multi-element behaviors during post-depositional alterations are source-dependent, determined by both protolith and fluids. However, the results of this part raise two questions: Why are the $^{87}Sr/^{86}Sr$ values of the seawater-derived low-temperature hydrothermal fluids higher than seawater at 3.5 Ga (they are supposed to be the same or the former lower)? And when were the primary Apex interstitial carbonates generated, in the early Archean or later?

Chapter 4 aims to answer the two aforementioned questions, as well as to test the basaltic origin of some important elements that are personally sorted into carbonate-related, REE+Y, and bioessential elements. The well-preserved volcanic concentric structures make it possible to study the geochemistry of small domains within Apex pillow basalts, from the basaltic core to the margin and breccia. In this part, the errorchron age of the Rb-Sr isotopic system indicates that carbonatization was syn-depositional or not much later than the eruption of Apex Basalt, and the Rb-Sr isotopic compositions were not reset after that. The finding that the whole-rock $^{87}Sr/^{86}Sr$ value at the metamorphic event was much higher than that of contemporary seawater can explain the intermediate $^{87}Sr/^{86}Sr$ values of seawater-derived low-temperature hydrothermal fluids. In addition, the element mobility during carbonatization of pillow basalts is also discussed in detail.

Chapter 5 aims to use the oxygen isotopes from Chapter 2, as well as Ca-Sr concentrations and $^{87}Sr/^{86}Sr$ values of the EPT carbonates from Chapter 3, to reconstruct their formation temperatures and the Sr/Ca ratios of the fluids from which they precipitated. The chapter also aims to study the water-rock reactions during alteration using numerical modeling based on the mass balance principle. However, the work is limited by some key reference values and is still in progress. Several estimates using different references are presented in this chapter.

Chapter 6 aims to test the authenticity of the controversial "oldest stromatolites" on Earth from the Isua Supracrustal Belt (ISB), Greenland, according to the findings in the study of the EPT carbonates. It is concluded that the controversial stromatolite-like rocks may be marine sedimentary carbonate rather than true stromatolites.

Chapter 7 is a final summary and outlook based on some problems found in this dissertation's framework.

References

Ahm, A.-S. C., Bjerrum, C. J., Blättler, C. L., Swart, P. K., and Higgins, J. A.: Quantifying early marine diagenesis in shallow-water carbonate sediments, Geochimica et Cosmochimica Acta, 236, 140–159, 2018.

Allwood, A. C., Walter, M. R., Kamber, B. S., Marshall, C. P., and Burch, I. W.: Stromatolite reef from the Early Archaean era of Australia, Nature, 441, 714–718, 2006.

Allwood, A. C., Walter, M. R., Burch, I. W., and Kamber, B. S.: 3.43 billion-year-old stromatolite reef from the Pilbara Craton of Western Australia: ecosystem-scale insights to early life on Earth, Precambrian Research, 158, 198–227, 2007.

Allwood, A. C., Grotzinger, J. P., Knoll, A. H., Burch, I. W., Anderson, M. S., Coleman, M. L., and Kanik, I.: Controls on development and diversity of Early Archean stromatolites, Proceedings of the National Academy of Sciences, 106, 9548–9555, 2009.

Allwood, A. C., Kamber, B. S., Walter, M. R., Burch, I. W., and Kanik, I.: Trace elements record depositional history of an Early Archean stromatolitic carbonate platform, Chemical Geology, 270, 148–163, 2010.

Allwood, A. C., Rosing, M. T., Flannery, D. T., Hurowitz, J. A., and Heirwegh, C. M.: Reassessing evidence of life in 3,700-million-year-old rocks of Greenland, Nature, 563, 241–244, 2018.

Anderson, T. F., and Arthur, M. A.: Stable isotopes of oxygen and carbon and their application to sedimentologic and paleoenvironmental problems. Stable Isotopes in Sedimentary Geology, 1983.

Awramik, S. M., J. W. Schopf, and M. R. Walter.: Filamentous fossil bacteria from the Archean of Western Australia, Developments in Precambrian Geology, Elsevier, 7, 249–266, 1983.

Banerjee, N. R., Simonetti, A., Furnes, H., Muehlenbachs, K., Staudigel, H., Heaman, L., and Van Kranendonk, M. J.: Direct dating of Archean microbial ichnofossils, Geology, 35, 6, 487–490, 2007.

Baumgartner, R. J., Van Kranendonk, M. J., Wacey, D., Fiorentini, M. L., Saunders, M., Caruso, S., Pages, A., Homann, M., and Guagliardo, P.: Nano- porous pyrite and organic matter in 3.5-billion-year-old stromatolites record primordial life, Geology, 47, 1039–1043, 2019.

Baumgartner, R. J., Caruso, S., Fiorentini, M. L., Van Kranendonk, M. J., Martin, L., Jeon, H., Pagès, A., and Wacey, D.: Sulfidization of 3.48 billion-year-old stromatolites of the Dresser Formation, Pilbara Craton: Constraints from in-situ sulfur isotope analysis of pyrite, Chemical Geology, 538, 119 488, 2020a.

Baumgartner, R. J., Van Kranendonk, M. J., Fiorentini, M. L., Pagès, A., Wacey, D., Kong, C., Saunders, M., and Ryan, C.: Formation of micro-spherulitic barite in association with organic matter within sulfidized stromatolites of the 3.48 billion-year-old Dresser Formation, Pilbara Craton, Geobiology, 18, 415–425, 2020b.

Baumgartner, R. J., Van Kranendonk, M. J., Pagès, A., Fiorentini, M. L., Wacey, D., and Ryan, C.: Accumulation of transition metals and metalloids in sulfidized stromatolites of the 3.48 billion–year–old Dresser Formation, Pilbara Craton, Precambrian Research, 337, 105 534, 2020c.

Berner, R. A.: Early diagenesis: a theoretical approach, 1, Princeton University Press, 1980.

Blättler, C. L. and Higgins, J. A.: Testing Urey's carbonate–silicate cycle using the calcium isotopic composition of sedimentary carbonates, Earth and Planetary Science Letters, 479, 241-251, 2017.

Bontognali, T. R., Sessions, A. L., Allwood, A. C., Fischer, W. W., Grotzinger, J. P., Summons, R. E., and Eiler, J. M.: Sulfur isotopes of organic matter preserved in 3.45-billion-year-old stromatolites

reveal microbial metabolism, Proceedings of the National Academy of Sciences, 109, 15 146–15 151, 2012.

Brasier, M. D., Green, O. R., Jephcoat, A. P., Kleppe, A. K., Van Kranendonk, M. J., Lindsay, J. F., Steele, A., and Grassineau, N. V.: Questioning the evidence for Earth's oldest fossils, Nature, 416, 76–81, 2002.

Brasier, M. D., Green, O. R., Lindsay, J. F., McLoughlin, N., Steele, A., and Stoakes, C.: Critical testing of Earth's oldest putative fossil assemblage from the 3.5 Ga Apex chert, Chinaman Creek, Western Australia, Precambrian Research, 140, 55–102, 2005

Brasier, M. D., Antcliffe, J., Saunders, M., and Wacey, D.: Changing the picture of Earth's earliest fossils (3.5–1.9 Ga) with new approaches and new discoveries, Proceedings of the National Academy of Sciences, 112, 4859–4864, 2015.

Buick, R. and Dunlop, J.: Evaporitic sediments of early Archaean age from the Warrawoona Group, North Pole, Western Australia, Sedimentology, 37, 247–277, 1990.

Burke, W., Denison, R., Hetherington, E., Koepnick, R., Nelson, H., and Otto, J.: Variation of seawater 87Sr/86Sr throughout Phanerozoic time, Geology, 10, 516–519, 1982.

Chen, X., Zhou, Y., and Shields, G. A.: Progress towards an improved Precambrian seawater $^{87}Sr/^{86}Sr$ curve, Earth-Science Reviews, 224, 103 869, 2022.

Coggon, R. M., Teagle, D. A., Smith-Duque, C. E., Alt, J. C., and Cooper, M. J.: Reconstructing past seawater Mg/Ca and Sr/Ca from mid-ocean ridge flank calcium carbonate veins, Science, 327, 1114–1117, https://doi.org/10.1126/science.1182252, 2010.

Coogan, L. A. and Dosso, S. E.: Alteration of ocean crust provides a strong temperature dependent feedback on the geological carbon cycle and is a primary driver of the Sr-isotopic composition of seawater, Earth and Planetary Science Letters, 415, 38–46, 2015.

Craddock, P. R. and Dauphas, N.: Iron and carbon isotope evidence for microbial iron respiration throughout the Archean, Earth and Planetary Science Letters, 303, 121–132, 2011.

Dauphas, N., Van Zuilen, M., Wadhwa, M., Davis, A. M., Marty, B., and Janney, P. E.: Clues from Fe isotope variations on the origin of early Archean BIFs from Greenland, Science, 306, 2077–2080, 2004.

Delarue, F., Robert, F., Derenne, S., Tartèse, R., Jauvion, C., Bernard, S., Pont, S., Gonzalez-Cano, A., Duhamel, R., and Sugitani, K.: Out of rock: A new look at the morphological and geochemical preservation of microfossils from the 3.46 Gyr-old Strelley Pool Formation, Precambrian Research, 336, 105 472, 2020.

Duda, J.-P., Van Kranendonk, M. J., Thiel, V., Ionescu, D., Strauss, H., Schäfer, N., and Reitner, J.: A rare glimpse of Paleoarchean life: Geobiology of an exceptionally preserved microbial mat facies from the 3.4 Ga Strelley Pool Formation, Western Australia, PLoS One, 11, e0147 629, 2016.

Duda, J.-P., Thiel, V., Bauersachs, T., Mißbach, H., Reinhardt, M., Schäfer, N., Van Kranendonk, M. J., and Reitner, J.: Ideas and perspectives: hydrothermally driven redistribution and sequestration of early Archaean biomass–the "hydrothermal pump hypothesis", Biogeosciences, 15, 1535–1548, 2018.

Fantle, M. S. and Tipper, E. T.: Calcium isotopes in the global biogeochemical Ca cycle: Implications for development of a Ca isotope proxy, Earth-Science Reviews, 129, 148-177, 2014.

Fantle, M. S., Barnes, B. D., and Lau, K. V.: The role of diagenesis in shaping the geochemistry of the marine carbonate record, Annual Review of Earth and Planetary Sciences, 48, 549–583, 2020.

Flannery, D. T., Allwood, A. C., Summons, R. E., Williford, K. H., Abbey, W., Matys, E. D., and

Ferralis, N.: Spatially-resolved isotopic study of carbon trapped in 3.43 Ga Strelley Pool Formation stromatolites, Geochimica et Cosmochimica Acta, 223, 21–35, 2018.

Flügel, E. and Munnecke, A.: Microfacies of carbonate rocks: analysis, interpretation and application, vol. 976, Springer, 2nd edn., 2010.

Folk, R. L.: Some aspects of recrystallization of ancient limestones, AAPG Bulletin, 48, 525–525, https://doi.org/10.1306/BC743C61-16BE- 11D7-8645000102C1865D, 1964.

Furnes, H., Banerjee, N. R., Muehlenbachs, K., Staudigel, H., and de Wit, M.: Early life recorded in Archean pillow lavas, Science, 304, 578–581, https://doi.org/10.1126/science.1095858, 2004.

Gussone, N., Ahm, A.-S. C., Lau, K. V., and Bradbury, H. J.: Calcium isotopes in deep time: potential and limitations, Chemical Geology, 544, 119 601, https://doi.org/10.1016/j.chemgeo.2020.119601, 2020.

Hays, P. D. and Grossman, E. L.: Oxygen isotopes in meteoric calcite cements as indicators of continental paleoclimate, Geology, 19, 441–444, https://doi.org/10.1130/0091-7613(1991)019<0441:OIIMCC>2.3.CO;2, 1991.

Hickman, A. H.: Geology of the Pilbara Block and its environments, Western Australia Geological Survey, Bulletin 127, 1983.

Hickman, A. H. and Van Kranendonk, M. J.: Early Earth evolution: evidence from the 3.5–1.8 Ga geological history of the Pilbara region of Western Australia, Episodes Journal of International Geoscience, 35, 283–297, https://doi.org/10.18814/epiiugs/2012/v35i1/028, 2012.

Hickman, A. H., Van Kranendonk, M. J., and Grey, K.: State Geoheritage Reserve R50149 (Trendall Reserve), North Pole, Pilbara Craton, Western Australia: Geology and Evidence for Early Archean Life, Geological Survey of Western Australia Perth, Australia, 2011.

Hickman-Lewis, K., Garwood, R. J., Brasier, M. D., Goral, T., Jiang, H., McLoughlin, N., and Wacey, D.: Carbonaceous microstructures from sedimentary laminated chert within the 3.46 Ga Apex Basalt, Chinaman Creek locality, Pilbara, Western Australia, Precambrian Research, 278, 161–178, https://doi.org/10.1016/j.precamres.2016.03.013, 2016.

Hickman-Lewis, K., Westall, F., and Cavalazzi, B.: Trace of early life in the Barberton greenstone belt, in: Earth's Oldest Rocks, edited by Van Kranendonk, M., Bennett, V., and Hoffmann, E., pp. 1029–1058, Elsevier, https://hal.science/hal-03041208, 2019.

Hofmann, H., Grey, K., Hickman, A., and Thorpe, R.: Origin of 3.45 Ga coniform stromatolites in Warrawoona group, Western Australia, Geological Society of America Bulletin, 111, 1256–1262, https://doi.org/10.1130/0016-7606(1999)111<1256:OOGCSI>2.3.CO;2, 1999.

James, N. P. and Ginsburg, R. N.: The seaward margin of Belize barrier and atoll reefs: International Association of Sedimentologists Special Publication 3, 1979.

Kamber, B. S. and Webb, G. E.: The geochemistry of late Archaean microbial carbonate: implications for ocean chemistry and continental erosion history, Geochimica et Cosmochimica Acta, 65, 2509–2525, https://doi.org/10.1016/S0016-7037(01)00613-5, 2001.

Kitajima, K., Maruyama, S., Utsunomiya, S., and Liou, J.: Seafloor hydrothermal alteration at an Archaean mid-ocean ridge, Journal of Metamorphic Geology, 19, 583–599, https://doi.org/10.1046/j.0263-4929.2001.00330.x, 2001.

Kozawa, T., Sugitani, K., Oehler, D. Z., House, C. H., Saito, I., Watanabe, T., and Gotoh, T.: Early Archean planktonic mode of life: Implications from fluid dynamics of lenticular microfossils, Geobiology, 17, 113–126, https://doi.org/10.1111/gbi.12319, 2019.

Lambert, I., Donnelly, T., Dunlop, J., Groves, and DI: Stable isotopic compositions of early Archaean

sulphate deposits of probable evaporitic and volcanogenic origins, Nature, 276, 808–811, https://doi.org/10.1038/276808a0, 1978.

Lepot, K., Williford, K. H., Ushikubo, T., Sugitani, K., Mimura, K., Spicuzza, M. J., and Valley, J. W.: Texture-specific isotopic compositions in 3.4 Gyr old organic matter support selective preservation in cell-like structures, Geochimica et Cosmochimica Acta, 112, 66–86, https://doi.org/10.1016/j.gca.2013.03.004, 2013.

Lepot, K.: Signatures of early microbial life from the Archean (4 to 2.5 Ga) eon, Earth-Science Reviews, 209, 103296, https://doi.org/10.1016/j.earscirev.2020.103296, 2020.

Marshall, C. P., Love, G. D., Snape, C. E., Hill, A. C., Allwood, A. C., Walter, M. R., Van Kranendonk, M. J., Bowden, S. A., Sylva, S. P., and Summons, R. E.: Structural characterization of kerogen in 3.4 Ga Archaean cherts from the Pilbara Craton, Western Australia, Precambrian Research, 155, 1–23, https://doi.org/10.1016/j.precamres.2006.12.014, 2007.

McLoughlin, N., Wacey, D., Phunguphungu, S., Saunders, M., and Grosch, E. G.: Deconstructing Earth's oldest ichnofossil record from the Pilbara Craton, West Australia: Implications for seeking life in the Archean subseafloor, Geobiology, 18, 525–543, https://doi.org/10.1111/gbi.12399, 2020.

Mojzsis, S. J., Arrhenius, G., McKeegan, K., Harrison, T., Nutman, A., and Friend, C.: Evidence for life on Earth before 3,800 million years ago, Nature, 384, 55–59, https://doi.org/10.1038/384055a0, 1996.

Moore, E. K., Jelen, B. I., Giovannelli, D., Raanan, H., and Falkowski, P. G.: Metal availability and the expanding network of microbial metabolisms in the Archaean eon, Nature Geoscience, 10, 629–636, https://doi.org/10.1038/ngeo3006, 2017.

Morag, N., Williford, K. H., Kitajima, K., Philippot, P., Van Kranendonk, M. J., Lepot, K., Thomazo, C., and Valley, J. W.: Microstructure- specific carbon isotopic signatures of organic matter from 3.5 Ga cherts of the Pilbara Craton support a biologic origin, Precambrian Research, 275, 429–449, https://doi.org/10.1016/j.precamres.2016.01.014, 2016.

Nakamura, K. and Kato, Y.: Carbonate minerals in the Warrawoona Group, Pilbara Craton: Implications for continental crust, life, and global carbon cycle in the Early Archean, Resource Geology, 52, 91–100, https://doi.org/10.1111/j.1751-3928.2002.tb00122.x, 2002.

Nakamura, K. and Kato, Y.: Carbonatization of oceanic crust by the seafloor hydrothermal activity and its significance as a CO2 sink in the Early Archean, Geochimica et Cosmochimica Acta, 68, 4595–4618, https://doi.org/10.1016/j.gca.2004.05.023, 2004.

Nutman, A. P., Friend, C. R., Bennett, V. C., Wright, D., and Norman, M. D.: ≥ 3700 Ma pre-metamorphic dolomite formed by microbial mediation in the Isua supracrustal belt (W. Greenland): simple evidence for early life?, Precambrian Research, 183, 725–737, https://doi.org/10.1016/j.precamres.2010.08.006, 2010.

Nutman, A. P., Bennett, V. C., Friend, C. R., Hidaka, H., Yi, K., Lee, S. R., and Kamiichi, T.: The Itsaq Gneiss Complex of Greenland: Episodic 3900 to 3660 Ma juvenile crust formation and recycling in the 3660 to 3600 Ma Isukasian orogeny, American Journal of Science, 313, 877–911, https://doi.org/10.2475/09.2013.03, 2013.

Nutman, A. P., Bennett, V. C., Friend, C. R., Van Kranendonk, M. J., and Chivas, A. R.: Rapid emergence of life shown by discovery of 3,700-million-year-old microbial structures, Nature, 537, 535–538, https://doi.org/10.1038/nature19355, 2016.

Nutman, A. P., Bennett, V. C., Friend, C. R., Van Kranendonk, M. J., Rothacker, L., and Chivas, A. R.: Cross-examining Earth's oldest stromatolites: Seeing through the effects of heterogeneous

deformation, metamorphism and metasomatism affecting Isua (Greenland) 3700 Ma sedimentary rocks, Precambrian Research, 331, 105 347, https://doi.org/10.1016/j.precamres.2019.105347, 2019.

Nutman, A. P., Bennett, V. C., Friend, C. R., and Van Kranendonk, M. J.: In support of rare relict 3700 Ma stromatolites from Isua (Green- land), Earth and Planetary Science Letters, 562, 116 850, https://doi.org/10.1016/j.epsl.2021.116850, 2021.

Oehler, D. Z., Robert, F., Walter, M. R., Sugitani, K., Allwood, A., Meibom, A., Mostefaoui, S., Selo, M., Thomen, A., and Gibson, E. K.: NanoSIMS: insights to biogenicity and syngeneity of Archaean carbonaceous structures, Precambrian Research, 173, 70–78, https://doi.org/10.1016/j.precamres.2009.01.001, 2009.

Pei, Y.: A geobiological approach to carbonate factories and ecosystem changes across the Permian–Triassic boundary, Ph.D. thesis, University of Göttingen, Germany, http://dx.doi.org/10.53846/goediss-9160, 2022.

Pei, Y., Duda, J.-P., and Reitner, J.: Sedimentary factories and ecosystem change across the Permian–Triassic Critical Interval (P–TrCI): insights from the Xiakou area (South China), PalZ, pp. 709–725, https://doi.org/10.1007/s12542-020-00530-x, 2021.

Pettijohn, F. J.: Paleocurrents of Lake Superior Precambrian quartzites, Geological Society of America Bulletin, 68, 4, 469-480, 1957.

Philippot, P., van Zuilen, M., Lepot, K., Thomazo, C., Farquhar, J., and Van Kranendonk, M. J.: Early Archaean microorganisms preferred elemental sulfur, not sulfate, Science, 317, 1534–1537, https://doi.org/10.1126/science.1145861, 2007.

Pidgeon, R. T.: 3450-my-old volcanics in the Archaean layered greenstone succession of the Pilbara Block, Western Australia, Earth and Planetary Science Letters, 37, 3, 421-428, 1978.

Rasmussen, B., Fletcher, I. R., and Muhling, J. R.: In situ U–Pb dating and element mapping of three generations of monazite: unravelling cryptic tectonothermal events in low-grade terranes, Geochimica et Cosmochimica Acta, 71, 670–690, https://doi.org/10.1016/j.gca.2006.10.020, 2007.

Reijmer, J. J.: Marine carbonate factories: review and update, Sedimentology, 68, 1729–1796, https://doi.org/10.1111/sed.12878, 2021.

Roberts, R. G.: Ore deposit models# 11. Archean lode gold deposits, Geoscience Canada, 14, 37–52, https://id.erudit.org/iderudit/geocan14_1art02, 1987.

Rollinson, H.: Metamorphic history suggested by garnet-growth chronologies in the Isua greenstone belt, west Greenland, Precambrian Research, 126, 181-196, 2003.

Rosing, M. T.: 13C-depleted carbon microparticles in> 3700-Ma sea-floor sedimentary rocks from West Greenland, Science, 283, 674–676, https://doi.org/10.1126/science.283.5402.674, 1999.

Rouillard, J., Van Kranendonk, M. J., Lalonde, S., Gong, J., and Van Zuilen, M. A.: Correlating trace element compositions, petrol- ogy, and Raman spectroscopy data in the 3.46 Ga Apex chert, Pilbara Craton, Australia, Precambrian Research, 366, 106415, https://doi.org/10.1016/j.precamres.2021.106415, 2021.

Runge, E. A., Duda, J.-P., Van Kranendonk, M. J., and Reitner, J.: Earth's oldest tsunami deposit? Early Archaean high-energy sediments in the ca 3.48 Ga Dresser Formation (Pilbara, Western Australia), The Depositional Record, 8, 590–602, https://doi.org/10.1002/dep2.175, 2022.

Satkoski, A. M., Fralick, P., Beard, B. L., and Johnson, C. M.: Initiation of modern-style plate tectonics recorded in MesoArchean marine chemical sediments, Geochimica et Cosmochimica Acta, 209, 216–232, https://doi.org/10.1016/j.gca.2017.04.024, 2017.

Schidlowski, M., Appel, P. W., Eichmann, R., and Junge, C. E.: Carbon isotope geochemistry of the 3.7× 109-yr-old Isua sediments, West Greenland: implications for the Archaean carbon and oxygen cycles. Geochimica et Cosmochimica Acta, 43, 2, 189-199, https://doi.org/10.1016/0016-7037(79)90238-2,1979.

Schlager, W.: Sedimentation rates and growth potential of tropical, cool-water and mud-mound carbonate systems, Geological Society, London, Special Publications, 178, 217–227, https://doi.org/10.1144/GSL.SP.2000.178.01.14, 2000.

Schlager, W.: Benthic carbonate factories of the Phanerozoic, International Journal of Earth Sciences, 92, 445–464, https://doi.org/10.1007/s00531-003-0327-x, 2003.

Schlager, W.: Carbonate sedimentology and sequence stratigraphy, 8, SEPM Soc for Sed Geology, 2005.

Schopf, J.: Paleobiology of Archean, The Proterozoic Biosphere. A Multidisciplinary Approach, pp. 25–39, 1992.

Schopf, J. W.: Microfossils of the Early Archean Apex chert: new evidence of the antiquity of life, Science, 260, 640–646, https://doi.org/10.1126/science.260.5108.640, 1993.

Schopf, J. W., Kudryavtsev, A. B., Agresti, D. G., Wdowiak, T. J., and Czaja, A. D.: Laser–Raman imagery of Earth's earliest fossils, Nature, 416, 73–76, https://doi.org/10.1038/416073a, 2002.

Schopf, J. W., Kudryavtsev, A. B., Osterhout, J. T., Williford, K. H., Kitajima, K., Valley, J. W., and Sugitani, K.: An anaerobic 3400 Ma shallow-water microbial consortium: Presumptive evidence of Earth's Paleoarchean anoxic atmosphere, Precambrian Research, 299, 309–318, https://doi.org/10.1016/j.precamres.2017.07.021, 2017.

Schopf, J. W., Kitajima, K., Spicuzza, M. J., Kudryavtsev, A. B., and Valley, J. W.: SIMS analyses of the oldest known assemblage of microfossils document their taxon-correlated carbon isotope compositions, Proceedings of the National Academy of Sciences, 115, 53– 58, https://doi.org/10.1073/pnas.1718063115, 2018.

Sforna, M.-C., Van Zuilen, M., and Philippot, P.: Structural characterization by Raman hyperspectral mapping of organic carbon in the 3.46 billion-year-old Apex chert, Western Australia, Geochimica et Cosmochimica Acta, 124, 18–33, https://doi.org/10.1016/j.gca.2013.09.031, 2014.

Shackleton, N. J. and Kennett, J. P.: Paleotemperature history of the Cenozoic and the initiation of Antarctic glaciation: oxygen and carbon isotope analyses in DSDP Sites 277, 279, and 281, Initial Reports Deep Sea Drilling Project, 29, 743–755, 1975.

Shen, Y., Buick, R., and Canfield, D.: Isotopic evidence for microbial sulphate reduction in the early Archaean era, Nature, 410, 77–81, https://doi.org/10.1038/35065071, 2001.

Shen, Y., Farquhar, J., Masterson, A., Kaufman, A. J., and Buick, R.: Evaluating the role of microbial sulfate reduction in the early Archean using quadruple isotope systematics, Earth and Planetary Science Letters, 279, 3-4, 383-391, https://doi.org/10.1016/j.epsl.2009.01.018, 2009.

Shields, G. and Veizer, J.: Precambrian marine carbonate isotope database: Version 1.1, Geochemistry, Geophysics, Geosystems, 3, 1–of, https://doi.org/10.1029/2001GC000266, 2002.

Shields, G. A.: Implications of Carbonate and Chert Isotope Records for the Early Earth, in: Earth's Oldest Rocks, edited by Van Kranendonk, M., Bennett, V., and Hoffmann, J., pp. 901–912, Elsevier, 2019.

Smithies, R., Champion, D., and Cassidy, K.: Formation of Earth's early Archaean continental crust, Precambrian Research, 127, 89–101, https://doi.org/10.1016/S0301-9268(03)00182-7, 2003.

Smithies, R. H., Champion, D. C., Van Kranendonk, M. J., Howard, H. M., and Hickman, A. H.:

Modern-style subduction processes in the Mesoarchaean: geochemical evidence from the 3.12 Ga Whundo intra-oceanic arc, Earth and Planetary Science Letters, 231, 221–237, https://doi.org/10.1016/j.epsl.2004.12.026, 2005.

Smithies, R. H., Champion, D. C., and Van Kranendonk, M. J.: The oldest well-preserved felsic volcanic rocks on Earth: Geochemical clues to the early evolution of the Pilbara Supergroup and implications for the growth of a Paleoarchean protocontinent, in: Earth's Oldest Rocks, edited by Van Kranendonk, M., Smithies, R., and Bennett, V., vol. Developments in Precambrian Geology 15, pp. 339–367, Elsevier,Amsterdam, https://doi.org/10.1016/S0166-2635(07)15042-8, 2007.

Sugitani, K., Lepot, K., Nagaoka, T., Mimura, K., Van Kranendonk, M., Oehler, D. Z., and Walter, M. R.: Biogenicity of morphologically di- verse carbonaceous microstructures from the ca. 3400 Ma Strelley Pool Formation, in the Pilbara Craton, Western Australia, Astrobiology, 10, 899–920, https://doi.org/10.1089/ast.2010.0513, 2010.

Sugitani, K., Mimura, K., Nagaoka, T., Lepot, K., and Takeuchi, M.: Microfossil assemblage from the 3400 Ma Strelley Pool Formation in the Pilbara Craton, Western Australia: results form a new locality, Precambrian Research, 226, 59–74, https://doi.org/10.1016/j.precamres.2012.11.005, 2013.

Sugitani, K., Mimura, K., Takeuchi, M., Yamaguchi, T., Suzuki, K., Senda, R., Asahara, Y., Wallis, S., and Van Kranendonk, M.: A Paleoarchean coastal hydrothermal field inhabited by diverse microbial communities: the Strelley Pool Formation, Pilbara Craton, Western Australia, Geobiology, 13, 522–545, https://doi.org/10.1111/gbi.12150, 2015a.

Sugitani, K., Mimura, K., Takeuchi, M., Lepot, K., Ito, S., and Javaux, E.: Early evolution of large micro-organisms with cytological complexity revealed by microanalyses of 3.4 Ga organic-walled microfossils, Geobiology, 13, 507–521, https://doi.org/10.1111/gbi.12148, 2015b.

Sugitani, K., Kohama, T., Mimura, K., Takeuchi, M., Senda, R., and Morimoto, H.: Speciation of Paleoarchean life demonstrated by analysis of the morphological variation of lenticular microfossils from the Pilbara Craton, Australia, Astrobiology, 18, 1057–1070, https://doi.org/10.1089/ast.2017.1799, 2018.

Tice, M. M., Bostick, B. C., and Lowe, D. R.: Thermal history of the 3.5–3.2 Ga Onverwacht and Fig Tree Groups, Barberton greenstone belt, South Africa, inferred by Raman microspectroscopy of carbonaceous material. Geology, 32, 37-40, https://doi.org/10.1130/G19915.1, 2004.

Ueno, Y., Isozaki, Y., Yurimoto, H., and Maruyama, S.: Carbon isotopic signatures of individual Archean microfossils (?) from Western Australia, International Geology Review, 43, 196–212, https://doi.org/10.1080/00206810109465008, 2001.

Ueno, Y., Yamada, K., Yoshida, N., Maruyama, S., and Isozaki, Y.: Evidence from fluid inclusions for microbial methanogenesis in the early Archaean era, Nature, 440, 516–519, https://doi.org/10.1038/nature04584, 2006.

Van Kranendonk, M. J.: Volcanic degassing, hydrothermal circulation and the flourishing of early life on Earth: A review of the evidence from ca. 3490-3240 Ma rocks of the Pilbara Supergroup, Pilbara Craton, Western Australia, Earth-Science Reviews, 74, 197–240, https://doi.org/10.1016/j.earscirev.2005.09.005, 2006.

Van Kranendonk, M. J.: A review of the evidence for putative Paleoarchean life in the Pilbara Craton, Western Australia, Developments in Precambrian Geology, 15, 855–877, https://doi.org/10.1016/S0166-2635(07)15072-6, 2007.

Van Kranendonk, M. J.., Hickman, A. H., Smithies, R. H., Nelson, D. R., and Pike, G.: Geology and

tectonic evolution of the Archean North Pilbara terrain, Pilbara Craton, Western Australia, Economic Geology, 97, 695–732, https://doi.org/10.2113/gsecongeo.97.4.695, 2002.

Van Kranendonk, M. J., Webb, G. E., and Kamber, B. S.: Geological and trace element evidence for a marine sedimentary environment of deposition and biogenicity of 3.45 Ga stromatolitic carbonates in the Pilbara Craton, and support for a reducing Archaean ocean, Geobiology, 1, 91–108, https://doi.org/10.1046/j.1472-4669.2003.00014.x, 2003.

Van Kranendonk, M. J., Hickman, A. H., and Huston, D. L.: Geology and Mineralization of the East Pilbara d A Field Guide, Western Australia Geological Survey. Record 2006/16, 2006.

Van Kranendonk, M. J., Hugh Smithies, R., Hickman, A. H., and Champion, D.: Secular tectonic evolution of Archean continental crust: interplay between horizontal and vertical processes in the formation of the Pilbara Craton, Australia, Terra Nova, 19, 1–38, https://doi.org/10.1111/j.1365-3121.2006.00723.x, 2007a.

Van Kranendonk, M. J., Smithies, R. H., Hickman, A. H., and Champion, D. C.: Paleoarchean development of a continental nu- cleus: the East Pilbara terrane of the Pilbara craton, Western Australia, Developments in Precambrian geology, 15, 307–337, https://doi.org/10.1016/S0166-2635(07)15041-6, 2007b.

Van Kranendonk, M. J., Philippot, P., Lepot, K., Bodorkos, S., and Pirajno, F.: Geological setting of Earth's oldest fossils in the ca. 3.5 Ga Dresser formation, Pilbara Craton, Western Australia, Precambrian Research, 167, 93–124, https://doi.org/10.1016/j.precamres.2008.07.003, 2008.

Van Kranendonk, M. J., Smithies, R. H., Hickman, A. H., and Champion, D. C.: Paleoarchean development of a continental nucleus: the East Pilbara Terrane of the Pilbara Craton, Western Australia, in: Earth's Oldest Rocks, edited by Van Kranendonk, M., Bennett, V., and Hoffmann, J., pp. 437–462, Elsevier, 2019a.

Van Kranendonk, M., Djokic, T., Poole, G., Tadbiri, S., Steller, L., and Baumgartner, R.: Depositional Setting of the Fossiliferous, ca.3480 Ma Dresser Formation, Pilbara Craton: A Review, in: Earth's Oldest Rocks, edited by Van Kranendonk, M., Bennett, V., and Hoffmann, J., pp. 985–1006, Elsevier, 2019b.

van Zuilen, M. A., Chaussidon, M., Rollion-Bard, C., and Marty, B.: Carbonaceous cherts of the Barberton Greenstone Belt, South Africa: Isotopic, chemical and structural characteristics of individual microstructures, Geochimica et Cosmochimica Acta, 71, 655–669, https://doi.org/10.1016/j.gca.2006.09.029, 2007.

van Zuilen, M. A.: Proposed early signs of life not set in stone, Nature, pp. 190–191, https://doi.org/10.1038/d41586-018-06994-x, 2018.

Veizer, J. and Compston, W.: $^{87}Sr/^{86}Sr$ composition of seawater during the Phanerozoic, Geochimica et Cosmochimica Acta, 38, 1461–1484, https://doi.org/10.1016/0016-7037(74)90099-4, 1974.

Veizer, J. and Compston, W.: $^{87}Sr/^{86}Sr$ in Precambrian carbonates as an index of crustal evolution, Geochimica et Cosmochimica Acta, 40, 905–914, https://doi.org/10.1016/0016-7037(76)90139-3, 1976.

Veizer, J. and Hoefs, J.: The nature of O^{18}/O^{16} and C^{13}/C^{12} secular trends in sedimentary carbonate rocks, Geochimica et Cosmochimica Acta, 40, 1387–1395, https://doi.org/10.1016/0016-7037(76)90129-0, 1976.

Veizer, J., Compston, W., Hoefs, J., and Nielsen, H.: Mantle buffering of the early oceans, Naturwissenschaften, 69, 173–180, https://doi.org/10.1007/BF00364890, 1982.

Veizer, J., Hoefs, J., Ridler, R., Jensen, L., and Lowe, D.: Geochemistry of Precambrian carbonates: I.

Archean hydrothermal systems, Geochimica et Cosmochimica Acta, 53, 845–857, https://doi.org/10.1016/0016-7037(89)90030-6, 1989a.

Veizer, J., Hoefs, J., Lowe, D., and Thurston, P.: Geochemistry of Precambrian carbonates: II. Archean greenstone belts and Archean sea water, Geochimica et Cosmochimica Acta, 53, 859–871, https://doi.org/10.1016/0016-7037(89)90031-8, 1989b.

Veizer, J., Clayton, R., and Hinton, R.: Geochemistry of Precambrian carbonates: IV. Early Paleoproterozoic (2.25 ± 0.25 Ga) seawater, Geochimica et Cosmochimica Acta, 56, 875–885, https://doi.org/10.1016/0016-7037(92)90033-F, 1992.

Veizer, J., Ala, D., Azmy, K., Bruckschen, P., Buhl, D., Bruhn, F., Carden, G. A., Diener, A., Ebneth, S., Godderis, Y., et al.: $^{87}Sr/^{86}Sr$, $\delta^{13}C$ and $\delta^{18}O$ evolution of Phanerozoic seawater, Chemical geology, 161, 59–88, https://doi.org/10.1016/S0009-2541(99)00081-9, 1999.

Wacey, D., McLoughlin, N., Whitehouse, M. J., and Kilburn, M. R.: Two coexisting sulfur metabolisms in a ca. 3400 Ma sandstone, Geology, 38, 1115–1118, https://doi.org/10.1130/G31329.1, 2010.

Wacey, D., Kilburn, M. R., Saunders, M., Cliff, J., and Brasier, M. D.: Microfossils of sulphur-metabolizing cells in 3.4-billion-year-old rocks of Western Australia, Nature Geoscience, 4, 698–702, https://doi.org/10.1038/ngeo1238, 2011.

Wacey, D., Noffke, N., Saunders, M., Guagliardo, P., and Pyle, D. M.: Volcanogenic pseudo-fossils from the 3.48 Ga dresser formation, Pilbara, Western Australia, Astrobiology, 18, 539–555, https://doi.org/10.1089/ast.2017.1734, 2018.

Walter, M., Buick, R., and Dunlop, J.: Stromatolites 3,400–3,500 Myr old from the North pole area, Western Australia, Nature, 284, 443–445, 1980.

Webb, G. E. and Kamber, B. S.: Rare earth elements in Holocene reefal microbialites: a new shallow seawater proxy, Geochimica et Cosmochimica Acta, 64, 1557–1565, https://doi.org/10.1016/S0016-7037(99)00400-7, 2000.

Wei, G.-Y., vS Hood, A., Chen, X., Li, D., Wei, W., Wen, B., Gong, Z., Yang, T., Zhang, Z.-F., and Ling, H.-F.: Ca and Sr isotope constraints on the formation of the Marinoan cap dolostones, Earth and Planetary Science Letters, 511, 202–212, https://doi.org/10.1016/j.epsl.2019.01.024, 2019.

Yamamoto, K., Itoh, N., Matsumoto, T., Tanaka, T., and Adachi, M.: Geochemistry of Precambrian carbonate intercalated in pillows and its host basalt: implications for the REE composition of circa 3.4 Ga seawater, Precambrian Research, 135, 331–344, https://doi.org/10.1016/j.precamres.2004.09.006, 2004.

Yoshiya, K., Sawaki, Y., Hirata, T., Maruyama, S., and Komiya, T.: In-situ iron isotope analysis of pyrites in ~3.7 Ga sedimentary protoliths from the Isua supracrustal belt, southern West Greenland, Chemical Geology, 401, 126–139, https://doi.org/10.1016/j.chemgeo.2015.02.022, 2015.

Zawaski, M. J., Kelly, N. M., Orlandini, O. F., Nichols, C. I., Allwood, A. C., and Mojzsis, S. J.: Reappraisal of purported ca. 3.7 Ga stromatolites from the Isua Supracrustal Belt (West Greenland) from detailed chemical and structural analysis, Earth and Planetary Science Letters, 545, 116 409, https://doi.org/10.1016/j.epsl.2020.116409, 2020.

Zawaski, M. J., Kelly, N. M., Orlandini, O. F., Nichols, C. I., Allwood, A. C., and Mojzsis, S. J.: Reply: The Isua (Greenland)" relict stromatolites" cannot be confidently interpreted as original sedimentary structures, Earth and Planetary Science Letters, 562, 116 851, https://doi.org/10.1016/j.epsl.2021.116851, 2021.

Zhang, S., Zhou, R., and DePaolo, D. J.: The seawater Sr/Ca ratio in the past 50 Myr from bulk

carbonate sediments corrected for diagenesis, Earth and Planetary Science Letters, 530, 115 949, https://doi.org/10.1016/j.epsl.2019.115949, 2020.

Zhao, Y., Wei, W., Li, S., Yang, T., Zhang, R., Somerville, I., Santosh, M., Wei, H., Wu, J., Yang, J., et al.: Rare earth element geochemistry of carbonates as a proxy for deep-time environmental reconstruction, Palaeogeography, Palaeoclimatology, Palaeoecology, 574, 110 443, https://doi.org/10.1016/j.palaeo.2021.110443, 2021.

Chapter-2 Were early Archean carbonate factories major carbon sinks on the Juvenile Earth?

Xiang, W., Duda, J.-P., Pack, A., van Zuilen, M., Reitner, J.*

(submitted to Biogeosciences)

Abstract

Paleoarchean carbonates in the Pilbara Craton (Western Australia) are important archives for early life and environment on early Earth. Amongst others, carbonates occur in interstitial spaces of ca. 3.5–3.4 Ga pillow basalts (North Star-, Mount Ada-, Apex-, and Euro Basalt, Dresser Formation) and associated with bedded deposits (Dresser- and Strelley Pool Formation, Euro Basalt). This study aims to understand the formation and geobiological significance of those early Archean carbonates by investigating their tempo-spatial distribution, petrography, mineralogy, and geochemistry (e.g., trace elemental compositions, $\delta^{13}C$, $\delta^{18}O$). Three carbonate factories are recognized: (i) an oceanic crust factory, (ii) an organo-carbonate factory, and (iii) a microbial factory. The oceanic crust factory is characterized by carbonates formed in interspaces between pillowed basalts ("interstitial carbonates"). These carbonates precipitated inorganically within the oceanic crust from CO_2-enriched seawater and seawater-derived alkaline hydrothermal fluids. The organo-carbonate factory is characterized by carbonate precipitates that are spatially associated with organic materials. The close association with organic matter suggests that the carbonates formed via taphonomy-controlled organo-mineralization, that is, linked to organic macromolecules (either biotic or abiotic) which provided nucleation sites for carbonate crystal growth. Organo-carbonate associations occur in a wide variety of hydrothermally influenced settings ranging from shallow marine environments to terrestrial hydrothermal ponds. The microbial factory included microbial-mediated carbonate precipitation as for instance in stromatolites, which formed through biomineralization controlled by microbial extracellular polymeric substances associated with biofilms. Since (anoxygenic) photoautotrophs might have been involved in carbonate formation, the microbial factory is commonly linked to shallow subaquatic environments, which show less influence by detritus and/or hydrothermal inputs. In case of all three carbonates factories, hydrothermal fluids play a key-role in the formation and preservation of precipitates. For instance, alkaline earth metals and organic materials delivered by fluids may promote carbonate precipitation, whilst soluble silica in the fluids drives early chert formation, delicately preserving authigenic carbonate precipitates and associated features. The implications are manifold: Carbonates of the microbial factory provide valuable insights into the interplay between geological processes and early microbial life, while geochemical information encoded in pristine interstitial carbonates of the oceanic crust factory provide a baseline reference for the early Archean ocean water composition. Regardless of the formation pathway, the Paleoarchean carbonates might have been major carbon sinks on the early Earth, thus modulating climate variability and, by extension,

habitability.

Keyword: Early life, habitability, seafloor hydrothermal alteration, biomineralization, organo-mineralization, Archean seawater composition

Introduction

Carbonate factories are conceptual models encompassing carbonate production and associated processes at various scales, from local precipitation to global sedimentation (Schlager, 2000; Schrag et al., 2013; Reijmer, 2021). Throughout most of Earth's history, carbonate precipitation has been closely linked to biological processes, ranging from direct to indirect precipitation (that is, biologically controlled vs induced) (Flügel and Munnecke, 2010). Over the past couple of years, awareness has risen that carbonate precipitation can also be induced by organic matter (i.e., "organo-mineralization"), regardless of its origin (Addadi and Weiner, 1985; Reitner, 1993; Reitner et al., 1995a, b, 2000, 2001; Trichet and Défarge, 1995; Pei et al., 2021). Based on previous works about "cold-water carbonates" (Lees and Buller, 1972) and "mud-mound carbonates" (Reitner and Neuweiler, 1995), Schlager (2000) summarized three modern carbonate factories in marine benthic systems, namely tropical shallow-water, cool-water, and mud-mound. Since then, the carbonate factories have extended in spatial and temporal scales (Pomar and Hallock, 2008; Reijmer, 2021; Pei et al, 2021; Wang et al., 2023).

Although skeletal, $CaCO_3$-forming eukaryotes (e.g. *Cloudina*) only evolved in the latest Ediacaran Period (Germs, 1972; Grant, 1990), carbonate deposits are widespread throughout the Precambrian (e.g., Grotzinger and Knoll, 1995; Grotzinger and James, 2000; Veizer, 1989a, b; Cantine et al., 2020). Particularly notable is the potential *in situ* precipitation of authigenic carbonates on the seafloor, which is only very rarely known from the Phanerozoic, where it seems to be driven by elevated $CaCO_3$ saturation of seawater associated with widespread anoxia (Grotzinger and Knoll, 1995; Copper, 2002; Pruss et al., 2006; Knoll et al., 2007; Higgins et al. 2009; Pei et al., 2019, 2023). Proposed mechanisms for carbonate formation prior to the advent of biomineralization in the terminal Precambrian include a variety of poorly constrained abiotic and microbial processes (Grotzinger and James, 2000). As a result, the underlying carbonate factories are still poorly understood, which is particularly true for the early Archean, when life still was in its infancy.

The earliest traces of life on our planet are preserved in a variety of different rock types, including banded iron formation (BIF), cherts, as well as (silicified) siliciclastic and carbonate sedimentary rocks (Van Kranendonk, 2006, 2007; Lepot, 2020). Many of those records can be found in the ca. 4.0–3.6 Ga Isua Supracrustal Belt (ISB; West Greenland), the 3.5–3.2 Ga East Pilbara Terrane (EPT; Pilbara Craton, Western Australia), and the 3.6–3.2 Ga Barberton Greenstone belt (BGB; South Africa). In contrast to the highly metamorphic ISB, rocks of the EPT and BGB only underwent regional metamorphism from prehnite-pumpellyite (100–250 °C) to lower greenschist facies (250–300 °C) (Nutman et al., 2019a, b; Van Kranendonk et al., 2019a; Hickman-Lewis et al., 2019).

Rocks of the EPT and BGB show evidence of pervasive carbonatization and silicification by seawater and/or hydrothermal fluids (Kitajima et al., 2001; Nakamura and Kato, 2002, 2004; Terabayashi et al., 2003; Hofmann and Harris, 2008; Hickman-Lewis et al., 2019). At the same time, however, they also preserve primary carbonate precipitates, which may provide important clues to early life and the physicochemical conditions in its habitats. Indeed, for decades researchers have focused on carbonates associated with microbial facies in the ~3.4 Ga Strelley Pool Formation, preserving a wealth of textural and (bio-) geochemical information that is geobiologically significant (e.g., trace elemental compositions, $\delta^{13}C$, $\delta^{18}O$) (Van Kranendonk, 2006, 2007; Allwood et al., 2006, 2007, 2009; Marshall et al., 2007; Wacey, 2010; Bontognali et al, 2012; Duda et al., 2016; Flannery et al., 2018). Notably, however, these carbonates are a minor component in the EPT lithostratigraphy (Van Kranendonk et al., 2007b). The geobiological significance of other carbonates, such as precipitates in the interspaces of (ultra)mafic rocks that possibly formed through seafloor hydrothermal alteration (referred to as "interstitial carbonates" in this work) (Kitajima et al., 2001; Nakamura and Kato, 2002, 2004; Terabayashi et al., 2003), remains poorly constrained.

This study comprehensively investigates early Archean carbonates in the EPT, including interstitial carbonates associated with basalts, carbonate stromatolites and other sedimentary carbonates. The combination of detailed petrography with mineralogical and geochemical analyses (e.g., trace elemental compositions, $\delta^{13}C$, $\delta^{18}O$) provides novel insights into the formation of carbonates during the early Archean. The results of this study demonstrate the presence of various types of carbonate factories on the juvenile Earth which might played a significant role in the early global carbon cycle.

1. Geological settings

The EPT (3.53-3.165 Ga) in Western Australia is famous for its well-preserved Paleoarchean volcano-sedimentary successions, which provide the world's most complete record of the evolution of the geo-, hydro-, bio- and atmosphere on the early Earth (Van Kranendonk et al., 2007a, b; Hickman and Van Kranendonk, 2012a, b). Particularly interesting is the Pilbara Supergroup, a 20 km thick succession of mainly volcanic rocks that can be subdivided into (from bottom to top) the Warrawoona Group (3.53–3.43 Ga), the Kelly Group (3.42–3.32 Ga), the Sulphur Springs Group (3.27–3.23 Ga), and the Soanesville Group (ca. 3.19 Ga) (Van Kranendonk et al., 2002, 2007b; Rasmussen et al., 2007; Hickman and Van Kranendonk, 2012a, b). The lower three groups comprise ultramafic to felsic volcanic rocks, chemical and clastic deposits, as well as swarms of subseafloor hydrothermal silica ± barite veins (Van Kranendonk, 2006). The tectonic setting of the EPT is controversial, ranging from mid-ocean ridge and island arc (Ueno et al., 2001; Komiya et al., 2002; Kato and Nakamura, 2003) to a thick ocean volcanic plateau (Smithies et al., 2003, 2005, 2007a, b; Van Kranendonk, 2006; Van Kranendonk et al., 2007a, b, 2019a).

A characteristic feature of the EPT is the so-called dome-and-keel structure, consisting of a central nucleus occupied by the 3459 ± 18 Ma North Pole Monzogranite ("North Pole

Dome") surrounded by little-deformed, predominantly mafic volcanic rocks of the Warrawoona Group and Kelly Group (Hickman and Van Kranendonk, 2012a). The oldest basaltic formation in this area is the North Star Basalt (3490 ± 15 Ma Ar/Ar), which is overlain by the Dresser Formation (3481 ± 2 Ma U-Pb) consisting of chert ± barite beds and veins that are associated with pillowed basalts and dolerite (Van Kranendonk et al., 2008; Hickman and Van Kranendonk, 2012b). Atop the Dresser Formation follows (from base to top) a ~ 4 km thick succession of mafic volcanic rocks (Mount Ada Basalt), a < 1.3 km thick succession of felsic volcanic rocks (Duffer Formation, Panorama Formation), and a < 150 m thick package of jasper (Marble Bar Chert Member, Towers Formation) (Byerly et al., 2002; Hickman and Van Kranendonk, 2012b). In the eastern part of the dome, the Panorama Formation is underlain by the Apex basalt (Nakamura and Kato, 2004), which is dated to 3463–3454 Ma based on zircon U-Pb ages of the underlying Duffer Formation and the overlying Panorama Formation (Thorpe et al., 1992; McNaughton et al., 1993). Surrounding the central dome, the Panorama Formation is disconformably overlain by the Strelley Pool Formation (SPF, 3414 ± 34 Ma, U–Pb ages, Gardiner et al., 2019), which is famous for its distinctive stromatolites (Hofmann et al., 1999; Van Kranendonk et al., 2003; Allwood et al., 2006; Hickman et al., 2011), followed by the high-Mg and tholeiitic Euro Basalt (3350 ± 3 to 3335 ± 7 Ma, GSWA, 2013) (Van Kranendonk et al., 2006; Hickman and Van Kranendonk, 2012b).

2. Materials and methods

2.1 Sample locality

Paleoarchean carbonate rocks analyzed in this study derive from the North Pole Dome in the EPT (Fig.1). Interstitial carbonates were sampled from the ~3.49 Ga North Star Basalt (drill core 102 AIDP-1; 21°06'38"S, 119°06'4"E, French et al., 2015), the ~3.46 Ga Apex Basalt ("Schopf Locality" at Chinaman Creek; Schopf, 1993), the ~3.47 Ga Mount Ada Basalt and the ~3.35 Ga Euro Basalt (both near "Trendall Locality" at Shaw River; Hickmann et al., 2011), as well as from the Middle Basalt Member of ~3.48 Ga Dresser Formation (Dresser Barite Mine). Bedded sedimentary carbonates were sampled from the Dresser Formation at the "Tsunami Locality" (Runge et al. 2022) near the Dresser Barite Mine, and the Euro Basalt at the east side of Shaw river near the "Trendall Locality". Stromatolitic carbonates were collected from the Strelley Pool Formation at the west side of Shaw river.

For comparison, we analyzed carbonate inclusions in black barites from the Dresser Formation, rhodochrosites in cherts from the ~3.25 Ga Fig Tree Group (Till Heinrichs, 1980), carbonates of controversial origin in the vicinity of the controversial ~3.7 Ga stromatolite site in the ISB in Greenland (Nutman et al., 2016; Allwood et al., 2018; provided by van Zuilen, 2018), as well as carbonatites from ~540 Ma Fen Complex in Norway (Andersen and Taylor, 1988) and the ~16 Ma Kaiserstuhl Volcanic Complex in Germany (Kraml et al., 2006).

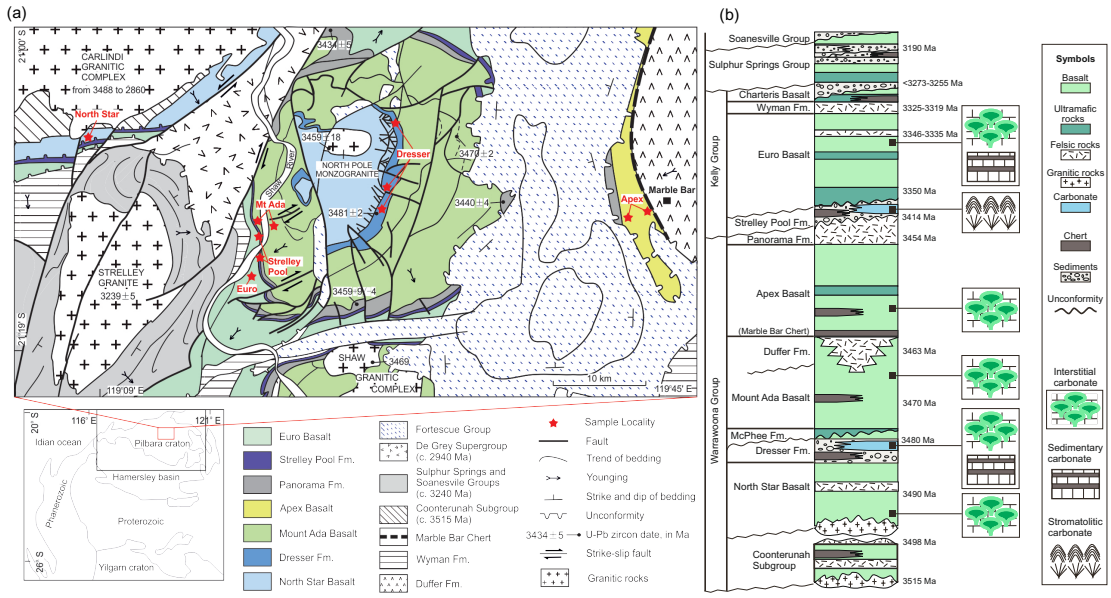

Fig.1 (a) The simplified geological map of the North Pole Dome, the Eastern Pilbara Terrane, Western Australia (modified from Van Kranendonk and Hickman, 2000, Hickman and Van Kranendonk, 2012b) and sampling localities (red stars). (b) The simplified stratigraphy of the studied Archean rocks (modified from Van Kranendonk et al., 2007b).

2.2 Methods

2.2.1 Petrography and geochemical imaging

Petrographic thin sections were prepared (polished to approximately 60 μm thickness) for all samples and examined using a Zeiss SteREO Discovery V12 stereomicroscope coupled with an AxioCam MRc camera. Selected carbonates were additionally analyzed with a Cathodoluminescence (CL) microscope. CL images were acquired with a Cambridge Instruments Citl CCL 8200 Mk3A cold-cathode system linked to a Zeiss Axiolab microscope (operating voltage of approximately 15 kV and electric current of approximately 250-300 μA) and a Zeiss AxioCam 703 camera.

Minerals were identified by their optical characteristics and Raman spectroscopy, using a Horiba Jobin-Yvon LabRam-HR 800 UV spectrometer with a focal length of 800 mm and an excitation wavelength of 488 nm produced by an Argon ion laser (Melles Griot IMA 106020B0S) and with a WITec alpha300 R fibre-coupled ultra-high throughput spectrometer. The former spectrometer was calibrated using a silicon standard with a major peak at 520.4 cm^{-1}, and the spectra were processed using software Fityk (Wojdyr, 2010) and comparatively analyzed based on references from the RRUFF database.

Element distributions were mapped using a Bruker M4 Tornado micro-X-ray fluorescence (micro-XRF) instrument equipped with a XFlash 430 Silicon Drift Detector.

Measurements were performed at a voltage of 50 kV and a current of 400 µA with a spot size of 20 µm and a chamber pressure of 20 mbar.

2.2.2 Stable carbon and oxygen isotopes ($\delta^{13}C$, $\delta^{18}O$)

For stable isotope analyses, sample chips (diameter ~1 cm) were obtained from pristine areas (i.e., free of visible alteration, inclusions, and secondary porosity) using a microdrill. The sample chips were cleaned with ethanol using ultrasound (3x) and gently dried at room temperature before being crushed into small pieces. Carbonate was then picked out and powdered in an agate mortar and well homogenized. Additionally, some carbonate facies, including carbonate veinlets and carbonate inclusions, were extracted using a high-precision drill from individual mineral phases from polished rock slabs.

Carbon and oxygen stable isotopes of the carbonates were measured at 70 °C using a Thermo Scientific Kiel IV carbonate device coupled with a Finnigan DeltaPlus gas isotope mass spectrometer at the Geoscience Center of the Georg-August-Universität Göttingen. All results were normalized as delta values $\delta^{13}C_{carb}$ and $\delta^{18}O_{carb}$ relative to the Vienna PeeDee Belemnite (VPDB) reference standard. The standard deviation is better than 0.03 ‰ for $\delta^{13}C_{carb}$ and 0.05 ‰ for $\delta^{18}O_{carb}$, calculated by multiple measurements of the in-house carbonate standard Solnhofen.

3. Results

3.1 Interstitial carbonate

3.1.1 Host basalt

The host basalts are pillow-shaped, are internally subdivided in more crystalline cores and quenched glassy rims, and commonly locally cut by tectonic fractures (see Fig.2). The interspaces and fractures are commonly filled with carbonate minerals and chert. In most outcrops, the host basalts and interstitial carbonate minerals are weathered, resulting in orange to brownish colors.

Although the host basalts show secondary mineral assemblages indicative of greenschist metamorphism (calcite +chlorite + anatase + quartz ± pyrite), phenocrysts (i.e., plagioclase and pyroxene) can still be recognized in the basalt core of the well-preserved samples, e.g. A22 from the Apex Basalt (Fig.3a). Specifically, the well-preserved basalts exhibit concentric green ophitic-holohyaline cores and yellow-green quenched margins. In the margins, the size and density of ovoid spherulites and variolites decrease outwards, merging into the glassy zone. Spherulitic and variolitic zones in the basalts are highly carbonatized, where carbonate minerals mainly constitute the variolites and concentric syngenetic veins. Element mappings of an area on thin section A22 are shown in Fig.3b. Notably, elemental distributions do not

vary between weathered and unweathered areas of the basalt, indicating a minor impact of weathering on elemental signatures. Except for the devitrified volcanic glass, Si is rich in the core of the pillow basalt but rare in the zone of spherulites and variolites, which are dominated by calcite.

Fig.2 The outcrop photos of Archean pillow basalts from the North Pole Dome in the Eastern Pilbara Terrane, Western Australia, showing the pillow shape consisting of core and quenched rim (black arrows), indicating their submarine eruption, with carbonate minerals (white arrows) filling the interspace (named as interstitial carbonate in this work). (a) The surficial weathered outcrop of 3.49 Ga North Star Basalt with the interspace filled by Fe-dolomite and chert cement; (b) The surficial weathered outcrop of 3.48 Ga Dresser Formation, that the interstitial calcite is largely absent due to weathering; (c) The surficial weathered outcrop of 3.47 Ga Mount Ada Basalt that (weathered brown) fibrous isopachous Fe-dolomite and white chert filled up the interspace. It is locally cut by deep carbonate veins shown in (d), inferring later fluid circulations. (e) The well-preserved outcrop of 3.46 Ga Apex Basalt, of which the interspace is filled with pink calcite, basaltic breccia and miner chert. (f) The outcrop of ca. 3.35 Ga Euro Basalt that pink calcite fills the interspace and fractures. The length of brown hammer is ca. 30 cm and the blue one is ca. 40 cm. (e) is in the same scale with (c). (Photos by Reitner J.).

In the altered host basalts, deformation and progressive metamorphism were documented by the elongated spherulites and variolites, migration and breakup of secondary minerals (e.g. chlorite), the erased volcanic textures, as well as transformation into schistose rocks (Fig.4a). Distinct from the well-preserved basalts, Fe is lost from basalt along with the migration of chlorite, which is a dominant Fe-bearing secondary mineral (Fig.4a). Chlorite is frequently observed in the interstitial carbonates near the basalt and the tectonic fractures cross-cutting pillow basalts.

3.1.2 Primary carbonate phases

The primary mineral phase of interstitial carbonates is acicular crystal-fan calcite. This phase is only preserved intact in some samples from the Apex Basalt, while it is reduced or absent in most other cases. The terminal tips of acicular crystal-fan calcite are partly recrystallized to sparry calcite (sparite) (Fig. 5a). Microcrystalline ankerite is rarely observed

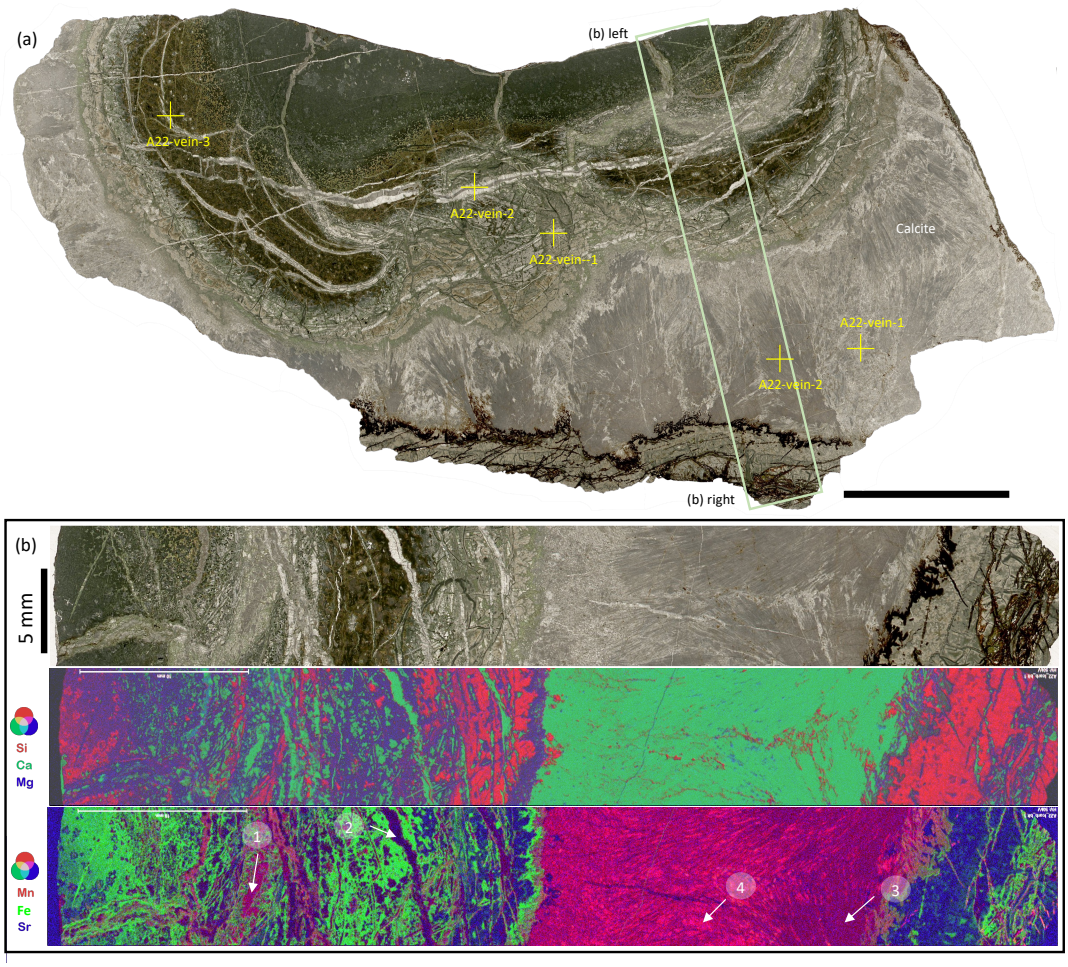

Fig.3 (a) Scan image (transmitted light) of thin section of sample "A22" from Apex Basalt, showing the well-preserved concentric volcanic structure of pillow basalt and the primary facies of interstitial carbonates as acicular crystal-fan calcite. The oxygen and carbon isotopes of the carbonate subsamples indicated by yellow crosses and labels can be found in Table 1. The rectangle area is magnified in the top panel in (b) and its μXRF mappings are shown in the bottom panels. False-color overlapping image of Si (red), Ca (green) and Mg (blue) in the middle panel verifies the interspace is dominantly filled by calcite and rare quartz. In addition, the carbonatized quenched margin is depleted in Si, compared with core, inferring Si is lost during the carbonatization that produces the Si-bearing fluid later cementing interstitial calcite. False-color overlapping image of Mn (red), Fe (green) and Sr (blue) indicates four facies of calcite based on distributions of Mn: Mn-enriched (white arrow 1) syngenetic veins and Mn-depleted (white arrow 2) later veins, and Mn-depleted acicular interstitial calcite (white arrow 3) and Mn-enriched calcite cement (white arrow 4). The scale bar in (a) is 20 mm.

at the basalt margin, mixing with microcrystalline quartz, chlorite, and anatase particles (~nm). Minor chert locally infills the intercrystalline space of sparite and crystal-fan calcite. Within basalt, blocky calcite is the primary carbonate facies in the concentric syngenetic veins, while fibrous isopachous calcite dominants the tectonic fractures, often showing shear bending during dynamic crystallization.

The irrelevant distribution of Mg and Ca confirms calcite as the dominant primary carbonate phase (Fig.3b). The acicular crystal-fan calcite and fibrous isopachous calcite in veins are depleted in Mn. Intercrystalline calcite cements associated with acicular crystal-fans

and calcite in concentric veins, in contrast, are Mn-enriched. Since Fe exists as chlorite with Si and Mg, it is pervasive in basalt, concentric syngenetic veins and fractures, where chlorite exists, but is rare in the interstitial calcite.

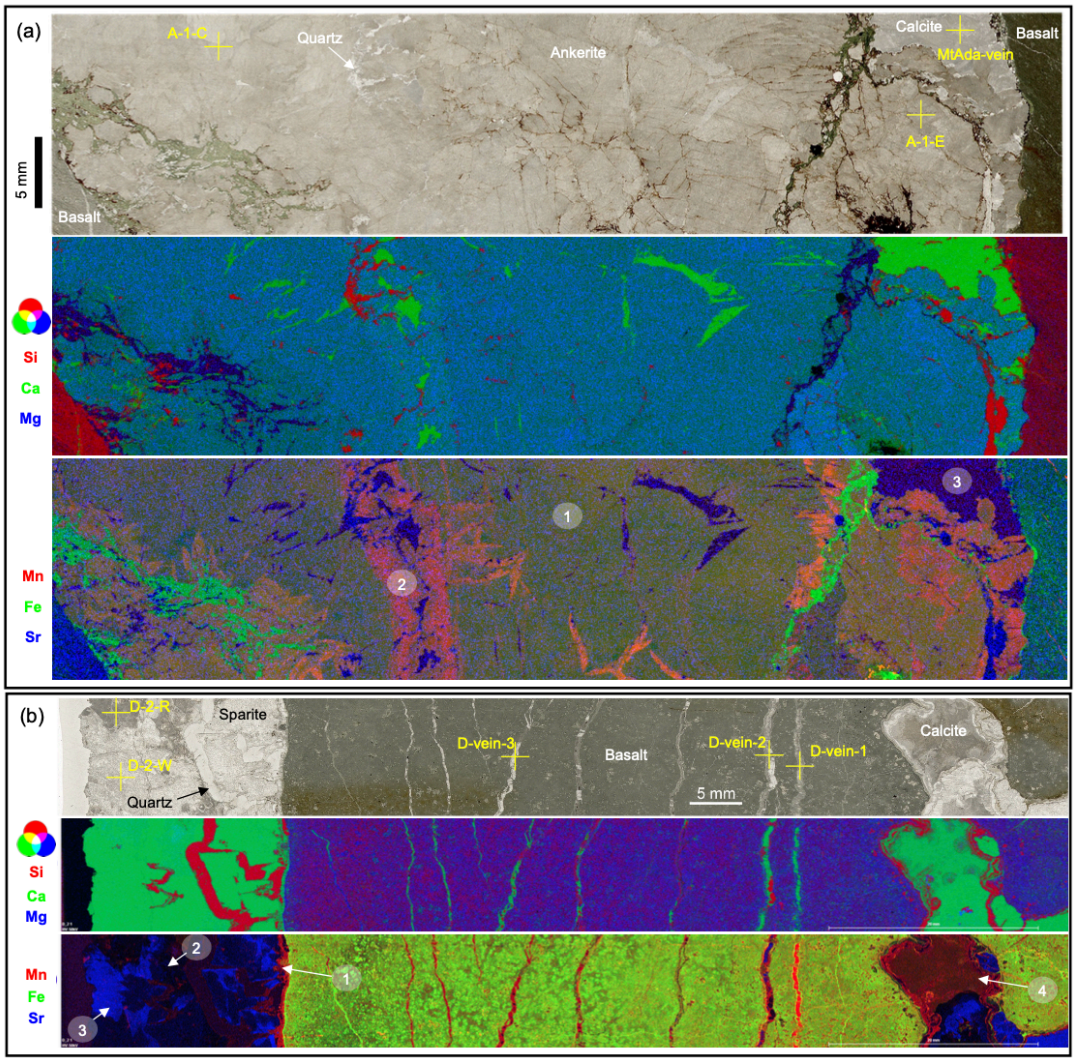

Fig.4 Scan images (transmitted light) and false-color overlapping images of elements of (a) the interstitial dolomite from Mount Ada Basalt and (b) the fracture filling calcite from Dresser Formation. (a) The interstitial carbonate is blocky and massive ankerite with minor calcite overgrowth and infilling quartz, with evidence of the false-color overlapping image of Si (red), Ca (green) and Mg (blue) in the middle panel. False-color overlapping image of Mn (red), Fe (green) and Sr (blue) indicates three facies of carbonates, that comparatively Mn-intermediate ankerite (facies-1) occurs far from the metabasalt, while the Mn-enriched ankerite (facies-2) occurs near metabasalt and in the place influenced by later fluids (indicated by calcite and quartz), whereas the calcite vein (facies-3) is Mn-depleted. In (b), four facies of calcite precipitate in the fracture and interspace. The first generation (facies-1) and fourth generation (facies-4) are Mn-enriched, identical to calcite within parallel fractures of basalt, inferring they precipitate from the same fluids derived from the fluid-basalt reaction. The Mn/Sr-depleted second generation (facies-2) and Mn-depleted/Sr-enriched third generation (facies-3) are distinctive from the aforementioned generations, indicating a different origin of the later fluids. The oxygen and carbon isotopes of the carbonate subsamples indicated by yellow crosses and labels can be found in Table 1. (Scale bar: 5 mm)

3.1.3 Secondary carbonate facies

The primary interstitial calcite might undergo recrystallization and dolomitization during post-depositional alteration (Fig.5). Indeed, recrystallization is widespread and causes a transformation from acicular crystal-fan calcite to inequigranular, blocky, massive, and sparry calcite (Fig.5a–d). The recrystallized interstitial calcites are cemented either by sparite or by quartz (Fig.5d, e), which are infilling minerals for two later tectonic fracture systems, respectively. Sparite cements in some samples exhibit a metamorphic S-C fabric (Fig.5f), reflecting dynamic metamorphism in a shear zone (Lister and Snoke, 1984). Noteworthy, sparite in sample D-2 from the Dresser Formation is rather associated with tectonic fractures rather than with basalt interspaces; therefore, it will be addressed as "fracture-filling calcite" in the following.

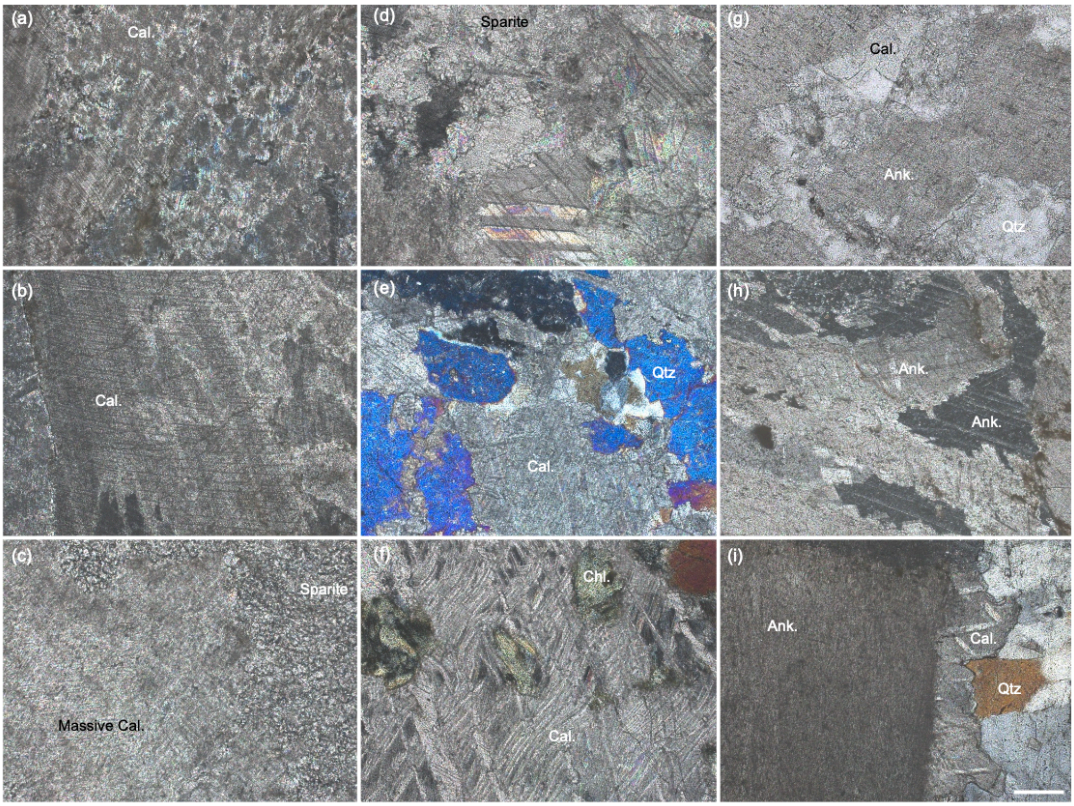

Fig.5 Photographs of the altered interstitial carbonates from the North Pole Dome in the Eastern Pilbara Terrane, Western Australia. The acicular crystal-fan calcite is altered to be (a) and (b) blocky calcite, (c) the massive calcite and sparite. (d) Large sparry calcite (sparite) precipitates in a wide fracture. (e) The blocky calcites are cemented by quartz. (f) The metamorphic S-C fabric of sparry calcite and chlorite indicates the dynamic metamorphism. (g) The blocky ankerites often have the calcite overgrowth on their edge. (h) Part of ankerites exhibit recrystallization and neomorphism. (i) The dewatering cracks of ankerites in deep carbonate vein are filled with calcite overgrowth and chert cement. (a) to (c) are from Apex Basalt, (d) is from Dresser Formation, (e) and (f) are from Euro Basalt, and (g) to (i) are from Mount Ada Basalt. Photos are taken under cross-polarized light, except (g) under plane-polarized light. (Scale bar: 200 μm. Cal.-calcite, Chl.- chlorite, Qtz- quartz, Ank.-ankerite.)

Carbonates from the Mount Ada Basalt underwent significant dolomitization, as indicated by abundant blocky and massive Fe-enriched dolomite (ankerite) cemented by

quartz (Fig.5g). Rarely observed relict structures "floating" in ankerite evidence acicular crystal-fan calcite as precursor. The interstitial dolomite locally underwent recrystallization and neomorphism (Fig.5h). Calcite veins locally cut the interstitial dolomite and the host basalt, that calcite overgrowth on the edge of ankerite are common in those samples (Fig.5g and i).

The recrystallized calcites are either Mn- or Sr-enriched (see Fig.4), indicating at least two diagenetic fluids involved in recrystallization. The Mn-enriched calcite is also observed in fractures as fibrous cement. The fracture-filling calcite shows the highest Sr-enrichments of all analyzed calcite facies. In contrast to the Fe-enriched interstitial dolomite, all calcite facies are Fe-depleted. The interstitial ankerite shows lower Sr enrichments than calcite cement in veins (Fig.4a). Instead, it is enriched in Mn, which increasing abundances of Mn towards the basaltic parts.

3.1.4 $\delta^{13}C$ and $\delta^{18}O$ of interstitial carbonate

The interstitial carbonates (including both calcite and dolomite) have the $\delta^{13}C$ values ranging from -2.37 to +0.99 ‰ (mean = 0.22 ± 0.98 ‰), and the $\delta^{18}O$ values ranging from -19.81 to -14.34 ‰ (mean = -17.57 ± 1.51 ‰) (Table 1). The fracture-filling calcites have the $\delta^{13}C$ values ranging from 2.03 to 2.34 ‰ (mean = 2.19 ± 0.13 ‰) and the $\delta^{18}O$ values ranging from -17.91 to -13.03 ‰ (mean = -15.70 ± 2.53 ‰) (Table 1). Carbonates in veins (see Figs.3, 4) have slightly lower values $\delta^{13}C$ values and the $\delta^{18}O$ values than the interstitial carbonates in the same samples.

3.2 Sedimentary carbonates

3.2.1 Laminated micritic carbonate

Laminated micritic carbonate occurs in a ca. 5 m thick sedimentary succession (Fig.6a, b), interbedded with the pillow basalts of the Dresser Formation (Fig.2b). The micritic carbonate is predominantly brownish and thinly bedded carbonate. The association with pillow basalts indicates an interval of generally quiet-water sedimentation, although the succession might preserve the oldest record of a tsunami event on Earth (Runge et al., 2022).

The laminated micritic carbonate consists of fine-grained dolomite crystals with abundant organic clots and flakes (Fig.7a), and locally euhedral and subhedral dolomite rhombs that have a cloudy center and clear rim enveloped by organic matter (Fig.7b). In-situ geochemical mappings and Raman spectra (Fig. 7c) indicate that the dolomite crystals are Mn-enriched ankerite that the cloudy centers consist of organic matter. Calculated Raman-based temperatures (Lünsdorf et al., 2017) are in agreement with a peak metamorphic temperature of ~300–350 °C. The laminae are caused by changing crystal sizes and organic matter contents, with finer-grained sizes and higher organic matter contents resulting in darker colors. A similar bedded micritic carbonate is observed in samples from drilling core PDP2c

(Van Kranendonk et al., 2019b).

Table 1 Stable carbon and oxygen isotopic compositions of the early Archean carbonates

Lithology	Formation	Age (Ma)	SampleID	$\delta^{13}C_{VPDB}$ (‰)	s.d.	$\delta^{18}O_{VSMOW}$ (‰)	s.d.	$\delta^{18}O_{VPDB}$ (‰)
Interstitial Carb.	Euro Basalt	3350	E-1	0.21	0.03	11.08	0.05	-19.23
			E-2	0.99	0.03	10.78	0.05	-19.52
			E-3	-2.37	0.03	11.00	0.05	-19.31
	Apex Basalt	3460	A14673-1	0.62	0.03	13.65	0.05	-16.74
			A22-1	0.44	0.03	13.09	0.05	-17.29
			A22-2	0.69	0.03	13.67	0.05	-16.72
			ABAS-1	0.65	0.03	13.41	0.05	-16.97
			ABAS-1	0.77	0.03	14.63	0.05	-15.79
			Apex-1	0.25	0.03	12.79	0.05	-17.58
			Apex-2	0.04	0.03	12.66	0.05	-17.70
			Apex-3	0.21	0.03	13.00	0.05	-17.37
	Mt.Ada Basalt	3470	MtAda-1-C	0.83	0.00	12.21	0.03	-18.14
			MtAda-1-E	0.77	0.03	11.77	0.05	-18.57
			MtAda-2	0.52	0.03	14.36	0.03	-16.05
	Dresser Fm.	3480	D-1	0.97	0.03	14.46	0.05	-15.95
			D-3	0.63	0.03	10.49	0.05	-19.81
	North Star Basalt	3490	CP-1	-2.31	0.03	11.14	0.05	-19.17
			CP-2	0.01	0.03	16.12	0.05	-14.34
Fracture Carb.	Dresser Fm.	3480	D-2-IC-1	2.03	0.03	12.45	0.03	-17.91
			D-2-IC-2	2.17	0.03	16.43	0.03	-14.04
			D-2-R	2.34	0.03	12.54	0.05	-17.81
			D-2-W	2.20	0.03	17.47	0.05	-13.03
Veinlet Carb.	Apex Basalt	3460	A22-vein-1	0.12	0.03	13.50	0.05	-16.88
			A22-vein-2	-0.14	0.03	13.31	0.05	-17.07
			A22-vein-3	-0.02	0.03	13.29	0.05	-17.09
	Mt.Ada Basalt	3470	MtAda-1-vein	0.47	0.03	10.47	0.05	-19.82
	Dresser Fm.	3480	D-2-vein-1	-3.77	0.03	11.30	0.05	-19.02
			D-2-vein-2	-2.35	0.03	11.25	0.05	-19.06
			D-2-vein-3	-1.69	0.03	11.36	0.05	-18.96
Sed. Carb	Euro Basalt	3350	E-4	1.88	0.00	15.24	0.03	-15.19
	Strelley Pool Fm.	3410	17Shaw 3/18 1	2.08		15.01		-15.42
		3410	18shaw 3/18 2	2.52		15.24		-15.20
		3410	19 shaw 3 /18 3	2.55		15.31		-15.13
	Dresser Fm.	3480	PDP	1.26	0.03	17.83	0.05	-12.69
			10'18 TSU 1/18/2	2.24		17.53		-12.98
			11Tsu 1/18 3	2.22		16.36		-14.11
			12TSU 1/18 4	2.17		16.71		-13.77
			13'Tsu 1/185	1.61		16.53		-13.95
			14 Tsu 2/18 1	2.24		17.68		-12.83
			15Tsu2/182	2.54		18.74		-11.80
			16Tsu/18 3	2.42		18.30		-12.23
			17_TSU1-Dress	2.34	0.05	18.43	0.07	-12.10
			18_TSU1-rb	1.21	0.05	27.10	0.07	-3.69
			19_TSU2018/3	1.34	0.05	15.93	0.07	-14.53
			6TSU oben 1/18 1	1.61		15.82		-14.63
			7Tsu oben 1/182	1.61		15.96		-14.50
			8TSU oben 1/18 3	1.49		15.74		-14.71
			Probe 2	1.38		21.45		-9.17
			Probe 7	1.10		22.60		-8.06
			Probe 8	1.78		23.37		-7.31
			wx_tsu	1.46		15.80		-14.66
			TSU	1.46	0.03	15.80	0.05	-14.66
Sed. Carb. DB	Dresser Fm.	3480	DB	-5.10	0.03	22.79	0.05	-7.88
			Dress 12613 10a 3	-5.38		20.54		-10.05
			Dress 12613 7c 1	-6.72		20.19		-10.40
			Dress 12613 7c 2	-6.38		19.81		-10.77
			Dress 12613 7c 4	-6.22		19.70		-10.87
			Dress 12613 7c 5	-6.01		19.94		-10.64
			Dress 12613 7c 6	-4.25		19.24		-11.32
			Dress4c_1	-5.96	1.72	1.25	4.76	-28.77
			Dress4c_2	-8.07	0.34	10.50	1.30	-19.79
			Dress4c_3	-3.15	0.07	19.93	0.15	-10.65
Stromatolite	Strelley Pool Fm.	3410	Strelley	2.50	0.00	17.34	0.03	-13.16
			Probe 4	2.46		13.92		-16.48
			Probe 5	3.28		15.01		-15.42
			Probe 6	3.38		14.84		-15.59
			Strell1_1	3.32	0.01	16.64	0.02	-13.84
			Strell1_2	2.69	0.01	15.74	0.03	-14.71
			Strell1_3	3.30	0.01	16.56	0.02	-13.92
			Strell1_4	3.33	0.01	16.66	0.02	-13.82
			Strell1_5	2.58	0.01	15.91	0.02	-14.55
			Strell7c_1	3.21	0.01	16.68	0.03	-13.80
			Strell7c_10	3.38	0.03	17.47	0.05	-13.04
			Strell7c_2	3.15	0.01	16.56	0.02	-13.92
			Strell7c_3	3.19	0.01	16.63	0.02	-13.84
			Strell7c_4	3.14	0.02	16.66	0.03	-13.82
			Strell7c_5	3.03	0.02	18.34	0.03	-12.19
			Strell7c_6	3.05	0.01	16.77	0.02	-13.71
			Strell7c_7	3.26	0.01	16.84	0.02	-13.65
			Strell7c_8	3.31	0.01	16.70	0.03	-13.78
			Strell7c_9	3.04	0.01	17.17	0.01	-13.33

(to be continued)

(continued)

Lithology	Formation	Age (Ma)	SampleID	$\delta^{13}C_{VPDB}$ (‰)	s.d.	$\delta^{18}O_{VSMOW}$ (‰)	s.d.	$\delta^{18}O_{VPDB}$ (‰)
Stromatolite (?)	Isua Supracrustal Belt	3700	12-1	2.35	0.08	18.80	0.11	-11.74
			12-2	1.21	0.08	19.69	0.11	-10.88
			12-3	1.18	0.08	19.57	0.11	-11.00
			12-4	1.11	0.08	19.59	0.11	-10.98
			12-6	1.18	0.13	19.36	0.18	-11.20
			12-7	1.27	0.08	19.01	0.11	-11.54
			12-8	0.45	0.08	16.85	0.11	-13.64
			1-3	0.74	0.08	19.30	0.11	-11.26
			39_IS19/12	0.98		19.23		-11.33
			IS-12	0.99	0.03	18.88	0.05	-11.66
			IS-12-C	1.03	0.03	19.44	0.03	-11.12
			IS-12-Q	0.78	0.03	19.27	0.03	-11.29
Metasomatic Carb.	Isua Supracrustal Belt	3700	38_IS19/09	-2.11		11.46		-18.86
			9-1	-2.37	0.08	11.64	0.11	-18.69
			9-2	-1.84	0.08	11.16	0.11	-19.15
			9-3	-1.74	0.08	10.93	0.11	-19.38
			9-4	-1.93	0.08	11.49	0.11	-18.83
			IS-09	-2.03	0.00	11.36	0.03	-18.96
Rhodochrosite	Fig Tree Fm.	3260	Fig tree Fm.1	-12.74		6.91		-23.28
			Fig tree Fm.2	-10.76		12.65		-17.71
			Fig tree Fm.3	-19.34		-4.93		-34.76
			Fig tree Fm.4	-12.12		5.90		-24.26
			Fig tree Fm.5	-18.23		-6.85		-36.62
			Fig tree Fm.6	-23.00		-12.32		-41.93
Carb. in barite	Dresser Fm.	3480	2 Aus Dress 120817 12	-18.14	0.20	9.37	0.50	-20.89
			4 Aus Dress 120817 12	-18.46	0.20	10.47	0.50	-19.82
			5a Aus Dress 120817 12	-11.37	0.20	11.32	0.50	-19.00
			6 Aus Dress 120817 12	-15.95	0.20	9.92	0.50	-20.36
			7 Aus Dress 150817 7	-11.07	0.20	10.81	0.50	-19.49
			1_AusBB2018/2	-15.09	0.05	11.51	0.07	-18.82
			2_AusBB2018/7	-11.81	0.10	12.06	0.30	-18.28
			6_AusBB2018/3	-12.40	0.10	13.78	0.30	-16.61
			7_DressBB2018	-9.79	0.10	12.85	0.30	-17.52
			9_AusBB2018/5	-14.53	0.10	12.03	0.30	-18.31
			4_Tara2018/1	-11.20	0.20	12.30	0.50	-18.05
			5_Tara2018/1w	-2.70	0.20	14.00	0.50	-16.40
			8_Tara2018/1	-10.83	0.10	12.54	0.30	-17.82
Carbonatite			C1	-4.91		7.13		-23.07
			C2	-5.84		7.13		-23.06
			C3	-5.91		7.00		-23.19
			C4	-3.29		18.35		-12.18

- $\delta^{18}O_{VPDB}$=0.970017*$\delta^{18}O_{VSMOW}$-29.98 (Coplen, 1988)
- s.d. is the standard deviation calculated by multiple measurements of the in-house carbonate standard Solnhofen.
- Abbreviations: Fm.- Formation , Sed.-sedimentary, Carb. –carbonate;
- The question mark in "Stromatolite (?)" indicates its controversial origin.
- "Carb. in barite" refers to carbonate inclusions in bladed black barite

3.2.2 Bedded silicified carbonate

The bedded silicified carbonate is characterized by carbonate-chert couples and occurs at the top of a chert layer from the Euro Basalt as well as the Dresser Formation (Fig.6; "Euro bedded carbonate" and "Dresser bedded carbonate" in the following). The Dresser bedded carbonate consists of 9 to 11 carbonate-chert couplets with radiating evaporative crystal splays. Because of its distinct appearance, it was previously named "zebra rock" (Hickman and Van Kranendonk, 2012b; see Van Kranendonk et al. 2019b for a detailed description). Notably, it occurs between a unit consisting of sulfidic stromatolites and bladed barite below and wave rippled volcanoclastic sediments above (Fig.6e).

Individual carbonate-chert couplets consist of fining-upward successions of euhedral to subhedral carbonate rhombs in a chert matrix (Fig.8a, b). Clusters of radiating crystal splays at the base of each couplet, initially proposed to be composed of gypsum or aragonite (Van Kranendonk et al., 2008; Otálora et al., 2018), but currently identified as calcite. In the Dresser bedded carbonate, some calcite rhombs have an organic core (Fig.7d) and show a strong patchy Mn enrichment pattern under CL (Fig.7e–g), somewhat similar to kutnahorite [$Ca(Mn,Mg,Fe)(CO_3)_2$] formed by modern *Idiomarina loihiensis* (ɣ-proteobacteria) strains

(Rincón-Tomás et al., 2016). The euhedral to subhedral carbonate rhombs and the highly porous chert matrix (Fig.8b) indicate low compaction after deposition. Although the Euro bedded carbonate exhibits the repeated grading of dolomite rhombs in a chert matrix, pressure dissolution features associated with carbonates and the nonporous microcrystalline chert matrix imply a stronger post-depositional compaction. In the Euro bedded carbonate, organic materials are rare and only interbedded between carbonate crystals.

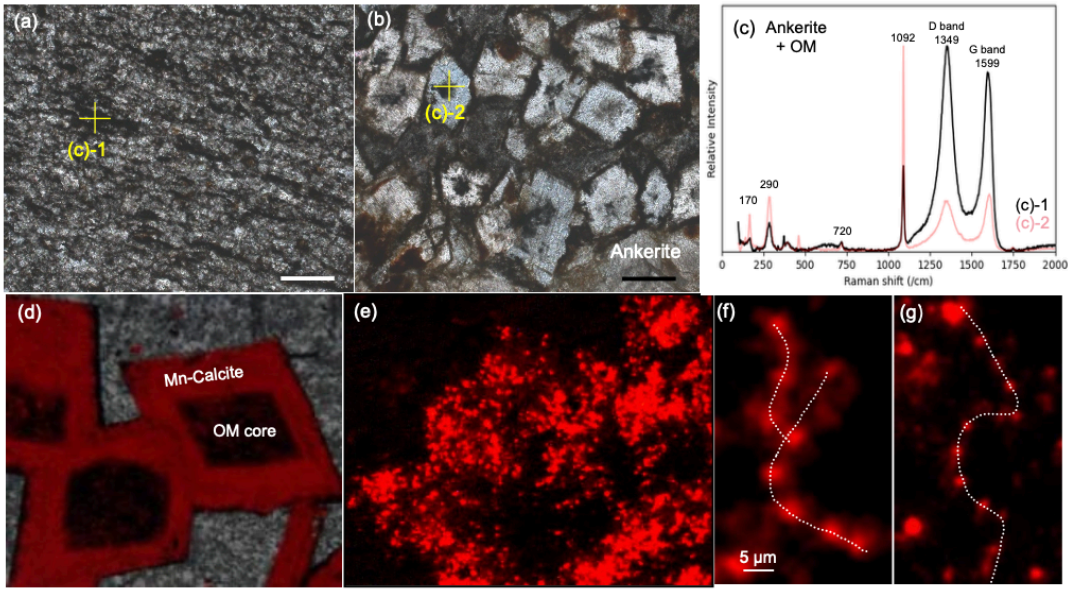

Fig.7 The sedimentary carbonates show a close association with organic matters. (a) The laminated micritic carbonates interbed with organic flakes and clots. (b) The euhedral and subhedral ankerite rhombs contain organic core and envelope cemented by ankerite, supported by the spot analysis of Raman spectroscopy in (c). (d) The euhedral calcite rhombs contain organic core cemented by chert, with the close-up view showing Mn-enriched dolomite particles (kutnahorite?) within the calcite crust. (f) and (g) show the arrangements of Mn-enriched dolomite particles resemble the microbial pattern of kutnahorite formed experimentally by *Idiomarina loihiensis (γ-proteobacteria)* strains (Rincón-Tomás et al., 2016), inferring the potential microbial induced carbonate precipitation. (a) and (b) are photos taken under plane-polarized light with the scale bar of 200 μm.

In-situ geochemical mappings reveal that the Dresser bedded carbonate predominantly consists of Fe-enriched calcite with Mn-enriched dolomite particles along its edges (Fig. 8c), in agreement with the observed CL patterns. The Euro bedded carbonate comprises Fe-Mn-enriched dolomite (ankerite).

3.2.3 $\delta^{13}C$ and $\delta^{18}O$ of bedded sedimentary carbonate

Laminated micritic carbonate and the Euro bedded carbonate show $\delta^{13}C$ values between 1.10 and 2.55 ‰ (mean = 1.85 ± 0.48‰) and $\delta^{18}O$ values between -15.42 and -3.69 ‰ (mean = -12.75 ± 3.00 ‰) (Table 1). The Dresser bedded carbonate, in contrast, exhibits more negative $\delta^{13}C$ values ranging from -8.07 to -3.15 ‰ (mean = -5.72 ± 1.36 ‰) and the $\delta^{18}O$

values ranging from -28.77 to -7.88 ‰ (mean = -13.11 ± 6.32 ‰) (Table 1).

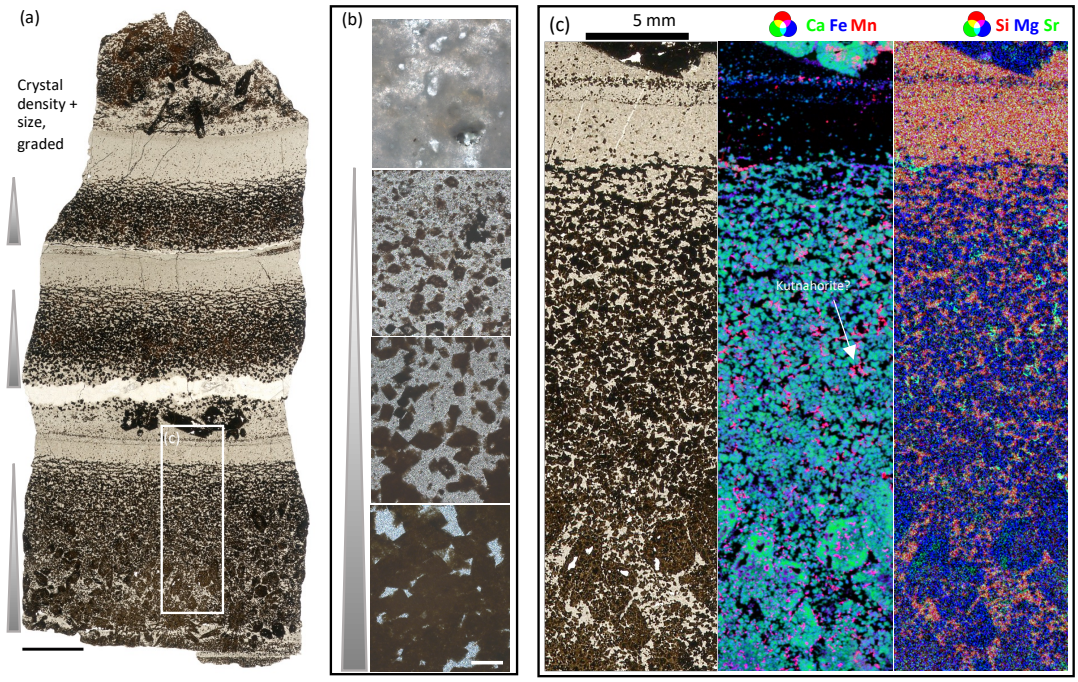

Fig.8 The bedded sedimentary carbonate-chert rock from Dresser Formation. (a) The scan image (transmitted light) of thin section shows repeated graded carbonate layers with the crystal size and density decreasing upwards. One layer is shown discontinuously in (b), that euhedral carbonates grade into the chert layer of high-porosity. The rectangle area is magnified in (c). (c) The false-color overlapping image of Si (red), Ca (green) and Mg (blue) in the middle panel shows the Mn-dolomite particles on the edge of calcite crystals. Scale bar in (a) is 10 mm and in (b) is 200 μm.

3.3 Stromatolites

The stromatolitic carbonates were collected from the second member of the Strelley Pool Formation. Stromatolite morphologies and arguments for the biogenicity have been reported in detail elsewhere (Allwood et al., 2006, 2007; Van Kranendonk, 2011; Duda et al., 2016; Viehmann et al., 2020). Briefly, stromatolites show a high morphological diversity, ranging from coniform and finely laminated to large domical forms, and overly centimeter-sized carbonate fans (Fig.9b, d).

The studied sample is a silicified coniform stromatolite with alternating laminae of equigranular anhedral dolomite (Fe and Mn-enriched) that often preserves organic matter. Detailed cement stratigraphy involving CL microscopy indicate the presence of at least three dolomite generations, consistent with previous works (Allwood et al., 2009, 2010; Flannery et al., 2018).

The stromatolites show the $\delta^{13}C$ values ranging from 2.46 to 3.38 ‰ (mean = 3.08 ± 0.30 ‰) and the $\delta^{18}O$ values ranging from -16.48 to -12.19 ‰ (mean = -14.03 ± 0.98 ‰),

consistent with data reported in Lindsay et al. (2005) and Flannery et al., (2018).

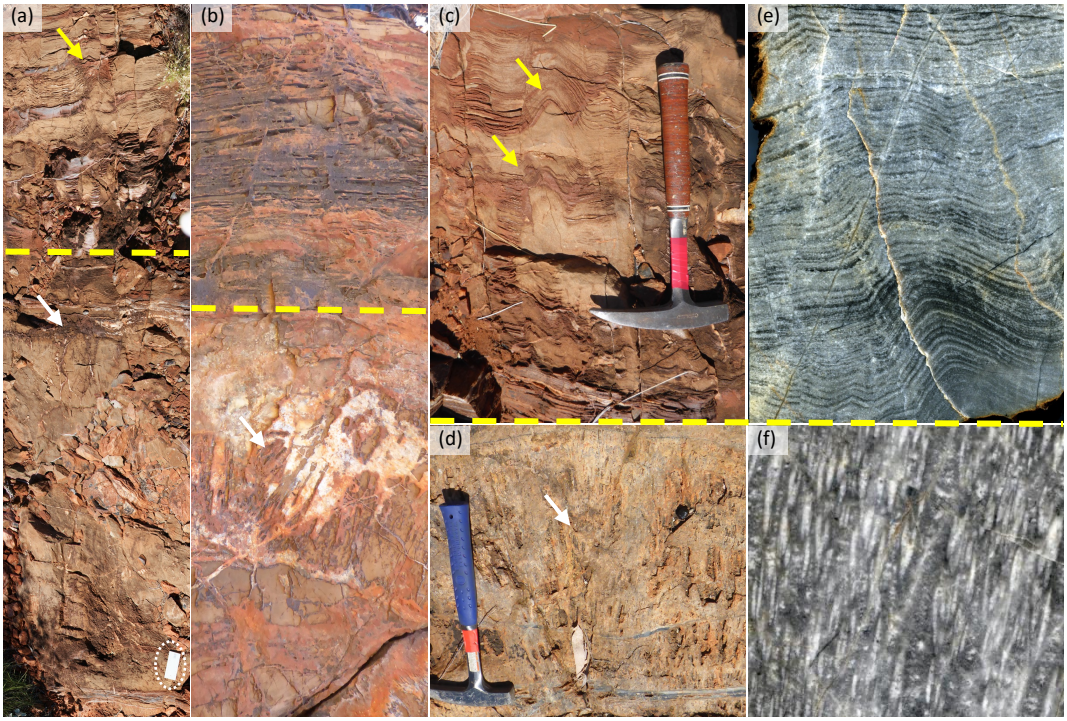

Fig.9 Photos of the stromatolites from the Strelley Pool Formation near the Trendall site in the East Pilbara Terrane, Western Australia. The yellow dashed line divides the stratigraphical upper unit of conical stromatolite (yellow arrow) and the lower unit of carbonate fans (white arrow). (a) A photo montage of the outcrop. The ruler in the white dotted circle is 15 cm in length. (b) The close-up view of an outcrop showing the layered stromatolite consisting of carbonate (weathered and partly absent) and chert (dark beds), atop the large carbonate fan on a chert matrix. The close-up view of the conical stromatolites (c) and carbonate fans (d), and the cross-section view of their hand specimen (e) and (f), respectively. The length of brown hammer is ca. 30 cm and the blue one is ca. 40 cm. (Photos by Reitner J.).

4. Discussion

4.1 Formation pathways of the EPT carbonates

To differentiate primary signatures and provides insights into the formation pathways is of significant importance for paleoenvironmental interpretation. In contrast to the modern marine carbonate factories dominated by biomineralization (Addadi et al., 2003; Weiner and Dove, 2003), the formation pathways of the early Archean carbonates were more "inorganic", and included abiotic precipitation (the interstitial carbonates between pillow basalts), organo-mineralization (the sedimentary carbonates), and microbially mediated biomineralization (the stromatolites from the Strelley Pool Formation).

4.1.1 Interstitial carbonate abiotically precipitated from hydrothermal fluids

The ubiquitous presence of interstitial carbonates within the interspaces between pillow basalts in the Archean greenstone belt, also known as "hydrothermal" carbonates (Roberts,

1987; Veizer, 1989a, b; Kitajima et al. 2001; Nakamura and Kato, 2004), and the absence of organic materials suggest that they were generated inorganically through physicochemical precipitation. In the modern world, this inorganic process is triggered by fluctuations in alkalinity, salinity and water temperature (Degens et al., 1984; Kempe, 1990; Reitner et al. 1995b; Flügel and Munnecke, 2010). Carbonate minerals (calcite and aragonite) are common low- to moderate-temperature minerals that are usually precipitated from cooled hydrothermal fluids during the latest stage of seafloor alteration, as veins within modern off-axis hydrothermal systems (Bach et al., 2001, 2011; Coogan and Gillis, 2013). Their abundance is high in older crusts, but very low in typical young (1-3 Ma) crusts (Gillis et al., 2001; Heft et al., 2008; Coogan and Gillis, 2013). Given the uncertainties associated with calculating temperature based on carbonate $\delta^{18}O$ values, the sources of alkalinity and salinity driving carbonate precipitation are more ascertainable and are therefore discussed in this work.

The alkalinity production and the release of cations are from the breakdown of igneous minerals during the interaction between basalt and fluids with high CO_2 fugacity. The leaching of basaltic components, forming Ca-Mg-Fe carbonates and silica-bearing fluids within a temperature range of 22 to 350 °C, has been identified and well documented in studies on modern oceanic crust (Bach et al., 2003; Coogan and Gillis, 2013), bench-scale experiments and pilot-scale geologic carbon sequestration (Gudbrandsson et al., 2011; Stockmann et al., 2011; Galeczka et al., 2013a, b, 2014; McGrail et al., 2017; Menefee et al., 2018; Wolff-Boenisch and Galeczka, 2018; Xiong et al., 2018; Voigt et al., 2018), Si isotopes of chert (van den Boorn et al., 2007), and numerical simulations (Gysi and Stefánsson, 2011).

In this study, a well-preserved interstitial carbonate-basalt pair from the Apex Basalt (Fig.3) illustrates that the released Ca may be captured autochthonously and precipitate calcite, which pseudomorphs phenocrysts, constitutes spherulites and variolites, precipitates as the infilling mineral in syngenetic vesicles and veins. The released Ca can be transported into the interspace forming acicular crystal-fan calcite, evident in the nucleation base at the quenched margin of pillow basalts. In-situ geochemical analysis indicates that the carbonatization of basalt occurs with the losses of Si and Mn, while Mg, Al, and Fe can be retained in the basalt part as chlorite (Fig.3b). However, chlorite is frequently observed to migrate out in the more altered samples and further breaks up, releasing Mg, Fe, Al, Si, and Mn into hydrothermal fluids, which consequently alter the primary interstitial calcite to blocky and massive calcite or ankerite during recrystallization and dolomitization (Fig.4 and 5).

On the other hand, CO_2-rich fluids are suggested to be seawater circulating into the basaltic basement (Kitajima et al. 2001; Nakamura and Kato, 2002; Yamamoto et al., 2004). The circulating seawater at 3.5 Ga has been documented by the existence of the fracture-filling calcite, supported by the evidence of its low $^{87}Sr/^{86}Sr$ ratio of 0.700596 and the Archean seawater-like REE+Y pattern (Chapter 3). Taking it as the reference, the lower $\delta^{13}C$ values of the interstitial carbonates (0.22 ± 0.98 ‰ on average; Fig.10) may reflect a mixture of seawater (the mean $\delta^{13}C$ value of 2.18 ± 0.13 ‰ in the fracture-filling calcites) and mantle fluxes ($\delta^{13}C$ values range from -5 ‰, Degens et al. (1984) to -6 ‰, Hayes and Waldbauer (2006)). The mantle fluxes are possibly provided via degassing during the cooling of pillow basalt. The hybrid signal is also supported by the radiogenic Sr isotopic compositions. The $^{87}Sr/^{86}Sr$ ratios of the Apex primary interstitial calcite (0.703094 ± 0.000979) are intermediate between the seawater endmember (0.700596) and Apex pillow basalt (the whole rock value of

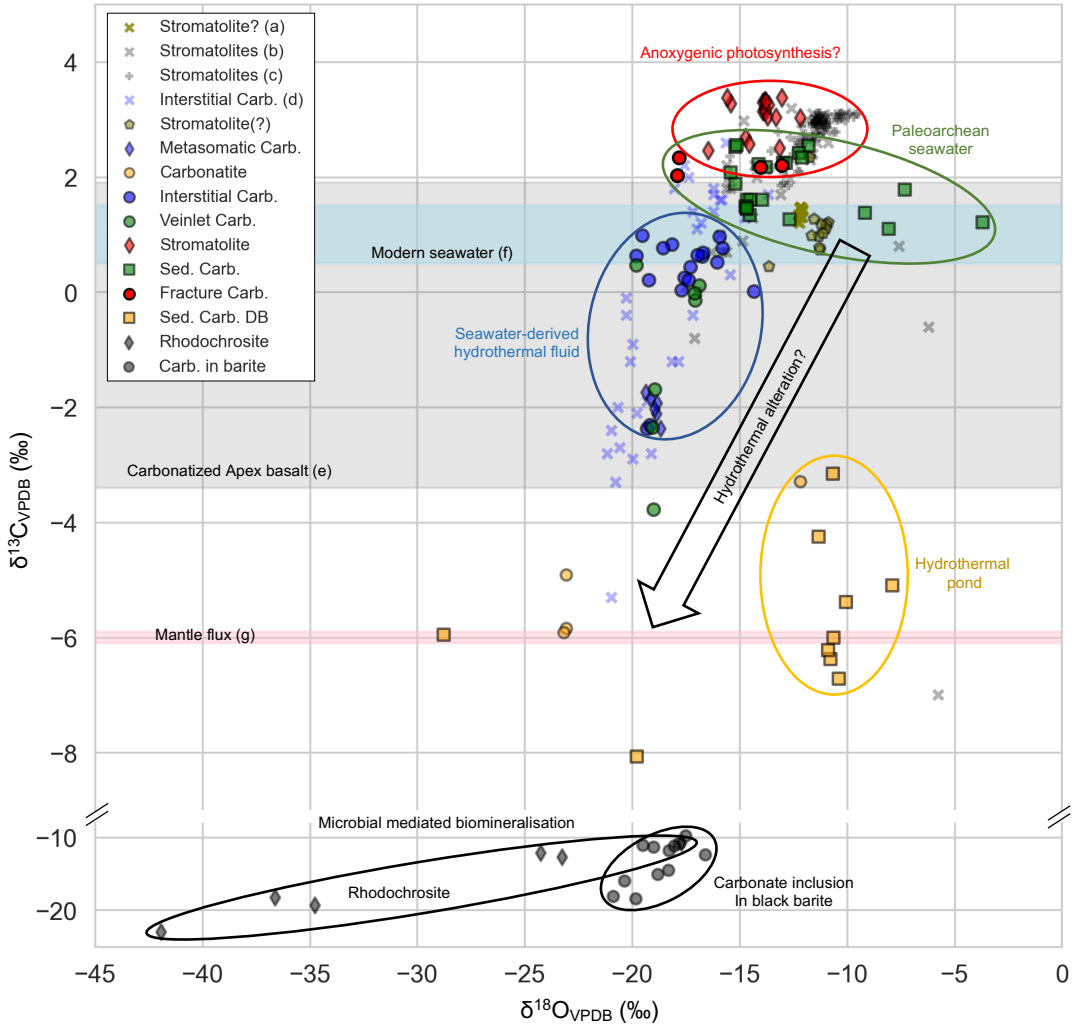

Fig.10 The stable carbon and oxygen isotopic compositions of the early Archean carbonates (Carb.). The $\delta^{13}C$ and $\delta^{18}O$ values roughly decrease from the SPF stromatolite, marine sedimentary carbonate (Sed. Carb.), to interstitial carbonate, possibly reflecting the negative deviation caused by hydrothermal alteration. The references are (a) Nutman et al. (2016), (b) Lindsay et al. (2005), (c) Flannery et al. (2018), (d) Shibuya et al. (2012), (e) Nakamura and Kato (2004), (f) Kroopnick (1980) and Tan (1988), and (g) Hayes and Waldbauer (2006). To be noted, "Carb. in barite" indicates carbonate inclusions in the black barite, and the question marks refer to the controversial origin. Data are in Table 1.

0.706337 ± 0.000954) (Chapter 3). The lack of organic matter in the EPT interstitial carbonates provides evidence for the abiotic genesis of inorganic precipitates, which could have originated from either CO_2-enriched seawater infiltration or hydrothermal fluids derived from basalt-water interactions during the eruption or metamorphism of pillow basalts (Fig.11).

4.1.2 Stromatolites induced by microbial activities

Stromatolites were first described by Kalkowsky (1908) as laminated benthic microbial deposits, characterized by two main elements: lamination and biogenicity (Hofmann, 1973; Buick et al., 1981; Riding, 1999; Flügel and Munnecke, 2010). Presently, stromatolite formation is initiated through biologically induced or controlled mineralization within microbial mats or biofilms, which provide a suitable microenvironment for physicochemical microgradients and organic nucleation templates for mineral precipitation. Nevertheless, sediment entrapment and consolidation alone are insufficient for stromatolite formation; a hiatus in sediment accumulation accompanied by the establishment and lithification of a microbial biofilm are the critical factors (Reitner and Thiel, 2011). Biofilms consist of attached microbial cells surrounded by a matrix of extracellular polymeric substances (EPS), which are organic macromolecules secreted by microbes to enhance their adaptability, resilience, and functional roles in environments (Reitner and Thiel, 2011; see in Fig.11).

The significant role of biologically mediated mineralization in forming calcium carbonate has been well-documented since the work of Arp et al. (2001). Certain functional groups (e.g., vacant carboxyls $-COO^-$ of amino acids such as aspartic acid Asp- and glutamic acid Glu-) on the EPS can efficiently sequester divalent cations such as Ca^{2+} and Mg^{2+} by forming bidentate bridges between adjacent EPS molecules, thereby inhibiting complexation with available carbonate anions and the consequent precipitation (Reitner et al. 1995a, b; Reitner and Thiel, 2011). The release of Ca^{2+} stemming from partial degradation or steric inhibition of these functional groups leads to locally supersaturated hydrated pockets within the EPS. Simultaneously, certain functional groups present on EPS molecules can act as potential nucleation sites by forming unidentate bonds with Ca^{2+} cations, which subsequently complex with carbonate anions, thereby initiating the precipitation of calcium carbonate ($CaCO_3$). The stereochemical arrangement of the highly reactive carboxylated groups is crucial in EPS-mediated nucleation. For example, highly ordered acidic groups at defined distances, aligned with the crystal lattice, can surpass the complexation capacity of EPS and enhance nucleation when there is an adequate diffusive supply of Ca^{2+}. Conversely, disorganized groups may impede the precipitation process.

Contrary to the indisputable biogenicity of modern stromatolites, determining the biogenicity of ancient stromatolites is always challenging due to their vulnerable mineral components, such as carbonates. However, after years of studies and discussions since the debut in 1978 (Lambert et al. 1978), the biogenicity of stromatolites from the Dresser Formation and the SPF has been previously accepted based on diverse macroscopic to microscopic morphologies, C and S isotopic compositions of preserved biogenic minerals and

kerogen (Van Kranendonk 2006, 2007; Allwood et al. 2006, 2007, 2009; Marshall et al. 2007; Wacey, 2010; Bontognali et al., 2012; Duda et al. 2016; Flannery et al. 2018). Additionally, the organic detritus detected in the SPF stromatolites is interpreted as the remains of microbial mats rather than transported allochthonous organic detritus (Allwood et al. 2009). Hence, the carbonate constituents within the SPF stromatolites are proposed to arise from biofilm/EPS-controlled biomineralization.

Anoxygenic photosynthesis likely appeared between about 3.8 and 3.4 billion years ago (Awramik, 1992; Brasier et al., 2006; Moore et al., 2017; Lepot, 2020). Flannery et al. (2018) documented a substantial $\delta^{13}C_{org}$ fractionation ranging from -29 to -45 ‰, ascertained via *in situ* SIMS analyses, as compelling evidence for the coexistence of autotrophic (possibly anoxygenic photosynthetic) or predominantly heterotrophic metabolisms alongside the Calvin-Benson-Bassham (CBB) cycle. The notably positive $\delta^{13}C$ values observed in the SPF stromatolites are in stark contrast to the highly depleted $\delta^{13}C$ values of rhodochrosite and carbonate inclusions found in black barite (Fig.10), strongly suggesting the microbial sequestration of lighter ^{12}C isotopes, partly possibly via anoxygenic photosynthesis. This perspective suggests that the secretion of EPS by anoxygenic photoautotrophs may have emerged early in the evolutionary history of life, as supported by their involvement in stromatolite formation and broader microbial mat phenomena.

4.1.3 Bedded sedimentary carbonates impacted by OM

The sedimentary textures and structures of the examined EPT bedded carbonate rocks, in conjunction with their close proximity to organic matter, such as dispersed organic flakes and clots within micrites, and the presence of a cloudy organic core within carbonate rhombs, indicate the in-situ precipitation of micritic carbonates through organo-mineralization. Since its introduction at the 7th International Symposium on Biomineralization in 1993, organomineralization has been identified as one of the main processes that precipitate automicrite (a micritic carbonate forms in place, Reitner et al., 1995b), widespread in microbial mats, biofilms, or more widely in benthic marine sediments (Riding, 2000; Schlager, 2003; Reitner and Thiel, 2011).

Reitner et al. (1995a) discovered that automicrites displayed elevated quantities of Asp- and Glu-rich macromolecules (soluble matrices), which played a crucial role in the initiation of carbonate crystal nucleation. Consequently, a distinct subset of automicrite, termed organomicrite, was coined to describe autochthonous micrite that is genetically linked to Ca-binding organic macromolecules (Reitner et al., 1995b). Utilizing this carbonate precipitation mechanism, mud mounds were proposed as a biocalcifying carbonate factory to characterize the development of fine-grained carbonate buildups at the macroscopic scale (Reitner et al., 1995a, b; Reitner and Neuweiler, 1995), and this proposition has gained acceptance among proponents (Schlager, 2000, 2003; Reijmer, 2021).

However, it is important to highlight that the sources of organic macromolecules are not exclusively limited to living microbial cells. Organomicrites can form within their EPS and

biofilm, where there is an abundance of organic macromolecules and under supersaturation of Ca cations and CO_2, as in the case of stromatolites and whitings (Robbins and Blackwelder, 1992; Thompson et al., 1997; Reitner and Thiel, 2011; Escoffier et al., 2022). Furthermore, the strongly acidic organic film of taphonomically reorganized organic macromolecules, including acidic polysaccharides, acidic protein remains, and lipid remains, can play the same role in generating carbonate minerals (Pei, 2022). In addition to biogenic organic materials, laboratory experiments by Reitner (2004) showed that the precipitation of carbonate bodies might also be induced in the presence of organic matters (likely abiotic) extracted from the Murchison CM2 meteorite.

In the early Archean ocean, microbial activity is supported by a diverse range of stromatolite morphotypes, including domical and wavy laminites (Allwood et al., 2006, 2007, 2009), microfossils (Sugitani et al., 2010, 2013, 2015a,b, 2018; Oehler et al., 2009; Wacey et al., 2011, 2018; Lepot et al., 2013; Brasier et al., 2015; Schopf et al., 2017; Kozawa et al., 2019; Delarue et al., 2020), kerogen preserved in carbonate and chert (Marshall et al., 2007; Duda et al., 2016; Flannery et al., 2018), S isotopes (Wacey et al., 2010; Bontognali et al, 2012), and other evidence (Wacey et al., 2011; Tice et al., 2011). Once fixed in sedimentation as stromatolites or microbialites, degraded organic matter can become mobile during early diagenesis or post-depositional alteration, and be redistributed by water currents. In addition, depleted ^{13}C organic materials are also commonly reported within hydrothermal chert veins, carbonates, and metamorphic rocks (Schopf, 1993; Mojzsis et al., 1996; Schopf et al., 2002; Brasier et al., 2002; Van Kranendonk and Pirajno, 2004; Van Kranendonk, 2006; McKeegan et al., 2007; Van Kranendonk et al., 2008; Ohtomo et al., 2014; Bower et al., 2016; Duda et al., 2018; Rouillard et al., 2021), although there is long-standing debate about their biological origin (Ueno et al., 2001, 2004; Glikson et al., 2008; Pinti et al., 2009; Morag et al., 2016) or non-biological origin (McCollom et al., 1999; McCollom and Seewald, 2006; Brasier et al., 2004, 2005; Lindsay et al., 2005). Biogenic kerogen, which differs markedly from the abiotic compounds experimentally formed via Fischer–Tropsch-type synthesis, has been observed in a hydrothermal chert vein of the Dresser Formation. This is summarized as the "hydrothermal pump hypothesis" by Duda et al. (2018), suggesting that microbial-derived organic matter accumulates in anoxic aquatic environments (both surface and subsurface), and subsequently undergoes assimilation, redistribution, and sequestration by hydrothermal fluids. Irrespective of its source, the early Archean ocean harbored substantial quantities of organic matter capable of facilitating carbonate precipitation through organo-mineralization, provided that environmental conditions met the criteria of divalent cation supersaturation and carbonate alkalinity.

Organo-mineralization can elucidate the genesis of finely laminated micritic carbonate rocks. However, it does not provide an explanation for the presence of bedded, graded carbonate rocks. In this rock type, organo-mineralization initiates the formation of organomicrites, which settle on the seafloor along with organic flakes and clots, and subsequently lithify into laminated carbonate rock (Fig. 11). However, organic matter and organomicrites can be re-suspended and re-distributed by currents or high-energy events like tsunamis, serving as new nucleation centers for the development of euhedral carbonate

rhombs. The presence of Fe/Mn-enriched carbonate and chert matrix indicates the involvement of Si-bearing hydrothermal fluids carrying significant alkaline metals. Within this time frame, fine-grained carbonate crystals precipitate gradually in the silica gel under low-energy conditions, displaying pronounced normal grading. This cyclical process repeats multiple times, ultimately culminating in the formation of bedded sedimentary carbonate rocks.

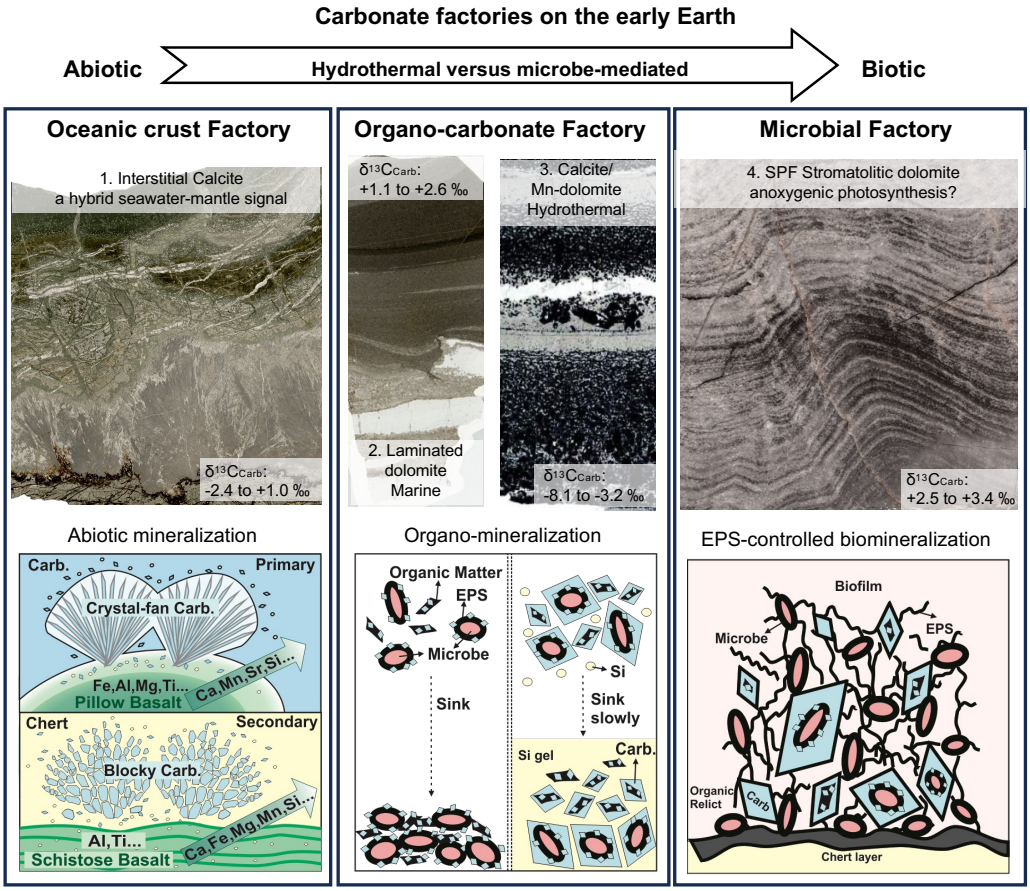

Fig.11 The lithological features and formation pathways of the three carbonate factories in the early Archean, including the oceanic crust factory, the organo-carbonate factory and the microbial factory. Carbon precipitation in the oceanic crust factory is an inorganic process driven by seawater-basalt interaction, which produce the hydrothermal fluids of high carbonate alkalinity and high cation concentrations. Carbonate precipitation in the organo-carbonate factory is triggered by organic macromolecules via organo-mineralization. Carbonate precipitation in the microbial factory occurs through microbial EPS-controlled biomiberalization (possibly anoxygenic photosynthesis). (Abbreviations in the figure: "Carb./ Carb"- carbonate; "EPS"- extracellular polymeric substances)

4.2 Depositional environments of the EPT carbonates

After extensive debate, a widely supported tectonic model of the EPT suggests the thick volcanic plateau above mantle plumes. This model indicates successive mantle melting events produced eruptive products that were deposited on a basement of older sialic crust (Smithies et al., 2003, 2005, 2007a, b; Van Kranendonk, 2006; Van Kranendonk et al, 2007a, b, 2019a). The uplift and basin deepening are attributed to mantle-derived magmatism, as indicated by the presence of pillow basalt successions interbedded with shallow water episodes (Van

Kranendonk et al, 2019a). In accordance with the tectonic model, our proposal suggests that the EPT carbonates were precipitated across a spectrum of environments, encompassing seafloor, shallow marine, and terrestrial hydrothermal ponds. The nature of these environments varied in the degree of influence from hydrothermal sources of diverse origins (see Fig. 12).

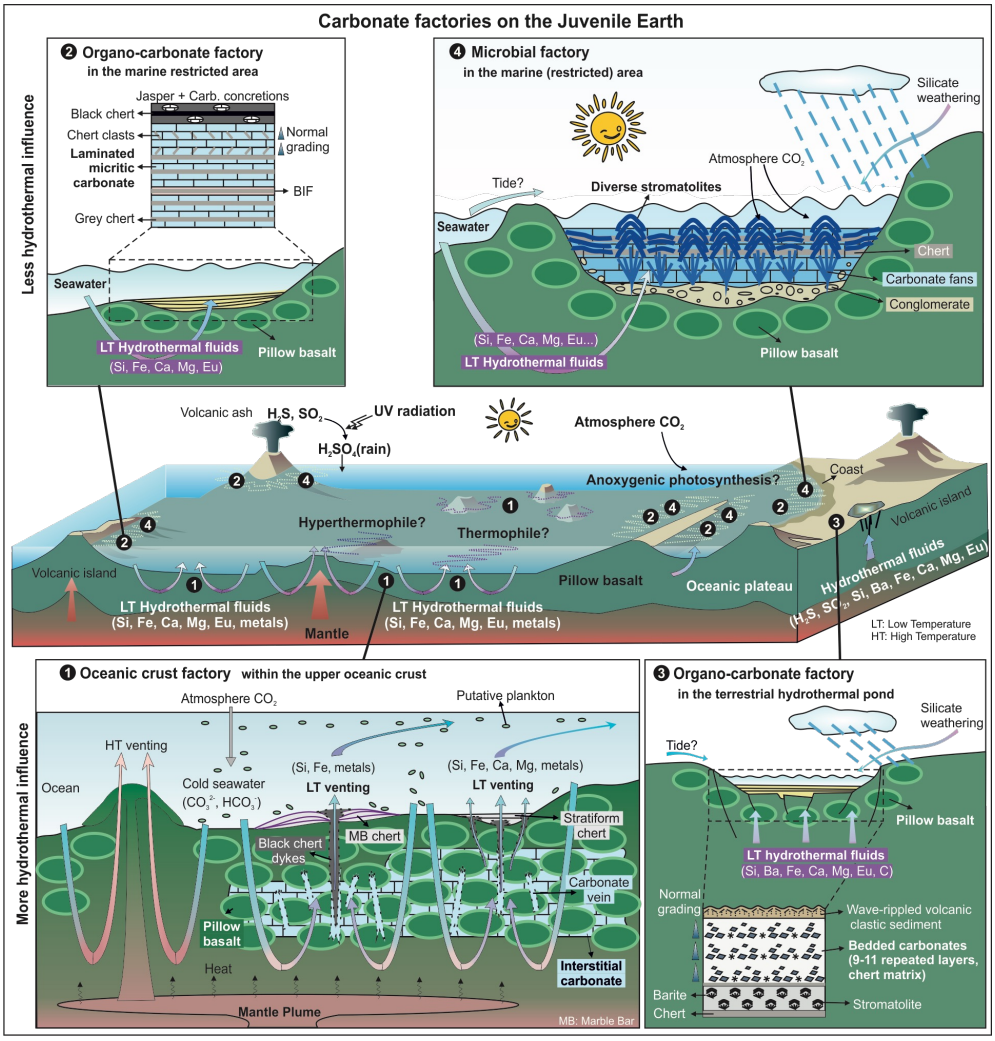

Fig.12 The possible localities of the three carbonate factories (adopted from Nisbet and Sleep, 2001). The oceanic crust factory commonly occurs in the deep marine environment within the upper oceanic crust (number 1). The organo-carbonate factory can form in the diverse environments, where there are abundant in organic materials (either biotic or abiotic) and supersaturated in Ca and CO_2, likely intermittently influenced by hydrothermal fluids (number 2 and 3). The microbial factory likely forms in the photic, relatively restricted, shallow marine environments like lagoon on the slope or platform, with minor detritus and rare hydrothermal inputs (number 4).

The interstitial carbonates occurring between pillow basalts are inferred to have precipitated on the seafloor within deep marine settings, where rapid cooling of hot basaltic lava by cold seawater facilitated the formation of interstitial carbonates of multiple generations. Subsequently, the hydrothermal fluids vented and ascended along deep-seated tectonic fractures, transporting substantial metal cations (e.g. Ca, Fe, Mg), trace elements, and abundant soluble Si. These materials progressively precipitated on the seafloor, either as Fe-Si

formations (BIFs and/or Fe-enriched chert) or Ca-Mg-Si formations (carbonate-chert rocks) (Fig. 12). Alternatively, interstitial carbonate may precipitate directly from shallow seawater circulating through wide fractures in the basaltic basement, as s exemplified by fracture-filling calcite. The formation of fracture-filling calcite is probably associated with basin deepening resulting from crustal extension (Nijman and de Vries, 2004; Van Kranendonk, 2006; Van Kranendonk et al., 2006, 2019a), which created fractures and facilitated an environmental transition from exposure settings (hot spring deposits, Djokic et al., 2021) to shallow water (rippled sandstones, stromatolites) and eventually to deeper settings (pillow basalt).

However, the SPF stromatolites precipitated in shallow marine environments, evident by their positive $\delta^{13}C$ values (Lindsay et al., 2005; Flannery et al., 2018; Fig.10). The diverse macroscopic morphologies and regional distribution of the SPF stromatolites indicate a biological origin in a peritidal marine platform (Allwood et al., 2006, 2007, 2009), with minor (low-temperature) hydrothermal input, as supported by the shale-normalized REE+Y patterns (Van Kranendonk et al., 2003; Allwood et al., 2010; Viehmann et al., 2020; Chapter 3). The underlying member 1 and overlying member 4 of conglomerate and quartz-rich sandstones (Allwood et al., 2006, 2007; Van Kranendonk, 2011; Duda et al., 2016; Viehmann et al., 2020) reflect detritus inputs. The arrangement of the large carbonate fans underlying the SPF stromatolites suggest *in situ* precipitation and growth of crystals at the sediment-water interface (Grotzinger and Knoll, 1999; Allwood et al., 2009), and periods of evaporitic conditions. Hence, the depositional environment of the SPF stromatolites may be a lagoon-like, relatively restricted basin (see Fig.12).

The sedimentary carbonates can develop in diverse environments enriched with abundant organic materials and substantial sources of cations that promote carbonate nucleation. The moderate $\delta^{13}C$ values exhibited by certain sedimentary carbonates (e.g., laminated carbonate and Euro bedded carbonate) situated between the SPF stromatolites and interstitial carbonates (Fig.10) suggest their probable deposition in marine environments. In these settings, the degradation of abundant organic materials (both biotic and abiotic) likely liberated ^{12}C, leading to the observed isotopic composition. The presence of hydrothermal inputs is supported by the REE+Y patterns of carbonates (Chapter 3) and the chert components (Fig.6). However, the depleted, mantle-like $\delta^{13}C$ values of the Dresser bedded carbonate (-5.72 ±1.36 ‰ on average) are indicative of the hydrothermal origin, with the support of the underlying bladed barite, which contains carbonate inclusions with highly depleted $\delta^{13}C$ values (Fig.10). The presence of normal grading within each carbonate layer, the occurrence of evaporative crystal splays, and the absence of internal current ripples (Fig. 8a) support deposition in relatively calm waters, occasionally subaerial conditions. The highly porous chert matrix, along with subhedral carbonates exhibiting limited compaction and pressure dissolution, indicates shallow burial conditions. The compact outcrop, accompanied by a delicate layer of rippled volcanic clastic sediments above, and the recurrent barite-stromatolite and carbonate-chert successions (Fig. 6e), propose a credible interpretation resembling a terrestrial pond hosting benthic microbial activity, intermittently impacted by hydrothermal fluid inputs, akin to recently identified hot spring deposits (Djokic et al., 2017,

2021). Hence, sedimentary carbonates can precipitate across a spectrum of environments, ranging from shallow marine to terrestrial settings, characterized by ample organic materials and significant cationic presence.

4.3 Carbonate factories in the early Archean

According to the discussion above, three carbonate factories are speculated to have existed in the early Archean: the oceanic crust factory, the organo-carbonate factory, and the microbial factory. The lithologies, formation pathways, depositional settings, and environments are summarized in Table 2.

Table 2 Features of the three carbonate factories in the early Archean

Features	Ocean crust factory	Organo-carbonate factory	Microbial factory
Primary lithology	Acicular crystal-fan calcite	Organomicrite, calcite or ankerite crystals of various size, on a chert matrix	Laminated dolomite layers cemented by chert
Secondary lithology	Sparite, blocky, massive, calcite and ankerite	Anhedral dolomite crystals showing compaction and pressure dissolution	Several generations of dolomites, including prismatic dolomite cement
Organic Materials (OM)	Absent	Abundant	Abundant
Origins of OM	-	Abiotic to biogenic	Biogenic
Hydrothermal inputs	Dominant	Common	Rare
Main origins of carbonate	Inorganic precipitation from seawater or seawater-derived hydrothermal fluids	Taphonomy-controlled organo-mineralization	EPS-controlled microbial mineralization
Silicon in fluid	Source/sink	Sink	Sink
Evaporite minerals	Absent	Common to rare	Common to rare
Siliciclastic sediments	Absent	Common	Common
Depositional setting	Deeper marine within the upper ocean basaltic crust	Diverse, shallow ocean to terrestrial hydrothermal pond	Photic shallow marine slope/ platform

4.3.1 Oceanic crust factory

The oceanic crust factory indicates the carbonate minerals formed within the pillow basalts and their interstices, mainly consisting of Mn-enriched or Sr-enriched calcite and Mn-enriched ankerite. They replace igneous minerals in basalt and occur in the interspaces as calcite (acicular crystal fans, sparry, blocky, massive) or ankerite (blocky, massive). The formation is an inorganic process, precipitating from CO_2-rich seawater-derived hydrothermal fluids of high alkalinity and cation concentrations. The geochemistry of these fluids evolves as basalt alteration progresses. The pillow morphology of basaltic lavas and the presence of quenched rims are indicative of submarine basaltic eruptions, likely occurring in abyssal settings characterized by the presence of cold bottom waters capable of efficiently quenching the hot lava.

The oceanic crust reservoir holds significant geological importance, which has previously been undervalued. Firstly, the prevalence of carbonatized Archean greenstones and interstitial carbonates attests to the formation of carbonate minerals during seafloor alteration, serving as a substantial carbon sink since the early Archean era. Based on studies of carbonatized pillow basalts in the Pilbara Craton, the CO_2 flux from the ocean to the oceanic crust is estimated to be $> 3.8 \times 10^{13}$ mol/yr in the early Archean (Nakamura and Kato, 2004) and 1.5×10^{14} mol/yr in the middle Archean (Shibuya et al., 2012). These

values are one to two orders of magnitude higher than present-day estimates ($1.5–2.4 \times 10^{12}$ mol/yr, Alt and Teagle, 1999). Consequently, the carbonatization of oceanic crust likely played a significant role in the global carbon cycle since the early Archean era (Nakamura and Kato, 2004; Shibuya et al., 2012; Coogan and Gillis, 2013), possibly serving as a major sink for atmosphere-ocean CO_2 in the infancy of the biological sink and the continental sink (via silicate weathering). Secondly, the carbonatization of Paleoarchean pillow basalts serves as an excellent analogue for contemporary CO_2 capture and storage (CCS) projects, representing an ideal model for long-term natural CO_2 sequestration.

4.3.2 Organo-carbonate factory

The organo-carbonate factory is dominated by organomicrite produced through taphonomy-controlled organo-mineralization. Its formation requires three preconditions: nucleation sites (soluble acidic organic macromolecules and/or resuspended fine organomicrites), supersaturation of divalent cations, and the carbonate alkalinity. The simplicity of its formation makes it pervasive in diverse environments. However, carbonate minerals, especially micrites, are vulnerable to later alteration. The organomicrite sediments formed in the early Archean may be hardly recognized after the long burial history, unless "protected" by refuge materials such as chert.

By far, the most important occurrences of Archean carbonaceous materials and microfossils have been reported to be delicately preserved in silica matrices (chert) from Western Australia and South Africa (Lepot, 2020). These materials are thought to have a hydrothermal origin based on geological settings, major and trace element geochemistry (Van Kranendonk and Pirajno, 2004; Lindsay et al., 2005; Van Kranendonk, 2006; Van Kranendonk et al., 2008; Glikson et al., 2008; Duda et al., 2018; Hickman-Lewis et al., 2019). Si-bearing hydrothermal fluids have been proposed to play a role in the preservation of carbonaceous materials and degraded structures through prompt silicification (Gilkson et al., 2008), a notion reinforced by recent investigations (Duda et al., 2018; van Zuilen, 2019; Hickman-Lewis, 2019; Ledevin, 2019). The preservative attributes of silica gel can be exemplified by sophisticated fossilization experiments conducted by Alleon et al. (2016) under sub-greenschist facies metamorphic conditions (250 bars and 250 °C). Encapsulation within silica gel, which gradually transforms into quartz, effectively curbs the degradation of microbial molecular signatures (Alleon et al., 2016). Consequently, chert possesses the capacity to uphold the preservation of ancient life in terms of both morphological and biochemical aspects.

However, the multifaceted contributions of hydrothermal fluids to the establishment of the organo-carbonate factory extend beyond silica preservation. These fluids supply substantial alkaline metal cations including Ca, Mg, Mn, and Fe, as well as abundant organic matter, facilitating the rapid precipitation of calcite, dolomite, and ankerite crystals that subsequently settle to the seafloor or the base of hydrothermal ponds. These crystals subsequently undergo sedimentation, forming bedded silicified carbonate rocks. Hence, the active participation of hydrothermal input is imperative for the establishment of the organo-

carbonate factory.

4.3.3 Microbial factory

Analogous to the organo-carbonate factory, the microbial factory is likewise influenced by Si-bearing hydrothermal inputs, facilitating carbonate precipitation and serving as a nutrient source for microbial life. Furthermore, these hydrothermal inputs contribute to the preservation of microbial buildups and diverse stromatolites. Organomicrite constitutes a prominent constituent within the microbial factory. Unlike the organo-carbonate factory where organomicrite precipitation is not influenced by the origins of organic macromolecules, carbonate production in the microbial factory is dominated by EPS-controlled microbial mineralization. The presence of possible anoxygenic photosynthesis suggests that the microbial factory might flourish in photic, shallow marine, low-energy settings, such as lagoons on slopes and/or platforms, influenced by detrital input and minor hydrothermal influences.

4.3.4 Implications

During the early Archean, the three carbonate factories served as crucial carbon sinks, exerting a significant influence on the global carbon cycle. In the modern exogenic system, the two dominant carbon reservoirs in the crust are carbonate rock, formed either as marine precipitates or during alteration of seafloor ocean crust, and biogenic organic matter (Hoefs, 2018; Shields, 2019). While biogenic carbon is initially stored in biogenic organic matter, it ultimately becomes incorporated into rocks, which constitute the Earth's largest carbon reservoir (Gislason and Oelkers, 2014). Carbon removal primarily occurs through processes such as terrestrial silicate weathering and seafloor weathering. However, exposure of continental crust was limited during the early Archean (Taylor and McLennan, 1981; Arndt, 1999; Flament et al., 2008; Cawood et al., 2013). Korenaga (2021) posits that during the late Hadean to early Archean, despite the continents reaching their current size, they remained submerged beneath a deeper ocean resulting from complete degassing of the mantle. As a consequence, oceanic islands were the only land surfaces exposed, leading to a significantly reduced terrestrial carbon sink through continental silicate weathering in the early Archean (Korenaga, 2021). Considering the carbonate production modes of the three carbonate factories, the oceanic crust factory likely functions as the primary carbon sink, supported by the presence of widespread carbonatized greenstones (Kitajima et al., 2001; Nakamura and Kato, 2002, 2004; Anhaeusser, 2014; Kasting, 2019; Nutman et al., 2019a; herein), and the organo-carbonate factory is subordinate, followed by the microbial factory.

On the other hand, the presence of abundant organic matter with highly depleted $\delta^{13}C$ values in the organo-carbonate factory may pose challenges in distinguishing the biogenicity of carbonate minerals. This is due to the potential ambiguity arising from the possibility of abiotic organic matter exhibiting similar $\delta^{13}C$ values. In this case, attention should be given to the chain-length distribution as a distinguishing factor. Duda et al., (2018) reported a sharp

decrease in homologue abundance beyond n-C_{18} in high-temperature Catalytic hydropyrolysis (HyPy) pyrolysates of biological organic matter (possibly from bacteria), whereas a unimodal distribution is exhibited by abiotic compounds experimentally formed via Fischer–Tropsch-type synthesis. Moreover, it is challenging to ascertain the validity of stromatolites. For example, despite the acceptance of marine origins for ISB stromatolite-like carbonates, supported by geochemical evidence such as $\delta^{13}C$ values resembling seawater and REE+Y patterns (Nutman et al., 2016, 2019b, 2021; Allwood et al., 2018; Zawaski et al., 2020, 2021; this work, Fig.10), the interpretation of these carbonates as stromatolites remains uncertain due to the potential presence of deformed marine laminated or bedded sedimentary carbonates.

Conclusion

Based on the various EPT Paleoarchean carbonates, three types of carbonate factories are identified as follows:

The oceanic crust factory is characterized by interstitial carbonates occurring within carbonatized pillow basalts. These carbonates primarily form through inorganic precipitation from CO_2-rich seawater or seawater-derived hydrothermal fluids resulting from interactions between seawater and basalt. The main product of this process is Fe/Mn-depleted acicular crystal-fan calcite, which can be locally altered to Fe/Mn-enriched blocky, massive calcite and ankerite. The presence of fresh basaltic oceanic crust is crucial for the establishment of this factory, typically occurring in deep marine environments within the upper oceanic crust.

The organo-carbonate factory is characterized by abundant organic materials, organomicrite and graded carbonates formed through taphonomy-controlled organo-mineralization. Organic macromolecules, regardless of their origin (biotic or abiotic), serve as nucleation sites for organomicrites and carbonate crystals. This straightforward formation process accounts for the widespread occurrence of this factory in diverse environments, ranging from shallow marine settings to terrestrial hydrothermal ponds. The depositional environments experience intermittent inputs of hydrothermal fluids, which provide sufficient organic macromolecules and alkaline cations to promote carbonate precipitation. The hydrothermal fluids contribute Si, leading to chert precipitation that aids in the preservation of sedimentary textures during diagenesis.

The microbial factory is characterized by diverse stromatolites formed through microbial extracellular polymeric substance (EPS)-controlled biomineralization, possibly involving anoxygenic photosynthesis. This factory is commonly found in the photic, relatively restricted, shallow marine settings, such as slope or platform lagoons. These environments receive minor inputs of detrital and hydrothermal materials, providing metal nutrients for benthic microbial communities and soluble silica for the preservation of microbial carbonate structures.

Acknowledgements

We would like to express our gratitude to those who provided technical assistance from the University of Göttingen: Axel Hackmann and Wolfgang Dröse for their assistance with sample preparation, and Dr. Burkhard Schmidt for his help with the Raman spectroscopic analysis and *in situ* geochemical mapping via micro-XRF. We also thank Dr. Tommaso Di Rocco, Dennis Kohl, and Thierry Wasselin for measuring stable carbon and oxygen isotopes.

We would like to extend our thanks to the following: Prof. Dr. Martin Van Kranendonk from the University of New South Wales, Australia, and Dr. Arthur Hickman from the Geological Survey of Western Australia for their indispensable logistical assistance in the field and their invaluable guidance in unraveling the intricate geological aspects of the Pilbara region; Faye and Geoffrey Myers, the caretakers of the old North Pole Gold Mine, whose gracious hospitality and exceptional assistance in locating suitable outcrops have played a pivotal role in our research (Faye and Geoffrey Myers epitomize the great Mimi spirit in the outback.); The core library of the Geological Survey of Western Australia, for granting us the necessary permission to sample drill core materials from the Pilbara region (approval for P954, 1014, 1091).

This study was financially supported by the China Council Scholarship (CSC) and SPP1833 (DFG-Schwerpunktprogramm) "Building a Habitable Earth". We would like to extend our sincere appreciation to the Göttingen Academy of Sciences and Humanities of Lower Saxony for the financial and scientific support, which has been instrumental in the successful execution of this research project.

References

Addadi, L., Weiner, S.: Interactions between acidic proteins and crystals: stereochemical requirements in biomineralization, Proceedings of the National Academy of Sciences, 82, 4110-4114, 1985.

Addadi, L., Raz, S., and Weiner, S.: Taking advantage of disorder: amorphous calcium carbonate and its roles in biomineralization, Advanced Materials, 15, 959–970, https://doi.org/10.1002/adma.200300381, 2003.

Alleon, J., Bernard, S., Le Guillou, C., Daval, D., Skouri-Panet, F., Pont, S., Delbes, L., and Robert, F.: Early entombment within silica minimizes the molecular degradation of microorganisms during advanced diagenesis, Chemical Geology, 437, 98–108, 2016.

Allwood, A. C., Walter, M. R., Kamber, B. S., Marshall, C. P., and Burch, I. W.: Stromatolite reef from the Early Archaean era of Australia, Nature, 441, 714–718, 2006.

Allwood, A. C., Walter, M. R., Burch, I. W., and Kamber, B. S.: 3.43 billion-year-old stromatolite reef from the Pilbara Craton of Western Australia: ecosystem-scale insights to early life on Earth, Precambrian Research, 158, 198–227, 2007.

Allwood, A. C., Grotzinger, J. P., Knoll, A. H., Burch, I. W., Anderson, M. S., Coleman, M. L., and Kanik, I.: Controls on development and diversity of Early Archean stromatolites, Proceedings of the National Academy of Sciences, 106, 9548–9555, 2009.

Allwood, A. C., Kamber, B. S., Walter, M. R., Burch, I. W., and Kanik, I.: Trace elements record depositional history of an Early Archean stromatolitic carbonate platform, Chemical Geology, 270, 148–163, 2010.

Allwood, A. C., Rosing, M. T., Flannery, D. T., Hurowitz, J. A., and Heirwegh, C. M.: Reassessing evidence of life in 3,700-million-year-old rocks of Greenland, Nature, 563, 241–244, 2018.

Alt, J. C. and Teagle, D. A.: The uptake of carbon during alteration of ocean crust, Geochimica et Cosmochimica Acta, 63, 1527–1535, 1999.

Andersen, T. and Taylor, P. N.: Pb isotope geochemistry of the Fen carbonatite complex, SE Norway: Age and petrogenetic implications, Geochimica et Cosmochimica Acta, 52, 209–215, https://doi.org/10.1016/0016-7037(88)90069-5, 1988.

Anhaeusser, C. R.: Archaean greenstone belts and associated granitic rocks–a review, Journal of African Earth Sciences, 100, 684–732, 2014.

Arndt, N.: Why was flood volcanism on submerged continental platforms so common in the Precambrian?, Precambrian Research, 97, 155–164, 1999.

Arp, G., Reimer, A., and Reitner, J.: Photosynthesis-induced biofilm calcification and calcium concentrations in Phanerozoic oceans, Science, 292, 1701–1704, 2001.

Awramik, S. M.: The oldest records of photosynthesis, Photosynthesis research, 33, 75–89, https://doi.org/10.1007/BF00039172, 1992.

Bach, W., Alt, J. C., Niu, Y., Humphris, S. E., Erzinger, J., and Dick, H. J.: The geochemical consequences of late-stage low-grade alteration of lower ocean crust at the SW Indian Ridge: Results from ODP Hole 735B (Leg 176), Geochimica et Cosmochimica Acta, 65, 3267–3287, 2001.

Bach, W., Peucker-Ehrenbrink, B., Hart, S. R., and Blusztajn, J. S.: Geochemistry of hydrothermally altered oceanic crust: DSDP/ODP Hole 504B–Implications for seawater-crust exchange budgets and Sr-and Pb-isotopic evolution of the mantle, Geochemistry, Geophysics, Geosystems, 4, 2003.

Bach, W., Rosner, M., Jöns, N., Rausch, S., Robinson, L. F., Paulick, H., and Erzinger, J.: Carbonate

veins trace seawater circulation during exhumation and uplift of mantle rock: Results from ODP Leg 209, Earth and Planetary Science Letters, 311, 242–252, 2011.

Bontognali, T. R., Sessions, A. L., Allwood, A. C., Fischer, W. W., Grotzinger, J. P., Summons, R. E., and Eiler, J. M.: Sulfur isotopes of organic matter preserved in 3.45-billion-year-old stromatolites reveal microbial metabolism, Proceedings of the National Academy of Sciences, 109, 15 146–15 151, 2012.

Bower, D., Steele, A., Fries, M., Green, O., and Lindsay, J.: Raman imaging spectroscopy of a putative microfossil from the 3.46 Ga Apex chert: Insights from quartz grain orientation, Astrobiology, 16, 169–180, 2016.

Brasier, M. D., Green, O. R., Jephcoat, A. P., Kleppe, A. K., Van Kranendonk, M. J., Lindsay, J. F., Steele, A., and Grassineau, N. V.: Questioning the evidence for Earth's oldest fossils, Nature, 416, 76–81, 2002.

Brasier, M., Green, O., Lindsay, J., and Steele, A.: Earth's Oldest (3.5 Ga) Fossils and theEarly Eden Hypothesis': Questioning the Evidence, Origins of Life and Evolution of the Biosphere, 34, 257–269, 2004.

Brasier, M. D., Green, O. R., Lindsay, J. F., McLoughlin, N., Steele, A., and Stoakes, C.: Critical testing of Earth's oldest putative fossil assemblage from the 3.5 Ga Apex chert, Chinaman Creek, Western Australia, Precambrian Research, 140, 55–102, 2005.

Brasier, M., McLoughlin, N., Green, O., and Wacey, D.: A fresh look at the fossil evidence for early Archaean cellular life, Philosophical Transactions of the Royal Society B: Biological Sciences, 361, 887–902, 2006.

Brasier, M. D., Antcliffe, J., Saunders, M., and Wacey, D.: Changing the picture of Earth's earliest fossils (3.5–1.9 Ga) with new approaches and new discoveries, Proceedings of the National Academy of Sciences, 112, 4859–4864, 2015.

Buick, R., Dunlop, J., and Groves, D.: Stromatolite recognition in ancient rocks: an appraisal of irregularly laminated structures in an Early Archaean chert-barite unit from North Pole, Western Australia, Alcheringa, 5, 161–181, https://doi.org/10.1080/03115518108566999, 1981.

Byerly, G. R., Lowe, D. R., Wooden, J. L., and Xie, X.: An Archean impact layer from the Pilbara and Kaapvaal cratons, Science, 297, 1325–1327, 2002.

Cantine, M. D., Knoll, A. H., and Bergmann, K. D.: Carbonates before skeletons: A database approach, Earth-Science Reviews, 201, 103 065, https://doi.org/10.1016/j.earscirev.2019.103065, 2020.

Cawood, P. A., Hawkesworth, C., and Dhuime, B.: The continental record and the generation of continental crust, Geological Society of America Bulletin, 125, 14–32, 2013.

Coogan, L. A. and Gillis, K. M.: Evidence that low-temperature oceanic hydrothermal systems play an important role in the silicate-carbonate weathering cycle and long-term climate regulation, Geochemistry, Geophysics, Geosystems, 14, 1771–1786, 2013.

Copper, P.: Reef development at the Frasnian/Famennian mass extinction boundary, Palaeogeography, Palaeoclimatology, Palaeoecology, 181, 27–65, 2002.

Degens, E. T., Wong, H.-K., Kempe, S., and Kurtman, F.: A geological study of Lake Van, eastern Turkey, Geologische Rundschau, 73, 701–734, https://doi.org/10.1007/BF01824978, 1984.

Delarue, F., Robert, F., Derenne, S., Tartèse, R., Jauvion, C., Bernard, S., Pont, S., Gonzalez-Cano, A., Duhamel, R., and Sugitani, K.: Out of rock: A new look at the morphological and geochemical preservation of microfossils from the 3.46 Gyr-old Strelley Pool Formation, Precambrian Research, 336, 105 472, 2020.

Djokic, T., Van Kranendonk, M. J., Campbell, K. A., Walter, M. R., and Ward, C. R.: Earliest signs of life on land preserved in ca. 3.5 Ga hot spring deposits, Nature communications, 8, 15 263, 2017.

Djokic, T., Van Kranendonk, M. J., Campbell, K. A., Havig, J. R., Walter, M. R., and Guido, D. M.: A reconstructed subaerial hot spring field in the 3.5 billion-year-old Dresser Formation, North Pole Dome, Pilbara Craton, Western Australia, Astrobiology, 21, 1–38, 2021.

Duda, J.-P., Van Kranendonk, M. J., Thiel, V., Ionescu, D., Strauss, H., Schäfer, N., and Reitner, J.: A rare glimpse of Paleoarchean life: Geobiology of an exceptionally preserved microbial mat facies from the 3.4 Ga Strelley Pool Formation, Western Australia, PLoS One, 11, e0147 629, 2016.

Duda, J.-P., Thiel, V., Bauersachs, T., Mißbach, H., Reinhardt, M., Schäfer, N., Van Kranendonk, M. J., and Reitner, J.: Ideas and perspectives: hydrothermally driven redistribution and sequestration of early Archaean biomass–the "hydrothermal pump hypothesis", Biogeosciences, 15, 1535–1548, 2018.

Escoffier, N., Perolo, P., Lambert, T., Rüegg, J., Odermatt, D., Adatte, T., Vennemann, T., and Perga, M.-E.: Whiting Events in a Large Peri-Alpine Lake: Evidence of a Catchment-Scale Process, Journal of Geophysical Research: Biogeosciences, 127, e2022JG006 823, 2022.

Flament, N., Coltice, N., and Rey, P. F.: A case for late-Archaean continental emergence from thermal evolution models and hypsometry, Earth and Planetary Science Letters, 275, 326–336, 2008.

Flannery, D. T., Allwood, A. C., Summons, R. E., Williford, K. H., Abbey, W., Matys, E. D., and Ferralis, N.: Spatially-resolved isotopic study of carbon trapped in 3.43 Ga Strelley Pool Formation stromatolites, Geochimica et Cosmochimica Acta, 223, 21–35, 2018.

Flügel, E. and Munnecke, A.: Microfacies of carbonate rocks: analysis, interpretation and application, vol. 976, Springer, 2nd., 2010.

French, K. L., Hallmann, C., Hope, J. M., Schoon, P. L., Zumberge, J. A., Hoshino, Y., Peters, C. A., George, S. C., Love, G. D., Brocks, J. J., et al.: Reappraisal of hydrocarbon biomarkers in Archean rocks, Proceedings of the National Academy of Sciences, 112, 5915–5920, https://doi.org/10.1073/pnas.1419563112, 2015.

Galeczka, I., Wolff-Boenisch, D., and Gislason, S.: Experimental studies of basalt-H2O-CO2 interaction with a high pressure column flow reactor: the mobility of metals, Energy Procedia, 37, 5823–5833, https://doi.org/10.1016/j.egypro.2013.06.505, 2013a.

Galeczka, I., Wolff-Boenisch, D., Jonsson, T., Sigfusson, B., Stefansson, A., and Gislason, S.: A novel high pressure column flow reactor for experimental studies of CO_2 mineral storage, Applied Geochemistry, 30, 91–104, https://doi.org/10.1016/j.apgeochem.2012.08.010, 2013b.

Galeczka, I., Wolff-Boenisch, D., Oelkers, E. H., and Gislason, S. R.: An experimental study of basaltic glass–H_2O–CO_2 interaction at 22 and 50 °C: Implications for subsurface storage of CO_2, Geochimica et Cosmochimica Acta, 126, 123–145, https://doi.org/10.1016/j.gca.2013.10.044, 2014.

Gardiner, N. J., Wacey, D., Kirkland, C. L., Johnson, T. E., and Jeon, H.: Zircon U–Pb, Lu–Hf and O isotopes from the 3414 Ma Strelley Pool Formation, East Pilbara Terrane, and the Palaeoarchaean emergence of a cryptic cratonic core, Precambrian Research, 321, 64–84, https://doi.org/10.1016/j.precamres.2018.11.023, 2019.

Geological Survey of Western Australia, cartographer. (GSWA), Western Australia. Department of Mines and Petroleum., and Exploration Incentive Scheme (W.A.): 1:100 000 GIS Pilbara 2013 update / Geological Survey of Western Australia, 2013.

Germs, G. J.: New shelly fossils from Nama Group, south west Africa, American Journal of Science, 272, 752–761, https://doi.org/10.2475/ajs.272.8.752, 1972.

Gillis, K. M., Muehlenbachs, K., Stewart, M., Gleeson, T., and Karson, J.: Fluid flow patterns in fast spreading East Pacific Rise crust exposed at Hess Deep, Journal of Geophysical Research: Solid Earth, 106, 26 311–26 329, https://doi.org/10.1029/2000JB000038, 2001.

Gislason, S. R. and Oelkers, E. H.: Carbon storage in basalt, Science, 344, 373–374, https://doi.org/10.1126/science.1250828, 2014.

Glikson, M., Duck, L. J., Golding, S. D., Hofmann, A., Bolhar, R., Webb, R., Baiano, J. C., and Sly, L. I.: Microbial re- mains in some earliest Earth rocks: comparison with a potential modern analogue, Precambrian Research, 164, 187–200, https://doi.org/10.1016/j.precamres.2008.05.002, 2008.

Grant, S.: Shell structure and distribution of Cloudina, a potential index fossil for the terminal Proterozoic, American Journal of Science, 290, 261–294, 1990.

Grotzinger, J. P. and Knoll, A. H.: Anomalous carbonate precipitates: is the Precambrian the key to the Permian?, Palaios, 10, 578–596, https://doi.org/10.2307/3515096, 1995.

Grotzinger, J. P. and Knoll, A. H.: Stromatolites in Precambrian carbonates: evolutionary mileposts or environmental dipsticks?, Annual review of earth and planetary sciences, 27, 313–358, https://doi.org/10.1146/annurev.earth.27.1.313, 1999.

Grotzinger, J. P. and James, N. P.: Precambrian carbonates: evolution of understanding, in: Carbonate Sedimentation and Diagenesis in the Evolving Precambrian World, SEPM Society for Sedimentary Geology, https://doi.org/10-2110/pec.00.67, 2000.

Gudbrandsson, S., Wolff-Boenisch, D., Gislason, S. R., and Oelkers, E. H.: An experimental study of crystalline basalt dissolution from 2⩽ pH⩽ 11 and temperatures from 5 to 75 C, Geochimica et Cosmochimica Acta, 75, 5496–5509, https://doi.org/10.1016/j.gca.2011.06.035, 2011.

Gysi, A. P. and Stefánsson, A.: CO_2–water–basalt interaction. Numerical simulation of low temperature CO_2 sequestration into basalts, Geochimica et Cosmochimica Acta, 75, 4728–4751, https://doi.org/10.1016/j.gca.2011.05.037, 2011.

Hayes, J. M. and Waldbauer, J. R.: The carbon cycle and associated redox processes through time, Philosophical Transactions of the Royal Society B: Biological Sciences, 361, 931–950, https://doi.org/10.1098/rstb.2006.1840, 2006.

Heft, K. L., Gillis, K. M., Pollock, M. A., Karson, J. A., and Klein, E. M.: Role of upwelling hydrothermal fluids in the development of alteration patterns at fast spreading ridges: Evidence from the sheeted dike complex at Pito Deep, Geochemistry, Geophysics, Geosystems, 9, https://doi.org/10.1029/2007GC001926, 2008.

Heinrichs, T.: Lithostratigraphische Untersuchungen in der Fig Tree Gruppe des Barberton Greenstone Belt zwischen Umsoli und Lomati (Südafrika), Ph.D. thesis, Goettingen University, 1980.

Hickman, A. H. and Van Kranendonk, M.: A Billion Years of Earth History: A Geological Transect Through the Pilbara Craton and the Mount Bruce Supergroup-a Field Guide to Accompany 34th IGC Excursion WA-2, Geological Survey of Western Australia, Record 2012/10, 2012a.

Hickman, A. H. and Van Kranendonk, M. J.: Early Earth evolution: evidence from the 3.5–1.8 Ga geological history of the Pilbara region of Western Australia, Episodes Journal of International Geoscience, 35, 283–297, https://doi.org/10.18814/epiiugs/2012/v35i1/028, 2012b.

Hickman, A., Van Kranendonk, M., and Grey, K.: State Geoheritage Reserve R50149 (Trendall Reserve), North Pole, Pilbara Craton, Western Australia — geology and evidence for early Archean life. Geological Survey of Western Australia Record 2011/10, 2011.

Hickman-Lewis, K., Westall, F., and Cavalazzi, B.: Trace of early life in the Barberton greenstone belt, in: Earth's Oldest Rocks, edited by Van Kranendonk, M., Bennett, V., and Hoffmann, E., pp. 1029–1058, Elsevier, https://hal.science/hal-03041208, 2019.

Higgins, J. A., Fischer, W., and Schrag, D.: Oxygenation of the ocean and sediments: consequences for the seafloor carbonate factory, Earth and Planetary Science Letters, 284, 25–33, https://doi.org/10.1016/j.epsl.2009.03.039, 2009.

Hoefs, J.: Stable isotope geochemistry, Springer International Publishing AG, part of Springer Nature, 8th ed., 2018.

Hofmann, H.: Stromatolites: characteristics and utility, Earth-Science Reviews, 9, 339–373, https://doi.org/10.1016/0012-8252(73)90002-0, 1973.

Hofmann, A. and Harris, C.: Silica alteration zones in the Barberton greenstone belt: a window into subseafloor processes 3.5–3.3 Ga ago, Chemical Geology, 257, 221–239, https://doi.org/10.1016/j.chemgeo.2008.09.015, 2008.

Hofmann, H., Grey, K., Hickman, A., and Thorpe, R.: Origin of 3.45 Ga coniform stromatolites in Warrawoona group, Western Australia, Geological Society of America Bulletin, 111, 1256–1262, https://doi.org/10.1130/0016-7606(1999)111<1256:OOGCSI>2.3.CO;2, 1999.

Kalkowsky, E.: Oolith und Stromatolith im norddeutschen Buntsandstein., Zeitschrift der deutschen geologischen Gesellschaft, pp. 68–125, 1908.

Kasting, J. F.: Early Earth Atmosphere and Oceans, in: Earth's Oldest Rocks, edited by Van Kranendonk, M.J., B. V. H. J., pp. 49–61, Elsevier, 2019.

Kato, Y. and Nakamura, K.: Origin and global tectonic significance of Early Archean cherts from the Marble Bar greenstone belt, Pilbara Craton, Western Australia, Precambrian Research, 125, 191–243, https://doi.org/10.1016/S0301-9268(03)00043-3, 2003.

Kempe, S.: Alkalinity: the link between anaerobic basins and shallow water carbonates?, Naturwissenschaften, 77, 426–427, 1990.

Kitajima, K., Maruyama, S., Utsunomiya, S., and Liou, J.: Seafloor hydrothermal alteration at an Archaean mid-ocean ridge, Journal of Metamorphic Geology, 19, 583–599, https://doi.org/10.1046/j.0263-4929.2001.00330.x, 2001.

Knoll, A. H., Bambach, R. K., Payne, J. L., Pruss, S., and Fischer, W. W.: Paleophysiology and end-Permian mass extinction, Earth and Planetary Science Letters, 256, 295–313, https://doi.org/10.1016/j.epsl.2007.02.018, 2007.

Komiya, T., Maruyama, S., Hirata, T., and Yurimoto, H.: Petrology and geochemistry of MORB and OIB in the mid-Archean North Pole region, Pilbara craton, Western Australia: implications for the composition and temperature of the upper mantle at 3.5 Ga, International Geology Review, 44, 988–1016, https://doi.org/10.2747/0020-6814.44.11.988, 2002.

Korenaga, J.: Was there land on the early Earth?, Life, 11, 1142, https://doi.org/10.3390/life11111142, 2021.

Kozawa, T., Sugitani, K., Oehler, D. Z., House, C. H., Saito, I., Watanabe, T., and Gotoh, T.: Early Archean planktonic mode of life: Implications from fluid dynamics of lenticular microfossils, Geobiology, 17, 113–126, https://doi.org/10.1111/gbi.12319, 2019.

Kraml, M., Pik, R., Rahn, M., Selbekk, R., Carignan, J., and Keller, J.: A new multi-mineral age reference material for $^{40}Ar/^{39}Ar$, (U-Th)/He and fission track dating methods: the Limberg t3 tuff, Geostandards and Geoanalytical Research, 30, 73–86, https://doi.org/10.1111/j.1751-908X.2006.tb00914.x, 2006.

Lambert, I., Donnelly, T., Dunlop, J., Groves, and DI: Stable isotopic compositions of early Archaean sulphate deposits of probable evaporitic and volcanogenic origins, Nature, 276, 808–811, https://doi.org/10.1038/276808a0, 1978.

Ledevin, M.: Archean cherts: Formation processes and paleoenvironments, in: Earth's Oldest Rocks, edited by Van Kranendonk, M., Bennett, V., and Hoffmann, J., pp. 913–944, Elsevier, 2019.

Lees, A. and Buller, A. T.: Modern temperate-water and warm-water shelf carbonate sediments contrasted, Marine Geology, 13, M67–M73, https://doi.org/10.1016/0025-3227(72)90011-4, 1972.

Lepot, K.: Signatures of early microbial life from the Archean (4 to 2.5 Ga) eon, Earth-Science Reviews, 209, 103296, https://doi.org/10.1016/j.earscirev.2020.103296, 2020.

Lepot, K., Williford, K. H., Ushikubo, T., Sugitani, K., Mimura, K., Spicuzza, M. J., and Valley, J. W.: Texture-specific isotopic compositions in 3.4 Gyr old organic matter support selective preservation in cell-like structures, Geochimica et Cosmochimica Acta, 112, 66–86, https://doi.org/10.1016/j.gca.2013.03.004, 2013.

Lindsay, J., Brasier, M., McLoughlin, N., Green, O., Fogel, M., Steele, A., and Mertzman, S.: The problem of deep carbon—an Archean paradox, Precambrian Research, 143, 1–22, https://doi.org/10.1016/j.precamres.2005.09.003, 2005.

Lister, G. and Snoke, A.: SC mylonites, Journal of Structural Geology, 6, 617–638, https://doi.org/10.1016/0191-8141(84)90001-4, 1984.

Lünsdorf, N. K., Dunkl, I., Schmidt, B. C., Rantitsch, G., and von Eynatten, H.: Towards a higher comparability of geothermometric data obtained by Raman spectroscopy of carbonaceous material. Part 2: A revised geothermometer, Geostandards and Geoanalytical Research, 41, 593–612, https://doi.org/10.1111/ggr.12178, 2017.

Marshall, C. P., Love, G. D., Snape, C. E., Hill, A. C., Allwood, A. C., Walter, M. R., Van Kranendonk, M. J., Bowden, S. A., Sylva, S. P., and Summons, R. E.: Structural characterization of kerogen in 3.4 Ga Archaean cherts from the Pilbara Craton, Western Australia, Precambrian Research, 155, 1–23, https://doi.org/10.1016/j.precamres.2006.12.014, 2007.

McCollom, T. M. and Seewald, J. S.: Carbon isotope composition of organic compounds produced by abiotic synthesis under hydrothermal conditions, Earth and Planetary Science Letters, 243, 74–84, https://doi.org/10.1016/j.epsl.2006.01.027, 2006.

McCollom, T. M., Ritter, G., and Simoneit, B. R.: Lipid synthesis under hydrothermal conditions by Fischer-Tropsch-type reactions, Origins of Life and Evolution of the Biosphere, 29, 153–166, https://doi.org/10.1023/A:1006592502746, 1999.

McGrail, B. P., Schaef, H. T., Spane, F. A., Cliff, J. B., Qafoku, O., Horner, J. A., Thompson, C. J., Owen, A. T., and Sulli- van, C. E.: Field validation of supercritical CO2 reactivity with basalts, Environmental Science & Technology Letters, 4, 6–10, https://doi.org/10.1021/acs.estlett.6b00387, 2017.

McKeegan, K. D., Kudryavtsev, A. B., and Schopf, J. W.: Raman and ion microscopic imagery of graphitic inclusions in apatite from older than 3830 Ma Akilia supracrustal rocks, west Greenland, Geology, 35, 591–594, https://doi.org/10.1130/G23465A.1, 2007.

McNaughton, N., Compston, W., and Barley, M.: Constraints on the age of the Warrawoona Group, eastern Pilbara block, Western Australia, Precambrian Research, 60, 69–98, https://doi.org/10.1016/0301-9268(93)90045-4, 1993.

Menefee, A. H., Giammar, D. E., and Ellis, B. R.: Permanent CO_2 trapping through localized and chemical gradient-driven basalt carbona- tion, Environmental science & technology, 52, 8954–

8964, https://doi.org/10.1021/acs.est.8b01814, 2018.

Mojzsis, S. J., Arrhenius, G., McKeegan, K., Harrison, T., Nutman, A., and Friend, C.: Evidence for life on Earth before 3,800 million years ago, Nature, 384, 55–59, https://doi.org/10.1038/384055a0, 1996.

Moore, E. K., Jelen, B. I., Giovannelli, D., Raanan, H., and Falkowski, P. G.: Metal availability and the expanding network of microbial metabolisms in the Archaean eon, Nature Geoscience, 10, 629–636, https://doi.org/10.1038/ngeo3006, 2017.

Morag, N., Williford, K. H., Kitajima, K., Philippot, P., Van Kranendonk, M. J., Lepot, K., Thomazo, C., and Valley, J. W.: Microstructure- specific carbon isotopic signatures of organic matter from 3.5 Ga cherts of the Pilbara Craton support a biologic origin, Precambrian Research, 275, 429–449, https://doi.org/10.1016/j.precamres.2016.01.014, 2016.

Nakamura, K. and Kato, Y.: Carbonate minerals in the Warrawoona Group, Pilbara Craton: Implications for continental crust, life, and global carbon cycle in the Early Archean, Resource Geology, 52, 91–100, https://doi.org/10.1111/j.1751-3928.2002.tb00122.x, 2002.

Nakamura, K. and Kato, Y.: Carbonatization of oceanic crust by the seafloor hydrothermal activity and its significance as a CO2 sink in the Early Archean, Geochimica et Cosmochimica Acta, 68, 4595–4618, https://doi.org/10.1016/j.gca.2004.05.023, 2004.

Neuweiler, F. and Reitner, J.: Initially indurated structures of fine-grained calcium carbonate formed in place (automicrite), Biomineralization 93: Proceedings of the 7th International Symposium on Biomineralization: Musée Océanographique, Monaco, pp. 265–271, 1993.

Nijman, W. and de Vries, S. T.: Early Archaean crustal collapse structures and sedimentary basin dynamics, in: The Precambrian Earth: Tempos and Events, edited by Eriksson, P., Altermann, W., Nelson, D., Mueller, W., and Catuneau, O., pp. 139–154, Elsevier, Amsterdam, 2004.

Nisbet, E. and Sleep, N.: The habitat and nature of early life, Nature, 409, 1083–1091, https://doi.org/10.1038/35059210, 2001.

Nutman, A. P., Bennett, V. C., Friend, C. R., Van Kranendonk, M. J., and Chivas, A. R.: Rapid emergence of life shown by discovery of 3,700-million-year-old microbial structures, Nature, 537, 535–538, https://doi.org/10.1038/nature19355, 2016.

Nutman, A. P., Friend, C. R., Bennett, V. C., Van Kranendonk, M., and Chivas, A. R.: Reconstruction of a 3700 Ma transgressive marine environment from Isua (Greenland): Sedimentology, stratigraphy and geochemical signatures, Lithos, 346, 105164, https://doi.org/10.1016/j.lithos.2019.105164, 2019a.

Nutman, A. P., Bennett, V. C., Friend, C. R., Van Kranendonk, M. J., Rothacker, L., and Chivas, A. R.: Cross-examining Earth's oldest stromatolites: Seeing through the effects of heterogeneous deformation, metamorphism and metasomatism affecting Isua (Greenland) 3700 Ma sedimentary rocks, Precambrian Research, 331, 105 347, https://doi.org/10.1016/j.precamres.2019.105347, 2019b.

Nutman, A. P., Bennett, V. C., Friend, C. R., and Van Kranendonk, M. J.: In support of rare relict 3700 Ma stromatolites from Isua (Green- land), Earth and Planetary Science Letters, 562, 116 850, https://doi.org/10.1016/j.epsl.2021.116850, 2021.

Oehler, D. Z., Robert, F., Walter, M. R., Sugitani, K., Allwood, A., Meibom, A., Mostefaoui, S., Selo, M., Thomen, A., and Gibson, E. K.: NanoSIMS: insights to biogenicity and syngeneity of Archaean carbonaceous structures, Precambrian Research, 173, 70–78, https://doi.org/10.1016/j.precamres.2009.01.001, 2009.

Ohtomo, Y., Kakegawa, T., Ishida, A., Nagase, T., and Rosing, M. T.: Evidence for biogenic graphite in early Archaean Isua metasedimentary rocks, Nature Geoscience, 7, 25–28, https://doi.org/10.1038/ngeo2025, 2014.

Otálora, F., Mazurier, A., Garcia-Ruiz, J. M., Van Kranendonk, M., Kotopoulou, E., El Albani, A., and Garrido, C.: A crystallographic study of crystalline casts and pseudomorphs from the 3.5 Ga Dresser Formation, Pilbara Craton (Australia), Journal of Applied Crystallography, 51, 1050–1058, https://doi.org/10.1107/S1600576718007343, 2018.

Pei, Y.: A geobiological approach to carbonate factories and ecosystem changes across the Permian–Triassic boundary, Ph.D. thesis, University of Göttingen, Germany, http://dx.doi.org/10.53846/goediss-9160, 2022.

Pei, Y., Chen, Z.-Q., Fang, Y., Kershaw, S., Wu, S., and Luo, M.: Volcanism, redox conditions, and microbialite growth linked with the end-Permian mass extinction: Evidence from the Xiajiacao section (western Hubei Province), South China, Palaeogeography, Palaeoclimatology, Palaeoecology, 519, 194–208, https://doi.org/10.1016/j.palaeo.2017.07.020, 2019.

Pei, Y., Duda, J.-P., and Reitner, J.: Sedimentary factories and ecosystem change across the Permian–Triassic Critical Interval (P–TrCI): insights from the Xiakou area (South China), PalZ, pp. 709–725, https://doi.org/10.1007/s12542-020-00530-x, 2021.

Pei, Y., Blumenberg, M., Duda, J.-P., Höche, N., Peckmann, J., Birgel, D., Luo, J., Kment, K., and Reitner, J.: Ecosystem changes through the Permian–Triassic and Triassic–Jurassic critical intervals: Evidence from sedimentology, palaeontology and geochemistry, Sedimentology, https://doi.org/10.1111/sed.13088, 2023.

Pinti, D. L., Hashizume, K., Sugihara, A., Massault, M., and Philippot, P.: Isotopic fractionation of nitrogen and carbon in Paleoarchean cherts from Pilbara craton, Western Australia: Origin of 15N-depleted nitrogen, Geochimica et Cosmochimica Acta, 73, 3819–3848, https://doi.org/10.1016/j.gca.2009.03.014, 2009.

Pomar, L. and Hallock, P.: Carbonate factories: a conundrum in sedimentary geology, Earth-Science Reviews, 87, 134–169, https://doi.org/10.1016/j.earscirev.2007.12.002, 2008.

Pruss, S. B., Bottjer, D. J., Corsetti, F. A., and Baud, A.: A global marine sedimentary response to the end-Permian mass extinction: examples from southern Turkey and the western United States, Earth-science reviews, 78, 193–206, https://doi.org/10.1016/j.earscirev.2006.05.002, 2006.

Rasmussen, B., Fletcher, I. R., and Muhling, J. R.: In situ U–Pb dating and element mapping of three generations of monazite: unravelling cryptic tectonothermal events in low-grade terranes, Geochimica et Cosmochimica Acta, 71, 670–690, https://doi.org/10.1016/j.gca.2006.10.020, 2007.

Reijmer, J. J.: Marine carbonate factories: review and update, Sedimentology, 68, 1729–1796, https://doi.org/10.1111/sed.12878, 2021.

Reitner, J.: Modern cryptic microbialite/metazoan facies from Lizard Island (Great Barrier Reef, Australia) formation and concepts, Facies, 29, 3-39, 1993.

Reitner, J.: Organomineralization: A clue to the understanding of meteorite-related “bacteria-shaped” carbonate particles, in: Origins: Genesis, Evolution and Diversity of Life, pp. 195–212, Springer, 2004.

Reitner, J. and Neuweiler, F.: Part I Mud mounds: recognizing a polygenetic spectrum of fine-grained carbonate buildups, in: Mud mounds: a polygenetic spectrum of fine-grained carbonate buildups, edited by Reitner, J. and Neuweiler, F., pp. 2–4, 1995.

Reitner, J. and Thiel, V.: Encyclopedia of geobiology, Springer Amsterdam, 2011.

Reitner, J., Wilmsen, M., and Neuweiler, F.: Cenomanian/Turonian sponge microbialite deep-water hardground community (Liencres, Northern Spain), Facies, 32, 203–212, https://doi.org/10.1007/BF02536869, 1995a.

Reitner, J., Neuweiler, F., and Gautret, P.: Part II Modern and fossil automicrites: implications for mud mound genesis, in: Mud Mounds: A Polygenetic Spectrum of Fine-grained Carbonate Buildups, edited by Reitner, J. and Neuweiler, F., vol. 32, pp. 4–17, 1995b.

Reitner, J., Thiel, V., Zankl, H., Michaelis, W., Wörheide, G., and Gautret, P.: Organic and biogeochemical patterns in cryptic microbialites, in: Microbial sediments, edited by Riding, R. E. and Awramik, S. M., pp. 149–160, Springer, Berlin, https://doi.org/10.1007/978-3-662-04036-2_17, 2000.

Reitner, J., Wörheide, G., Lange, R., and Schumann-Kindel, G.: Coralline demosponges; a geobiological portrait, Bulletin/The Tohoku University Museum, pp. 219–235, https://doi.org/10.23689/fidgeo-2565, 2001.

Riding, R.: The term stromatolite: towards an essential definition, Lethaia, 32, 321–330, https://doi.org/10.1111/j.1502-3931.1999.tb00550.x, 1999.

Riding, R.: Microbial carbonates: the geological record of calcified bacterial–algal mats and biofilms, Sedimentology, 47, 179–214, https://doi.org/10.1046/j.1365-3091.2000.00003.x, 2000.

Rincón-Tomás, B., Khonsari, B., Mühlen, D., Wickbold, C., Schäfer, N., Hause-Reitner, D., Hoppert, M., and Reitner, J.: Manganese carbonates as possible biogenic relics in Archean settings, International Journal of Astrobiology, 15, 219–229, https://doi.org/10.1017/S1473550416000264, 2016.

Robbins, L. and Blackwelder, P.: Biochemical and ultrastructural evidence for the origin of whitings: A biologically induced calcium carbonate precipitation mechanism, Geology, 20, 464–468, https://doi.org/10.1130/0091-7613(1992)020<0464:BAUEFT>2.3.CO;2, 1992.

Roberts, R. G.: Ore deposit models# 11. Archean lode gold deposits, Geoscience Canada, 14, 37–52, https://id.erudit.org/iderudit/geocan14_1art02, 1987.

Rouillard, J., Van Kranendonk, M. J., Lalonde, S., Gong, J., and Van Zuilen, M. A.: Correlating trace element compositions, petrol- ogy, and Raman spectroscopy data in the 3.46 Ga Apex chert, Pilbara Craton, Australia, Precambrian Research, 366, 106415, https://doi.org/10.1016/j.precamres.2021.106415, 2021.

Runge, E. A., Duda, J.-P., Van Kranendonk, M. J., and Reitner, J.: Earth's oldest tsunami deposit? Early Archaean high-energy sediments in the ca 3.48 Ga Dresser Formation (Pilbara, Western Australia), The Depositional Record, 8, 590–602, https://doi.org/10.1002/dep2.175, 2022.

Schlager, W.: Sedimentation rates and growth potential of tropical, cool-water and mud-mound carbonate systems, Geological Society, London, Special Publications, 178, 217–227, https://doi.org/10.1144/GSL.SP.2000.178.01.14, 2000.

Schlager, W.: Benthic carbonate factories of the Phanerozoic, International Journal of Earth Sciences, 92, 445–464, https://doi.org/10.1007/s00531-003-0327-x, 2003.

Schopf, J. W.: Microfossils of the Early Archean Apex chert: new evidence of the antiquity of life, Science, 260, 640–646, https://doi.org/10.1126/science.260.5108.640, 1993.

Schopf, J. W., Kudryavtsev, A. B., Agresti, D. G., Wdowiak, T. J., and Czaja, A. D.: Laser–Raman imagery of Earth's earliest fossils, Nature, 416, 73–76, https://doi.org/10.1038/416073a, 2002.

Schopf, J. W., Kudryavtsev, A. B., Osterhout, J. T., Williford, K. H., Kitajima, K., Valley, J. W., and Sugitani, K.: An anaerobic 3400 Ma shallow-water microbial consortium: Presumptive evidence

of Earth's Paleoarchean anoxic atmosphere, Precambrian Research, 299, 309–318, https://doi.org/10.1016/j.precamres.2017.07.021, 2017.

Schrag, D. P., Higgins, J. A., Macdonald, F. A., and Johnston, D. T.: Authigenic carbonate and the history of the global carbon cycle, Science, 339, 540–543, https://doi.org/10.1126/science.1229578, 2013.

Shibuya, T., Tahata, M., Kitajima, K., Ueno, Y., Komiya, T., Yamamoto, S., Igisu, M., Terabayashi, M., Sawaki, Y., Takai, K., et al.: Depth variation of carbon and oxygen isotopes of calcites in Archean altered upperoceanic crust: Implications for the CO_2 flux from ocean to oceanic crust in the Archean, Earth and Planetary Science Letters, 321, 64–73, https://doi.org/10.1016/j.epsl.2011.12.034, 2012.

Shields, G. A.: Implications of Carbonate and Chert Isotope Records for the Early Earth, in: Earth's Oldest Rocks, edited by Van Kranendonk, M., Bennett, V., and Hoffmann, J., pp. 901–912, Elsevier, 2019.

Smithies, R., Champion, D., and Cassidy, K.: Formation of Earth's early Archaean continental crust, Precambrian Research, 127, 89–101, https://doi.org/10.1016/S0301-9268(03)00182-7, 2003.

Smithies, R. H., Champion, D. C., Van Kranendonk, M. J., Howard, H. M., and Hickman, A. H.: Modern-style subduction processes in the Mesoarchaean: geochemical evidence from the 3.12 Ga Whundo intra-oceanic arc, Earth and Planetary Science Letters, 231, 221–237, https://doi.org/10.1016/j.epsl.2004.12.026, 2005.

Smithies, R., Champion, D., Van Kranendonk, M., and Hickman, A.: Geochemistry of volcanic rocks of the northern Pilbara Craton, Western Australia, Geological Survey of Western Australia Report, 104, 1–47, 2007a.

Smithies, R. H., Champion, D. C., and Van Kranendonk, M. J.: The oldest well-preserved felsic volcanic rocks on Earth: Geochemical clues to the early evolution of the Pilbara Supergroup and implications for the growth of a Paleoarchean protocontinent, in: Earth's Oldest Rocks, edited by Van Kranendonk, M., Smithies, R., and Bennett, V., vol. Developments in Precambrian Geology 15, pp. 339–367, Elsevier, Amsterdam, https://doi.org/10.1016/S0166-2635(07)15042-8, 2007b.

Stockmann, G. J., Wolff-Boenisch, D., Gislason, S. R., and Oelkers, E. H.: Do carbonate precipitates affect dissolution kinetics? 1: Basaltic glass, Chemical Geology, 284, 306–316, https://doi.org/10.1016/j.chemgeo.2011.03.010, 2011.

Sugitani, K., Lepot, K., Nagaoka, T., Mimura, K., Van Kranendonk, M., Oehler, D. Z., and Walter, M. R.: Biogenicity of morphologically diverse carbonaceous microstructures from the ca. 3400 Ma Strelley Pool Formation, in the Pilbara Craton, Western Australia, Astrobiology, 10, 899–920, https://doi.org/10.1089/ast.2010.0513, 2010.

Sugitani, K., Mimura, K., Nagaoka, T., Lepot, K., and Takeuchi, M.: Microfossil assemblage from the 3400 Ma Strelley Pool Formation in the Pilbara Craton, Western Australia: results form a new locality, Precambrian Research, 226, 59–74, https://doi.org/10.1016/j.precamres.2012.11.005, 2013.

Sugitani, K., Mimura, K., Takeuchi, M., Yamaguchi, T., Suzuki, K., Senda, R., Asahara, Y., Wallis, S., and Van Kranendonk, M.: A Paleoarchean coastal hydrothermal field inhabited by diverse microbial communities: the Strelley Pool Formation, Pilbara Craton, Western Australia, Geobiology, 13, 522–545, https://doi.org/10.1111/gbi.12150, 2015a.

Sugitani, K., Mimura, K., Takeuchi, M., Lepot, K., Ito, S., and Javaux, E.: Early evolution of large micro-organisms with cytological complexity revealed by microanalyses of 3.4 Ga organic-walled

microfossils, Geobiology, 13, 507–521, https://doi.org/10.1111/gbi.12148, 2015b.
Sugitani, K., Kohama, T., Mimura, K., Takeuchi, M., Senda, R., and Morimoto, H.: Speciation of Paleoarchean life demonstrated by analysis of the morphological variation of lenticular microfossils from the Pilbara Craton, Australia, Astrobiology, 18, 1057–1070, https://doi.org/10.1089/ast.2017.1799, 2018.
Taylor, S. R. and McLennan, S.: The composition and evolution of the continental crust: rare earth element evidence from sedimentary rocks, Philosophical Transactions of the Royal Society of London. Series A, Mathematical and Physical Sciences, 301, 381–399, https://doi.org/10.1098/rsta.1981.0119, 1981.
Terabayashi, M., Masada, Y., and Ozawa, H.: Archean ocean-floor metamorphism in the North Pole area, Pilbara Craton, western Australia, Precambrian Research, 127, 167–180, https://doi.org/10.1016/S0301-9268(03)00186-4, 2003.
Thompson, J. B., Schultze-Lam, S., Beveridge, T. J., and Des Marais, D. J.: Whiting events: biogenic origin due to the photosynthetic activity of cyanobacterial picoplankton, Limnology and oceanography, 42, 133–141, https://doi.org/10.4319/lo.1997.42.1.0133, 1997.
Thorpe, R., Hickman, A., Davis, D., Mortensen, J., and Trendall, A.: U-Pb zircon geochronology of Archaean felsic units in the Marble Bar region, Pilbara Craton, Western Australia, Precambrian Research, 56, 169–189, https://doi.org/10.1016/0301-9268(92)90100-3, 1992.
Tice, M. M., Thornton, D. C., Pope, M. C., Olszewski, T. D., and Gong, J.: Archean microbial mat communities, Annual review of earth and planetary sciences, 39, 297–319, https://doi.org/10.1146/annurev-earth-040809-152356, 2011.
Trichet, J., Defarge, C., et al.: Non-biologically supported organomineralization, Bulletin de l'Institut océanographique, Monaco. Numéro spécial, pp. 203–236, 1995.
Ueno, Y., Isozaki, Y., Yurimoto, H., and Maruyama, S.: Carbon isotopic signatures of individual Archean microfossils (?) from Western Australia, International Geology Review, 43, 196–212, https://doi.org/10.1080/00206810109465008, 2001.
Ueno, Y., Yoshioka, H., Maruyama, S., and Isozaki, Y.: Carbon isotopes and petrography of kerogens in 3.5-Ga hydrothermal silica dikes in the North Pole area, Western Australia, Geochimica et Cosmochimica Acta, 68, 573–589, https://doi.org/10.1016/S0016-7037(03)00462- 9, 2004.
van den Boorn, S. H., van Bergen, M. J., Nijman, W., and Vroon, P. Z.: Dual role of seawater and hydrothermal fluids in Early Archean chert formation: evidence from silicon isotopes, Geology, 35, 939–942, https://doi.org/10.1130/G24096A.1, 2007.
Van Kranendonk, M. J.: Volcanic degassing, hydrothermal circulation and the flourishing of early life on Earth: A review of the evi- dence from ca. 3490-3240 Ma rocks of the Pilbara Supergroup, Pilbara Craton, Western Australia, Earth-Science Reviews, 74, 197–240, https://doi.org/10.1016/j.earscirev.2005.09.005, 2006.
Van Kranendonk, M. J.: A review of the evidence for putative Paleoarchean life in the Pilbara Craton, Western Australia, Developments in Precambrian Geology, 15, 855–877, https://doi.org/10.1016/S0166-2635(07)15072-6, 2007.
Van Kranendonk, M.: Stromatolite morphology as an indicator of biogenicity for Earth's oldest fossils from the 3.5-3.4 Ga Pilbara Craton, Western Australia, in: Advances in stromatolite geobiology. Lecture notes in earth sciences, edited by Reitner, J., Queric, N., and Arp, G., vol. 131, pp. 517–534, 2011.
Van Kranendonk, M. J. and Pirajno, F.: Geochemistry of metabasalts and hydrothermal alteration zones

associated with ca. 3.45 Ga chert and barite deposits: implications for the geological setting of the Warrawoona Group, Pilbara Craton, Australia, Geochemistry: Exploration, Environment, Analysis, 4, 253–278, https://doi.org/10.1144/1467-7873/04-205, 2004.

Van Kranendonk, M. J., Hickman, A. H., Smithies, R. H., Nelson, D. R., and Pike, G.: Geology and tectonic evolution of the Archean North Pilbara terrain, Pilbara Craton, Western Australia, Economic Geology, 97, 695–732, https://doi.org/10.2113/gsecongeo.97.4.695, 2002.

Van Kranendonk, M. J., Webb, G. E., and Kamber, B. S.: Geological and trace element evidence for a marine sedimentary environment of deposition and biogenicity of 3.45 Ga stromatolitic carbonates in the Pilbara Craton, and support for a reducing Archaean ocean, Geobiology, 1, 91–108, https://doi.org/10.1046/j.1472-4669.2003.00014.x, 2003.

Van Kranendonk, M. J., Hickman, A. H., and Huston, D. L.: Geology and Mineralization of the East Pilbara d A Field Guide, Western Australia Geological Survey. Record 2006/16, 94p, 2006.

Van Kranendonk, M. J., Hugh Smithies, R., Hickman, A. H., and Champion, D.: Secular tectonic evolution of Archean continental crust: interplay between horizontal and vertical processes in the formation of the Pilbara Craton, Australia, Terra Nova, 19, 1–38, https://doi.org/10.1111/j.1365-3121.2006.00723.x, 2007a.

Van Kranendonk, M. J., Smithies, R. H., Hickman, A. H., and Champion, D. C.: Paleoarchean development of a continental nucleus: the East Pilbara terrane of the Pilbara craton, Western Australia, Developments in Precambrian geology, 15, 307–337, https://doi.org/10.1016/S0166-2635(07)15041-6, 2007b.

Van Kranendonk, M. J., Philippot, P., Lepot, K., Bodorkos, S., and Pirajno, F.: Geological setting of Earth's oldest fossils in the ca. 3.5 Ga Dresser formation, Pilbara Craton, Western Australia, Precambrian Research, 167, 93–124, https://doi.org/10.1016/j.precamres.2008.07.003, 2008.

Van Kranendonk, M. J., Smithies, R. H., Hickman, A. H., and Champion, D. C.: Paleoarchean development of a continental nucleus: the East Pilbara Terrane of the Pilbara Craton, Western Australia, in: Earth's Oldest Rocks, edited by Van Kranendonk, M.J., Bennett, V.C., Hoffmann, J.E., pp. 437–462, Elsevier, 2019a.

Van Kranendonk, M., Djokic, T., Poole, G., Tadbiri, S., Steller, L., and Baumgartner, R.: Depositional Setting of the Fossiliferous, ca.3480 Ma Dresser Formation, Pilbara Craton: A Review, in: Earth's Oldest Rocks, edited by Van Kranendonk, M.J., Bennett, V.C., Hoffmann, J.E., pp. 985–1006, Elsevier, 2019b.

van Zuilen, M. A.: Proposed early signs of life not set in stone, Nature, pp. 190–191, https://doi.org/10.1038/d41586-018-06994-x, 2018.

van Zuilen, M.: The Significance of Carbonaceous Matter to Understanding Life Processes on Early Earth. In: Van Kranendonk, M.J., Bennett, V.C., Hoffmann, J.E. (Eds.), in: Earth's Oldest Rocks. Elsevier, 945–963, 2019.

Veizer, J., Hoefs, J., Ridler, R., Jensen, L., and Lowe, D.: Geochemistry of Precambrian carbonates: I. Archean hydrothermal systems, Geochimica et Cosmochimica Acta, 53, 845–857, https://doi.org/10.1016/0016-7037(89)90030-6, 1989a.

Veizer, J., Hoefs, J., Lowe, D., and Thurston, P.: Geochemistry of Precambrian carbonates: II. Archean greenstone belts and Archean sea water, Geochimica et Cosmochimica Acta, 53, 859–871, https://doi.org/10.1016/0016-7037(89)90031-8, 1989b.

Viehmann, S., Reitner, J., Tepe, N., Hohl, S. V., Van Kranendonk, M., Hofmann, T., Koeberl, C., and Meister, P.: Carbonates and cherts as archives of seawater chemistry and habitability on a

carbonate platform 3.35 Ga ago: Insights from Sm/Nd dating and trace element analysis from the Strelley Pool Formation, Western Australia, Precambrian Research, 344, 105742, https://doi.org/10.1016/j.precamres.2020.105742, 2020.

Voigt, M., Pearce, C. R., Baldermann, A., and Oelkers, E. H.: Stable and radiogenic strontium isotope fractionation during hydrothermal seawater-basalt interaction, Geochimica et Cosmochimica Acta, 240, 131–151, https://doi.org/10.1016/j.gca.2018.08.018, 2018.

Wacey, D.: Stromatolites in the 3400 Ma Strelley Pool Formation, Western Australia: examining biogenicity from the macro-to the nano- scale, Astrobiology, 10, 381–395, https://doi.org/10.1089/ast.2009.0423, 2010.

Wacey, D., McLoughlin, N., Whitehouse, M. J., and Kilburn, M. R.: Two coexisting sulfur metabolisms in a ca. 3400 Ma sandstone, Geology, 38, 1115–1118, https://doi.org/10.1130/G31329.1, 2010.

Wacey, D., Kilburn, M. R., Saunders, M., Cliff, J., and Brasier, M. D.: Microfossils of sulphur-metabolizing cells in 3.4-billion-year-old rocks of Western Australia, Nature Geoscience, 4, 698–702, https://doi.org/10.1038/ngeo1238, 2011.

Wacey, D., Noffke, N., Saunders, M., Guagliardo, P., and Pyle, D. M.: Volcanogenic pseudo-fossils from the 3.48 Ga dresser formation, Pilbara, Western Australia, Astrobiology, 18, 539–555, https://doi.org/10.1089/ast.2017.1734, 2018.

Wang, J., Tarhan, L. G., Jacobson, A. D., Oehlert, A. M., and Planavsky, N. J.: The evolution of the marine carbonate factory, Nature, pp. 1–5, https://doi.org/10.1038/s41586-022-05654-5, 2023.

Weiner, S. and Dove, P. M.: An overview of biomineralization processes and the problem of the vital effect, Reviews in mineralogy and geochemistry, 54, 1–29, https://doi.org/10.2113/0540001, 2003.

Wojdyr, M.: Fityk: a general-purpose peak fitting program, Journal of Applied Crystallography, 43, 1126–1128, https://doi.org/10.1107/S0021889810030499, 2010.

Wolff-Boenisch, D. and Galeczka, I.: Flow-through reactor experiments on basalt-(sea)water-CO_2 reactions at 90 °C and neutral pH. What happens to the basalt pore space under post-injection conditions?, International Journal of Greenhouse Gas Control, 68, 176–190, https://doi.org/10.1016/j.ijggc.2017.11.013, 2018.

Xiong, W., Wells, R. K., Horner, J. A., Schaef, H. T., Skemer, P. A., and Giammar, D. E.: CO_2 mineral sequestration in naturally porous basalt, Environmental Science & Technology Letters, 5, 142–147, https://doi.org/10.1021/acs.estlett.8b00047, 2018.

Yamamoto, K., Itoh, N., Matsumoto, T., Tanaka, T., and Adachi, M.: Geochemistry of Precambrian carbonate intercalated in pillows and its host basalt: implications for the REE composition of circa 3.4 Ga seawater, Precambrian Research, 135, 331–344, https://doi.org/10.1016/j.precamres.2004.09.006, 2004.

Zawaski, M. J., Kelly, N. M., Orlandini, O. F., Nichols, C. I., Allwood, A. C., and Mojzsis, S. J.: Reappraisal of purported ca. 3.7 Ga stromatolites from the Isua Supracrustal Belt (West Greenland) from detailed chemical and structural analysis, Earth and Planetary Science Letters, 545, 116 409, https://doi.org/10.1016/j.epsl.2020.116409, 2020.

Zawaski, M. J., Kelly, N. M., Orlandini, O. F., Nichols, C. I., Allwood, A. C., and Mojzsis, S. J.: Reply: The Isua (Greenland)" relict stromatolites" cannot be confidently interpreted as original sedimentary structures, Earth and Planetary Science Letters, 562, 116 851, https://doi.org/10.1016/j.epsl.2021.116851, 2021.

Appendix

This appendix is a supplementary work for the dissertation.

Part-1 Petrological observation of altered interstitial calcite

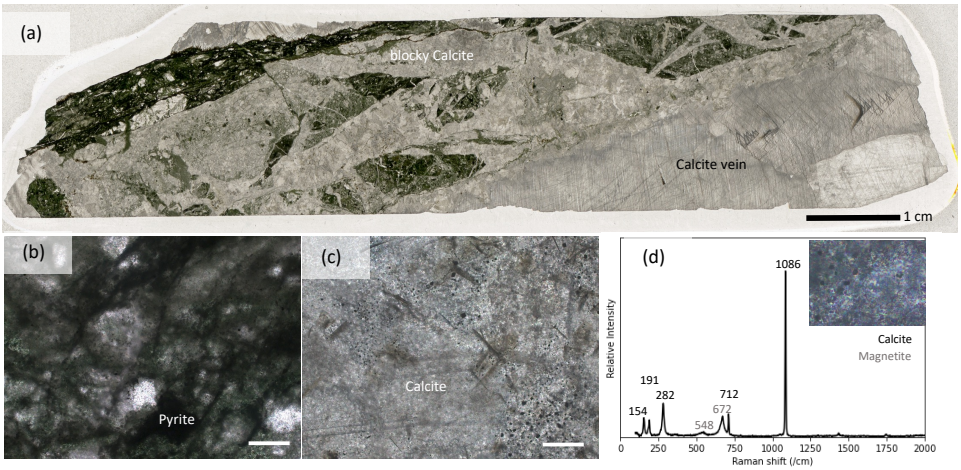

Fig.S1 The interstitial carbonate sample (CP-1) of North Star Basalt from the AIDP-1 core (292.0m-292.2m). (a) Scan image (transmitted light) of thin section. The interspace of basalt is filled dominantly by blocky calcite. (b) PPL image of basalt with the mineral assemblage of calcite + chlorite + anatase + quartz + pyrite, and no volcanic texture. (c) XPL image of blurred blocky calcite and fine opaque particles in the interspace of basalt, which is indicated to be magnetite via (d) the analysis of its Raman spectrum. (PPL: Plane-polarized light. XPL: Cross-polarized light. Scale bar: 200 μm.)

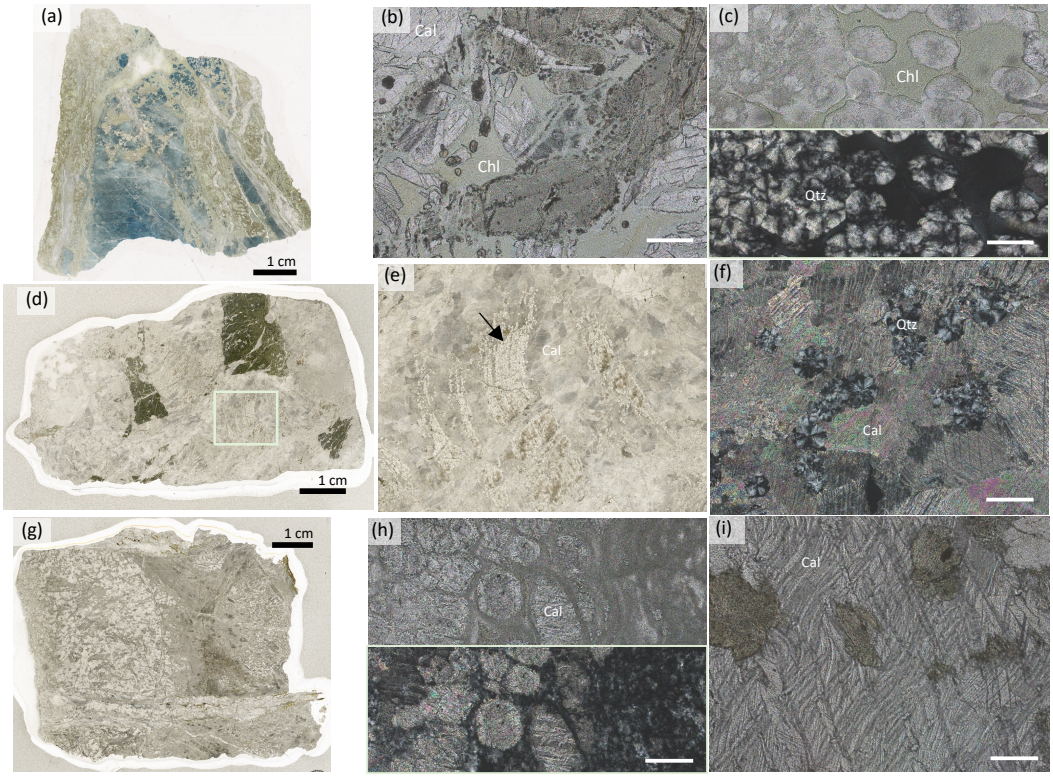

Fig.S2 Photographs of three Euro Basalt samples. (a) Scan image (transmitted light) of thin section E-1 stained by potassium hexacyanoferrate (II) trihydrate, showing the Fe-rich carbonate (blue) afterwards. Images of the altered basalts can be seen in (b) and (c). (b) PPL image of the disintegrated spherulites of calcite (Cal) and anatase on the matrix of cryptocrystalline chlorite (Chl). (c) PPL (up) and XPL (down) images of chalcedony spherulites (or fibrous quartz spherulites, Qtz). (d) Scan image (transmitted light) of thin section E-2. Amplified image of the square area is shown in (e). (e) Deformed basaltic breccia that the chlorite matrix is almost lost (black arrow). (f) XPL image of the fibrous quartz spherulites that are released into interspace and cemented by blocky calcite. (g) Scan image (transmitted light) of thin section E-3. (h) PPL (up) and XPL (down) images of the calcite spherulites that are transformed from spherulites within metabasalt; (i) The metamorphic S-C fabric in calcite and chlorite, indicating the influence of dynamic metamorphism. (PPL: plane-polarized light; XPL: cross-polarized light; Scale bar: 200 μm.)

Part-2 Petrological observation and in-situ geochemistry of interstitial dolomite

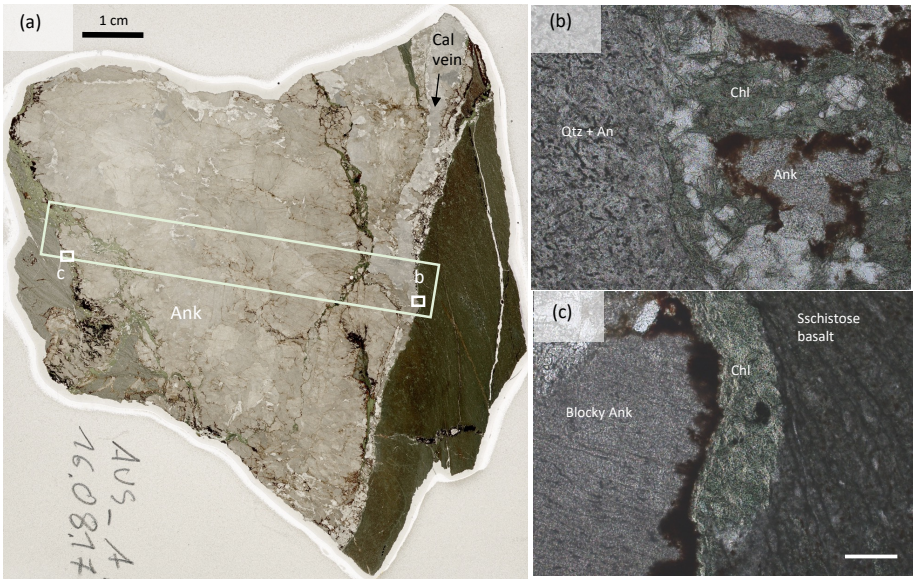

Fig.S3 Photographs of the more altered interstitial carbonate sample MtAda-1 from Mount Ada Basalt. (a) Scan image (transmitted light). The interstitial carbonate is blocky and massive ankerite with minor calcite overgrowth and infilling quartz. The rectangle area is magnified in Fig.4a, with the false-color overlapping images of several elements. Close-up PPL images show (b) the highly altered basalt and (c) the less altered schistose basalt, from which chlorite migrates out and becomes crystalline. (Abbreviations in images: Cal-calcite, Chl-chlorite, Qtz-quartz, Ank-ankerite, An-anatase. PPL: Plane-polarized light. Scale bar: 200 μm.)

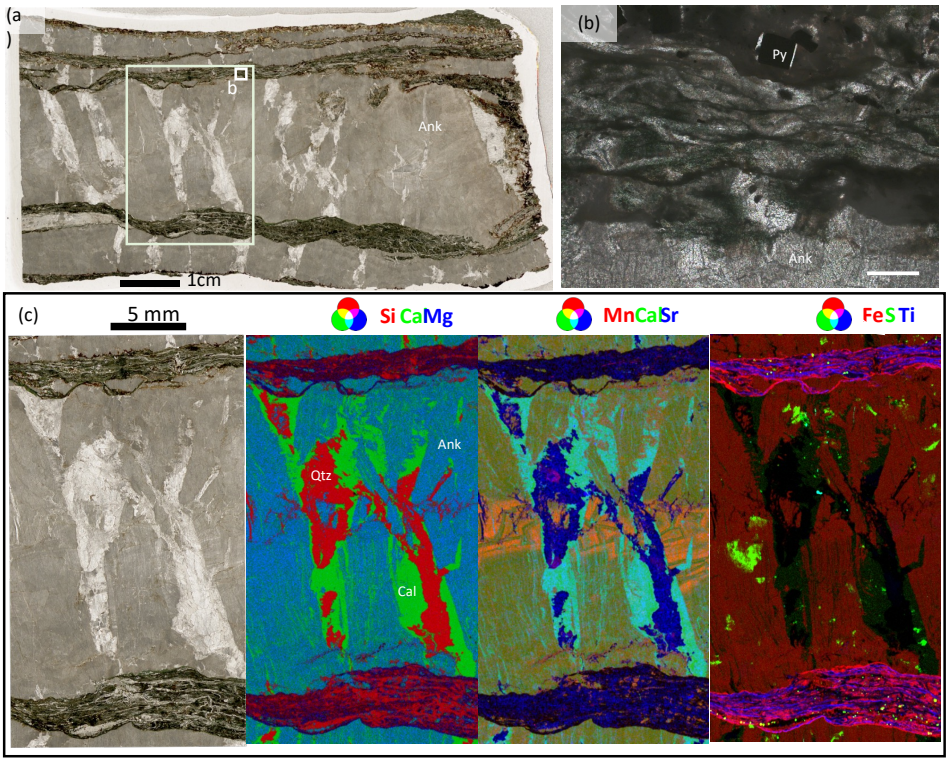

Fig.S4 The images of the deep-vein carbonate sample MtAda-2 from Mount Ada Basalt. (a) Scan image under transmitted light, and the rectangle area is magnified in (c). (b) The schistose basalt breccia consists of ankerite (Ank) + chlorite + anatase + quartz + euhedral pyrite (Py). The pyrite crystal occurs with short strain fringes, indicating a ductile deformation during formation (Scale bar: 200 μm). (c) False-color overlapping images show that the dominant interstitial carbonate is Mn-enriched ankerite of two generations, with dewatering cracks and intercrystalline spaces filling by Mn-depleted and Sr-enriched calcite (Cal), as well as quartz (Qtz). Pyrite crystals are abundant within the schistose basalt.

Part-3 Petrological observation of fracture filling calcite

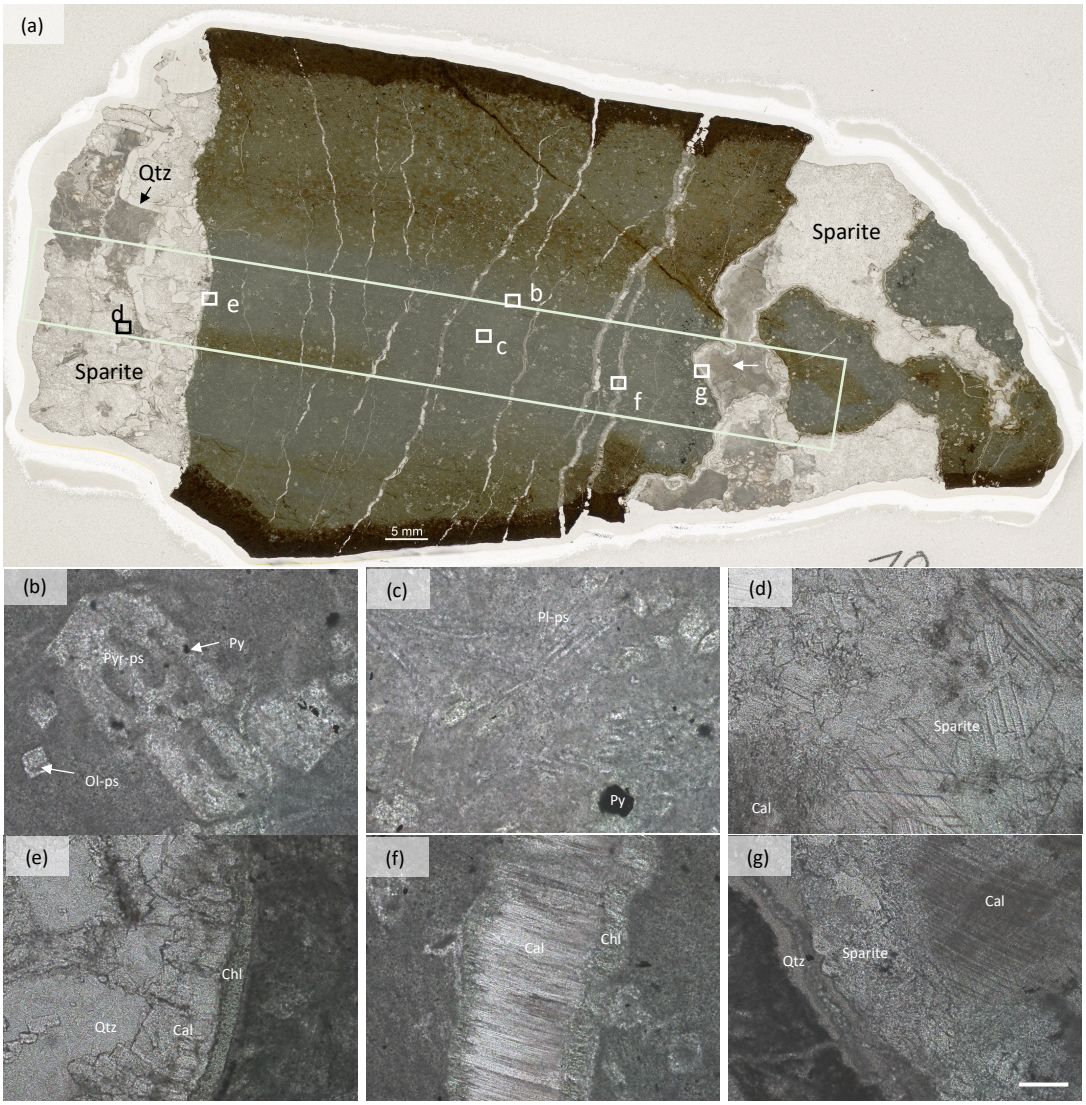

Fig.S5 Photographs of sample D-2 from the middle basalt member, Dresser Formation. (a) Scan image (transmitted light) of the thin section. The basalt exhibits ophitic-holohyaline and intersertal textures but no quenched margin with a set of parallel veins. The interspace is infilled by sparry calcite, the residue of acicular crystal-fan calcite (white arrow) and quartz cement. Close-up images (PPL) of the marked areas will be shown below. The geochemical imaging of the rectangle area is shown in Fig.4b. Phenocrysts (ps) of pyroxene (Pyr-ps) and olivine (Ol-ps) in (b), as well as plagioclase (Pl-ps) in (c) are pseudomorphed by calcite (Cal) + chlorite (Chl) + quartz (Qtz) + pyrite (Py). (d) The sparite forms through the recrystallization of the earlier acicular calcite. The sharp contacts of (e) basalt-chlorite-isopachous sparite on the edge of basalt and (f) in the parallel veins within basalt, indicates the sparite forms within a wide fracture of the basalt and thus is renamed as fracture-filling calcite. (g) The migration zone consists of microcrystalline quartz and chlorite, contacting with sparites in the terminal tips of acicular crystal-fan calcite. Scale bar of 200 μm in (g) is applicable to images (b) to (g). (PPL: Plane-polarized light.)

Part-4 A summary for interstitial carbonates

Table S1 Lithology description of the studied interstitial carbonates

SampleID	Formation	Age (Ma)	Lithology		Interpretation of interstitial carbonate
			Interstitial material	Basalt	
E-1	Euro Basalt	3335 to 3350	Acicular crystal-fan calcite (Fe-rich, white), partly altered to bloky calcite	Basalt preserves part of volcanic texture with disintegrated spherulites of calcite + anatase and spherulites of fibrous quartz both on the cryptocrystalline chlorite groundmass.	More altered
E-2			Pink blocky calcite, cementing metabasalt breccia	Pieces of pillow basalt exist as breccia, part of which are highly deformed. Spherulites of fibrous quartz scatter in interstitial calcite along with the loss of chlorite matrix.	
E-3			White to grey calcite cemented by quartz, possibly as the residue of acicular fan calcite. Recrystalization is prevasive and some crystals are highly deformed.	Basalt is preserved as a tiny piece of carbonatized basalt. Chlorite in the interspace is usually deformed.	Highly altered, possibly influenced by tecotic events
A22	Apex Basalt	3454 to 3463	The least altered acicular crystal-fan calcite, with miner intercrystalline quartz	Basalt has the best-preserved volcanic textures of ophitic-holohyaline and intersertal textures in core and size-dicreasing spherulites of calcite and anatase in quenched margin.	Primary facies
ABAS			Similar to A22	Similar to A22	
A14673			Acicular crystal-fan calcite, partly recrytalized to sparite	Basalt occurs as carbonatized breccia of pillow basalt that spherulites start to disintegrate and chlorite migrates out.	Primary facies, partly influenced by the later alteration of the host basalt
Apex			Blocky and sparry calcite with two vein sets of calcite and quartz, respectively. The residue of acicular crystal-fan calcite can be observed.	Carbonatized pillow basalt occurs with the original minerals replaced by calcite + chlorite + anatase + epidote.	More altered
MtAda-1	Mount Ada Basalt	3470±2	Blocky and massive ankerite (partly recrystallization and neomorphism) with calcite overgrowth and quartz cement and sometimes cut by clear calcite veins.	Basalt occurs to be more metamorphic with schitose basalt part consisting of chlorit+ quartz+ antase, that chlorite is lost in the highly altered basalt. Interstitial chlorite is crystalline.	Ankerite may be generated from the alteration of the primary interstitial calcite by Fe- and Mg-enriched diagenetic fluids.
MtAda-2			Blocky ankerite with dewatering cracks that are filled by calcite overgrowth and quartz cement.	Basalt is schitose, consisting of chlorit+quartz+ antase+ankerite+ pyrite (usually occurs with strain fringes).	
D-2	Middle Basalt (Dresser Fm.)	3480 ±2	Blocky sparites from the crystallization of acicular crystal-fan calcite with quartz cements.	Basalt is preserved with ophitic-holohyaline and intersertal textures, and cut by a set of parallel veins infilled by calcite and chlorite.	The interstitial carbonate is generated in the fractures instead of interspace between pillow basalts, thus termed as fracture-filling calcite.
CP-1	North Star Basalt	> 3490	Blocky calcite with fine particles of magnetite.	Metabasalt with the mineral assemblage of calcite + chlorite + anatase + quartz.	More altered interstitial carbonate

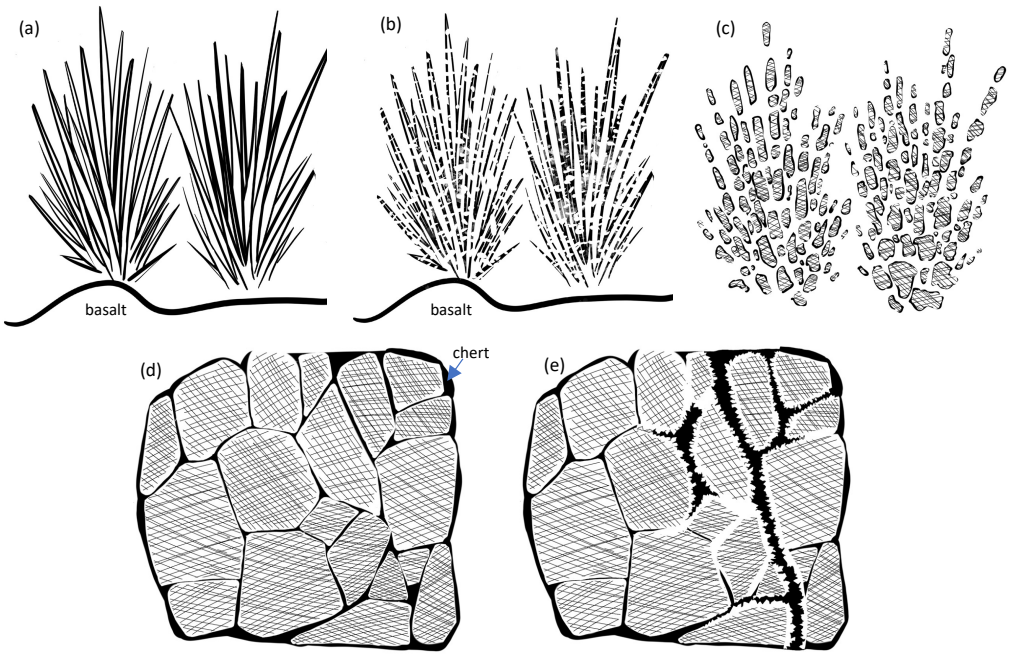

Fig.S6 Sketches of the various interstitial carbonates. (a) The acicular crystal-fan calcite is the primary facies of interstitial carbonates. (b) shows the start of dissolution and recrystallization (to be sparite) of acicular crystal-fan calcite. (c) The acicular crystal-fan calcite is altered to blocky calcite, however, retains the fan-like shape. (d) The blocky to massive ankerites in the interstitial dolomite samples are commonly cemented by chert. (e) Later fluid circulations in the fractures form the calcite overgrowth on the edge of ankerite.

Part-5 “Microfossils”? No, they are volcanic artifacts!

The putative Archean microfossils have been reported from the Strelley Pool Formation (Sugitani et al., 2007; Delarue et al., 2020; SPF) and Apex chert dike (Schopf, 1993). However, many of these fossils have been questioned to be volcanic and hydrothermal microstructures (Brasier et al., 2002, 2015; Pinti et al., 2009; Wacey et al., 2018). Wacey et al. (2018) reported an assemblage of tephra, including scoria, tubular pumice, vesicular and non-vesicular volcanic glass shards from the SPF. They closely resemble the previously described microfossils from this unit and elsewhere, and are enveloped by anatase and small amounts of organic materials (Wacey et al., 2018). Similar microstructures are also observed in the metabasalts from the studied basalt formations or members in this area, which are commonly silicate spherulites and carbonate variolites in the quenched margin of pillow basalts and altered basaltic breccias (Fig.S7a to c). When the groundmass, generally calcite and chlorite, breaks up during the progressive alteration, the silicate spherulites are released into hydrothermal fluids and adsorb organic matter, which is abundant in hydrothermal ventings. They consequently may be wrongly interpreted as microfossils. The same fate falls on the microtextures of titanite in pillow lavas of Euro Basalt, which were proposed as the ichnofossils of subseafloor microbes by Banerjee et al. (2007). However, they were rejected by McLoughlin et al. (2020) to be of abiotic origin, which formed by spontaneous nucleation and growth of titanite and/or anatase during seafloor hydrothermal metamorphism, confirmed in this work (Fig.S7d).

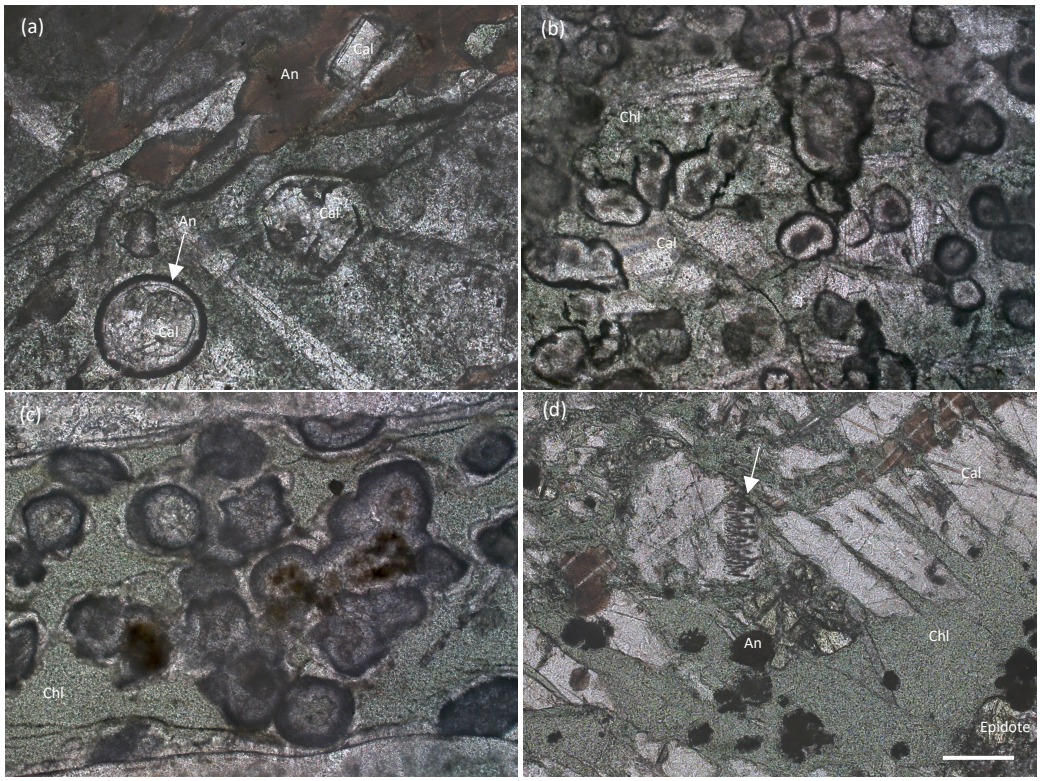

Fig.S7 The volcanic microstructures in Apex Basalt that resemble microfossils and ichnofossils. The variolites in the quenched margin of Apex pillow basalts, consisting of (a) a calcite core and a anatase crust, and (b) an anatase core, a calcite intermediate layer and an anatase crust. (c) Similar variolites can be found in the altered basaltic breccias. (d) Anatase filaments in calcite exhibit an ichnofossil-like morphology (white arrow). (Cal-calcite, Chl- chlorite, An-anatase; Scale bar of 200 µm in (d) is applicable to all images)

References

Banerjee, N. R., Simonetti, A., Furnes, H., Muehlenbachs, K., Staudigel, H., Heaman, L., and Van Kranendonk, M. J.: Direct dating of Archean microbial ichnofossils, Geology, 35, 487–490, https://doi.org/10.1130/G23534A.1, 2007.

Brasier, M. D., Green, O. R., Jephcoat, A. P., Kleppe, A. K., Van Kranendonk, M. J., Lindsay, J. F., Steele, A., and Grassineau, N. V.: Questioning the evidence for Earth's oldest fossils, Nature, 416, 76–81, 2002.

Brasier, M. D., Antcliffe, J., Saunders, M., and Wacey, D.: Changing the picture of Earth's earliest fossils (3.5–1.9 Ga) with new approaches and new discoveries, Proceedings of the National Academy of Sciences, 112, 4859–4864, 2015.

Delarue, F., Robert, F., Derenne, S., Tartèse, R., Jauvion, C., Bernard, S., Pont, S., Gonzalez-Cano, A., Duhamel, R., and Sugitani, K.: Out of rock: A new look at the morphological and geochemical preservation of microfossils from the 3.46 Gyr-old Strelley Pool Formation, Precambrian Research, 336, 105 472, 2020.

McLoughlin, N., Wacey, D., Phunguphungu, S., Saunders, M., and Grosch, E. G.: Deconstructing Earth's oldest ichnofossil record from the Pilbara Craton, West Australia: Implications for seeking life in the Archean subseafloor, Geobiology, 18, 525–543, https://doi.org/10.1111/gbi.12399, 2020.

Pinti, D. L., Hashizume, K., Sugihara, A., Massault, M., and Philippot, P.: Isotopic fractionation of nitrogen and carbon in Paleoarchean cherts from Pilbara craton, Western Australia: Origin of ^{15}N-depleted d nitrogen, Geochimica et Cosmochimica Acta, 73, 3819–3848, https://doi.org/https://doi.org/10.1016/j.gca.2009.03.014, 2009.

Schopf, J. W.: Microfossils of the Early Archean Apex chert: new evidence of the antiquity of life, Science, 260, 640–646, https://doi.org/10.1126/science.260.5108.640, 1993.

Sugitani, K., Grey, K., Allwood, A., Nagaoka, T., Mimura, K., Minami, M., Marshall, C. P., Van Kranendonk, M. J., and Walter, M. R.: Diverse microstructures from Archaean chert from the Mount Goldsworthy–Mount Grant area, Pilbara Craton, Western Australia: micro- fossils, dubiofossils, or pseudofossils?, Precambrian Research, 158, 228–262, https://doi.org/10.1016/j.precamres.2007.03.006, 2007.

Wacey, D., Saunders, M., and Kong, C.: Remarkably preserved tephra from the 3430 Ma Strelley Pool Formation, Western Australia: Implications for the interpretation of Precambrian microfossils, Earth and Planetary Science Letters, 487, 33–43, https://doi.org/10.1016/j.epsl.2018.01.021, 2018.

Part-6 Petrological observation and in-situ geochemistry of marine sedimentary carbonates

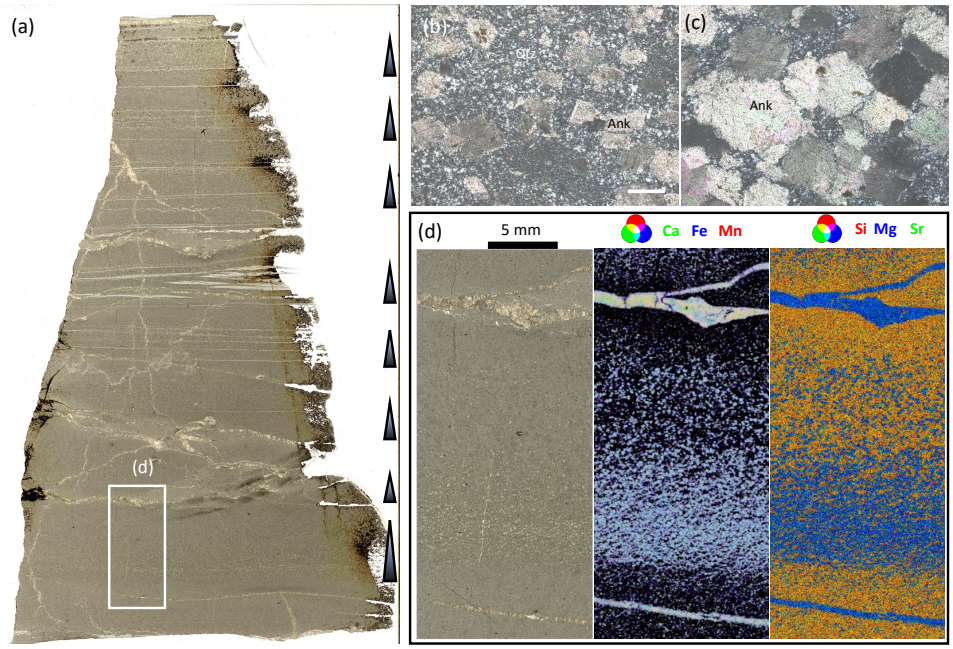

Fig.S8 The bedded sedimentary silicified carbonate from Euro Basalt. (a) Scan image (transmitted light) of the thin section. The rectangle area is magnified in (d). (b) The subhedral to anhedral ankerite rhombs on the microcrystalline quartz groundmass in the upper part of one layer. (c) The ankerite rhombs are larger in the lower part of one layer and experience pressure dissolution. (d) False-color overlapping images show the size-grading crystals of Fe- and Mn-enriched dolomite crystals and veins on a chert matrix. (Ank-ankerite, Qtz-quartz; (b) and (c) share the scale bar of 200 μm)

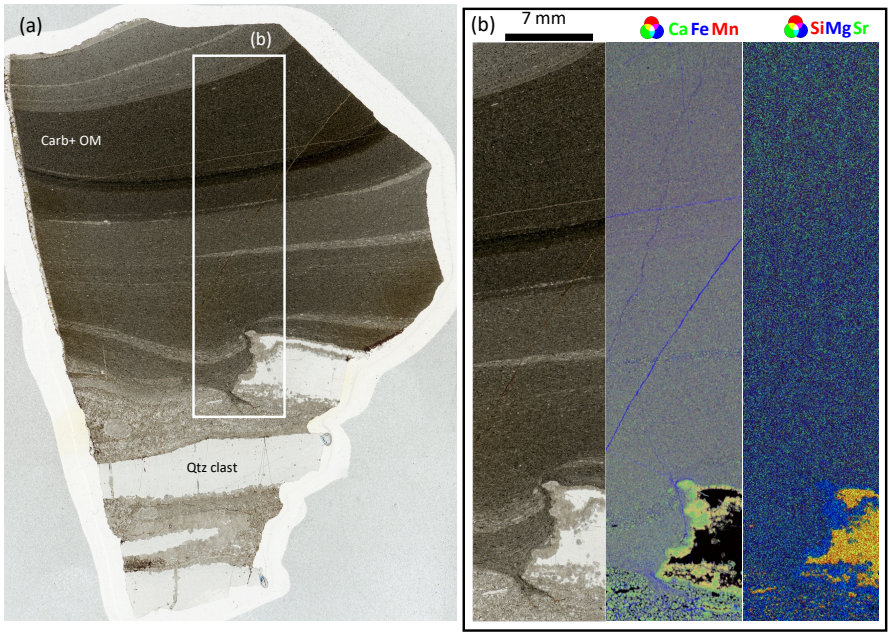

Fig.S9 The laminated micritic carbonate from the tsunami deposit, Dresser Formation. (a) Scan image (transmitted light) of the thin section. The rectangle area is magnified in (b). (b) False-color overlapping images indicate the laminae only consist of Mn-enriched ankerites, that the light and dark colors are not caused by mineralogy but amounts of organic matter. The euhedral dolomite overgrowths have a Mn-enriched rim and a relatively Mn-depleted core.

Part-7 Temperature of the early Archean ocean

There are many uncertainties in calculating seawater temperature using the $\delta^{18}O$ values of carbonates, especially for the early Archean ocean. It is discussed with details in Chapter 5. In this section, the calculated formation temperatures of some Archean carbonates are listed in Table S2, which may suffer less from later alteration and be of marine or marine-hydrothermal origins. Specifically, the $\delta^{18}O$ values of carbonates including the SPF laminated carbonates Strelley (this work), the highest $\delta^{18}O$ value of -10.9 ‰ (except two outliers) in Lindsay et al., 2005, and -9.5‰ in Flannery et al., 2018, as well as the bedded sedimentary carbonates Tsu and E-3 (this work) are used for estimating possible shallow marine temperatures. The highest $\delta^{18}O$ value of fracture filling calcites D-2-W is used for the seawater circulating into oceanic crust. The $\delta^{18}O$ values of PDP (this work) and TK859 in Shibuya et al., 2012, and the $\delta^{18}O$ values of interstitial carbonates D-3 (this work) and TK619 in Shibuya et al., 2012 are used as the minimum and maximum temperature of the modified seawater after reacting with basalt, respectively. A22-2 is regarded as the best preserved primary interstitial carbonate for the original hydrothermal fluid. Assuming the Archean seawater $\delta^{18}O$ of -1.2 ‰ (Shackleton and Kennett, 1975), the calculated marine temperature ranges from 60 to 98 °C, consistent with previous work (Robert and Chaussidon, 2006; Jaffrés et al. 2007; McGunnigle et al., 2022). However, considering the peak metamorphic temperature of 300~350 °C given by organic matter preserved in TSU and E-4, the calculated temperatures of 94 and 98 °C are obviously influenced by diagenesis and probably higher than the true values. The calculated temperatures for hydrothermal fluids are from 80 to 133 °C, indicating the low-temperature hydrothermal circulation through the upper oceanic crust. They are slightly lower than the temperatures ranging from 87 to 144 °C of Mid-Archean interstitial carbonates from Cleaverville Greenstone (Shibuya et al., 2012). However, the temperatures decline sharply using the highly depleted Archean seawater $\delta^{18}O$ value of −13.3 ‰ (Jaffrés et al., 2007), which result in a modern-like Archean ocean and the colder hydrothermal alteration of oceanic crust. The calculated formation temperatures of Paleoarchean interstitial carbonate are closer to that of carbonate veins hosted in ultramafic basement (Bach et al., 2011).

Table S2 The calculated formation temperatures of the selected Archean carbonates based on two seawater $\delta^{18}O$ values.

SampleID	Formation	Age (Ma)	Lithology	$\delta^{13}C_{VPDB}$ (‰)	$\delta^{18}O_{VPDB}$ (‰) *	T (°C) assuming seawater $\delta^{18}O$ −1.2‰ (a)	T (°C) assuming seawater $\delta^{18}O$ −13.3‰ (b)	Reference
13-7-07-2a 2a	Strelley Pool Formation	3410	Stromatolite	3.1	-9.5	60	2	Flannery et al., 2018
S-51a				2.6	-10.9	69	7	Lindsay et al., 2005
Strelley				2.5	-13.2	84	16	this work
TSU	Dresser Formation	3480	Sedimentary carbonate	1.5	-14.7	94	23	this work
E-4	Euro Basalt	3350		1.9	-15.2	98	26	this work
D-2-W		3480	Fracture carbonate	2.2	-13.0	83	16	this work
PDP	Dresser Formation	3480		1.3	-12.7	80	14	this work
D-3		3480		0.6	-19.8	133	50	this work
TK859	Cleaverville Greenstone	3000	Interstitial carbonate	1.7	-13.7	87	19	Shibuya et al., 2012
TK619		3000		-2.8	-21.2	144	57	Shibuya et al., 2012
A22-2	Apex Basalt	3460		0.7	-16.7	109	33	this work

- $\delta^{18}O_{VPDB}=0.970017*\delta^{18}O_{VSMOW}$ -29.98 (Coplen, 1988)
- Reference: a. Shackleton and Kennett, 1975; b. Jaffrés et al., 2007
- $T\ (°C) = 16.9 - 4.38(\ \delta^{18}O_{caco3} - \delta^{18}O_w) + 0.1\ (\ \delta^{18}O_{caco3} - \delta^{18}O_w)^2$ (from Shackleton and Kennett, 1975)

References

Bach, W., Rosner, M., Jöns, N., Rausch, S., Robinson, L. F., Paulick, H., and Erzinger, J.: Carbonate veins trace seawater circula- tion during exhumation and uplift of mantle rock: Results from ODP Leg 209, Earth and Planetary Science Letters, 311, 242–252, https://doi.org/10.1016/j.epsl.2011.09.021, 2011.

Flannery, D. T., Allwood, A. C., Summons, R. E., Williford, K. H., Abbey, W., Matys, E. D., and Ferralis, N.: Spatially-resolved isotopic study of carbon trapped in 3.43 Ga Strelley Pool Formation stromatolites, Geochimica et Cosmochimica Acta, 223, 21–35, 2018.

Jaffrés, J. B., Shields, G. A., and Wallmann, K.: The oxygen isotope evolution of seawater: A critical review of a long-standing controversy and an improved geological water cycle model for the past 3.4 billion years, Earth-Science Reviews, 83, 83–122, https://doi.org/10.1016/j.earscirev.2007.04.002, 2007.

Lindsay, J., Brasier, M., McLoughlin, N., Green, O., Fogel, M., Steele, A., and Mertzman, S.: The problem of deep carbon—an Archean paradox, Precambrian Research, 143, 1–22, https://doi.org/10.1016/j.precamres.2005.09.003, 2005.

McGunnigle, J., Cano, E., Sharp, Z., Muehlenbachs, K., Cole, D., Hardman, M., Stachel, T., and Pearson, D.: Triple oxygen isotope evidence for a hot Archean ocean, Geology, 50, 991–995, https://doi.org/10.1130/G50230.1, 2022.

Robert, F. and Chaussidon, M.: A palaeotemperature curve for the Precambrian oceans based on silicon isotopes in cherts, Nature, 443, 969–972, https://doi.org/10.1038/nature05239, 2006.

Shackleton, N. J., Kennett, J. P.: Paleotemperature history of the Cenozoic and the initiation of Antarctic glaciation: oxygen and carbon isotope analyses in DSDP Sites 277, 279, and 281, Initial Reports Deep Sea Drilling Project, 29, 743–755, 1975.

Shibuya, T., Tahata, M., Kitajima, K., Ueno, Y., Komiya, T., Yamamoto, S., Igisu, M., Terabayashi, M., Sawaki, Y., Takai, K., et al.: Depth variation of carbon and oxygen isotopes of calcites in Archean altered upper oceanic crust: Implications for the CO_2 flux from ocean to oceanic crust in the Archean, Earth and Planetary Science Letters, 321, 64–73, https://doi.org/10.1016/j.epsl.2011.12.034, 2012.

Chapter-3 Characteristics of REE+Y and radiogenic Sr isotopic compositions of 3.5-3.3 Ga carbonates from the East Pilbara Terrane, Western Australia, and their variations during diagenesis

Xiang*, W., Duda, J.-P., Pack, A., Willbold, M., Bach, W., Karius, V., Reitner, J.

Abstract

The carbonate minerals are ubiquitous in the 3.5 to 3.3 Ga Warrawoona Group and Kelly Group of the East Pilbara Terrane in Western Australia. Carbonates in this area occur in a variety of facies, including ca. 3.5–3.4 Ga interstitial carbonates between pillow basalts (North Star-, Mount Ada-, Apex-, Euro Basalt, and middle basalt member of the Dresser Formation), ca. 3.5-3.4 Ga bedded sedimentary carbonate rocks (Dresser Formation, Euro Basalt), and ca. 3.4 Ga stromatolites (Strelley Pool Formation). The geochemical features, including the abundances of major and trace elements, rare earth elements plus yttrium (abbreviated as REE+Y) patterns, and radiogenic Sr isotopic compositions, support the interpretation that the carbonates are important archives for reconstructing environments on Early Earth. The pristine signatures of seawater and seawater-derived low-temperature hydrothermal fluid at 3.5 Ga are recorded in interstitial carbonates from the 3.48 Ga Dresser Formation and 3.46 Ga Apex Basalt, respectively. These two fluid endmembers share some REE+Y features of near-chondritic Y/Ho weight ratios and PAAS-normalized REE+Y patterns (subscript $_{SN}$) characterized by light REE depletion, no Ce_{SN} yet positive La_{SN} and Y_{SN} anomalies. However, the seawater endmember exhibits the higher Sr concentration of 1789 ppm and lower REE+Y concentration, no Eu_{SN} anomaly, the diagnostic shallow seawater-like $\delta^{13}C$ value of +2.20 ‰ and the age-corrected $^{87}Sr/^{86}Sr$ ratio of 0.700596. In contrast, the hydrothermal endmember has the lower Sr concentration (119 ± 17 ppm) and higher REE+Y concentration, positive Eu_{SN} anomaly, the hybrid $\delta^{13}C$ value (+ 0.63 ± 0.12 ‰), and the age-corrected $^{87}Sr/^{86}Sr$ ratio (0.703094 ± 0.000979) that are both intermediate between seawater and basalt. In addition, the multi-element behaviors during post-depositional alterations have been identified to be source-dependent: recrystallization is commonly induced by low-temperature hydrothermal fluid or seawater, slightly deviating from the original geochemical compositions but less impacting on the REE+Y pattern and the $\delta^{13}C$ value, while dolomitization is triggered by high-temperature hydrothermal fluid, usually leading to dissolution and neomorphism. Thus, it shows the greatly increased elemental abundances of basaltic origin, the variant normalized REE+Y patterns with middle REE enrichment plus the strong positive Eu_{SN} anomaly, and largely elevated $^{87}Sr/^{86}Sr$ ratios yet consistent $\delta^{13}C$ values. Therefore, this work not only provides the pristine geochemical compositions of seawater and low-temperature hydrothermal fluid at 3.5 Ga but also assists in recognizing the origin of ancient carbonate rocks, i.e., sedimentary carbonate and stromatolite, and geochemically estimating the influence of possible post-depositional alteration.

Keywords: Pristine Archean carbonate, $^{87}Sr/^{86}Sr$, REE+Y, Archean seawater, Hydrothermal alteration.

Introduction

Carbonate minerals can adsorb and/or incorporate trace elements during precipitation in diverse environments, inheriting geochemical information of the parent fluid. Thus, the accumulation of certain trace elements and isotopes in carbonate can be used as proxies for reconstructing environmental conditions (Veizer, 1983; Smrzka et al., 2019). The formation of carbonate minerals is commonly associated with physicochemical precipitation triggered by alkalinity and temperature fluctuations, biologically induced precipitation mediated by organic matrices, and biologically controlled precipitation by metabolic processes of carbonate skeletal autotrophic and heterotrophic organisms (Reitner et al., 1995; Flügel and Munnecke, 2010). The inorganic and organic origins of various Paleoarchean carbonates in the East Pilbara Terrane (EPT), Western Australia, have been proposed, with interstitial carbonate between pillow basalts being an abiotic product of basalt-seawater interaction, sedimentary carbonate being precipitated via organo-mineralization, and stromatolite being generated through microbially EPS-controlled biomineralization, respectively (Chapter 2). Therefore, carbonate minerals are good materials to reconstruct the paleoenvironment and understand the co-evolution of Earth and early life since the early Archean.

However, there is a problem that frustrates researchers studying ancient carbonate. Carbonate is vulnerable to post-depositional alteration that may overprint primary signatures and act as an obstacle to reflecting original depositional conditions. Consequently, distinguishing pristine and secondary signatures is vital for utilizing carbonate as a proxy for the geochemical composition of the parent fluid. There are two fashionable methods for doing so: microfacies and geochemistry. Carbonate microfacies always respond to depositional and burial conditions. Thus, microfacies analysis, especially when combined with field geology (mapping and profiling), provides visual evidence for the primary generation and later alteration, which is an irreplaceable prerequisite for successful geochemical analysis. Some major and trace elements are mobile during alteration, and hence their abundance can be used to estimate primary and secondary facies. For example, an inverse relationship of Sr and Mn was observed in the alteration of carbonate rocks where progressive recrystallization led to a continuous loss of Sr and a gain of Mn (Veizer et al., 1989a; Banner and Hanson, 1990). As a consequence of the high mobility of Sr during alteration, the primary $^{87}Sr/^{86}Sr$ ratio of carbonate minerals is easily deviated towards that of the diagenetic fluid. In practice, post-depositional alteration nearly always causes an alteration in $^{87}Sr/^{86}Sr$ ratios (Veizer and Compston, 1974; Burke et al., 1982). Alteration by a radiogenic source, i.e., interaction with clay minerals, will tend to increase $^{87}Sr/^{86}Sr$ ratios, while alteration by fluids affected by a juvenile volcanic source or by dissolution of older, less radiogenic authigenic minerals will tend to decrease $^{87}Sr/^{86}Sr$ ratios (Shields and Veizer, 2002). Similarly, the least depleted oxygen isotopic composition of carbonate may indicate the original carbonate, considering the negative deviation caused by diagenetic fluid during depositional alteration.

Nonetheless, there are some relatively robust tracers for depositional conditions that may survive post-depositional alteration and retain the original information. For example, the abundance of rare earth elements (plus yttrium, abbreviated as REE+Y) and carbon isotopic composition (Parekh et al., 1977; Johannesson et al., 2006) can be used. Carbonate minerals, especially calcite, can be considered long-term repositories of lanthanides that are more effectively incorporated into calcite than other trace elements (Sabau et al., 2014), and only complete mineral dissolution leads to an effective loss of trace elements from the mineral lattice (Stipp et al., 2006). The good resistance of REE+Y to alteration makes them useful for deep-time reconstruction of environments and water sources (Bau and Dulski, 1996; Webb and Kamber, 2000; Kamber and Webb, 2001; Bolhar et al., 2005; Bau et al., 2010; Zhao et al., 2021). Therefore, the combination of petrology and geochemistry can certainly assist in recognizing primary and secondary carbonate facies and estimating the impacts of diagenetic alteration.

Faced with the “complex and prolonged” diagenetic histories of marine carbonates (Bathurst, 1975), attempts either to identify and analyze unaltered materials or to correct the record for diagenesis must be taken that require a clear understanding of the processes acting in a given diagenetic settings (Fantle et al., 2020). The focus of this work is cast on geochemical compositions of the EPT Paleoarchean carbonates that are diverse facies of different origins and diagenetic histories, through abundances of the major and trace elements, REE+Y patterns and age-corrected $^{87}Sr/^{86}Sr$ ratios. Results can be applied to reconstruct the environment conditions in the early Archean, and estimate impacts of post-depositional alteration on several geochemical signatures that likely benefit the relative works in the future.

Faced with the "complex and prolonged" diagenetic histories of marine carbonates (Bathurst, 1975), it is necessary to either identify and analyze unaltered materials or to correct the record for diagenesis, which requires a clear understanding of the processes acting in a given diagenetic setting (Fantle et al., 2020). This work focuses on the geochemical compositions of the EPT Paleoarchean carbonates, which represent diverse facies of different origins and diagenetic histories, through the abundances of major and trace elements, REE+Y patterns, and age-corrected $^{87}Sr/^{86}Sr$ ratios. The results can be used to reconstruct environmental conditions in the early Archean and estimate the impacts of post-depositional alteration on several geochemical signatures, which will likely benefit future studies.

1. Geological setting

The Pilbara Craton of Western Australia, with its well-exposed Paleoarchean rocks of little deformation and low metamorphic grade, is one of only two cratons on Earth that contain such rocks, the other being the Kaapvaal Craton in southern Africa (Van Kranendonk et al., 2019a). The Pilbara Craton is divided into five terranes based on different structural and tectonic styles: (1) East Pilbara Terrane; (2) Roebourne Terrane; (3) Sholl Terrane; (4) Regal Terrane; and (5) Kurrana Terrane (Van Kranendonk et al., 2002, 2006a, b, 2007a, b, 2019a). Among them, the 3.53~3.17 Ga East Pilbara Terrane (EPT) is the ancient cratonic nuclei of

the craton, which hosts valuable evidence of the oldest life on Earth, such as microfossils and stromatolites (Van Kranendonk et al., 2002, 2008; Allwood et al., 2006, 2007). The EPT grew as the result of a series of (at least three) mantle plume events at 3.53~3.42 Ga (Warrawoona event), 3.35~3.29 Ga (Kelly event), and 3.27~3.24 Ga (Sulphur Springs event), which formed a complex, multistage volcanic plateau (Smithies et al., 2005b; Huston et al., 2007; Van Kranendonk et al., 2002, 2006a, b, 2007b, 2015; Champion and Smithies, 2007; Pirajno, 2007a, b). These mantle events formed a > 20 km thick (ultra)mafic and felsic volcano-sedimentary succession with granite intrusion and accompanying hydrothermal systems, as a stratigraphic part of the Pilbara Supergroup, which is subdivided into four demonstrably autochthonous groups: the Warrawoona (3.53~3.42Ga), Kelly (3.35~3.30Ga) groups, the Sulphur Springs (3.26~3.23Ga), and Soanesville (ca. 3.18 Ga) groups (Van Kranendonk, 2006; Van Kranendonk et al., 2006a, 2007a, 2008, 2015, 2019a).

The > 12 km thick Warrawoona Group comprises volcanic rocks erupted as eight (ultra)mafic through felsic volcanic cycles of ca. 15 Ma duration (Hickman and Van Kranendonk, 2004), each capped by thin sedimentary rock units silicified by syndepositional hydrothermal fluids (Van Kranendonk, 2006; Van Kranendonk et al., 2019a). Specifically, the dominant mafic and ultramafic components consist of pillow basalt, komatiitic basalt, and komatiite, ranging from old to young including the Table Top, Double Bar, North Star, Mount Ada, and Apex formations (Van Kranendonk et al., 2002, 2006a). This is followed by less felsic volcanic rocks in the Coucal, Duffer, and Panorama formations (Thorpe et al., 1992; McNaughton et al., 1993), and minor sedimentary units of volcaniclastic rocks, quartz-rich sandstone, carbonates, and dominant colorful layered cherts derived from silicified carbonates formed during the felsic volcanic interval, such as the 3470 ± 2 Ma Antarctic Creek Member of the Mount Ada Basalt and ca. 3.47 Ga Marble Bar Chert Member of the Duffer Formation (Buick and Barnes, 1984; Lowe and Byerly, 1986; Byerly et al., 2002; Van Kranendonk, 2006). The pillow basalts and mm to cm-scale, well-layered cherts indicate the deposition of the Warrawoona Group under quiet water, deep marine conditions (Van Kranendonk et al., 2019a). In contrast, the 3481 ± 2 Ma Dresser Formation was suggested to deposit under tectonically active conditions, presumed to be a restricted shallow marine basin, but more recently suggested to be within a felsic volcanic caldera affected by syndepositional growth faults and voluminous hydrothermal circulation (Nijman et al., 1999; Van Kranendonk, 2006; Van Kranendonk et al., 2008, 2019a; Harris et al., 2009).

A regional unconformity between the Warrawoona Group and the Kelly Group indicates a time interval during which the terrane was uplifted and eroded under at least locally subaerial conditions, resulting in the deposition of the 30-1000 m thick sedimentary rocks of the Strelley Pool Formation at the base of the Kelly Group (Buick et al., 1995; Van Kranendonk et al., 2006a, 2007; Hickman, 2008). The Strelley Pool Formation comprises fluviatile to shallow marine conglomerates and quartzite, as well as well-preserved stromatolitic marine carbonates of various macroscopic and microscopic morphologies, along with some coarse clastic rocks, that these deposits occurred on a carbonate platform that extended across the EPT (Lowe, 1983; Hoffmann et al., 1999; Van Kranendonk et al., 2003; Van Kranendonk, 2006, 2007; Allwood et al., 2006). The Strelley Pool Formation is

conformably overlain by the 3.35-3.32 Ga Euro Basalt, which is composed of a 1.5 km thick basal unit of komatiite and up to 5 km of overlying, interbedded komatiitic basalt and tholeiitic basalt (Van Kranendonk et al., 2019a). This is followed by the eruption of the ca. 3.325 Ga high-K rhyolites of the Wyman Formation and, locally, the 1 km thick undated Charteris Basalt (Hickman, 1984; Van Kranendonk et al., 2019a).

The ≤ 3.27-3.23 billion years old Sulphur Springs Group, up to 4 km thick, was deposited over an unconformity on older greenstones in the western part of the EPT, consisting of basal sandstone and felsic volcaniclastic rocks (3.27-3.25 Ga Leilira Formation), komatiite to komatiitic basalt (<2 km thick) in the ca. 3.25 Ga Kunagunarrina Formation, and basaltic andesite to rhyolite (<1.5 km thick) in the 3.245-3.235 Ga Kangaroo Caves Formation, capped by <30 m of silicified epiclastic and siliciclastic rocks (Van Kranendonk and Hickman, 2000; Buick et al., 2002; GSWA, 2006). The Sulphur Springs Group is unconformably overlain by the 3.235-3.18 Ga Soanesville Group of clastic sedimentary rocks (such as shale, sandstone, and siltstone), interbedded high-Mg and tholeiitic basalt, and banded iron formation (Buick et al., 2002; Van Kranendonk et al., 2006a, 2010; Rasmussen et al., 2007).

The East Pilbara Terrane (EPT) is characterized by a classical dome-and-keel structure of broad (average 60 km wide) dome-shaped granitic complexes separated by intervening synclinal greenstone keels, where the Pilbara Supergroup is deposited as a laterally accreting succession within developing synclinal basins on the flanks of amplifying granitic domes, during periods of lithospheric extension (Hickman, 1984; Hickman and Van Kranendonk, 2004; Van Kranendonk et al., 2004, 2007a, b). The lithostratigraphic, geochemical, and structural features of the EPT show crust formation processes dominated by mantle melting and a vertical or gravity-driven style of tectonism prior to 3.2 Ga (Smith et al., 1998; Hickman, 2004; Smithies et al., 2005a, b, 2007; Van Kranendonk et al., 2004, 2006a, 2007a, b; Pease et al., 2008). Several models for the tectonic setting of Pilbara Supergroup volcanic rocks have been suggested, with basaltic rocks as either a continuous succession of greenstones erupted onto older continental basement (Glikson and Hickman, 1981; Hickman, 1983, 1984), as an oceanic plateau (Arndt et al., 2001), or as mid-ocean crust (Ueno et al., 2001; Kitajima et al., 2001; Kato and Nakamura, 2003), while for felsic volcanic rocks, as convergent margins involving continental magmatic arcs above subduction (Bickle et al., 1983, 1993; Barley et al., 1984; Barley, 1993). However, the oceanic plateau model has been gained support from more recent geochronological, geochemical, isotopic, and modeling works, and the plateau was formed through a succession of discrete mantle melting events with the resulting eruptive products deposited on a basement of older sialic crust (Van Kranendonk et al., 2002, 2007, 2015; Hickman and Van Kranendonk, 2004; Van Kranendonk and Pirajno, 2004; Fischer and Gerya, 2016). The development of the dome-and-keel map pattern is linked to the diapiric rise of granitic domes during punctuated episodes of partial convective overturn of the upper to middle crust (Van Kranendonk et al., 2019a). The alternated presence of a thick pillow basalt succession, shallow water depositions, and erosion infers the tectonic history of repeated uplift and deepening in this area.

In the studied area, the oldest basaltic formation is the North Star Basalt (>3490 Ma), overlain by the Dresser Formation with a U-Pb zircon date of 3481± 2 Ma (Van Kranendonk et al., 2008; Hickman and Van Kranendonk, 2012b). The overlying Antarctic Creek Member of Mount Ada Basalt is an approximately 4 km thick mafic succession, with U-Pb zircon dating of 3470 ± 2 Ma (Byerly et al., 2002; Hickman and Van Kranendonk, 2012b). It underlies up to 1.3 km of felsic volcanic and volcaniclastic rocks of the Duffer and Panorama Formations, and up to 150 m of the Marble Bar Chert Member of the Towers Formation in the far southeastern corner of the dome (Hickman and Van Kranendonk, 2012b). The stratigraphically youngest basaltic formation of the Warrawoona Group is the Apex Basalt, with a depositional age between 3463 and 3454 Ma, restricted by zircon U-Pb ages of the underlying Duffer Formation (Thorpe et al., 1992; McNaughton et al., 1993) and overlying Panorama Formation (Thorpe et al., 1992). The Strelley Pool Formation, disconformably overlies the Panorama Formation, and underlies the (ultra)mafic volcanic rocks of Euro Basalt (3350-3335 Ma) (Van Kranendonk et al., 2006; Hickman and Van Kranendonk, 2012b). The Strelley Pool Formation has a detrital zircon U-Pb age of 3414 ± 34 Ma (Gardiner et al., 2019) and a similar age of 3253 ± 320 Ma, dated by carbonate Sm-Nd isotopic compositions (Viehmann et al., 2020).

2. Sample description

The studied EPT carbonates occur in a variety of facies of different origins, including ca. 3.5–3.4 Ga interstitial carbonates between pillow basalts (North Star-, Mount Ada-, Apex-, Euro Basalt, and middle basalt member of the Dresser Formation), ca. 3.5 Ga hydrothermal bedded carbonate-chert rock (Dresser Formation), ca. 3.5-3.4 Ga bedded sedimentary micritic carbonates (Dresser Formation, Euro Basalt), and ca. 3.4 Ga stromatolites (Strelley Pool Formation, briefly SPF). Sampling sites are labeled on the geological map of the EPT, and the three carbonate types from different formations are marked on the stratigraphic section (Fig. 1).

The detailed petrographic work, formation pathways, and depositional environments have been introduced in Chapter 2 and are briefly described here. The interstitial carbonates are dominantly calcite, transformed from acicular crystal-fan calcite to blocky sparry calcite by circulating seawater and/or seawater-derived fluids originating from the progressive alteration of the host basalt, or to blocky ankerite during intensive hydrothermal alteration. The interstitial carbonates are suggested to have precipitated abiotically from hydrothermal fluids of high alkalinity derived from the reactions between basalt and seawater. The bedded sedimentary carbonates are precipitated via organo-mineralization, influenced to a greater or lesser extent by hydrothermal inputs. They are closely associated with organic materials (OM), usually as the core of carbonate rhombs. The bedded sedimentary rocks from the Dresser Formation (sample DB) and Euro Basalt (E-4) exhibit repeated silicified carbonate beds, where euhedral to subhedral carbonate rhombs occur with normal grading on a chert matrix within each bed, indicating restricted quiet-water depositional environments. The other micritic sedimentary carbonate (Tsu) was reported to be the oldest tsunami deposit on Earth (Runge et al., 2022) and shows OM-abundant laminae consisting of micritic dolomite, organic

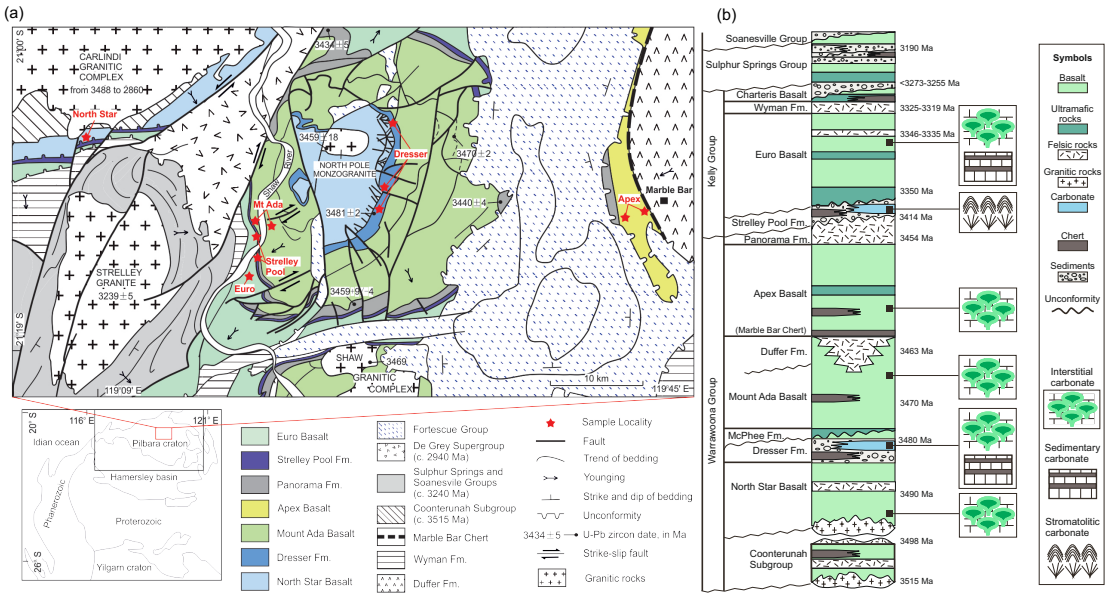

Fig.1 (a) The simplified geological map of the North Pole Dome, the Eastern Pilbara Terrane, Western Australia (modified from Van Kranendonk and Hickman, 2000, Hickman and Van Kranendonk, 2012b). The sampling localities are indicated by red stars. (b) The simplified stratigraphy of the studied Archean rocks (modified from Van Kranendonk et al., 2007b).

clots and flakes, as well as euhedral dolomite with an organic core. DB is likely generated in a subaerial hydrothermal pond, while the other two are likely precipitated in shallow marine environments with minor hydrothermal input. The SPF stromatolites, generated through microbial EPS-controlled biomineralization, are locally isopachous and consist of a few generations of dolomites (or ankerites). The latter two types of carbonates are commonly cemented by chert of hydrothermal origin that assists in preserving OM and primary depositional structures.

3. Methods

3.1 Sample preparation

All procedures and measurements were carried at the Geoscience center of Göttingen University. The bedded sedimentary carbonates “Tsu” and “DB”, and the SPF stromatolites “Strelley” and “SHAW” were thoroughly powdered and homogenized using an agate ball mill as whole-rock samples. For the other samples, chips with a diameter of approximately 1cm, free of visible alteration, inclusions, and secondary porosity, were drilled from sample sections, and ultrasonically cleaned in ethanol three times and air-dried in room temperature. The chips were crushed into small pieces that the carbonate pieces were handpicked and powdered using an agate mortar.

A sequential leaching procedure was performed to isolate carbonate fraction and avoid contamination as much as possible. All procedures employed ultrapure reagents. The

carbonate powder (~50 mg) was digested in around 0.3 mol·L^{-1} HNO_3 in Teflon beakers overnight at room temperature, and subsequently centrifuged to collect the supernatants and any possible precipitates, respectively. The supernatants were dried at 80 ℃ while the precipitates at 60 ℃. To remove putative organic materials that may hinder precise measurement and purification via specific resins, the dehydrated supernatant materials were dissolved in 0.2 ml concentrated HNO_3 at 80℃ for 2 hours and successively reacted with 0.2 ml concentrated H_2O_2 for 15 hours and 0.2 ml 6 mol·L^{-1} HCl for another 2 hours, and then dried down at 80 ℃. Afterwards, they were further refluxed in 1.2 ml 3 mol·L^{-1} HNO_3, and centrifuged to collect the supernatants and any possible insoluble fractions, respectively. After being dehydrated, the supernatant parts were finally refluxed in 3 mol·L^{-1} HNO_3 for further analyses, while the insoluble fractions collected from the two centrifugations were weighed to calculate the mass of truly used samples and dissolved fractions. The international carbonate reference materials Jls-1, JDo-1 and Cals-1 were digested in the same procedure along with the samples, as well as procedure blanks, for reproducibility and quality control.

3.2 Elemental concentrations

The concentrations of major elements and some minor elements were determined using an inductively coupled plasma-optical emission spectrometry (ICP-OES) Agilent 5100 VDV. An aliquot of the digested sample solution was diluted to 10 ml in 2 wt% HNO_3 + 0.5 wt % HCl, and the individual dilution factors were calculated gravimetrically. A blank solution and six calibration solutions of matched multi-elements were measured first for calibration. The two measurements of Jls-1, JDo-1 and Cals-1 bracketed the measurements of the samples, and the standard deviations of Jls-1 and JDo-1 were used to estimate precision of the measurement for calcite and dolomite, respectively. Seven procedural blanks were measured every few samples, and the mean value of measurements was subtracted from each calibrated value before applying individual dilution factors.

For trace element analysis, aliquots of digested sample solutions were dried, dissolved in 5 mL of 0.4 mol·L^{-1} HNO_3-0.05 mol·L^{-1} HF (running solution), and then diluted in a 50 mL centrifuge tube with a dilution factor of 1000 to create the stock solution. Then, 0.8 mL of the stock solution, 2.95 mL of the running solution, and 0.25 mL of internal standard (GIG 02, containing 100 ng/g ^{9}Be, 10 ng/g ^{115}In, and 10 ng/g ^{209}Bi) were added to a 4 mL test tube and mixed thoroughly. In this final step, the dilution factors were about 5000, and the precise values were calculated gravimetrically based on the mass changes of each addition. Procedural blanks were dried and dissolved in 3.75 mL of the running solution, transferred to 4 mL test tubes, and mixed with 0.25 mL of the internal standard. Spectral overlaps of oxide formation, such as $^{135}Ba^{16}O^{+}$ on $^{151}Eu^{+}$, $^{141}Pr^{16}O^{+}$ on $^{157}Gd^{+}$, $^{146}Nd^{16}O^{+}$ on $^{162}Dy^{+}$, were reduced by mathematical corrections based on the measurement of two standard solutions performed with the same procedure, containing 20 ppb Ba-Nd and Pr, respectively. The trace element measurements were carried out on a ThermoFisher Scientific iCAP Q ICP-MS equipped with an Apex-IR desolvating nebulizer with a PFA spray chamber. Prior to analysis, calibration was done with two eight-point calibration curves based on multi-element standard solutions prepared gravimetrically from certified multi-element standard solutions with a concentration

range of 0.15 to 500 ng/g. The oxides of Ce are lower than 0.6% and can be neglected. Element oxide formation was monitored at the beginning of an analytical session and followed by procedural blanks, reference materials, and samples. For the assessment of data quality, a new set of reference materials was measured for every 5 samples. The element concentrations were calculated online via the factory-supplied software Qtegra, whereas data correction for procedural blank contribution and oxide formation was carried out offline. The results of reference materials Cal-s, JLs-1, and JDo-1 were shown in Table S1, demonstrating a long-term precision of REEs < 10% (RSD) and an accuracy < 10%, except for Sm, Eu, and Gd of JLs-1 with an accuracy < 20%, compared with the values of Potts et al. (2000) and Dulski (2001). Consequently, only the elements with accuracy < 10% were used to correct for matrix effects and drift of the instrument that are not covered by internal standardization, and JLs-1 is for calcite samples, while JDo-1 is for dolomite samples, respectively. The concentrations of ^{151}Eu and ^{153}Eu are the same after correcting for the formation of Ba oxide, but ^{153}Eu will be selected for this study because of its better long-term reproducibility, based on measurements with three reference materials (see Table S1). The concentrations of ^{45}Sc, ^{47}Ti, ^{51}V, ^{60}Ni, ^{66}Zn, ^{85}Rb, ^{88}Sr, ^{89}Y, ^{90}Zr, ^{95}Mo, ^{137}Ba, ^{139}La, ^{140}Ce, ^{141}Pr,^{146}Nd, ^{147}Sm, ^{153}Eu, ^{157}Gd, ^{159}Tb, ^{162}Dy, ^{165}Ho, ^{166}Er, ^{169}Tm, ^{172}Yb,^{175}Lu, ^{178}Hf, ^{232}Th, and ^{238}U were used to represent the relative element concentrations.

REEs in natural samples exhibit a "zig-zag" or herringbone-type distribution pattern due to differences in the abundance of elements with odd and even atomic numbers resulting from nucleosynthesis (Schmitt et al. 1963; Piper and Bau 2013). To eliminate this distraction and facilitate comparison, the concentrations of REEs and Y are normalized to Post-Archean Australian Shale (PAAS, subscript $_{SN}$, after Pourmand et al. 2012), which reflects the composition of weathered and recycled terrigenous material derived from the continental crust (Taylor and McLennan 1985). The following equations were used to quantify anomalous behavior: $Ce/Ce^* = Ce_{SN}/(0.5Pr_{SN} + 0.5La_{SN})$, $Pr/Pr^* = Pr_{SN}/ (0.5Ce_{SN} + 0.5Nd_{SN})$ (after Bau and Dulski, 1996) ; $La/La^* = La_{SN}/(3Pr_{SN}– 2Nd_{SN})$ and $Gd/Gd^* = Gd_{SN}/(2Tb_{SN} - Dy_{SN})$ (after Alexander et al., 2008), whereas $Eu/Eu^* = Eu_{SN}/(Sm_{SN}^2 * Tb_{SN})^{1/3}$ and $Y/ Y^* = Y_{SN}/(0.5Er_{SN} \times 0.5Ho_{SN})$ (after Lawrence et al., 2006). The widespread positive La anomaly in Archean samples may affect the calculation of Ce anomaly, thus the Ce/Ce* anomaly of the new equation will be discussed but verified in the cross-plot of old Ce/Ce* and Pr/Pr*. Similarly, the light-to-heavy REE ratio of Archean carbonates is expressed by Pr_{SN} /Yb_{SN} (Planavsky et al., 2010), and Sm_{SN} /Yb_{SN} is used to reflect middle-to-heavy REE ratio in this work instead of LREE depletion suggested in Kamber and Webb (2001). To comparatively study Y and REE behaviors, we inserted Y between Dy and Ho in plots showing PAAS-normalized REE+Y patterns (Fig. 4 and 8) because Y has a similar ionic radius to Dy and Ho (Y (+3): 1.02 Å, Dy (+3): 1.03 Å, Ho (+3): 1.02 Å; https://chemglobe.org/ptoe/). Meanwhile, the anomalous behavior of Y in relation to REEs is evaluated by non-normalized Y/Ho weight ratios, where the closest similarity between Y and Ho is taken into account (Bau and Dulski 1996).

3.3 Radiogenic Sr isotopic composition

Aliquots of sample solutions and reference materials Jls-1 and Jdo-1 were spiked with ^{87}Rb-^{84}Sr tracer solutions. The spiked aliquots were dried down and dissolved in 2.5 mL of 3.0 mol·L^{-1} HCl for the cation exchange procedures that employed Bio-Rad AG 50 × 8 (200–400 mesh) resin to separate Rb and Sr from matrix elements. The Rb cut was collected, dried, and dissolved in 0.5 mol·L^{-1} HNO_3, and measured on the ThermoFisher Scientific Element2 using an ID-SF-ICPMS technique as described in Willbold and Jochum (2005). The Sr cut was further purified with Triskem Sr-spec Resin (50–100 μm) to eliminate the possible interference of remaining ^{87}Rb on ^{87}Sr during mass spectrometry using the method described in Pin et al. (2014). The measurements were performed on a ThermoFisher Scientific Neptune Plus MC-ICP-MS equipped with a Teledyne Cetac Aridus3 desolvation system to introduce sample solutions into the plasma. The ion currents of Sr isotopes were measured with 10^{11} Ω amplifiers, and the interfering isotope monitors (i.e., ^{83}Kr and ^{85}Rb for Sr isotopes) were measured with 10^{12} Ω amplifiers. The determinations of $^{87}Sr/^{86}Sr$ ratios were obtained in static ion-collection mode, based on 100 mass scans for sample solutions and 40 scans for procedural blanks, respectively. The sample solutions were roughly diluted to 100 ppb Sr in 0.5 mol·L^{-1} HNO_3, which is the same Sr concentration as an in-house reference ESI for better determination. ESI and NIST SRM 987 were run between every five samples, and the measurement ended with reference materials and procedural blanks.

The correction for instrumental mass fractionation was performed offline using a Python script that utilized the 'double' isotope dilution equation of Boelrijk (1968). The mean value of two blank solution analyses was used for correction of acid and gas blank contributions and electronic background, and the $^{86}Sr/^{88}Sr$ ratio was normalized to 0.1194 using an exponential law. Following the correction, the current long-term, mean $^{87}Sr/^{86}Sr$ ratio of NIST SRM 987 is 0.710246 ± 0.000009 (2σ, n =48). The $^{87}Sr/^{86}Sr$ ratios of JDo-1 and JLs-1 are 0.707575±28 (2σ, n=2) and 0.707847±19 (2σ, n=2), respectively.

4. Results

Combined with petrographic work (Chapter 2) and the work on the Rb-Sr isotopic system of Apex pillow basalt (Chapter 4), the EPT carbonates are grouped into primary interstitial calcite, recrystallized/altered interstitial calcite, interstitial dolomite, fracture(-filling) calcite, sedimentary carbonate, and stromatolite. The details of the EPT carbonates are listed in Table 1, along with the concentrations of major and trace elements and the PAAS-normalized REE+Y anomalies. The dissolved fraction indicates the mass ratio of the dissolved sample to the weighed sample. For the studied interstitial carbonate, the lower dissolved fractions imply a higher fraction of quartz cement or veins that were generated after the formation of interstitial carbonates. With two exceptions (D-1 and E-3), interstitial carbonates have a common dissolved fraction above 70 wt%. However, the whole rock samples of bedded sedimentary carbonates and the SPF stromatolites have lower dissolved fractions (down to 16.5 wt%) due to the large fractions of chert beds and matrix. A SPF

stromatolite sample, SHAW, with an extremely low dissolved fraction (0.37 wt%), is excluded in this work, except for its REE+Y pattern, considering its high degree of silicification.

Table 1 Geochemical compositions of the various carbonates from the East Pilbara Terrane, Western Australia

(To be continued)

Formation	North Star Basalt	North Star Basalt	Dresser Fm.	Mt Ada Basalt	Mt Ada Basalt	Mt Ada Basalt	Apex Basalt	Apex Basalt	Apex Basalt	Apex Basalt	Apex Basalt	Apex Basalt	Apex Basalt
Age (Ma)	3490	3490	3480	3470	3470	3470	3460	3460	3460	3460	3460	3460	3460
Lithology	Interstitial Cal.(A)	Interstitial Dol.	Interstitial Cal.(A)	Interstitial Dol.	Interstitial Dol.	Interstitial Dol.	Interstitial Cal.(P)	Interstitial Cal.(P)	Interstitial Cal.(P)	Interstitial Cal.(P)	Interstitial Cal.(P)	Interstitial Cal.(A)	Interstitial Cal.(A)
Sample ID	CP-1	CP-2	D-3	A-1-C	A-1-E	A-2	A14673-1	A22-1	A22-2	ABAS-2	ABAS-3	Apex1	Apex2
(wt%)													
Dissolved fraction(%)	96.7	99.7	71.6	98.6	82.9	92.7	92.0	93.9	91.9	75.9	96.6	75.5	82.8
Al	0.014	0.003	0.005	0.009	0.403	0.008	0.072	0.007	0.024	0.996	0.013	0.020	0.201
Ca	41.596	22.069	41.162	23.701	30.644	23.819	39.796	39.637	39.000	38.418	40.570	40.896	40.387
Fe	0.292	8.925	0.710	10.409	7.322	8.423	0.810	1.152	1.434	2.534	1.109	0.558	0.797
K	bd	bd	bd	bd	bd	bd	bd	bd	bd	bd	bd	bd	bd
Mg	0.153	8.191	0.244	6.099	4.624	7.245	0.199	0.465	0.612	0.774	0.198	0.115	0.254
Mn	0.940	0.598	1.068	0.827	0.834	0.497	0.780	0.951	0.808	0.623	0.611	0.685	0.544
Na	bd	bd	bd	bd	bd	bd	bd	bd	bd	bd	bd	bd	bd
(ppm)													
Sc	7.351	0.464	0.393	1.297	10.695	0.408	1.487	2.430	11.437	15.749	3.426	1.188	2.664
Ti	0.284	0.243	0.117	0.259	5.346	0.000	1.317	0.200	0.488	8.088	0.925	0.530	1.498
V	1.006	1.273	2.118	62.298	55.349	7.350	3.968	2.658	3.125	55.570	3.309	1.320	7.666
Ni	nd	nd	nd	5.151	13.040	nd	8.585	5.233	5.988	32.884	5.251	7.634	13.230
Zn	nd	nd	nd	33.148	35.887	nd	3.413	1.950	6.740	19.351	1.390	1.888	4.699
Rb	0.116	0.030	0.011	0.090	0.110	0.042	0.030	0.012	0.039	0.038	0.020	0.029	0.007
Sr	74.047	26.952	78.124	159.617	216.531	202.047	108.339	100.443	112.337	141.104	133.304	120.572	115.930
Y	115.176	15.990	7.261	22.683	38.089	3.918	11.066	26.054	62.464	13.509	12.695	10.762	13.030
Zr	0.008	0.000	0.011	0.000	0.090	0.000	0.169	0.198	0.170	0.235	0.255	0.149	0.098
Mo	0.209	0.175	0.240	0.173	0.204	0.141	0.185	0.196	0.197	0.389	0.187	0.215	0.207
Ba	0.931	0.459	5.778	18.400	8.113	91.466	34.427	5.060	7.110	23.867	11.632	4.268	6.287
La	31.071	7.105	0.711	0.577	3.717	2.513	1.391	3.277	6.265	1.917	1.235	1.590	1.690
Ce	84.082	11.126	1.340	2.710	14.595	4.476	2.841	7.443	16.116	4.652	2.538	3.275	3.815
Pr	12.335	1.495	0.161	0.775	3.304	0.626	0.402	1.079	2.544	0.716	0.354	0.452	0.572
Nd	57.269	6.729	0.711	6.193	21.188	2.742	1.929	5.078	12.843	3.645	1.698	2.157	2.921
Sm	18.313	1.933	0.196	4.897	11.237	0.786	0.662	1.723	4.881	1.428	0.586	0.691	1.014
Eu	6.704	0.781	0.052	2.672	6.757	0.656	0.248	0.626	1.572	0.587	0.226	0.200	0.316
Gd	22.411	3.059	0.386	7.880	14.034	1.059	0.986	2.431	6.845	1.884	0.988	1.020	1.447
Tb	3.234	0.425	0.071	1.114	1.732	0.139	0.168	0.432	1.258	0.287	0.182	0.164	0.228
Dy	21.389	2.414	0.636	5.371	8.112	0.689	1.215	3.251	9.379	1.909	1.447	1.212	1.624
Ho	4.109	0.414	0.172	0.797	1.227	0.109	0.301	0.790	2.167	0.428	0.372	0.298	0.390
Er	11.098	1.116	0.593	1.702	2.577	0.223	0.933	2.557	6.762	1.271	1.250	0.968	1.249
Tm	1.670	0.135	0.107	0.194	0.291	0.023	0.138	0.410	1.075	0.190	0.206	0.152	0.190
Yb	9.693	0.756	0.688	1.067	1.619	0.126	0.895	2.724	7.529	1.295	1.471	1.038	1.317
Lu	1.238	0.098	0.109	0.134	0.206	0.015	0.145	0.450	1.251	0.212	0.247	0.179	0.228
Hf	nd	nd	nd	0.007	0.016	nd	0.004	0.007	0.019	0.007	0.004	0.006	0.005
Th	0.017	0.024	0.000	0.001	0.015	0.000	0.006	0.000	0.007	0.028	0.000	0.002	0.001
U	0.001	0.002	0.007	0.001	0.002	0.001	0.028	0.048	0.039	0.019	0.019	0.006	0.004
REY	399.79	53.58	13.19	58.77	128.68	18.10	23.32	58.33	142.95	33.93	25.49	24.16	30.03
Y/Ho	28.03	38.61	42.33	28.47	31.05	36.00	36.72	32.98	28.82	31.60	34.17	36.07	33.43
Ce/Ce*	1.00	0.82	0.95	0.69	0.81	0.86	0.91	0.94	0.93	0.93	0.92	0.93	0.92
Pr/Pr*	0.98	0.96	0.93	0.78	0.89	0.99	0.94	0.96	0.95	0.94	0.94	0.94	0.93
La/La*	1.21	1.96	1.69	-0.13	-0.52	1.48	2.04	1.57	2.21	2.64	2.03	1.98	3.03
Gd/Gd*	1.14	1.01	1.57	0.87	0.98	0.96	1.10	1.12	1.07	1.09	1.20	1.19	1.15
Eu/Eu*	1.87	1.92	1.07	2.56	3.21	4.26	1.70	1.65	1.45	2.01	1.63	1.34	1.47
Y/Y*	0.18	2.51	5.17	1.21	0.87	11.68	2.85	0.93	0.31	1.80	1.98	2.70	1.94
(‰) [Ref.a]													
$\delta^{13}C_{VPDB}$	-2.31	0.01	0.63	0.83	0.77	0.52	0.62	0.44	0.69	0.65	0.77	0.25	0.04
$\delta^{18}O_{VPDB}$	-19.17	-14.34	-19.81	-18.14	-18.57	-16.05	-16.74	-17.29	-16.72	-16.97	-15.79	-17.58	-17.70

4.1 Major and trace elements

The molar ratios of major elements Ca, Mg, Fe, and Mn in the carbonate are calculated based on their concentrations as follows:

$$M\_mol = M\_wt\% / M\_mm \quad \text{(eq. 1)}$$

$$M\ (mol\%) = M\_mol / \sum M\_mol \quad \text{(eq. 2)}$$

where M indicates Ca, Mg, Fe and Mn, and M_wt% means their concentration via ICP-OES, M_mm is their molar mass. According to the carbonate rock classification (Fig.2a), the

EPT carbonates are dominantly of two geochemical facies, low-Mg calcite and ferroan dolomite, consistent with the petrological work (Chapter 2).

(Continued)

Formation	Apex Basalt	Euro Basalt	Euro Basalt	Euro Basalt	Dresser Fm.	Dresser Fm.	Dresser Fm.	Dresser Fm.	Dresser Fm.	Dresser Fm.	Euro Basalt	Strelley Pool Fm.
Age (Ma)	3460	3350	3350	3350	3480	3480	3490	3480	3480	3480	3350	3410
Lithology	Interstitial Cal.(A)	Interstitial Cal.(A)	Interstitial Cal.(A)	Interstitial Cal.(A)	Fracture Cal.	Fracture Cal..	Sedimentary Carb.	Sedimentary Carb.	Sedimentary Carb.	Sedimentary Carb.	Sedimentary Carb.	Stromatolite
Sample ID	Apex3	E-1	E-2	E-3	D-2-R	D-2-W	D-1	PDP	DB	TSU	E-4	Strelley
(wt%)												
Dissolved fraction(%)	86.0	90.2	92.0	32.5	99.0	99.9	30.5	81.3	16.5	27.9	63.4	76.7
Al	0.025	0.022	0.001	0.007	0.002	0.003	0.113	0.008	0.100	0.031	0.074	0.000
Ca	40.442	41.153	40.372	40.405	42.159	42.199	21.088	26.167	36.557	21.543	22.504	22.664
Fe	0.661	0.556	0.187	0.093	0.000	0.068	12.098	9.623	0.156	10.008	7.339	1.671
K	bd	bd	bd	bd	bd	bd	bd	bd	bd	bd	bd	bd
Mg	0.162	0.129	0.091	0.090	0.000	0.177	6.470	9.884	2.255	7.323	9.339	11.986
Mn	0.732	0.508	0.757	0.817	0.000	0.007	0.965	1.331	0.200	1.060	0.962	0.440
Na	bd	bd	bd	bd	bd	bd	bd	bd	bd	bd	bd	bd
(ppm)												
Sc	1.200	2.391	14.310	1.002	0.266	0.236	9.557	4.768	46.775	7.298	11.821	1.813
Ti	0.565	0.405	0.000	0.369	0.102	0.034	8.776	0.134	5.300	2.403	7.548	1.429
V	1.574	1.716	0.856	1.013	0.178	0.194	36.445	5.201	5.481	19.733	51.124	2.169
Ni	7.404	6.204	5.833	nd	nd	nd	nd	nd	nd	nd	167.581	nd
Zn	1.433	0.000	0.000	nd	nd	nd	nd	nd	nd	nd	30.683	nd
Rb	0.046	0.011	0.013	0.033	0.012	0.009	1.018	0.019	1.379	0.435	0.514	0.060
Sr	112.434	100.155	67.115	46.766	1198.471	1789.259	46.869	127.956	66.446	37.982	21.624	47.821
Y	15.885	15.600	32.563	18.240	1.116	1.363	14.653	26.309	23.191	10.961	12.443	2.133
Zr	0.136	0.073	0.004	0.003	0.000	0.000	0.332	0.095	0.865	1.154	1.052	0.936
Mo	0.223	0.134	0.154	0.306	0.026	0.012	0.456	0.301	0.100	0.238	1.832	0.103
Ba	6.425	7.887	4.430	3.005	112.364	1.456	33.261	132.848	4594.744	110.834	5.418	55.556
La	2.248	1.994	5.661	2.100	0.121	0.083	1.863	2.410	2.175	1.257	3.673	0.274
Ce	4.392	4.039	13.882	3.386	0.236	0.120	4.716	4.654	1.517	3.206	9.950	0.439
Pr	0.602	0.562	2.011	0.441	0.034	0.016	0.784	0.709	0.658	0.517	1.579	0.069
Nd	2.863	2.715	9.406	2.142	0.166	0.072	4.059	3.555	3.282	2.710	7.183	0.360
Sm	0.920	0.861	3.246	0.727	0.061	0.027	1.829	1.627	1.316	1.180	2.101	0.166
Eu	0.266	0.339	1.547	0.288	0.020	0.008	0.737	1.035	0.985	0.461	0.798	0.088
Gd	1.432	1.365	4.678	1.488	0.125	0.078	2.712	2.629	2.354	1.610	2.746	0.302
Tb	0.231	0.223	0.781	0.251	0.021	0.015	0.417	0.463	0.432	0.261	0.409	0.046
Dy	1.674	1.634	5.297	2.090	0.168	0.151	2.484	3.305	3.486	1.665	2.276	0.253
Ho	0.410	0.400	1.114	0.519	0.037	0.037	0.499	0.745	0.768	0.348	0.408	0.046
Er	1.298	1.247	3.065	1.696	0.103	0.122	1.339	2.242	2.313	1.029	0.977	0.118
Tm	0.203	0.183	0.435	0.284	0.014	0.019	0.180	0.328	0.383	0.156	0.115	0.016
Yb	1.299	1.153	2.850	1.834	0.076	0.111	1.144	2.151	2.411	1.075	0.651	0.101
Lu	0.219	0.188	0.446	0.300	0.010	0.015	0.170	0.317	0.341	0.167	0.091	0.016
Hf	0.005	0.004	0.012	nd	nd	nd	nd	nd	nd	nd	0.039	nd
Th	0.000	0.001	0.010	0.000	0.000	0.000	0.340	0.002	0.013	0.174	0.161	0.015
U	0.012	0.016	0.009	0.005	0.002	0.001	0.096	0.005	0.413	0.036	0.016	0.027
REY	33.95	32.50	86.98	35.79	2.31	2.24	37.59	52.48	45.61	26.60	45.40	4.43
Y/Ho	38.74	38.96	29.24	35.17	30.48	36.57	29.35	35.33	30.19	31.50	30.52	46.50
Ce/Ce*	0.91	0.91	0.97	0.85	0.88	0.79	0.90	0.85	0.30	0.92	0.95	0.77
Pr/Pr*	0.94	0.94	0.97	0.91	0.94	0.95	0.95	0.94	1.23	0.93	1.02	0.94
La/La*	2.05	2.16	1.41	3.02	2.29	2.24	2.93	2.82	2.64	3.76	1.01	5.00
Gd/Gd*	1.16	1.16	1.02	1.44	1.33	2.06	0.96	1.04	1.23	0.98	0.93	0.91
Eu/Eu*	1.32	1.77	2.20	1.62	1.32	1.05	1.89	2.77	3.11	1.85	1.88	2.32
Y/Y*	2.16	2.26	0.69	1.50	21.34	21.64	1.59	1.14	0.95	2.22	2.26	28.49
(‰) [Ref.a]												
$\delta^{13}C_{VPDB}$	0.21	0.21	0.99	-2.37	2.34	2.20	0.97	1.26	-5.10	1.46	1.88	2.50
$\delta^{18}O_{VPDB}$	-17.37	-19.23	-19.52	-19.31	-17.81	-13.03	-15.95	-12.69	-7.88	-14.66	-15.19	-13.16

Note:
1. Anomalies were calculated based on PAAS-normalized values (after Pourmand et al., 2012) :
   $Ce/Ce^* = Ce_{SN}/(0.5Pr_{SN} + 0.5La_{SN})$ and $Pr/Pr^* = Pr_{SN}/(0.5Ce_{SN} + 0.5Nd_{SN})$ (after Bau and Dulski, 1996)
   $La/La^* = La_{SN}/(3Pr_{SN} - 2Nd_{SN})$ and $Gd/Gd^* = Gd_{SN}/(2Tb_{SN} - Dy_{SN})$ (after Alexander et al., 2008)
   $Eu/Eu^* = Eu_{SN}/(Sm_{SN}^2 * Tb_{SN})^{1/3}$ and $Y/Y^* = Y_{SN}/(0.5Er_{SN} \times 0.5Ho_{SN})$ (after Lawrence et al. 2006)
2. bd: below the limits of detection; nd: not determined
3. Stable carbon and oxygen isotopes are from Ref a: Xiang et al., 2023
4. Abbreviations: Cal. –calcite; ; P-primary; A-altered; Dol.- dolomite; Carb. -carbonate; Fm. -Formation; SPF- Strelley Pool Formation.

Specifically, the primary interstitial calcite has an average Ca content of 39.484 ± 0.814 wt%, Mg 0.450 ± 0.254 wt%, Fe 1.408 ± 0.667 wt% and Mn 0.755 ± 0.142 wt%. The altered interstitial calcite has a comparable Ca content of 40.802 ± 0.814 wt% and Mn 0.756 ± 0.188 wt%, but lower Mg content of 0.155 ± 0.064 wt% and Fe 0.482 ± 0.259 wt%. Except for CP-2, the interstitial dolomites from Mount Ada Basalt are mixture of calcite and ferroan dolomite, with the mean contents of Ca 25.058 ± 3.808 wt%, Mg 6.540 ± 1.537 wt%, Fe

8.770 ± 1.282 wt% and Mn 0.689 ± 0.168 wt%. The fracture-filling calcite has Ca content of 42.179 ± 0.028 wt%, with low maximum Mg content of 0.177 wt%, Fe 0.068 wt% and Mn 0.007 wt%. The sedimentary carbonates are mainly ferroan dolomite, with the average contents of Ca 22.826 ± 2.305 wt%, Mg 8.254 ± 1.621 wt%, Fe 9.767± 1.950 wt% and Mn 1.079 ± 0.174 wt%, except for DB, which is calcite mixed with minor dolomite having Ca 36.557 wt%, Mg 2.255 wt%, Fe 0.156 wt% and Mn 0.200 wt%. The SPF stromatolite is dolomite with a Ca content of 22.664 wt%, Mg 11.986 wt%, Fe 1.671 wt% and Mn 0.440 wt%.

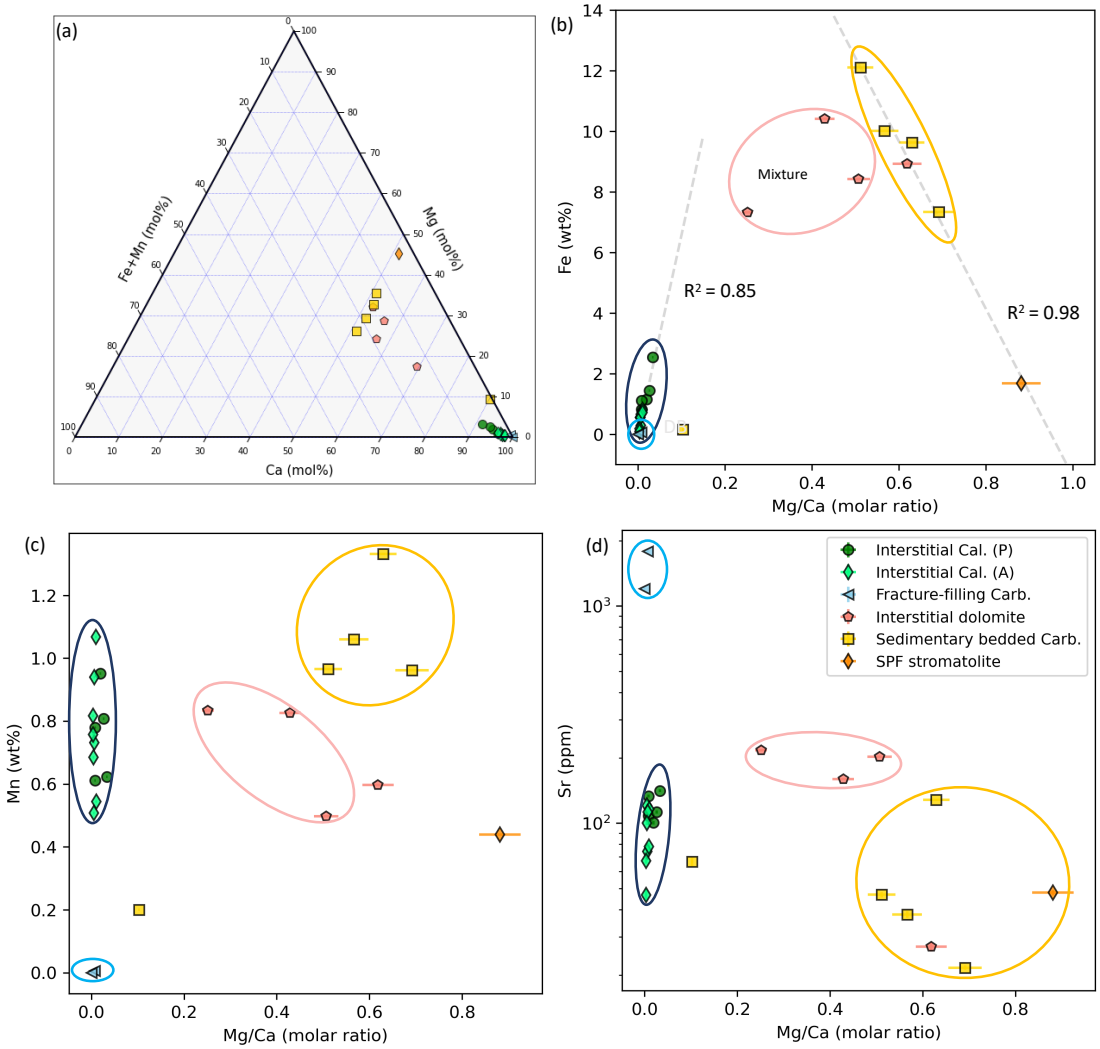

Fig. 2 (a) Carbonate rock classification based on the compositions (mol%) of Ca, Mg and Fe+Mn, showing the EPT carbonates are dominantly low-Mg calcite and ferroan dolomite. The cross-plots of the EPT carbonates between molar ratio of Mg/Ca and (b) Fe (wt%), (c) Mn (wt%), (d) Sr (ppm), indicating the various concentrations of Fe, Mn and Sr in the different carbonate facies. The grey dashed lines in (b) show the good correlations between Fe content and lithology, implying the dissolved Fe is mainly from carbonate. (Abbreviations: Cal. –calcite; P-primary; A-altered; Carb. -carbonate; SPF- Strelley Pool Formation.)

The contents of Fe, Mn and Sr against the Ca/Mg molar ratios of the EPT carbonates are plotted in Fig.2b to d, which is consistent with their distribution on different carbonate facies via micro-XRF analysis (Chapter 2). Sr is extremely enriched in the fracture-filling calcites ranging from 1198.471 to 1789.259 ppm, whereas it is much lower in all interstitial

carbonates with an average value of 112.695 ppm, sedimentary carbonates and stromatolite, averaging 44.148 ppm.

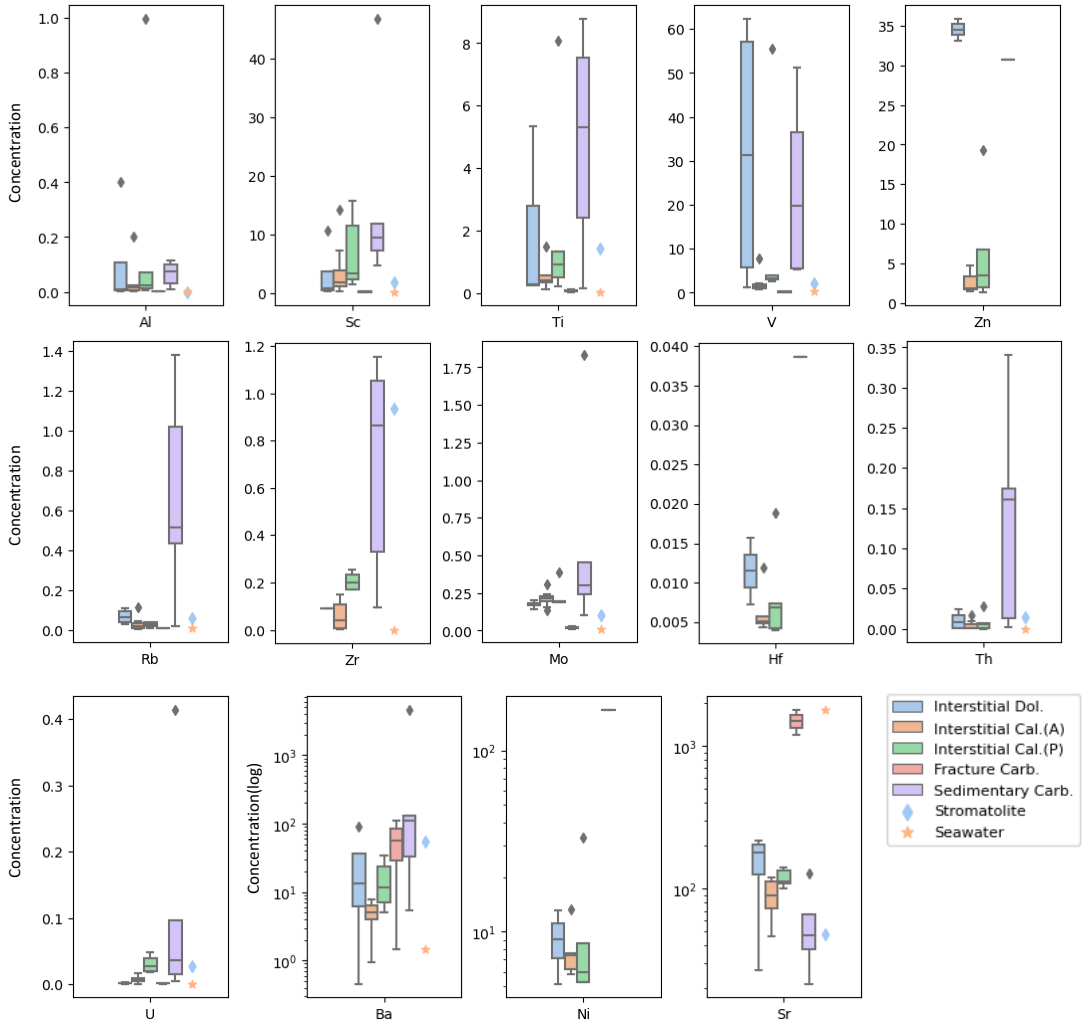

Fig.3 Boxplots of some trace element concentrations (Al in wt%, the others in ppm) of the EPT carbonates, while the SPF stromatolite and the Paleoarchean seawater endmember (D-2-W, details in Section 5.2.1) are marked by diamond and star, respectively. (Abbreviations: Cal. –calcite; P-primary; A-altered; Dol.- dolomite; Carb. -carbonate)

The concentrations of trace elements are plotted in Fig.3, and some diagnostic elements are briefly introduced below (without considering outliers). The Al contents of interstitial carbonates are consistently low, ranging from 0.001 to 0.072 wt%, with an average value of 0.016 wt%. The sedimentary carbonate has a similar range of Al content with a higher mean value of 0.065 ± 0.045 wt%, while the fracture-filling calcite and SPF stromatolite have almost no Al. The Sc concentrations increase from the fracture-filling calcite, the interstitial dolomite, the altered interstitial calcite, the primary interstitial calcite to sedimentary carbonate, with mean values of 0.251, 0.723, 2.313, 2.448, 8.361 (ppm), respectively, while that of stromatolite is on average 1.813 ppm. A similar trend is observed in Ti concentration which is more likely in anatase (Chapter 2), increasing from 0.068, 0.167, 0.324, 0.733, 4.832 (ppm, on average), while the stromatolite has 1.429 ppm Ti. Ba is commonly of hydrothermal origin, lower in the interstitial carbonates with a mean value of 9.255 ppm, and higher in sedimentary carbonate and stromatolite of 67.583 ppm on average. The extremely high Ba

4594.744 ppm in DB corresponds to its occurrence on the top of bedded barite layers at the outcrop. Rb is generally low in carbonate minerals, that the interstitial carbonate has an average concentration of 0.035 ppm, the fracture-filling calcite 0.011 ppm and stromatolite 0.060 ppm, while the sedimentary carbonate has 0.673 ppm.

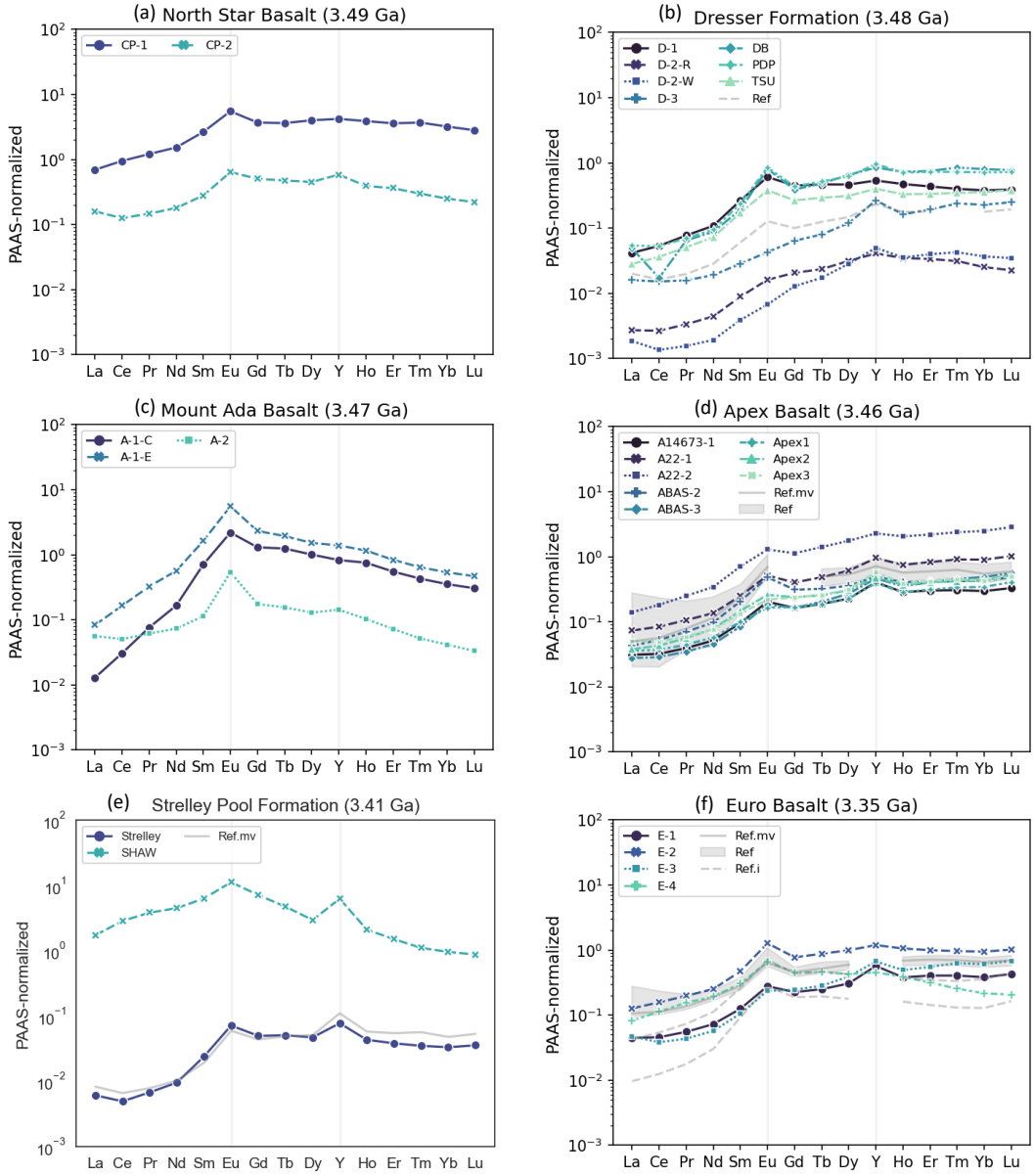

Fig.4 The PAAS-normalized REE+Y patterns of the EPT carbonates and counterparts from references. The results are shown according to the stratigraphy: (a) North Star Basalt; (b) Dresser Formation, "Ref" indicates the sample of the same type with DB in Van Kranendonk et al. (2003); (c) Mount Ada Basalt; (d) Apex Basalt, that "Ref. mv" indicates the mean value of reference values shown in grey area "Ref" , data from Nakamura and Kato (2004); (e) Strelley Pool Formation, "Ref. mv" indicates an average line from Fig.S1 with data from Van Kranendonk et al. (2003), Allwood et al. (2010); Viehmann et al. (2020); (f) Euro Basalt, "Ref" and "Ref. mv" from Yamamoto et al. (2004) that the dashed lines "Ref.i" indicate the carbonates within the margin of pillow basalt, which was labelled as "carbonate-inclusion".

4.2 Rare earth elements and REE+Y patterns

The PAAS-normalized patterns of REE+Y are illustrated in Fig.4 according to stratigraphy, and the anomalies are cross-plotted in Fig.5. Specifically, non-normalized Y/Ho ratios of the EPT carbonates are uniform, ranging from 28 to 47 with an average value of 34 ± 4.7. This value is slightly higher than the chondritic value of 26 to 28 (Kamber and Webb, 2001; Pack et al., 2007), but lower than the Y/Ho ratios of the SPF stromatolite and sedimentary carbonate (Fig.5a; Van Kranendonk et al., 2003; Allwood et al., 2010; Viehmann

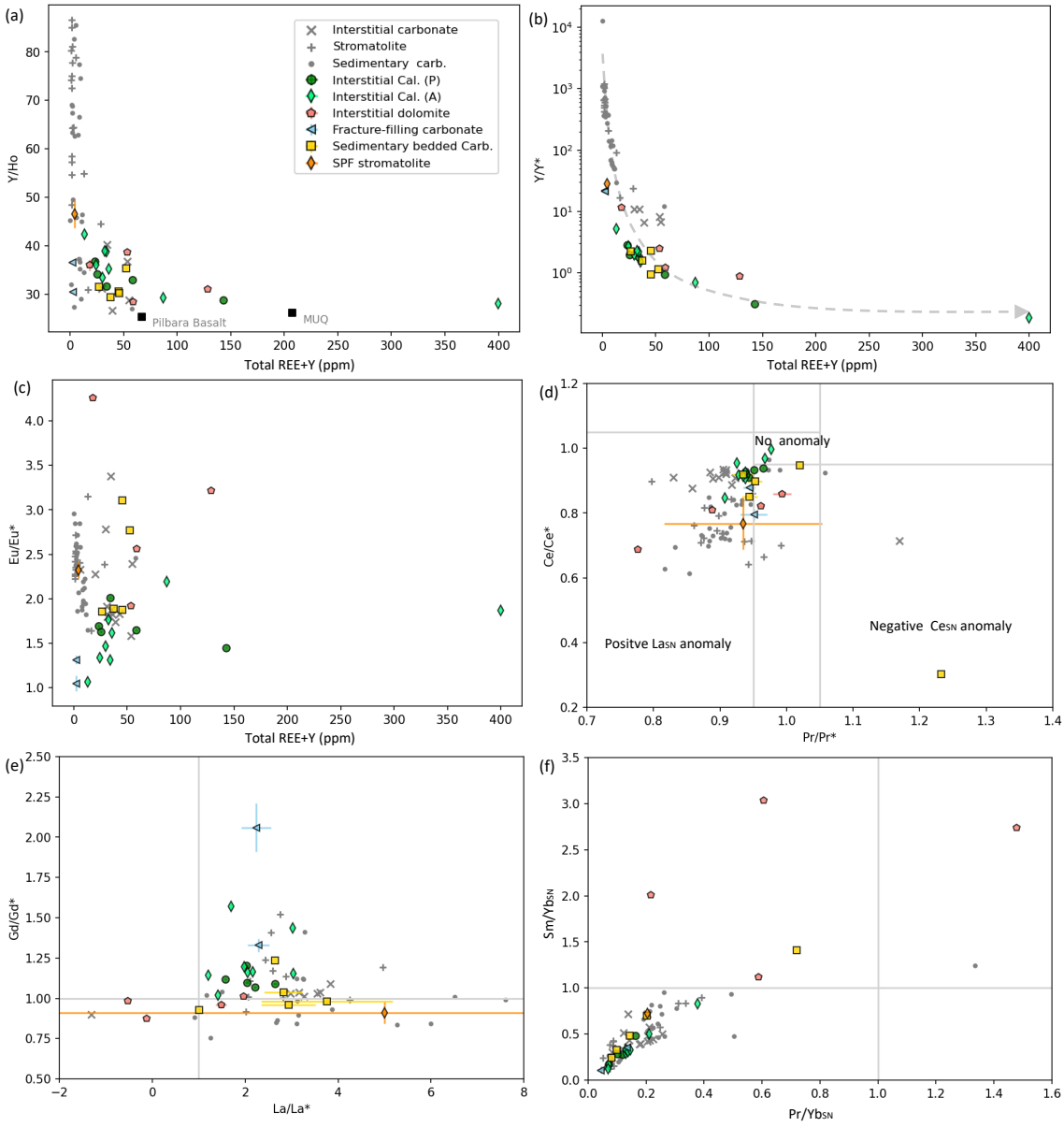

Fig.5 The cross-plots of the non-normalized Y/Ho weight ratios and the total concentration of REE+Y, and the PAAS-normalized REE+Y anomalies of the EPT carbonates and references.(a) Y/Ho weight ratios, (b) Y/ Y* , (c) Eu/ Eu* vs the total concentration of REE+Y (ppm); (d) Ce/ Ce * vs Pr/ Pr *, (e) Gd/ Gd * vs La/ La*, and (f) Sm/Yb_{SN} vs Pr/Yb_{SN}, indicating the EPT carbonates generally exhibit the near-chondritic or higher Y/Ho weight ratios, no Ce anomaly and positive La, Eu, Y anomalies, as well as LREE depletion. Reference values are from Van Kranendonk et al. (2003), Nakamura and Kato (2004), Yamamoto et al. (2004), Allwood et al. (2010), Viehmann et al. (2020). (Abbreviations: Cal. –calcite; P-primary; A-altered; Carb. -carbonate)

et al., 2020). The interstitial carbonates have an average Y/ Y* ratio of 1.82 ± 1.22, and similarly, the sedimentary carbonates 1.63 ± 0.60, whereas the fracture-filling calcites have a higher average value of 21.49 ± 0.21, as does the SPF stromatolite (28.49). The Eu/Eu* ratios increase from the fracture-filling calcite (mean value of 1.18 ± 0.19), through the interstitial calcite (1.62 ± 0.30), to interstitial dolomite (2.99 ± 1.00). The Eu/Eu* ratios of sedimentary carbonates (2.30 ± 0.60) and stromatolite (2.32) are within the range of interstitial dolomite. The Ce/ Ce* ratios of the EPT carbonates range from 0.69 to 1.00, excluding the outlier DB. However, the cross-plot of Ce/Ce * vs Pr/Pr * (Fig. 5d) indicates that there are no Ce anomaly but slightly positive La anomalies with an average La/La* ratio of 2.31 ± 0.88. The total REE+Y concentrations of interstitial carbonates range from 13.19 to 142.95 ppm, with an average value of 50.1 ± 37.20 ppm without CP-1 of 399.8 ppm. Similarly, the sedimentary carbonates have a mean value of 41.54 ± 9.87 ppm. However, the total REE+Y concentrations are much lower in the fracture-filling calcite and stromatolite, with a mean value of 2.99 ±1.24 ppm.

Table 2 The age-corrected radiogenic Sr isotopic compositions of the EPT carbonates

Lithology	Formation	Age (Ma)	SampleID	Sr (ppm)	Rb (ppm)	$^{87}Rb/^{86}Sr$	$^{87}Sr/^{86}Sr$	2sigma (2σ)	N	$^{87}Sr/^{86}Sr$ (i)
Interstitial Cal.(P)	Apex Basalt	3460	A14673-1	93.89	0.03	0.0009	0.703205	0.000004	95	0.703159
			A22-2	103.2	0.03	0.0007	0.704209	0.000004	96	0.704172
			ABAS-2	127.9	0.04	0.0008	0.703291	0.000005	92	0.703250
			ABAS-3	119.7	0.02	0.0005	0.701822	0.000004	96	0.701796
Interstitial Cal.(A)	Euro Basalt	3350	E-1	98.21	0.01	0.0002	0.706552	0.000004	98	0.706543
			E-3	34.91	0.02	0.0016	0.706605	0.000005	95	0.706540
	Apex Basalt	3460	Apex1	112.02	0.03	0.0008	0.704684	0.000005	95	0.704657
			Apex2	105.78	0.01	0.0003	0.703327	0.000006	97	0.703326
			Apex3	102.38	0.02	0.0007	0.703687	0.000005	97	0.703664
	Dresser Fm.	3480	D-3	71.57	0.01	0.0003	0.701919	0.000005	94	0.701917
	North Star Basalt	3490	CP-1	62.72	0.08	0.0038	0.703678	0.000004	97	0.703496
Interstitial Dol.	Mt Ada Basalt	3470	A-1-C	116.99	0.07	0.0017	0.707917	0.000004	97	0.707833
			A-1-E	160.05	0.09	0.0016	0.708825	0.000004	97	0.708746
			A-2	165.2	0.03	0.0005	0.712846	0.000005	98	0.712832
	North Star Basalt	3490	CP-2	20.02	0.02	0.0025	0.705454	0.000004	93	0.705341
Fracture Carb.	Dresser Fm.	3480	D-2-R	1089.56	0	0	0.700666	0.000005	96	0.700678
			D-2-W	1754.68	0	0	0.700583	0.000005	96	0.700596
Sedimentary. Carb.	Euro Basalt	3350	E-4	14.81	0.36	0.0706	0.714446	0.000006	99	0.711009
	Dresser Fm.	3480	D-1	33.11	0.72	0.0632	0.71216	0.000005	98	0.708969
			DB	61.34	1.09	0.0516	0.718059	0.000005	96	0.715458
			TSU	30.79	0.36	0.0337	0.70985	0.000004	96	0.708153
			PDP	103.96	0.01	0.0003	0.702207	0.000005	97	0.702203
SPF Stromatolite	Strelley Pool Fm.	3410	Strelley	40.05	0.05	0.0035	0.705377	0.000005	96	0.705217

Note:
1. $^{86}Sr/^{88}Sr$ ratio was normalized to 0.1194 using an exponential law.
2. $^{87}Sr/^{86}Sr$ ratio of NIST SRM 987 is 0.710246 ± 0.000009 (2σ, n =48).
3. $^{87}Sr/^{86}Sr$ ratios of JDo-1 and JLs-1 are 0.707575±28 (2σ, n=2) and 0.707847±19 (2σ, n=2), respectively.
4. $^{87}Sr/^{86}Sr$ (i) are $^{87}Sr/^{86}Sr$ ratios after correction of Rb and age.
5. Abbreviations: Cal. –calcite; ; P-primary; A-altered; Dol.- dolomite; Carb. -carbonate

Therefore, the EPT carbonates, in general, show the LREE depletion (Sm_{SN} /Yb_{SN} and Pr_{SN} /Yb_{SN} <1), no Ce anomaly, no or slightly positive La and Gd anomalies, with strong positive Eu and Y anomalies, consistent with previous works (Van Kranendonk et al., 2003; Nakamura and Kato, 2004; Yamamoto et al., 2004; Allwood et al., 2010; Viehmann et al., 2020). However, there are some exceptions. For example, it is noteworthy in Fig.5a that the sample with the highest REE+ Y concentration (CP-1) only has a positive Eu anomaly and no

obvious Y anomaly, while the three samples of low REE+ Y concentrations from the Dresser Formation only have positive Y anomalies and no Eu anomaly (Fig.5b and c). A decline in Y anomalies against total REE+ Y concentrations is observed the cross-plot, but no obvious correlation found in Eu anomalies (Fig.5b and c). Another outstanding REE+Y pattern is the convex shape of interstitial dolomite from Mount Ada Basalt (Fig. 4c), charactered by the MREE depletion ($Sm_{SN}/Yb_{SN}>1$ and $Pr_{SN}/Yb_{SN}<1$) and strong positive Eu anomalies. This pattern is also observed in the highly silicified SPF stromatolite (SHAW), showing a variant pattern combining that of its less altered counterpart with the Mount Ada interstitial dolomite.

4.3 Radiogenic Sr isotopic composition

The age-corrected radiogenic Sr isotopic compositions of the EPT carbonates are listed in Table 2 and illustrated in the cross-plots with Eu/Eu* in Fig.6. The fracture-filling calcites have the lowest $^{87}Sr/^{86}Sr$ ratios down to 0.700596, which is close to data of Dresser barites (McCulloch, 1994; Chen at el., 2022), making it plausive as a candidate of seawater at 3.5 Ga. The $^{87}Sr/^{86}Sr$ ratios of the primary interstitial calcites range from 0.701796 to 0.704172 with an average value of 0.703094 ± 0.000979, while the $^{87}Sr/^{86}Sr$ ratios of the altered interstitial calcite are slightly higher, ranging from 0.701917 to 0.706543 with an average value of 0.704306 ± 0.001725. The interstitial dolomites have the $^{87}Sr/^{86}Sr$ ratios within a large range, from 0.705341 to 0.712832, with a mean value of 0.708688 ± 0.003115. The $^{87}Sr/^{86}Sr$ ratios of the sedimentary carbonates are variable, ranging from 0.702203 to 0.715458, with a mean value of 0.709158 ± 0.004810, higher than interstitial calcites and comparable to interstitial

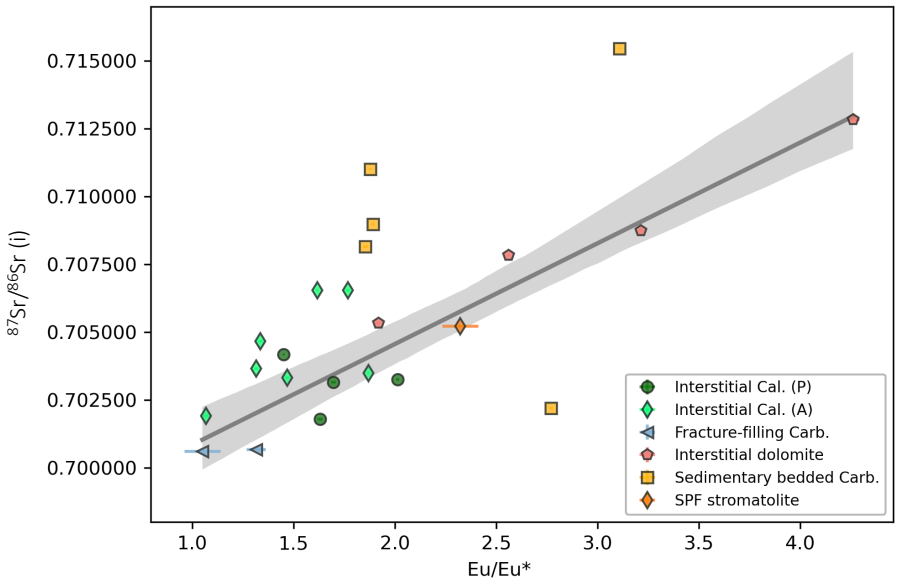

Fig.6 The cross-plots of the age-corrected $^{87}Sr/^{86}Sr$ ratios vs the PAAS-normalized Eu/ Eu* ratios of the EPT carbonates, reflecting progressive hydrothermal alterations of carbonates can elevate their Eu/ Eu* and $^{87}Sr/^{86}Sr$ ratios. The grey line indicates the regression line based on data of fracture-filling calcite D-2-W, the primary interstitial calcite and interstitial dolomite. The grey envelope is plotted with the confidence interval of 95%, generated via Seaborn regplot (default). To be noted, some altered interstitial calcite and SPF stromatolite are located in the area. (Abbreviations: P-primary; A-altered; Cal. –calcite; Dol.- dolomite; Carb. -carbonate)

dolomites. The SPF stromatolite has an intermediate $^{87}Sr/^{86}Sr$ ratio of 0.705217.

5. Discussion

5.1 Evaluation of clastic contamination

Even small amounts of clastic or terrigenous components can potentially affect the REE+Y patterns and Sr isotopic compositions of carbonates due to the disparity in REE+Y concentration between shale (relatively high) and carbonate (very low) (Kamber and Webb, 2001). However, the possible influence of clastic contamination has been minimized in this work. First, no textural evidence or detrital material was observed in the petrographic study of thin sections. Second, the micro-drilling technique for interstitial carbonates and chemical separation of mineral phases using low-concentration HNO_3 acid at room temperature significantly reduced the dissolution of putative silicates. Third, systematic relationships between Fe contents and molar ratios of Mg/Ca indicate the measured soluble Fe is from calcite or ferroan dolomite, rather than iron silicate and (oxy)hydroxide minerals (Fig.2b).

Nonetheless, multiple parameters have been evaluated to support the absence of the possible clastic components. The minor dissolution of detrital contaminations (usually aluminosilicate minerals) may contribute to higher concentrations of Al, Th, Sc and Zr in the leachate, hence positive correlations between Al content and the others have been adopted to identify terrigenous detrital contamination (Webb and Kamber, 2000; Nothdurft et al., 2004; Ling et al., 2013). Different empirical “cut-off values” have been applied to screen samples possibly affected by detrital aluminosilicates, i.e. 2000 ppm Al and 5 ppm Zr (Schier et al., 2018), 0.5 ppm Th and 2 ppm Sc (Ling et al., 2013). In this work, the Al contents of most samples (except two interstitial calcites) are below 2000 ppm and are independent of the silicate contents inferred by dissolved fractions. The Zr and Th concentrations of all samples are below the empirical values, while the Sc concentrations of some samples are higher. However, the lack of a systematic correlation of concentrations between Al and any other elements (Fig.7) precludes the detritus contamination, confirming the compositions studied in this work essentially inherit from carbonates.

The void or rare existence of dissolved components from Paleoarchean basaltic rocks and weathered upper continental crust is further supported by the binary mixing lines (methods see in Appendix) between a Paleoarchean seawater composition (D-2-W, discussed in Sect 5.2.1) and an average composition of the Paleoarchean EPT basalts (in Appendix; data from Van Kranendonk and Pirajno, 2004; Yamamoto et al., 2004; Nakamura and Kato, 2004; Smithies et al., 2005b; Jenner et al., 2009; Johnson et al., 2017; Nakamura et al., 2020; Tusch et al., 2021; Tympel et al., 2021; Caruso et al., 2021) and the composition of MUQ (MUd from Queensland, Kamber et al., 2005), respectively (Fig.7). Most EPT carbonates are far apart from the binary mixing lines of either basalt or MUQ, indicating a lack of volcanic detritus. However, the sedimentary carbonates commonly contain more Th and Rb closer to the binary mixing line of MUQ, Ti to that of basalt, and Zr to both, but only with a possible

detritus input of around 1.5% (maximum 3%). Nonetheless, this minor fraction is unlikely to change the REE+Y patterns of sedimentary carbonates significantly, as illustrated in Fig.8b,

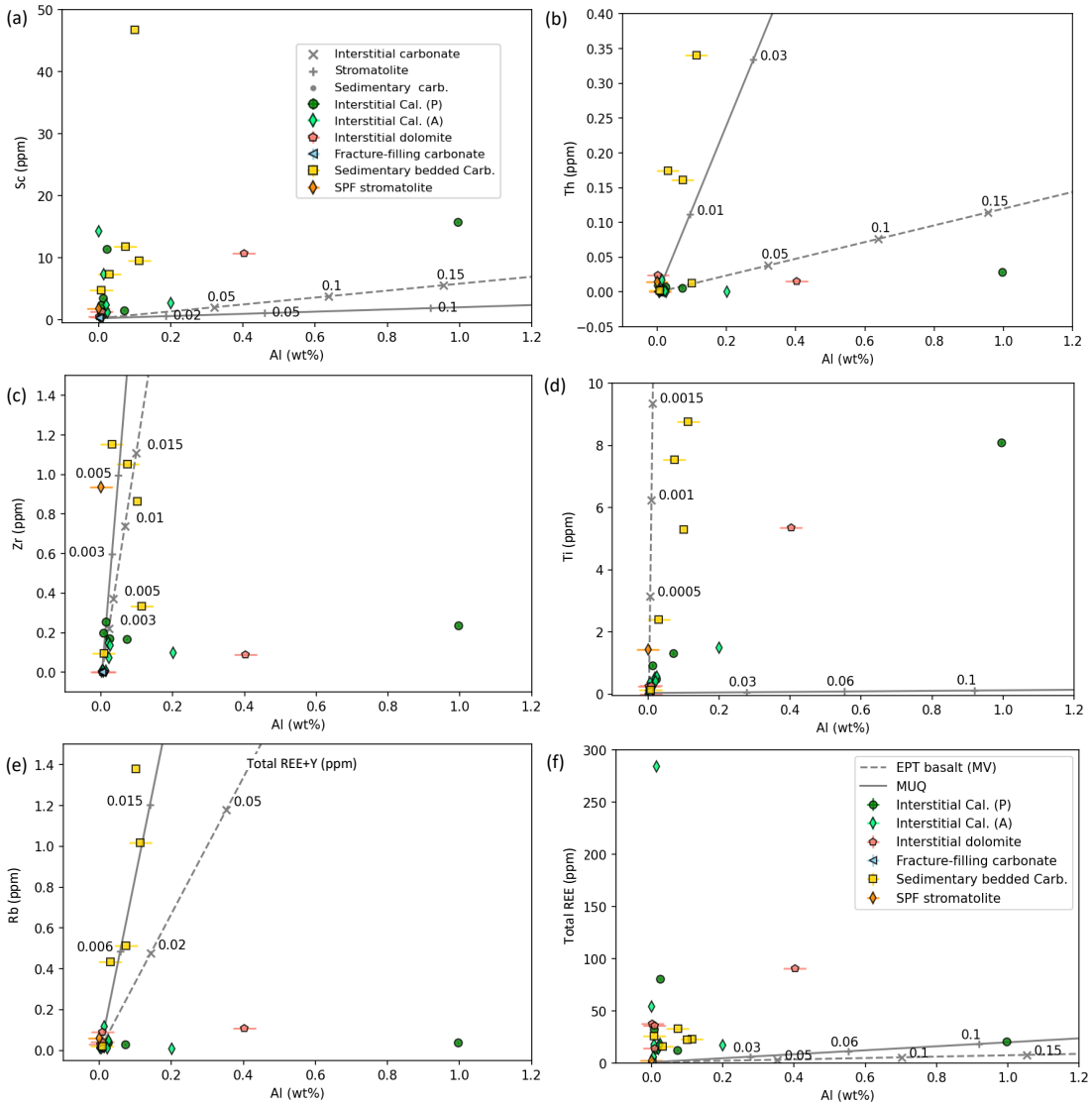

Fig. 7 The cross-plots of the Al content (wt%) against the concentrations (ppm) of (a) Sc, (b) Th, (c) Zr, (d) Ti, (e) Rb and (f) the total REE for assessing the possible detritus contamination. The grey dashed line indicates the binary mixing line of seawater endmenber D-2-W and the EPT basalt endmember (mean value, MV), while the other grey line indicates the binary mixing line of seawater endmenber D-2-W and the MUQ endmember (Kamber et al., 2005), with the numbers indicating the weight fractions of basalt or MUQ. As shown, only some sedimentary carbonates were likely influenced by a minor fraction of detritus up to 0.03. (Abbreviations: Cal. –calcite; P-primary; A-altered; Carb. –carbonate; SPF- Strelley Pool Formation)

by subtracting 3% of the average composition of the EPT basalts and MUD from the mean value of sedimentary carbonates based on the binary mixing model.

5.2 Pristine proxies in the early Archean

5.2.1 Proxy of the Paleoarchean surface seawater

Among the interstitial carbonates, the fracture-filling calcite is an exception that precipitated from fluids circulating through parallel fractures of the basaltic basement, causing recrystallization of the earlier interstitial carbonate. The high Sr contents (>1000 ppm) and positive $\delta\ ^{13}C_{VPDB}$ values ranging from + 2.03 to + 2.34 ‰ make their parent fluids good candidates for the Paleoarchean seawater.

The direct evidence for the seawater origin of fracture-filling calcite is the least radiogenic $^{87}Sr/^{86}Sr$ ratio of 0.700596 (D-2-W), identical to the values of barites from the same 3.48 Ga Dresser Formation (McCulloch, 1994; Chen at el., 2022). A rule of thumb has been commonly accepted in studies of seawater Sr isotopic evolution that the lowest $^{87}Sr/^{86}Sr$ ratios can represent the best maximum estimate of seawater $^{87}Sr/^{86}Sr$ at any particular time (Veizer and Compston, 1974; Burke et al., 1982). However, almost all of the ~1000 Precambrian carbonate samples collected in the Precambrian marine carbonate isotope database (PMCID) have suffered post-depositional alteration, deviating their $^{87}Sr/^{86}Sr$ ratios to some degree (Shields and Veizer, 2002). It, therefore, requires a concession to using the $^{87}Sr/^{86}Sr$ ratios of barites to represent the radiogenic Sr isotopic composition of seawater (Veizer et al., 1999; Shields and Veizer, 2002; Satkoski et al., 2016; Chen et al., 2022), giving the lowest $^{87}Sr/^{86}Sr$ ratio of 0.700447 at ~ 3.5 Ga (based on barites from Dresser Formation; Chen et al., 2022). However, it may be argued that barite is commonly of hydrothermal origin or hybrid origin with seawater, and accordingly inherits the less radiogenic Sr isotopic composition that cannot unambiguously reflect seawater. In contrast, the uncertainty can easily be eliminated by a combination of Sr, O, and C isotopic studies, as well as the REE+Y patterns on the same carbonate samples.

In addition to marine $\delta^{13}C$ values and $\delta^{18}O$ values and the less radiogenic $^{87}Sr/^{86}Sr$ ratios, the PAAS-normalized REE+Y patterns of fracture-filling calcites support the interpretation that they retained the original seawater signatures of the Paleoarchean ocean, at least regionally. First, the REE+Y concentrations of fracture-filling calcites are much lower than those of other interstitial and sedimentary carbonates, and slightly lower than that of the SPF stromatolite (Fig.8a and b). Second, their PAAS-normalized REE+Y patterns are characterized by LREE depletion, the absence of Ce_{SN} and Eu_{SN} anomalies, but positive La_{SN} and Y_{SN} anomalies, with near-chondritic Y/Ho weight-ratios (Fig.5), consistent with the patterns of the SPF stromatolites (the average value of data from Van Kranendonk et al., 2003; Allwood et al., 2010; Viehmann et al., 2020; herein), except for the lack of Eu_{SN} anomaly, which are negative when normalized to Primitive Mantle (PM, Palme and O'Neil, 2014). In addition, the PM-normalized pattern of fracture-filling calcite is identical to those of modern North Pacific deep and surface water (Fig.8c and d; Alibo and Nozaki, 1999; Hongo and Nozaki, 2001), with only one exception of no negative Ce anomaly. Therefore, all these results indicate that the parent fluid of fracture-filling calcite is the shallow marine water at

3.5 Ga, which circulated into the basaltic basement along the fractures possibly caused by

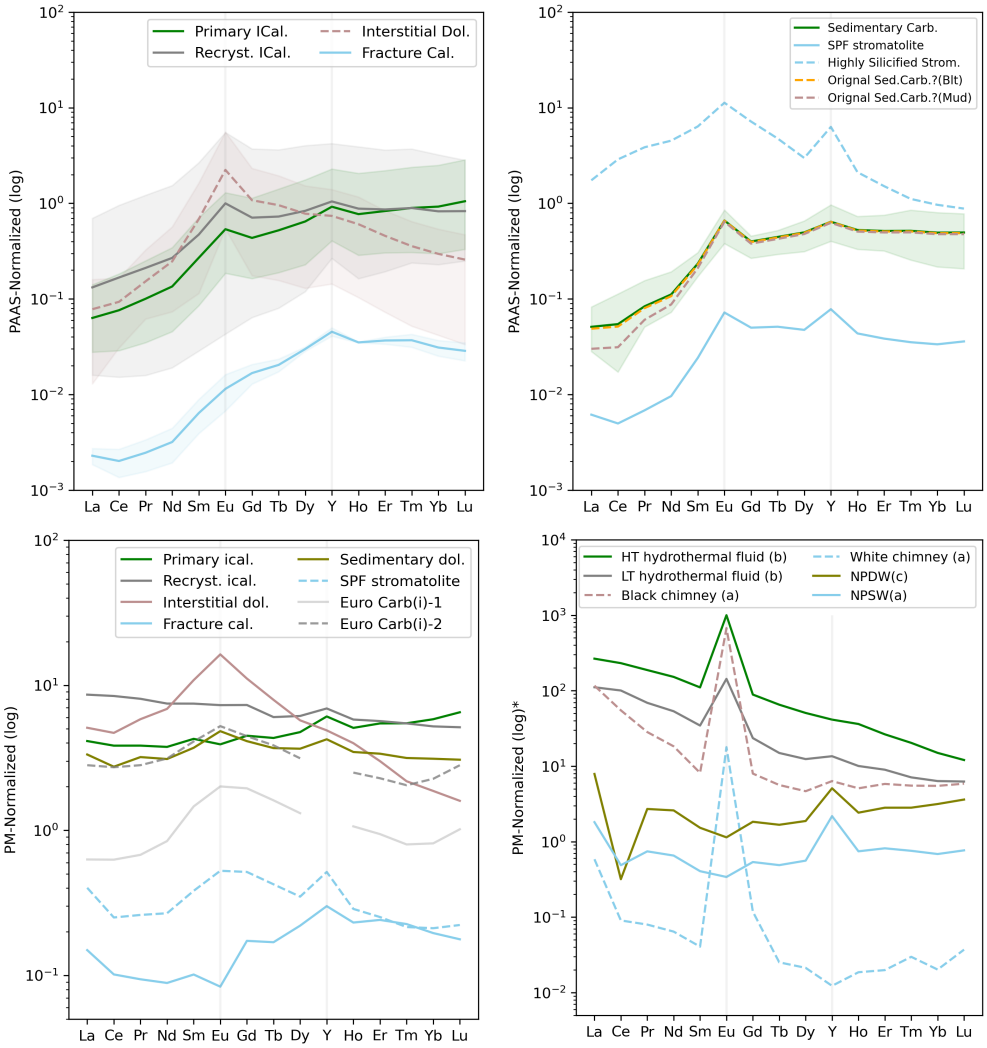

Fig. 8 The normalized REE+Y patterns of the EPT carbonates and references that (a) and (b) are normalized to PAAS, whereas (c) and (d) are normalized to PM. The lithologies are various, including (a) the primary interstitial calcite (Primary ICal.), the altered recrystallized interstitial calcite (Recryst. ICal.), the interstitial dolomite (Dol.) and fracture-filling calcite (Fracture Cal.), as well as (b) sedimentary carbonates (Carb.) and the Strelley Pool (SPF) stromatolites. The dashed blue line represents the highly silicified counterpart of the less-altered stromatolite shown in blue line. The orange dashed line represents an assumed line based on the binary mixing model, where 3% of the average composition of the EPT basalt is subtracted from the mean value of sedimentary carbonates, indicating a maximum contribution of basalt detritus to carbonate (Fig.7). The same approach is used to plot the rose-brown dashed line by subtracting 3% of the MUD composition. The PM-normalized mean REE+Y patterns of (c) the EPT carbonates and (d) modern references. In (c), two carbonates located within the margin of Euro pillow basalt (Yamamoto et al., 2004) are plotted, with Euro Carb (i)-1 spatially outer than Euro Carb (i)-2. Lines in (c) show a smooth transition from the seawater endmember to interstitial carbonates. In (d), the true values are multiplied by E6 and presented in the log y-scale. Abbreviations in (d): HT –High Temperature; LT – Low Temperature; NPDW- North Pacific Deep Water; NPSW- North Pacific Surface Water, data from ref. a. Hongo and Nozaki, 2001; b. Bau and Dulski, 1999; c. Alibo and Nozaki, 1999.

tectonic events, without hydrothermal modification.

As a consequence, the fracture-filling calcite D-2-W with the least $^{87}Sr/^{86}Sr$ ratio will be

used as the 3.5 Ga seawater endmember in next sections to discuss impacts of seawater-basalt reaction and hydrothermal alteration on the geochemical compositions of various carbonates. It will help to distinguish the primary signatures and trace the depositional and burial environments. The geochemical features of the seawater endmember are listed as follows: a high Sr concentration of 1789 ppm, $\delta^{13}C$ value of +2.20 ‰, $\delta^{18}O_{VPDB}$ value of -13.03‰, an age-corrected $^{87}Sr/^{86}Sr$ ratio of 0.700596, and the PAAS-normalized REE+Y pattern charactered by LREE depletion, the absence of Ce_{SN} and Eu_{SN} anomalies but positive La_{SN} and Y_{SN} anomalies with a near-chondritic Y/Ho weight-ratio.

5.2.2 Proxies for low temperature hydrothermal seafloor alteration

The element compositions with long residence times of modern seawater depend mainly on input and output fluxes, including rivers and submarine groundwater discharge, sediment formation and diagenesis, and seafloor hydrothermal systems that are subdivided into on-axis high-temperature or off-axis low-temperature hydrothermal systems (Coogan et al., 2018). Despite active debates on the relative importance of high- and low-temperature hydrothermal circulations (Davis et al., 2003; German and Lin, 2004; Nielsen et al., 2006; Vance et al., 2009), it has been well demonstrated that these hydrothermal seafloor alterations play significant but long underestimated roles in the cycling of energy and mass between the solid earth and ocean (German and Seyfried, 2014; Coogan et al., 2018). In the early Archean, their contributions to marine geochemical cycling might have been more considerable when freshwater fluxes were limited due to less subaerial continental crust.

The EPT interstitial carbonate was commonly precipitated from the seawater-derived hydrothermal fluids generated during the basalt-seawater interaction (Chapter 2). The primary petrological facies is acicular crystal-fan calcite, optimally preserved in Apex Basalt, which is isotopically supported by the Rb-Sr errorchron age of the host pillow basalts of 3570.7 ± 144.3 Ma (n=6, MSWD =150) (Chapter 4). This age is identical to the assumed depositional age of Apex Basalt between 3463 and 3454 Ma, as constrained by zircon U-Pb ages of the underlying Duffer Formation and overlying Panorama Formation (Thorpe et al., 1992; McNaughton et al., 1993). Accordingly, the primary interstitial carbonates have the hybrid geochemical compositions inheriting from seawater and basaltic basement. For example, their $^{87}Sr/^{86}Sr$ ratios are intermediate, ranging from 0.701796 to 0.704172, between the seawater value of 0.700596 and the whole rock value (host basalts) of 0.706337 ± 0.000078 given by the errorchron (Chapter 4). The mean $\delta^{13}C$ value of + 0.63 ± 0.12 ‰ also indicates a mixture of seawater (+2.20 ‰) and “mantle” fluxes (-6 ‰, Hayes and Waldbauer, 2006). The mean formation temperature calculated by the $\delta^{18}O_{VPDB}$ values of primary interstitial calcites were 108.9 ± 4.1 (assuming the seawater $\delta^{18}O$ value of −1.2‰, Shackleton and Kennett, 1975) or 33.0 ± 2.8 °C (assuming the seawater $\delta^{18}O$ value of −13.3 ‰, Jaffrés et al., 2007), both of which imply low-temperature hydrothermal fluids (Chapter 5).

On the other hand, the primary interstitial calcite exhibits a higher REE+Y concentration and a near-chondritic Y/Ho weight-ratio, and the PAAS-normalized REE+Y pattern is characterized by LREE depletion, no Ce anomaly, and positive La, Gd, Eu and Y anomalies.

To be noted when normalized to PM, there is rarely any REE fractionation, and only positive Y anomalies are observed (Fig.8c), suggesting that the REE abundance of the seawater-derived hydrothermal fluid is predominantly controlled by the basaltic basement of putative mantle origin and the Y enrichment is inherited from seawater. Compared to the seawater endmember, the primary interstitial calcite has the higher concentrations of Mg, Fe, Mn, Al, Sc, Ti, V, Rb, Mo, and U (Fig.3), indicating the basaltic origin of those trace elements. However, the much lower concentration Sr infers that there is likely at least one input of Sr to the ocean besides hydrothermal venting from basaltic oceanic crust, possibly from infant continental weathering.

5.3 Geochemical variations during post-depositional alteration

Taking the interstitial carbonate as example, the primary acicular calcite transforms into either recrystallized calcite or blocky ferroan dolomite, dependent on the fluid sources during post-depositional alteration. The former type is likely caused by seawater and low-temperature hydrothermal fluids, while the latter type is caused by high-temperature hydrothermal fluids.

5.3.1. Geochemical deviation during recrystallization

In Chapter 2, recrystallization commonly converts the fan-like primary interstitial calcite to blocky, massive sparry calcite with quartz cement usually replacing the primary calcite cement. The geochemical compositions of recrystallized calcites are various, depending on the compositions of alteration fluids. For example, recrystallization induced by low-temperature hydrothermal fluid, similar to the parent fluids, may cause declines in Mg, Fe, V, Zr, Ba and U, but not greatly influence Mn, Sc, Ti, Rb, Sr, Mo, Th, Ni, Zn and Hf (Fig.3). However, this process does not greatly change the abundances of REE+Y, only slightly shifting both PAAS- and PM-normalized REE+Y patterns towards the LREE enrichment (Fig.8). The similar phenomenon is found in the geochemical work of Mississippian carbonates in which the recrystallization process of two-generation dolomites did not affect their REE patterns (Banner et al. 1988). Most recrystallized interstitial calcites have identical $\delta^{13}C$ values, lower $\delta^{18}O$ values and higher $^{87}Sr/^{86}Sr$ ratios compared to the primary interstitial calcites, verifying the sensitivity of O and Sr isotopic compositions to post-depositional alteration. However, the recrystallization triggered by contemporary seawater can lead to a different tendency, as observed in D-3 and the other fracture-filling calcite D-2-R, whereby hydrothermal signatures (element abundances of basaltic origin, including REE) are decreased, whereas seawater signatures (Sr content, positive Y anomaly, isotopic compositions of C, O and Sr) are shifted toward the seawater endmember.

5.3.2. Geochemical deviation during dolomitization

This type is predominantly observed in interstitial carbonate samples of Mount Ada Basalt consisting of blocky, massive ankerite with calcite overgrowth on the edge of ankerite

cemented by quartz. The common occurrence of calcite overgrowth makes it difficult to recognize the geochemical signals individually. However, the in-situ geochemical analysis via micro-XRF illustrated that the calcite overgrowth is Fe/Mn-poor and Sr-rich, identical to the fracture-filling calcite (Chapter 2). This implies that the later alteration after dolomitization is possibly triggered by seawater. If so, the geochemical deviation by seawater discussed above must be considered.

In addition to the significant elevation in Mg and Fe, dolomitization of interstitial calcite causes increases in V, Rb, Sr, Zn, Hf, decreases of Zr and U, yet has no influence on Mn, Sc, Ti, Mo, Ba, Th, Ni (Fig.3). Different from other carbonates, the PAAS- and PM- normalized REE+Y patterns of the interstitial dolomite are characterized by Middle REE (MREE) enrichment and strong positive Eu anomalies (Fig.8). The strong positive Eu anomaly is commonly found in hydrothermal venting fluids and precipitates in the modern ocean, which is caused by preferential leaching of igneous plagioclase with a positive Eu anomaly (Klinkhammer et al., 1994). However, it is absent in seawater (Fig.8d; Bau and Dulski, 1999; Alibo and Nozaki, 1999; Hongo and Nozaki, 2001). The decoupling of Eu from the other REEs occurs during high-T metamorphism (exceed 250°C) under reducing conditions (Sverjensky, 1984; Bau, 1991, 1993; Bilal, 1991), yielding the chondrite-normalized Eu anomaly $(Eu/Eu^*)_{CN} > 1$ in high-T hydrothermal fluids (> 250°C) and $(Eu/ Eu^*)_{CN} = 1$ in low-temperature hydrothermal fluids (< 250°C), respectively (Bau and Dulski, 1996). Therefore, the strong positive Eu anomalies of interstitial dolomite suggest they might have precipitated from high-temperature hydrothermal fluids rather than low-temperature fluids. The $\delta^{13}C$ and $\delta^{18}O$ values of interstitial dolomite are comparable with the primary and secondary interstitial calcites, but their $^{87}Sr/^{86}Sr$ ratios are significantly higher. It is noteworthy that a good positive correlation between Eu anomalies and $^{87}Sr/^{86}Sr$ ratios with Pearson correlation coefficient of +0.96 occurred among fracture-filling calcite, the primary interstitial calcite and the interstitial dolomite (Fig.6), indicating the same cause for the elevations of Eu anomalies and $^{87}Sr/^{86}Sr$ ratios by the progressive hydrothermal alteration of the host basaltic rocks along with the temperature increases. It should be noted that parts of the altered interstitial calcites and the SPF stromatolite are located within the envelope (95% confidence interval) of the regression line of the aforementioned Eu anomalies and $^{87}Sr/^{86}Sr$ ratios, verifying again the later alteration by hydrothermal fluids of the same origin.

5.3.3 Case-study about sedimentary carbonates and stromatolite

The peak metamorphic temperature of 300 to 350 °C for organic matter in the bedded sedimentary carbonates indicates post-depositional metamorphism of greenschist facies (Chapter 2). This is supported by the large deviation of $^{87}Sr/^{86}Sr$ ratios and the similarly high concentrations of trace elements close to or higher than those in interstitial dolomites (Fig.3 and 6). Nonetheless, some primary sedimentary textures somehow survived during metamorphism, such as the loose normal grading of carbonate rhombs, indicating shallow burial conditions that did not homogenize the entire rock. Except for DB, which consists of calcite and Mn-rich dolomite particles, the EPT sedimentary carbonates are dominantly ferroan dolomite exhibiting similar PAAS-normalized REY patterns comparable to those of interstitial

calcites, and the intermediate $\delta^{13}C$ and $\delta^{18}O$ values between seawater endmember and the primary interstitial calcites. As discussed in Section 5.3.1, the REE+Y pattern of carbonate can significantly change only through dissolution and neomorphism, however, the inherited original textures eliminated this thorough transform. Therefore, there are two possibilities for the formation of sedimentary carbonates: (1) they were essentially hydrothermal alteration products of earlier marine carbonates; (2) they were precipitated in the marine environment, which was more or less influenced by hydrothermal inputs. Based on petrographic work, the sedimentary carbonates are subdivided into two types, the laminated carbonate TSU that likely generated during one Tsunami event (Runge et al., 2022), and the bedded carbonate rocks DB and E-4 that are characterized by the repeat graded carbonate layers, making the first possibility less convincing. Hence, the second possibility is a better explanation for the formation of sedimentary carbonates. However, unlike the marine sediments E-4 and Tsu, DB is likely formed within a restricted hydrothermal pond with minor seawater input (possibly by tide), supported by the mantle-like $\delta^{13}C$ value and the hydrothermal REE+Y pattern.

As for the SPF stromatolite, the various generations of dolomite on the chert matrix indicate the occurrence of post-depositional alteration (Chapter 2). The less altered one has concentrations of trace elements and an $^{87}Sr/^{86}Sr$ ratio within the range of altered interstitial carbonates and sedimentary carbonate, but higher than the seawater endmember (Fig.3 and 6), inferring the geochemical deviation by hydrothermal fluids. Based on the Raman spectra of the syngenetic carbonaceous materials, Allwood et al. (2006b) suggested that the SPF sedimentary rocks (i.e. chert and stromatolite) reached a maximum temperature of around 200-500 °C during their long history. However, some primary signatures may be retained. For example, biomarker molecules might be sufficiently preserved in some rocks under the lower metamorphism (~200 °C) (Allwood et al., 2006b). The relatively robust signatures like $\delta^{13}C$ values and the PAAS-normalized REE +Y pattern, comparable with the seawater endmember, illustrate the shallow marine origin of the SPF stromatolite. Nonetheless, the REE +Y patterns of the SPF stromatolites may be slightly influenced by hydrothermal alteration (Fig.8). For instance, the dissolution of dolomite that was precipitated in the last stage of hydrothermal alteration possibly stains the original REE +Y pattern of earlier carbonate generations. The highly silicified stromatolite sample SHAW has a strongly variant PAAS-normalized REE +Y pattern, consistent with interstitial dolomite, whereas its least altered counterpart Strelley has a slightly variant pattern (Fig.8b), which is more obvious when normalized to PM (Fig.8c), in which it is intermediate between the pattern of the seawater endmember and the carbonate mineral at the outermost crust of Euro pillow basalt (Yamamoto et al., 2004). According to the REE+Y patterns of the footwall metabasalts of the Warrawoona Group, Van Kranendonk and Pirajno (2004) assumed the hydrothermal circulation was possibly driven by heat from the overlying erupted Euro Basalt and contaminated by a basement of older continental crust. However, the recrystallization and frequent bending of Euro interstitial calcite indicate the occurrence of hydrothermal alteration accompanying tectonic events after the eruption of Euro Basalt (Chapter 2). Additionally, the Sm-Nd isotopic compositions of the SPF stromatolites yield an age of 3253 ±320 Ma that matches within the error with the deposition age of the Strelley Pool Formation, but also overlaps with a thermal event triggering the eruption of the 3.2 Sulfur Springs Group, or younger e.g. 2718 ± 220 M (Viehmann et al.,

2020).

5.4 Implication for seawater Sr isotopic evolution

The marine Sr isotopic composition has been greatly influenced by the relative contributions of the more radiogenic riverine input from continental weathering and less radiogenic mantle input from mid-ocean ridges, which can be retained in well-preserved marine carbonate rocks (Veizer, 1989a, b). However, recently, more and more attention has been paid to the off-axis, low-temperature hydrothermal systems occurring across much of the abyssal plains, the contributions of which to marine geochemical cycles had been long underestimated (Coogan et al., 2018). In contrast to the modern ocean where continental river discharge acts as the major controlling factor, the Archean ocean was dominantly influenced by large-scale hydrothermal interaction between seawater and ocean floor basalts (Veizer et al., 1982). The marine Sr isotopic composition was accordingly supposed to be less radiogenic, close to that of Bulk Silicate Earth, and elevated $^{87}Sr/^{86}Sr$ ratios have been commonly explained by the occurrence of continental weathering (Satkoski et al., 2016, 2017; Ravindran et al., 2020; Roerdink et al., 2022), with the assumption that the continental materials have higher Rb/Sr ratios and their weathering produced the higher $^{87}Sr/^{86}Sr$ ratios of continental Sr flux due to Rb decay. This is true at present-day. However, continental weathering is not the only factor that can increase the $^{87}Sr/^{86}Sr$ ratios of marine authigenic minerals in the early Archean.

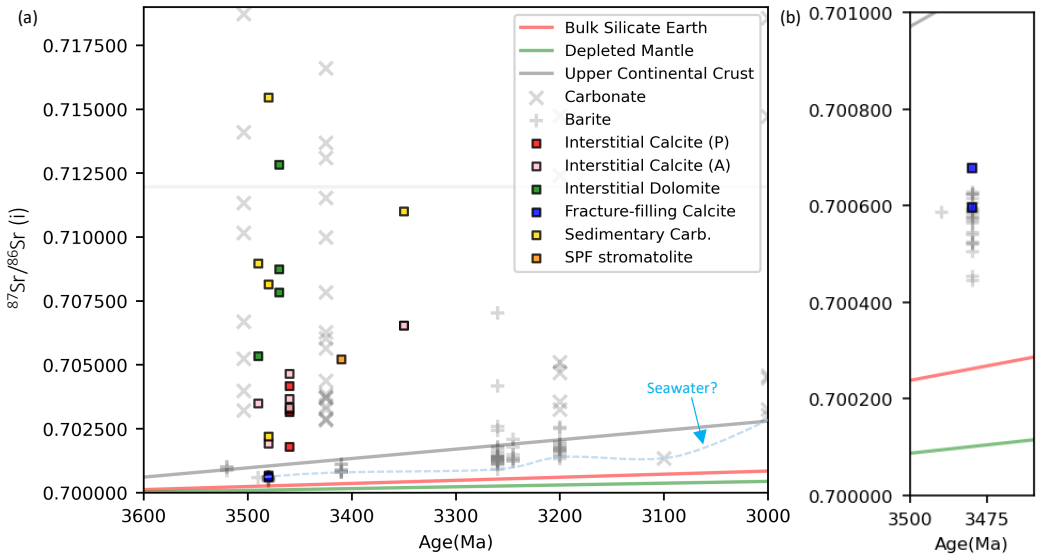

Fig. 9 (a) The Sr isotopic compositions of the EPT carbonates and references of carbonate and barite against time, with the Sr isotopic evolution line of the Bulk Silicate Earth (BSE), Depleted Mantle (DM), Upper Continental Crust (UCC). The dashed blue line indicates the Seawater Sr isotopic evolution based on the least radiogenic Sr isotopic composition at any time. The details of the evolution lines are in Appendix, and references of carbonate and barite are from McCulloch (1994), Shields and Veizer (2002), Satkoski et al. (2016), Ravindran et al. (2020), Roerdink et al. (2021), Chen et al. (2022). The data of barite and carbonate from Dresser Formation is magnified in (b). (Abbreviations: P-primary; A-altered; Carb. –carbonate; SPF- Strelley Pool Formation)

In this study, the age-corrected $^{87}Sr/^{86}Sr$ ratios of the EPT carbonates of various facies are illustrated in Fig. 9, together with data from carbonate and barite (McCulloch, 1994; Shields and Veizer, 2002; Satkoski et al., 2016; Ravindran et al., 2020; Roerdink et al., 2022; Chen et al., 2022) and Sr isotopic evolution lines of seawater, Bulk Silicate Earth (BSE), Depleted Mantle (DM), Upper Continental Crust (UCC) (details in Appendix). The age-corrected $^{87}Sr/^{86}Sr$ ratios of fracture-filling calcites greatly overlap data of Dresser barite, which is intermediate between the evolution lines of BSE and UCC, and well represents the less radiogenic Sr isotopic composition of seawater at ~3.5 Ga. However, other carbonates exhibit the higher $^{87}Sr/^{86}Sr$ ratios, although above the UCC evolution line, which are interpreted to be elevated by hydrothermal alteration of the oceanic basaltic crust. This interpretation is supported by the good positive correlation between Eu anomaly and $^{87}Sr/^{86}Sr$ ratio of the interstitial carbonates (Fig.6). In other words, hydrothermal fluid is not always less radiogenic than contemporary seawater. Instead, it can be higher if it develops from the interaction between seawater and ocean basaltic crust or felsic basement with more radiogenic Sr isotopic compositions. If this scenario occurred, the higher age-corrected $^{87}Sr/^{86}Sr$ ratio than the assumed contemporary seawater value cannot alone serve as proof for the emergence of continental weathering without estimating the influence by hydrothermal input during deposition.

5.5 Controls on ocean geochemistry in the early Archean

Modern marine geochemistry is determined by the main material fluxes to the ocean, including river run-off (which deliver materials to the surface ocean at the land-sea boundaries), atmospheric deposition (which occurs in all regions of the surface ocean), hydrothermal activity (which occurs in deep and intermediate waters above seafloor), and subsequent fate of the materials via various sinks (Chester, 2009).

Larger impacts of continental weathering flux on ocean chemistry at 3.26 Ga than previously suggested were proposed by Satkoski et al. (2016) with evidence of more radiogenic $^{87}Sr/^{86}Sr$ ratios in barite than contemporaneous mantle. This was predated at approximately 3.70 ± 0.15 Ga by Roerdink et al. (2022) with the same method using stratiform barite from three 3.52 -3.20 Ga cratons (i.e. Kaapvaal, Pilbara and Dharwar). Regardless of the validity of this application using $^{87}Sr/^{86}Sr$ ratios of barite or carbonate, the Archean continents were largely flooded (Arndt, 1999; Kitajima et al., 2001; Kump and Barley, 2007), with less than ~4% of Earth's area emerging (Kump and Barley, 2007; Flament et al., 2013). The periods of subaerial exposure of the EPT were recorded in several erosional unconformities, local preservation of desiccation cracks, the more widespread occurrence of rippled sedimentary carbonate rocks and stromatolites, alluvial paleosols (Lambert et al., 1978; Walter et al., 1980; Groves et al., 1981; Buick and Dunlop, 1990; Van Kranendonk, 2006; Djokic et al., 2017; Retallack, 2018; Van Kranendonk et al., 2019a). Djokic et al. (2017, 2021) reported geyserite and siliceous sinter in the Dresser formation and interpreted it to be a fluvial, subaerial hot spring indicated by abrupt lateral facies changes and associated channelized clastic deposits, distinctive geochemical data. The subaerial area in the EPT is also supported by the sedimentary carbonate rock DB with its unique mantle-like $\delta^{13}C$ values

of -5.79 ‰ on average and sedimentological textures indicating a restrict hydrothermal pond rarely influenced by seawater (Chapter 2). Therefore, terrigenous inputs due to subaerial weathering are one factor impacting ocean geochemistry on the regional scale. Nonetheless, the REE+ Y patterns of marine authigenic sediments are likely less influenced by this input, as discussed in Section 5.1, only sedimentary carbonates may accept a maximum 0.3% detritus or terrigenous input, with LREE being more vulnerable than other REEs (Fig.7 and 8), possibly due to their higher mobility.

The most distinguishing characteristic of Archean environment was negligible atmospheric O_2 (Catling and Zahnle, 2020). It was reflected in many Archean proxies, including mass-independent isotopic signatures of multiple sulfur isotopes (Farquhar et al., 2001; Pavlov and Kasting, 2002; Bontognali et al., 2012; Endo et al., 2016) and the absence of negative Ce_{SN} anomalies (Van Kranendonk et al. 2003; Allwood et al., 2010; Shibuya et al., 2010; Westall et al., 2015; Nutman et al, 2019a, b; Hickman-Lewis et al., 2020; Viehmann et al., 2020; herein). On the other hand, atmospheric CO_2 enters global carbon cycle via organic carbon, dissolved inorganic carbon and carbonate minerals. Due to a kinetic isotope effect that enriches biological and non-biological organic matter in the lighter isotope ^{12}C (Shields, 2019), the mean $\delta\ ^{13}C$ value of the total dissolved carbon in modern seawater is ~1±0.5‰ (Kroopnick, 1980; Tan, 1988), while a 2 ‰ fractionation occurs between dissolved inorganic carbon and carbonate precipitated from it (Hayes and Waldbauer, 2006). In previous studies, the Archean marine sedimentary carbonates were found to have an average value of ~ 0 ‰ (Veizer et al., 1989; Lindsay et al., 2005; Nutman et al., 2016; Chapter 2), which is indistinguishable from the values of interstitial carbonates (Nakamura and Kato, 2004; Shibuya et al., 2012; Chapter 2). However, few of these studies have reported detailed mineralogical and petrographic information for the samples used in carbon isotope studies, making it difficult to unequivocally determine the carbon origin of studied carbonates. In Chapter 2, a covariation between $\delta\ ^{13}C$ and $\delta\ ^{18}O$ is observed, with the $\delta^{13}C$ and $\delta\ ^{18}O$ values declining from the SPF stromatolites (2.3 to 3.8 ‰), to marine sedimentary carbonates (1.0 to 1.9 ‰) and then to interstitial carbonates (0.0 to 1.0 ‰). The most positive $\delta\ ^{13}C$ values of the SPF stromatolites were explained by the biological preference of the lighter isotope ^{12}C in anoxygenic photosynthesis, indicating a photic shallow marine environment that was favorable for microbial organisms. The decreasing covariation between $\delta\ ^{13}C$ and $\delta\ ^{18}O$ was likely caused by a mixture of the isotopically lighter shallow seawater and isotopically heavier mantle carbon flux (ca. -6 ‰, Hayes and Waldbauer, 2006) derived from degassing of CO_2 during eruption and alteration of basaltic crust, or isotopic exchange during hydrothermal overprinting, in accordance with Lindsay et al. (2005). Therefore, the $\delta\ ^{13}C$ value of ~ 0‰ essentially reflects a balance between the carbon sources (atmosphere and mantle) and the carbon sinks (organic carbon and carbonate).

Comparatively, hydrothermal flux via a large-scale interaction between seawater and seafloor basalts was likely a major control on ocean geochemistry in the early Archean (Veizer et al., 1982). There were extensive hydrothermal activities, with evidence of omnipresent sediments in the three greenstone belts, such as cherts, BIFs and carbonates, that formations were explained by the chemical reactions between hydrothermal fluids and

seawater (Dymek and Klein, 1988; Veizer et al., 1989a, b; Bau and Dulski, 1996; Van Kranendonk et al. 2003; Van den Boorn et al., 2007; Allwood et al., 2010; Shibuya et al., 2010; Ledevin et al., 2014; Westall et al., 2015; Nutman et al, 2019a; Hickman-Lewis et al., 2020; Viehmann et al., 2020; Rouillard et al., 2021). The widespread hydrothermal inputs left footprints in the REE+Y abundance of marine authigenic sediments, with the pronounced, positive Eu_{SN} anomalies generally regarded as a diagnostic indicator for hydrothermal fluids under reducing conditions (Sverjensky, 1984; Bau, 1991, 1993; Bilal, 1991; Bau and Dulski, 1996, 1999). According to the PAAS-normalized REE+Y pattern of the SPF stromatolites, Van Kranendonk et al. (2003) suggested a characteristic pattern for shallow seawater in the early Archean, including the smooth LREE depletion, positive La and Y anomalies, and a positive Eu anomaly indicating the hydrothermal component, which has been applied in subsequent studies (Allwood et al., 2010; Nutman et al, 2019a, b; Hickman-Lewis et al., 2020; Viehmann et al., 2020; herein). Nevertheless, the LREE-to-HREE depletion still exists in our seawater endmember when normalized to PM, but it is eliminated in other carbonates (Fig.8c). It may be explained by the preferential uptake of the LREEs over the HREEs in calcite at high dissolved REE and CO_3^{2-} concentrations (Zhong and Mucci 1995; Smrzka et al., 2019), or LREEs preferentially adsorbed by particulate organic carbon when the HREEs form more stable dissolved carbonate complexes in solution (Cantrell and Byrne 1987; Hathorne et al. 2015). In addition, the SPF stromatolites and many sedimentary carbonates commonly have higher Y/Ho ratios (> 45) and relative high Y/Y* anomalies (Van Kranendonk et al., 2003; Allwood et al., 2010; Viehmann et al., 2020; herein). Although as a geochemical twin to Ho, Y behaves conservatively during mixing of high-temperature hydrothermal fluids and seawater, whereas Ho (as well as other REEs) is scavenged by particulate matter or iron (oxy)hydroxides (Nozaki et al. 1997; Bau 1999; Bau and Dulski, 1999; Smrzka et al., 2019). As a consequence, the super-chondritic Y/Ho ratios and strongly positive Y/Y* anomalies in the reported SPF stromatolites and some sedimentary carbonates indicate the strong fractionation between Y and Ho caused by the preferential removal by particulate matter or iron (oxy)hydroxides. However, the near-chondritic Y/Ho ratios and slightly positive Y/Y* anomalies in some sedimentary carbonates, all interstitial carbonates and fracture-filling calcites are ascribed to the absence of iron (oxy)hydroxides (Fe and Mn are mainly in the carbonate lattice) (Fig.5a and b). In addition to acting as a predominant REE +Y input, hydrothermal fluids exported abundant elements (Ca, Mg, Fe, Mn, Si, and many trace elements) to the ocean, and these processes were recorded in enrichment of those elements in the various EPT carbonates and pervasive chert cements or units. The anoxic Archean ocean guaranteed them solubility and easily accessibility, acting as significant metal nutrients for early life.

However, more caution should be exercised when extrapolating the geochemical compositions of some samples to a global scale. Carbonates can only record the geochemical compositions of ambient fluids, and are therefore most representative for regional water columns. The differences in the REE+Y patterns and carbon isotopic compositions of the EPT carbonates demonstrate the diverse depositional environments, where inputs and outputs can greatly influence the geochemical compositions of local waters. Nonetheless, D-2-W can be temporarily used as the seawater endmember at 3.5 Ga until a better choice is provided in the

future. It reflects a shallow marine environment where anoxygenic photosynthesis likely flourished during the interval of volcanic and hydrothermal activities. Encouraging more researches on ancient carbonates of various facies and potential depositional environments is necessary for a comprehensive understanding of the geochemical cycles and compositional evolution of seawater, especially with respect to Sr isotopic composition.

Conclusion

The carbonate minerals occur in the East Pilbara Terrane, Western Australia, in a variety of facies, including interstitial carbonate between pillow basalts, sedimentary carbonate and stromatolite. The high spatial resolution geochemical features, such as the abundances of major and trace elements, REE+Y patterns, and isotopic compositions of stable C, O and radiogenic Sr, support the interpretation that the EPT carbonates are important archives for reconstructing environments on Early Earth.

(1) The fracture-filling calcite D-2-W from the Middle Basalt Member of Dresser Formation (3.48 Ga) can act as a proxy for the Paleoarchean shallow seawater, characterized by the high Sr concentration of 1789 ppm, the $\delta^{13}C$ value of +2.20 ‰, the $\delta^{18}O_{VPDB}$ value of -13.03‰, the age-corrected $^{87}Sr/^{86}Sr$ ratio of 0.700596, low REE+Y concentration, near-chondritic Y/Ho weight-ratio, and the PAAS-normalized REE+Y patterns with features of LREE depletion, absence of Ce_{SN} and Eu_{SN} anomalies but positive La_{SN} and Y_{SN} anomalies. This indicates a shallow marine environment where anoxygenic photosynthesis likely flourished during the interval of volcanic and hydrothermal activities.

(2) The EPT interstitial carbonates are good proxies for Paleoarchean seafloor hydrothermal systems where the hydrothermal fluids are derived from the interaction between basaltic oceanic crust and seawater. The best archive for the low-temperature hydrothermal system is preserved in Apex Basalt (3.46 Ga) as acicular crystal-fan calcite, showing the trace element enrichments of basaltic origin (Mg, Fe, Mn, Al, Sc, Ti, V, Rb, Mo, and U), lower Sr concentration (119 ±17 ppm), the hybrid isotopic compositions of C (mean $\delta^{13}C$= + 0.63 ± 0.12 ‰) and Sr (mean $^{87}Sr/^{86}Sr$ = 0.703094 ± 0.000979) that are intermediate between seawater and basalt, higher REY concentration plus near-chondritic Y/Ho weight-ratio, and the PAAS-normalized REE+Y pattern characterized by LREE depletion, no Ce anomaly, but positive La, Gd, Eu and Y anomalies.

(3) Two post-depositional alterations are recognized for interstitial carbonates, namely recrystallization and dolomitization, and the multi-element behaviors during alteration are source-dependent. For example, recrystallization is commonly induced by alteration fluids similar to the parent fluid, such as the low-temperature hydrothermal fluid or seawater in this study. It slightly deviates the original geochemical compositions towards those of alteration fluids, but has less influence on the normalized REE+Y pattern and the $\delta^{13}C$ value. However, dolomitization is triggered by the high-temperature hydrothermal fluids, usually leading to dissolution and neomorphism. It shows highly elevated element abundance of basaltic origin, a variant PAAS- and PM-normalized REE+Y pattern with MREE enrichment, a strong

positive Eu_{SN} anomaly, and a largely increased $^{87}Sr/^{86}Sr$ ratio, yet consistent $\delta^{13}C$. Applications to sedimentary carbonates and stromatolites imply that they still retain some primary signatures, even although they suffer from later hydrothermal alteration to some degree.

Acknowledgements

We would like to acknowledge the contributions of Axel Hackmann and Wolfgang Dröse at the University of Göttingen for their preliminary preparation of the samples. We are also grateful for the assistance provided by Dr. Dirk Hoffmann, Brigitte Dietrich, Dr. Volker Karius, and Nils Meßling, all from the University of Göttingen, in sample solution preparation, purification, and geochemical data acquisition and analysis. We also thank Dr. Jakub Surma and Oliver Jäger for their valuable discussions on triple oxygen isotopes, which greatly benefited this study. Finally, we acknowledge the financial support of the China Council Scholarship (CSC) and SPP1833 (DFG-Schwerpunktprogramm) "Building a Habitable Earth"

References

Alexander, B. W., Bau, M., Andersson, P., and Dulski, P.: Continentally-derived solutes in shallow Pilbara seawater: rare earth element and Nd isotope evidence in iron formation from the 2.9 Ga Pongola Supergroup, South Africa, Geochimica et Cosmochimica Acta, 72, 378–394, 2008.

Alibo, D. S. and Nozaki, Y.: Rare earth elements in seawater: particle association, shale-normalization, and Ce oxidation, Geochimica et Cosmochimica Acta, 63, 363–372, 1999.

Allwood, A. C., Walter, M. R., Kamber, B. S., Marshall, C. P., and Burch, I. W.: Stromatolite reef from the Early Archaean era of Australia, Nature, 441, 714–718, 2006a.

Allwood, A. C., Walter, M. R., and Marshall, C. P.: Raman spectroscopy reveals thermal palaeoenvironments of ca. 3.5 billion-year-old organic matter, Vibrational Spectroscopy, 41, 190–197, 2006b.

Allwood, A. C., Walter, M. R., Burch, I. W., and Kamber, B. S.: 3.43 billion-year-old stromatolite reef from the Pilbara Craton of Western Australia: ecosystem-scale insights to early life on Earth, Precambrian Research, 158, 198–227, 2007.

Allwood, A. C., Kamber, B. S., Walter, M. R., Burch, I. W., and Kanik, I.: Trace elements record depositional history of an Early Archean stromatolitic carbonate platform, Chemical Geology, 270, 148–163, 2010.

Alt, J. C. and Teagle, D. A.: The uptake of carbon during alteration of ocean crust, Geochimica et Cosmochimica Acta, 63, 1527–1535, 1999.

Arndt, N.: Why was flood volcanism on submerged continental platforms so common in the Precambrian?, Precambrian Research, 97, 155–164, 1999.

Arndt, N., Bruzak, G., and Reischmann, T.: The oldest continental and oceanic plateaus: Geochemistry of basalts and komatiites of the Pilbara Craton, Australia, in: Mantle plumes: their identification through time, 352–359, Geological Society of America, https://doi.org/10.1130/0-8137-2352-3.359, 2001.

Banner, J. L. and Hanson, G. N.: Calculation of simultaneous isotopic and trace element variations during water-rock interaction with applications to carbonate diagenesis, Geochimica et Cosmochimica Acta, 54, 3123–3137, 1990.

Banner, J. L., Hanson, G., and Meyers, W.: Rare earth element and Nd isotopic variations in regionally extensive dolomites from the Burlington-Keokuk Formation (Mississippian); implications for REE mobility during carbonate diagenesis, Journal of Sedimentary Research, 58, 415–432, 1988.

Barley, M., Sylvester, G., Groves, D., Borley, G., and Rogers, N.: Archaean calc-alkaline volcanism in the Pilbara Block, Western Australia, Precambrian Research, 24, 285–319, 1984.

Barley, M.: Volcanic, sedimentary and tectonostratigraphic environments of the 3.46 Ga Warrawoona Megasequence: a review, Precambrian Research, 60, 47–67, 1993.

Bathurst, R. G.: Carbonate sediments and their diagenesis, Elsevier, Amsterdam, 1975.

Bau, M.: Rare-earth element mobility during hydrothermal and metamorphic fluid-rock interaction and the significance of the oxidation state of europium, Chemical Geology, 93, 219–230, 1991.

Bau, M.: Effects of syn-and post-depositional processes on the rare-earth element distribution in Precambrian iron-formations, European Journal of Mineralogy, pp. 257–268, 1993.

Bau, M.: Controls on the fractionation of isovalent trace elements in magmatic and aqueous systems: evidence from Y/Ho, Zr/Hf, and lanthanide tetrad effect, Contributions to Mineralogy and Petrology, 123, 323–333, 1996.

Bau, M. and Dulski, P.: Distribution of yttrium and rare-earth elements in the Penge and Kuruman iron-formations, Transvaal Supergroup, South Africa, Precambrian Research, 79, 37–55, 1996.

Bau, M. and Dulski, P.: Comparing yttrium and rare earths in hydrothermal fluids from the Mid-Atlantic Ridge: implications for Y and REE behaviour during near-vent mixing and for the Y/Ho ratio of Proterozoic seawater, Chemical Geology, 155, 77–90, 1999.

Bau, M., Möller, P., and Dulski, P.: Yttrium and lanthanides in eastern Mediterranean seawater and their fractionation during redox-cycling, Marine Chemistry, 56, 123–131, 1997.

Bau, M., Balan, S., Schmidt, K., and Koschinsky, A.: Rare earth elements in mussel shells of the Mytilidae family as tracers for hidden and fossil high-temperature hydrothermal systems, Earth and Planetary Science Letters, 299, 310–316, 2010.

Bickle, M., Bettenay, L., Barley, M., Chapman, H., Groves, D., Campbell, I., and De Laeter, J.: A 3500 Ma plutonic and volcanic calc-alkaline province in the Archaean East Pilbara Block, Contributions to Mineralogy and Petrology, 84, 25–35, 1983.

Bickle, M., Bettenay, L., Chapman, H. J., Groves, D., McNaughton, N., Campbell, I., and De Laeter, J.: Origin of the 3500-3300 Ma calc-alkaline rocks in the Pilbara Archaean: isotopic and geochemical constraints from the Shaw Batholith, Precambrian Research, 60, 117–149, 1993.

Bilal, B.: Thermodynamic study of Eu^{3+}/Eu^{2+} redox reaction in aqueous solutions at elevated temperatures and pressures by means of cyclic voltammetry, Zeitschrift für Naturforschung A, 46, 1108–1116, 1991.

Boelrijk, N.: A general formula for “double” isotope dilution analysis, Chemical Geology, 3, 323–325, 1968.

Bolhar, R., Van Kranendonk, M. J., and Kamber, B. S.: A trace element study of siderite–jasper banded iron formation in the 3.45 Ga Warrawoona Group, Pilbara Craton—formation from hydrothermal fluids and shallow seawater, Precambrian Research, 137, 93–114, 2005.

Bontognali, T. R., Sessions, A. L., Allwood, A. C., Fischer, W. W., Grotzinger, J. P., Summons, R. E., and Eiler, J. M.: Sulfur isotopes of organic matter preserved in 3.45-billion-year-old stromatolites reveal microbial metabolism, Proceedings of the National Academy of Sciences, 109, 15 146–15 151, 2012.

Buick, R. and Barnes, K.: Cherts in the Warrawoona Group: Early Archaean silicified sediments deposited in shallow-water environments, in: Archaean and Proterozoic Basins of the Pilbara, Western Australia: Evolution and Mineralization Potential, edited by Muhling, J., Groves, D., and Blake, T., p. 3753, The Geology Department and University Extension, University of Western Australia, publication 9 edn., 1984.

Buick, R. and Dunlop, J.: Evaporitic sediments of early Archaean age from the Warrawoona Group, North Pole, Western Australia, Sedimentology, 37, 247–277, 1990.

Buick, R., Thornett, J., McNaughton, N., Smith, J., Barley, M., and Savage, M.: Record of emergent continental crust 3.5 billion years ago in the Pilbara Craton of Australia, Nature, 375, 574–577, 1995.

Buick, R., Brauhart, C., Morant, P., Thornett, J., Maniw, J., Archibald, N., Doepel, M., Fletcher, I., Pickard, A., Smith, J., et al.: Geochronology and stratigraphic relationships of the Sulphur Springs Group and Strelley Granite: a temporally distinct igneous province in the Archaean Pilbara Craton, Australia, Precambrian Research, 114, 87–120, 2002.

Burke, W., Denison, R., Hetherington, E., Koepnick, R., Nelson, H., and Otto, J.: Variation of seawater 87Sr/86Sr throughout Phanerozoic time, Geology, 10, 516–519, 1982.

Byerly, G. R., Lowe, D. R., Wooden, J. L., and Xie, X.: An Archean impact layer from the Pilbara and Kaapvaal cratons, Science, 297, 1325–1327, 2002.

Cantrell, K. J. and Byrne, R. H.: Rare earth element complexation by carbonate and oxalate ions, Geochimica et Cosmochimica Acta, 51, 597–605, 1987.

Carpenter, S. J. and Lohmann, K. C.: SrMg ratios of modern marine calcite: Empirical indicators of ocean chemistry and precipitation rate, Geochimica et Cosmochimica Acta, 56, 1837–1849, 1992.

Caruso, S., Van Kranendonk, M. J., Baumgartner, R. J., Fiorentini, M. L., and Forster, M. A.: The role of magmatic fluids in the ~3.48 Ga Dresser Caldera, Pilbara Craton: New insights from the geochemical investigation of hydrothermal alteration, Precambrian Research, 362, 106 299, 2021.

Catling, D. C. and Zahnle, K. J.: The Archean atmosphere, Science advances, 6, eaax1420, 2020.

Champion, D. C. and Smithies, R. H.: Geochemistry of Paleoarchean granites of the East Pilbara terrane, Pilbara craton, Western Australia: implications for Early Archean crustal growth, Developments in Precambrian geology, 15, 369–409, 2007.

Chen, X., Zhou, Y., and Shields, G. A.: Progress towards an improved Precambrian seawater 87Sr/86Sr curve, Earth-Science Reviews, 224, 103 869, 2022.

Chester, R.: Marine geochemistry, John Wiley & Sons, 2009.

Coggon, R. M., Teagle, D. A., Cooper, M. J., and Vanko, D. A.: Linking basement carbonate vein compositions to porewater geochemistry across the eastern flank of the Juan de Fuca Ridge, ODP Leg 168, Earth and Planetary Science Letters, 219, 111–128, 2004.

Coogan, L. A. and Gillis, K. M.: Low-temperature alteration of the seafloor: impacts on ocean chemistry, Annual Review of Earth and Planetary Sciences, 46, 21–45, 2018.

Davis, A. C., Bickle, M. J., and Teagle, D. A.: Imbalance in the oceanic strontium budget, Earth and Planetary Science Letters, 211, 173–187, 2003.

Djokic, T., Van Kranendonk, M. J., Campbell, K. A., Walter, M. R., and Ward, C. R.: Earliest signs of life on land preserved in ca. 3.5 Ga hot spring deposits, Nature communications, 8, 15 263, 2017.

Djokic, T., Van Kranendonk, M. J., Campbell, K. A., Havig, J. R., Walter, M. R., and Guido, D. M.: A reconstructed subaerial hot spring field in the 3.5 billion-year-old Dresser Formation, North Pole Dome, Pilbara Craton, Western Australia, Astrobiology, 21, 1–38, 2021.

Dulski, P.: Reference materials for geochemical studies: New analytical data by ICP-MS and critical discussion of reference values, Geostandards Newsletter, 25, 87–125, 2001.

Dymek, R. F., BROTHERS, S. C., and SCHIFFRIES, C. M.: Petrogenesis of ultramafic metamorphic rocks from the 3800 Ma Isua supracrustal belt, West Greenland, Journal of Petrology, 29, 1353–1397, 1988.

Endo, Y., Ueno, Y., Aoyama, S., and Danielache, S. O.: Sulfur isotope fractionation by broadband UV radiation to optically thin SO_2 under reducing atmosphere, Earth and Planetary Science Letters, 453, 9–22, 2016.

Fantle, M. S., Barnes, B. D., and Lau, K. V.: The role of diagenesis in shaping the geochemistry of the marine carbonate record, Annual Review of Earth and Planetary Sciences, 48, 549–583, 2020.

Farquhar, J., Savarino, J., Airieau, S., and Thiemens, M. H.: Observation of wavelength-sensitive mass-independent sulfur isotope effects during SO_2 photolysis: Implications for the early atmosphere, Journal of Geophysical Research: Planets, 106, 32 829–32 839, 2001.

Fischer, R. and Gerya, T.: Early Earth plume-lid tectonics: A high-resolution 3D numerical modelling approach, Journal of Geodynamics, 100, 198–214, 2016.

Flament, N., Coltice, N., and Rey, P. F.: The evolution of the $^{87}Sr/^{86}Sr$ of marine carbonates does not

constrain continental growth, Precambrian Research, 229, 177–188, 2013.
Flügel, E. and Munnecke, A.: Microfacies of carbonate rocks: analysis, interpretation and application, vol. 976, Springer, second edn., 2010.
Gardiner, N. J., Wacey, D., Kirkland, C. L., Johnson, T. E., and Jeon, H.: Zircon U–Pb, Lu–Hf and O isotopes from the 3414 Ma Strelley Pool Formation, East Pilbara Terrane, and the Palaeoarchaean emergence of a cryptic cratonic core, Precambrian Research, 321, 64–84, https://doi.org/10.1016/j.precamres.2018.11.023, 2019.
German, C. R. and Lin, J.: The thermal structure of the ocean crust, ridge spreading and hydrothermal circulation: How well do we understand their inter-connections, In: German CR, Lin J, and Parsons LM (eds.) Mid-Ocean Ridges: Hydrothermal Interactions between the Lithosphere and Ocean, Geophysical Monograph Series, 148, pp. 1–19, Washington, DC: American Geophysical Union, 2004.
German, C. R. and Seyfried, W.: 8.7 - Hydrothermal Processes, in: Treatise on Geochemistry, edited by Holland, H. D. and Turekian, K. K., vol. 6, chap. 8.7, pp. 191–233, Elsevier, Oxford, second edition edn., https://doi.org/http://dx.doi.org/10.1016/B978-0-08-095975- 7.00607-0, 2014.
Glikson, A. Y. and Hickman, A. H.: Geochemistry of Archaean volcanic successions, eastern Pilbara Block western Australia, Australian Bureau of Mineral Resources, Geology and Geophysics. Record 1981/36, 56p, 1981.
Groves, D. I., Dunlop, J. S. R., and Buick, R.: An Early Habitat of Life, Scientific American, 245, 64–73, http://www.jstor.org/stable/ 24964579, 1981.
GSWA: Compilation of Geochronology Data, June 2006 Update. Geological Survey of Western Australia on compact disc, 2006.
Harris, A. C., White, N. C., McPhie, J., Bull, S. W., Line, M. A., Skrzeczynski, R., Mernagh, T. P., and Tosdal, R. M.: Early Archean hot springs above epithermal veins, North Pole, Western Australia: new insights from fluid inclusion microanalysis, Economic Geology, 104, 793–814, https://doi.org/10.2113/gsecongeo.104.6.793, 2009.
Hathorne, E. C., Stichel, T., Brück, B., and Frank, M.: Rare earth element distribution in the Atlantic sector of the Southern Ocean: The balance between particle scavenging and vertical supply, Marine Chemistry, 177, 157–171, https://doi.org/10.1016/j.marchem.2015.03.011, 2015.
Hayes, J. M. and Waldbauer, J. R.: The carbon cycle and associated redox processes through time, Philosophical Transactions of the Royal Society B: Biological Sciences, 361, 931–950, https://doi.org/10.1098/rstb.2006.1840, 2006.
Henderson, P.: General geochemical properties and abundances of the rare earth elements, in: Developments in geochemistry, vol. 2, pp. 1–32, Elsevier, 1984.
Hickman, A. H.: Geology of the Pilbara Block and its environments, Western Australia Geological Survey, Bulletin 127, 1983.
Hickman, A.: Archaean diapirism in the Pilbara block, Western Australia, in: Kröner, A., Greiling, R. (Eds.), Precambrian tectonics illustrated, Stuttgart, pp. 113–127, 1984.
Hickman, A.: Regional review of the 3426–3350 Ma Strelley Pool Formation, Pilbara Craton, Western Australia, Geological Survey of Western Australia, Record 2008/15, 27 p, 2008.
Hickman, A. H. and Van Kranendonk, M. J.: Diapiric processes in the formation of Archaean continental crust, East Pilbara granite- greenstone terrane, Australia, in: The Precambrian Earth: tempos and events, edited by Eriksson, P.G., Altermann, W., Nelson, D.R., Mueller, W.U., Catuneau, O., vol. 12, pp. 118–139, Elsevier Amsterdam, 2004.

Hickman, A. H. and Van Kranendonk, M.: A Billion Years of Earth History: A Geological Transect Through the Pilbara Craton and the Mount Bruce Supergroup-a Field Guide to Accompany 34th IGC Excursion WA-2, Geological Survey of Western Australia, Record 2012/10, 2012a.

Hickman, A. H. and Van Kranendonk, M. J.: Early Earth evolution: evidence from the 3.5–1.8 Ga geological history of the Pilbara region of Western Australia, Episodes Journal of International Geoscience, 35, 283–297, https://doi.org/10.18814/epiiugs/2012/v35i1/028, 2012b.

Hickman-Lewis, K., Gourcerol, B., Westall, F., Manzini, D., and Cavalazzi, B.: Reconstructing Palaeoarchaean microbial biomes flourishing in the presence of emergent landmasses using trace and rare earth element systematics, Precambrian Research, 342, 105 689, https://doi.org/10.1016/j.precamres.2020.105689, 2020.

Hofmann, H., Grey, K., Hickman, A., and Thorpe, R.: Origin of 3.45 Ga coniform stromatolites in Warrawoona group, Western Australia, Geological Society of America Bulletin, 111, 1256–1262, https://doi.org/10.1130/0016-7606(1999)111<1256:OOGCSI>2.3.CO;2, 1999.

Hongo, Y. and Nozaki, Y.: Rare earth element geochemistry of hydrothermal deposits and Calyptogena shell from the Iheya Ridge vent field, Okinawa Trough, Geochemical journal, 35, 347–354, https://doi.org/10.2343/geochemj.35.347, 2001.

Huston, D. L., Morant, P., Pirajno, F., Cummins, B., Baker, D., and Mernagh, T. P.: Paleoarchean mineral deposits of the Pilbara Craton: genesis, tectonic environment and comparisons with younger deposits, Developments in Precambrian Geology, 15, 411–450, https://doi.org/10.1016/S0166-2635(07)15044-1, 2007.

Jaffrés, J. B., Shields, G. A., and Wallmann, K.: The oxygen isotope evolution of seawater: A critical review of a long-standing controversy and an improved geological water cycle model for the past 3.4 billion years, Earth-Science Reviews, 83, 83–122, https://doi.org/10.1016/j.earscirev.2007.04.002, 2007.

James, R., Elderfield, H., and Palmer, M.: The chemistry of hydrothermal fluids from the Broken Spur site, 29 N Mid-Atlantic Ridge, Geochimica et Cosmochimica Acta, 59, 651–659, https://doi.org/10.1016/0016-7037(95)00003-I, 1995.

Jenner, F., Bennett, V., Nutman, A., Friend, C., Norman, M., and Yaxley, G.: Evidence for subduction at 3.8 Ga: geo- chemistry of arc-like metabasalts from the southern edge of the Isua Supracrustal Belt, Chemical Geology, 261, 83–98, https://doi.org/10.1016/j.chemgeo.2008.09.016, 2009.

Jochum, K. P., Nohl, U., Herwig, K., Lammel, E., Stoll, B., and Hofmann, A. W.: GeoReM: a new geochemical database for reference materi- als and isotopic standards, Geostandards and Geoanalytical Research, 29, 333–338, https://doi.org/10.1111/j.1751-908X.2005.tb00904.x, 2005.

Johannesson, K. H., Hawkins Jr, D. L., and Cortés, A.: Do Archean chemical sediments record ancient seawater rare earth element patterns?, Geochimica et Cosmochimica Acta, 70, 871–890, https://doi.org/10.1016/j.gca.2005.10.013, 2006.

Johnson, T. E., Brown, M., Gardiner, N. J., Kirkland, C. L., and Smithies, R. H.: Earth's first stable continents did not form by subduction, Nature, 543, 239–242, https://doi.org/10.1038/nature21383, 2017.

Kamber, B. S. and Webb, G. E.: The geochemistry of late Archaean microbial carbonate: implications for ocean chemistry and continental erosion history, Geochimica et Cosmochimica Acta, 65, 2509–2525, https://doi.org/10.1016/S0016-7037(01)00613-5, 2001.

Kamber, B. S., Greig, A., and Collerson, K. D.: A new estimate for the composition of weathered young upper continental crust from alluvial sediments, Queensland, Australia, Geochimica et

Cosmochimica Acta, 69, 1041–1058, https://doi.org/10.1016/j.gca.2004.08.020, 2005.
Kato, Y. and Nakamura, K.: Origin and global tectonic significance of Early Archean cherts from the Marble Bar greenstone belt, Pilbara Craton, Western Australia, Precambrian Research, 125, 191–243, https://doi.org/10.1016/S0301-9268(03)00043-3, 2003.
Kitajima, K., Maruyama, S., Utsunomiya, S., and Liou, J.: Seafloor hydrothermal alteration at an Archaean mid-ocean ridge, Journal of Metamorphic Geology, 19, 583–599, https://doi.org/10.1046/j.0263-4929.2001.00330.x, 2001.
Klinkhammer, G., Elderfield, H., Edmond, J., and Mitra, A.: Geochemical implications of rare earth element patterns in hydrothermal fluids from mid-ocean ridges, Geochimica et Cosmochimica Acta, 58, 5105–5113, https://doi.org/10.1016/0016-7037(94)90297-6, 1994.
Kroopnick, P.: The distribution of 13C in the Atlantic Ocean, Earth and Planetary Science Letters, 49, 469–484, https://doi.org/10.1016/0012- 821X(80)90088-6, 1980.
Kump, L. R. and Barley, M. E.: Increased subaerial volcanism and the rise of atmospheric oxygen 2.5 billion years ago, Nature, 448, 1033– 1036, https://doi.org/10.1038/nature06058, 2007.
Lambert, I., Donnelly, T., Dunlop, J., Groves, and DI: Stable isotopic compositions of early Archaean sulphate deposits of probable evaporitic and volcanogenic origins, Nature, 276, 808–811, https://doi.org/10.1038/276808a0, 1978.
Lawrence, M. G., Greig, A., Collerson, K. D., and Kamber, B. S.: Rare earth element and yttrium variability in South East Queensland waterways, Aquatic Geochemistry, 12, 39–72, https://doi.org/10.1007/s10498-005-4471-8, 2006.
Lebrato, M., Garbe-Schönberg, D., Müller, M. N., Blanco-Ameijeiras, S., Feely, R. A., Lorenzoni, L., Molinero, J.-C., Bremer, K., Jones, D. O., Iglesias-Rodriguez, D., et al.: Global variability in seawater Mg: Ca and Sr: Ca ratios in the modern ocean, Proceedings of the National Academy of Sciences, 117, 22 281–22 292, https://doi.org/10.1073/pnas.1918943117, 2020.
Ledevin, M., Arndt, N., Simionovici, A., Jaillard, E., and Ulrich, M.: Silica precipitation triggered by clastic sedimentation in the Archean: new petrographic evidence from cherts of the Kromberg type section, South Africa, Precambrian Research, 255, 316–334, https://doi.org/10.1016/j.precamres.2014.10.009, 2014.
Lindsay, J., Brasier, M., McLoughlin, N., Green, O., Fogel, M., Steele, A., and Mertzman, S.: The problem of deep carbon—an Archean paradox, Precambrian Research, 143, 1–22, https://doi.org/10.1016/j.precamres.2005.09.003, 2005.
Ling, H.-F., Chen, X., Li, D., Wang, D., Shields-Zhou, G. A., and Zhu, M.: Cerium anomaly variations in Ediacaran–earliest Cambrian carbonates from the Yangtze Gorges area, South China: implications for oxygenation of coeval shallow seawater, Precambrian Research, 225, 110–127, https://doi.org/10.1016/j.precamres.2011.10.011, 2013.
Lowe, D. R.: Restricted shallow-water sedimentation of Early Archean stromatolitic and evaporitic strata of the Strelley Pool Chert, Pilbara Block, Western Australia, Precambrian Research, 19, 239–283, https://doi.org/10.1016/0301-9268(83)90016-5, 1983.
Lowe, D. R. and Byerly, G. R.: Early Archean silicate spherules of probable impact origin, South Africa and Western Australia, Geology, 14, 83–86, https://doi.org/10.1130/0091-7613(1986)14<83:EASSOP>2.0.CO;2, 1986.
McCulloch, M. T.: Primitive $^{87}Sr/^{86}Sr$ from an Archean barite and conjecture on the Earth's age and origin, Earth and planetary science letters, 126, 1–13, https://doi.org/10.1016/0012-821X(94)90238-0, 1994.

McNaughton, N., Compston, W., and Barley, M.: Constraints on the age of the Warrawoona Group, eastern Pilbara block, Western Australia, Precambrian Research, 60, 69–98, https://doi.org/10.1016/0301-9268(93)90045-4, 1993.

Nakamura, H., Sano, A., Kagami, S., Yokoyama, T., Ishikawa, A., Komiya, T., and Iwamori, H.: Compositional heterogeneity of Archean mantle estimated from Sr and Nd isotopic systematics of basaltic rocks from North Pole, Australia, and the Isua supracrustal belt, Greenland, Precambrian Research, 347, 105 803, https://doi.org/10.1016/j.precamres.2020.105803, 2020.

Nakamura, K. and Kato, Y.: Carbonate minerals in the Warrawoona Group, Pilbara Craton: Implications for continental crust, life, and global carbon cycle in the Early Archean, Resource Geology, 52, 91–100, https://doi.org/10.1111/j.1751-3928.2002.tb00122.x, 2002.

Nakamura, K. and Kato, Y.: Carbonatization of oceanic crust by the seafloor hydrothermal activity and its significance as a CO2 sink in the Early Archean, Geochimica et Cosmochimica Acta, 68, 4595–4618, https://doi.org/10.1016/j.gca.2004.05.023, 2004.

Nielsen, S. G., Rehkämper, M., Teagle, D. A., Butterfield, D. A., Alt, J. C., and Halliday, A. N.: Hydrothermal fluid fluxes cal- culated from the isotopic mass balance of thallium in the ocean crust, Earth and Planetary Science Letters, 251, 120–133, https://doi.org/10.1016/j.epsl.2006.09.002, 2006.

Nijman, W., de Bruijne, K. C. H., and Valkering, M. E.: Growth fault control of Early Archaean cherts, barite mounds and chert- barite veins, North Pole Dome, Eastern Pilbara, Western Australia, Precambrian Research, 95, 247–274, https://doi.org/10.1016/S0301- 9268(99)00014-5, 1999.

Nothdurft, L. D., Webb, G. E., and Kamber, B. S.: Rare earth element geochemistry of Late Devonian reefal carbonates, Canning Basin, Western Australia: confirmation of a seawater REE proxy in ancient limestones, Geochimica et Cosmochimica Acta, 68, 263–283, https://doi.org/10.1016/S0016-7037(03)00422-8, 2004.

Nozaki, Y., Zhang, J., and Amakawa, H.: The fractionation between Y and Ho in the marine environment, Earth and Planetary Science Letters, 148, 329–340, https://doi.org/10.1016/S0012-821X(97)00034-4, 1997.

Nutman, A. P., Bennett, V. C., Friend, C. R., Van Kranendonk, M. J., and Chivas, A. R.: Rapid emergence of life shown by discovery of 3,700-million-year-old microbial structures, Nature, 537, 535–538, https://doi.org/10.1038/nature19355, 2016.

Nutman, A. P., Friend, C. R., Bennett, V. C., Van Kranendonk, M., and Chivas, A. R.: Reconstruction of a 3700 Ma transgressive marine environment from Isua (Greenland): Sedimentology, stratigraphy and geochemical signatures, Lithos, 346, 105164, https://doi.org/10.1016/j.lithos.2019.105164, 2019a.

Nutman, A. P., Bennett, V. C., Friend, C. R., Van Kranendonk, M. J., Rothacker, L., and Chivas, A. R.: Cross-examining Earth's oldest stromatolites: Seeing through the effects of heterogeneous deformation, metamorphism and metasomatism affecting Isua (Greenland) 3700 Ma sedimentary rocks, Precambrian Research, 331, 105 347, https://doi.org/10.1016/j.precamres.2019.105347, 2019b.

Ohno, T. and Hirata, T.: Simultaneous determination of mass-dependent isotopic fractionation and radiogenic isotope variation of strontium in geochemical samples by multiple collector-ICP-mass spectrometry, Analytical Sciences, 23, 1275–1280, https://doi.org/10.2116/analsci.23.1275, 2007.

Palme, H. and O'Neill, H.: 3.1 Cosmochemical estimates of mantle composition, in: Treatise on Geochemistry: Oxford, pp. 1–39, Elsevier, 2nd edn.,

https://doi.org/http://dx.doi.org/10.1016/B978-0-08-095975-7.00201-1, 2014.

Parekh, P., Möller, P., Dulski, P., and Bausch, W.: Distribution of trace elements between carbonate and non-carbonate phases of limestone, Earth and Planetary Science Letters, 34, 39–50, https://doi.org/10.1016/0012-821X(77)90103-0, 1977.

Pavlov, A. and Kasting, J.: Mass-independent fractionation of sulfur isotopes in Archean sediments: strong evidence for an anoxic Archean atmosphere, Astrobiology, 2, 27–41, https://doi.org/10.1089/153110702753621321, 2002.

Pease, V., Percival, J., Smithies, H., Stevens, G., and Van Kranendonk, M.: When did plate tectonics begin? Evidence from the orogenic record, in: When did plate tectonics begin on planet Earth, edited by Condie, K. and Pease, V., vol. 440, pp. 199–228, Geological Society of America, 2008.

Piper, D. Z. and Bau, M.: Normalized rare earth elements in water, sediments, and wine: identifying sources and environmental redox conditions, American Journal of Analytical Chemistry, https://doi.org/10.4236/ajac.2013.410A1009, 2013.

Pirajno, F.: Ancient to modern earth: The role of mantle plumes in the making of continental crust, Developments in Precambrian Geology, 15, 1037–1064, https://doi.org/10.1016/S0166-2635(07)15083-0, 2007a.

Pirajno, F.: Mantle plumes, associated intraplate tectonomagmatic processes and ore systems, Episodes Journal of International Geoscience, 30, 6–19, https://doi.org/10.18814/epiiugs/2007/v30i1/003, 2007b.

Planavsky, N., Bekker, A., Rouxel, O. J., Kamber, B., Hofmann, A., Knudsen, A., and Lyons, T. W.: Rare earth element and yttrium com- positions of Archean and Paleoproterozoic Fe formations revisited: new perspectives on the significance and mechanisms of deposition, Geochimica et Cosmochimica Acta, 74, 6387–6405, https://doi.org/10.1016/j.gca.2010.07.021, 2010.

Potts, P. J., Thompson, M., Kane, J. S., Webb, P. C., and Carignan, J.: GEOPT6- An international proficiency test for analytical geochem- istry laboratories - report on round 6 (OU-3: Nanhoron microgranite) and 6A (Cal-s: CRPG limestone), International Association of Geoanalysts, 52, 2000.

Pourmand, A., Dauphas, N., and Ireland, T. J.: A novel extraction chromatography and MC-ICP-MS technique for rapid analysis of REE, Sc and Y: Revising CI-chondrite and Post-Archean Australian Shale (PAAS) abundances, Chemical Geology, 291, 38–54, https://doi.org/10.1016/j.chemgeo.2011.08.011, 2012.

Rasmussen, B., Fletcher, I. R., and Muhling, J. R.: In situ U–Pb dating and element mapping of three generations of monazite: unravelling cryptic tectonothermal events in low-grade terranes, Geochimica et Cosmochimica Acta, 71, 670–690, https://doi.org/10.1016/j.gca.2006.10.020, 2007.

Ravindran, A., Mezger, K., Balakrishnan, S., Kooijman, E., Schmitt, M., and Berndt, J.: Initial 87Sr/86Sr as a sensitive tracer of Archaean crust-mantle evolution: Constraints from igneous and sedimentary rocks in the western Dharwar Craton, India, Precambrian research, 337, 105 523, https://doi.org/10.1016/j.precamres.2019.105523, 2020.

Reitner, J., Wilmsen, M., and Neuweiler, F.: Cenomanian/Turonian sponge microbialite deep-water hardground community (Liencres, Northern Spain), Facies, 32, 203–212, https://doi.org/10.1007/BF02536869, 1995.

Retallack, G. J.: The oldest known paleosol profiles on Earth: 3.46 Ga Panorama Formation, western Australia, Palaeogeography, Palaeoclimatology, Palaeoecology, 489, 230–248, https://doi.org/10.1016/j.palaeo.2017.10.013, 2018.

Richter, F. M. and Liang, Y.: The rate and consequences of Sr diagenesis in deep-sea carbonates, Earth and Planetary Science Letters, 117, 553–565, https://doi.org/10.1016/0012-821X(93)90102-F, 1993.

Rimstidt, J. D., Balog, A., and Webb, J.: Distribution of trace elements between carbonate minerals and aqueous solutions, Geochimica et Cosmochimica Acta, 62, 1851–1863, https://doi.org/10.1016/S0016-7037(98)00125-2, 1998.

Roerdink, D. L., Ronen, Y., Strauss, H., and Mason, P. R.: Emergence of felsic crust and subaerial weathering recorded in Palaeoarchaean barite, Nature Geoscience, 15, 227–232, https://doi.org/10.1038/s41561-022-00902-9, 2022.

Rouillard, J., Van Kranendonk, M. J., Lalonde, S., Gong, J., and Van Zuilen, M. A.: Correlating trace element compositions, petrol- ogy, and Raman spectroscopy data in the 3.46 Ga Apex chert, Pilbara Craton, Australia, Precambrian Research, 366, 106415, https://doi.org/10.1016/j.precamres.2021.106415, 2021.

Runge, E. A., Duda, J.-P., Van Kranendonk, M. J., and Reitner, J.: Earth's oldest tsunami deposit? Early Archaean high-energy sediments in the ca 3.48 Ga Dresser Formation (Pilbara, Western Australia), The Depositional Record, 8, 590–602, https://doi.org/10.1002/dep2.175, 2022.

Sabau, A., Pipon, Y., Toulhoat, N., Lomenech, C., Jordan, N., Moncoffre, N., Barkleit, A., Marmier, N., Brendler, V., Surblé, S., et al.: Interaction of europium and nickel with calcite studied by Rutherford Backscattering Spectrometry and Time-Resolved Laser Fluorescence Spectroscopy, Nuclear Instruments and Methods in Physics Research Section B: Beam Interactions with Materials and Atoms, 332, 111– 116, https://doi.org/10.1016/j.nimb.2014.02.041, 2014.

Satkoski, A. M., Lowe, D. R., Beard, B. L., Coleman, M. L., and Johnson, C. M.: A high continental weathering flux into Pa- leoArchean seawater revealed by strontium isotope analysis of 3.26 Ga barite, Earth and Planetary Science Letters, 454, 28–35, https://doi.org/10.1016/j.epsl.2016.08.032, 2016.

Satkoski, A. M., Fralick, P., Beard, B. L., and Johnson, C. M.: Initiation of modern-style plate tectonics recorded in MesoArchean marine chemical sediments, Geochimica et Cosmochimica Acta, 209, 216–232, https://doi.org/10.1016/j.gca.2017.04.024, 2017.

Schier, K., Bau, M., Muenker, C., Beukes, N., and Viehmann, S.: Trace element and Nd isotope composition of shallow seawater prior to the Great Oxidation Event: Evidence from stromatolitic bioherms in the Paleoproterozoic Rooinekke and Nelani Formations, South Africa, Precambrian Research, 315, 92–102, https://doi.org/10.1016/j.precamres.2018.07.014, 2018.

Schmitt, R., Smith, R., Lasch, J., Mosen, A., Olehy, D., and Vasilevskis, J.: Abundances of the fourteen rare-earth elements, scandium, and yttrium in meteoritic and terrestrial matter, Geochimica et Cosmochimica Acta, 27, 577–622, https://doi.org/10.1016/0016-7037(63)90014-0, 1963.

Shackleton, N. J. and Kennett, J. P.: Paleotemperature history of the Cenozoic and the initiation of Antarctic glaciation: oxygen and carbon isotope analyses in DSDP Sites 277, 279, and 281, Initial Reports Deep Sea Drilling Project, 29, 743–755, 1975.

Shibuya, T., Komiya, T., Nakamura, K., Takai, K., and Maruyama, S.: Highly alkaline, high-temperature hydrothermal fluids in the early Archean ocean, Precambrian Research, 182, 230–238, https://doi.org/10.1016/j.precamres.2010.08.011, 2010.

Shibuya, T., Tahata, M., Kitajima, K., Ueno, Y., Komiya, T., Yamamoto, S., Igisu, M., Terabayashi, M., Sawaki, Y., Takai, K., et al.: Depth variation of carbon and oxygen isotopes of calcites in Archean altered upperoceanic crust: Implications for the CO_2 flux from ocean to oceanic crust in the

Archean, Earth and Planetary Science Letters, 321, 64–73, https://doi.org/10.1016/j.epsl.2011.12.034, 2012.

Shields, G. and Veizer, J.: Precambrian marine carbonate isotope database: Version 1.1, Geochemistry, Geophysics, Geosystems, 3, 1–of, https://doi.org/10.1029/2001GC000266, 2002.

Shields, G. A.: Implications of Carbonate and Chert Isotope Records for the Early Earth, in: Earth's Oldest Rocks, edited by Van Kranendonk, M., Bennett, V., and Hoffmann, J., pp. 901–912, Elsevier, 2019.

Sholkovitz, E. and Shen, G. T.: The incorporation of rare earth elements in modern coral, Geochimica et Cosmochimica Acta, 59, 2749–2756, https://doi.org/10.1016/0016-7037(95)00170-5, 1995.

Smith, J., Barley, M., Groves, D., Krapez, B., McNaughton, N., Bickle, M., and Chapman, H.: The Sholl Shear Zone, West Pilbara: evidence for a domain boundary structure from integrated tectonostratigraphic analyses, SHRIMP U Pb dating and isotopic and geochemical data of granitoids, Precambrian Research, 88, 143–171, https://doi.org/10.1016/S0301-9268(97)00067-3, 1998.

Smithies, R. H., Champion, D. C., Van Kranendonk, M. J., Howard, H. M., and Hickman, A. H.: Modern-style subduction processes in the Mesoarchaean: geochemical evidence from the 3.12 Ga Whundo intra-oceanic arc, Earth and Planetary Science Letters, 231, 221–237, https://doi.org/10.1016/j.epsl.2004.12.026, 2005a.

Smithies, R. H., Van Kranendonk, M. J., and Champion, D. C.: It started with a plume–early Archaean basaltic proto-continental crust, Earth and Planetary Science Letters, 238, 284–297, https://doi.org/10.1016/j.epsl.2005.07.023, 2005b.

Smithies, R., Van Kranendonk, M., and Champion, D.: The Mesoarchean emergence of modern-style subduction, Gondwana Research, 11, 50–68, https://doi.org/10.1016/j.gr.2006.02.001, 2007.

Smithies, R., Champion, D., and Van Kranendonk, M.: Formation of Paleoarchean continental crust through infracrustal melting of enriched basalt, Earth and Planetary Science Letters, 281, 298–306, https://doi.org/10.1016/j.epsl.2009.03.003, 2009.

Smrzka, D., Zwicker, J., Bach, W., Feng, D., Himmler, T., Chen, D., and Peckmann, J.: The behavior of trace elements in seawater, sedimen- tary pore water, and their incorporation into carbonate minerals: a review, Facies, 65, 1–47, https://doi.org/10.1007/s10347-019-0581-4, 2019.

Stipp, S., Christensen, J., Lakshtanov, L., Baker, J., and Waight, T.: Rare Earth element (REE) incorporation in natural calcite: upper limits for actinide uptake in a secondary phase, Radiochimica Acta, 94, 523–528, https://doi.org/10.1524/ract.2006.94.9-11.523, 2006.

Sverjensky, D. A.: Europium redox equilibria in aqueous solution, Earth and Planetary Science Letters, 67, 70–78, https://doi.org/10.1016/0012-821X(84)90039-6, 1984.

Tan, F. C.: Stable carbon isotopes in dissolved inorganic carbon in marine and estuarine environments, in: Handbook of environmental isotope geochemistry, edited by Fritz, P. and Fontes, J., vol. 3, pp. 171–190, Elsevier, Amsterdam, 1989.

Taylor, S. R. and McLennan, S. M.: The continental crust: its composition and evolution, Blackwell Scientific Pub., Palo Alto, CA, 1985.

Thorpe, R., Hickman, A., Davis, D., Mortensen, J., and Trendall, A.: U-Pb zircon geochronology of Archaean felsic units in the Marble Bar region, Pilbara Craton, Western Australia, Precambrian Research, 56, 169–189, https://doi.org/10.1016/0301-9268(92)90100-3, 1992.

Tusch, J., Münker, C., Hasenstab, E., Jansen, M., Marien, C. S., Kurzweil, F., Van Kranendonk, M. J., Smithies, H., Maier, W., and Garbe- Schönberg, D.: Convective isolation of Hadean mantle

reservoirs through Archean time, Proceedings of the National Academy of Sciences, 118, e2012626 118, https://doi.org/10.1073/pnas.2012626118, 2021.

Tympel, J. F., Hergt, J. M., Maas, R., Woodhead, J. D., Greig, A., Bolhar, R., and Powell, R.: Mantle-like Hf-Nd isotope signatures in ~3.5 Ga greenstones: No evidence for Hadean crust beneath the East Pilbara Craton, Chemical Geology, 576, 120273, https://doi.org/10.1016/j.chemgeo.2021.120273, 2021.

Ueno, Y.: Early Archean (ca. 3.5 Ga) microfossils and ^{13}C-depleted carbonaceous matter in the North Pole area, Western Australia: Field occurrence and geochemistry, Geochemistry and the Origin of Life, 2001.

van den Boorn, S. H., van Bergen, M. J., Nijman, W., and Vroon, P. Z.: Dual role of seawater and hydrothermal fluids in Early Archean chert formation: evidence from silicon isotopes, Geology, 35, 939–942, https://doi.org/10.1130/G24096A.1, 2007.

Van Kranendonk, M. J.: Volcanic degassing, hydrothermal circulation and the flourishing of early life on Earth: A review of the evi- dence from ca. 3490-3240 Ma rocks of the Pilbara Supergroup, Pilbara Craton, Western Australia, Earth-Science Reviews, 74, 197–240, https://doi.org/10.1016/j.earscirev.2005.09.005, 2006.

Van Kranendonk, M. J.: A review of the evidence for putative Paleoarchean life in the Pilbara Craton, Western Australia, Developments in Precambrian Geology, 15, 855–877, https://doi.org/10.1016/S0166-2635(07)15072-6, 2007.

Van Kranendonk, M. J. and Hickman, A. H.: Archaean Geology of the North Shaw Region, East Pilbara Granite-Greenstone Terrane, Western Australia: A Field Guide, Geological Survey of Western Australia, Record 2000/5, 2000.

Van Kranendonk, M. J. and Pirajno, F.: Geochemistry of metabasalts and hydrothermal alteration zones associated with ca. 3.45 Ga chert and barite deposits: implications for the geological setting of the Warrawoona Group, Pilbara Craton, Australia, Geochemistry: Exploration, Environment, Analysis, 4, 253–278, https://doi.org/10.1144/1467-7873/04-205, 2004.

Van Kranendonk, M. J., Hickman, A. H., Smithies, R. H., Nelson, D. R., and Pike, G.: Geology and tectonic evolution of the Archean North Pilbara terrain, Pilbara Craton, Western Australia, Economic Geology, 97, 695–732, https://doi.org/10.2113/gsecongeo.97.4.695, 2002.

Van Kranendonk, M. J., Webb, G. E., and Kamber, B. S.: Geological and trace element evidence for a marine sedimentary environment of deposition and biogenicity of 3.45 Ga stromatolitic carbonates in the Pilbara Craton, and support for a reducing Archaean ocean, Geobiology, 1, 91–108, https://doi.org/10.1046/j.1472-4669.2003.00014.x, 2003.

Van Kranendonk, M. J., Hickman, A. H., Smithies, R. H., and et al: Revised lithostratigraphy of Archean supracrustal and intrusive rocks in the northern Pilbara Craton, Western Australia, Geological Survey of Western Australia. Record 2006/15, 2006a.

Van Kranendonk, M. J., Hickman, A. H., and Huston, D. L.: Geology and Mineralization of the East Pilbara d A Field Guide, Western Australia Geological Survey. Record 2006/16, 2006b.

Van Kranendonk, M. J., Hugh Smithies, R., Hickman, A. H., and Champion, D.: Secular tectonic evolution of Archean continental crust: interplay between horizontal and vertical processes in the formation of the Pilbara Craton, Australia, Terra Nova, 19, 1–38, https://doi.org/10.1111/j.1365-3121.2006.00723.x, 2007a.

Van Kranendonk, M. J., Smithies, R. H., Hickman, A. H., and Champion, D. C.: Paleoarchean development of a continental nucleus: the East Pilbara terrane of the Pilbara craton, Western

Australia, Developments in Precambrian geology, 15, 307–337, https://doi.org/10.1016/S0166-2635(07)15041-6, 2007b.

Van Kranendonk, M. J., Philippot, P., Lepot, K., Bodorkos, S., and Pirajno, F.: Geological setting of Earth's oldest fossils in the ca. 3.5 Ga Dresser formation, Pilbara Craton, Western Australia, Precambrian Research, 167, 93–124, https://doi.org/10.1016/j.precamres.2008.07.003, 2008.

Van Kranendonk, M. J., Smithies, R. H., Griffin, W. L., Huston, D. L., Hickman, A. H., Champion, D. C., Anhaeusser, C. R., and Pirajno, F.: Making it thick: a volcanic plateau origin of Palaeoarchean continental lithosphere of the Pilbara and Kaapvaal cratons, Geological Society, London, Special Publications, 389, 83–111, https://doi.org/10.1144/SP389.12, 2015.

Van Kranendonk, M. J., Smithies, R. H., Hickman, A. H., and Champion, D. C.: Paleoarchean development of a continental nucleus: the East Pilbara Terrane of the Pilbara Craton, Western Australia, in: Earth's Oldest Rocks, edited by Van Kranendonk, M., Bennett, V., and Hoffmann, J., pp. 437–462, Elsevier, 2019a.

Van Kranendonk, M., Djokic, T., Poole, G., Tadbiri, S., Steller, L., and Baumgartner, R.: Depositional Setting of the Fossiliferous, ca. 3480 Ma Dresser Formation, Pilbara Craton: A Review, in: Earth's Oldest Rocks, edited by Van Kranendonk, M., Bennett, V., and Hoffmann, J., pp. 985–1006, Elsevier, 2019b.

Vance, D., Teagle, D. A., and Foster, G. L.: Variable Quaternary chemical weathering fluxes and imbalances in marine geochemical budgets, Nature, 458, 493–496, https://doi.org/10.1038/nature07828, 2009.

Veizer, J.: Chemical Diagenesis of Carbonates: Theory and Application of Trace Element Technique, in: Stable Isotopes in Sedimentary Geology, SEPM Society for Sedimentary Geology, https://doi.org/10.2110/scn.83.01.0000, 1983.

Veizer, J. and Compston, W.: $^{87}Sr/^{86}Sr$ composition of seawater during the Phanerozoic, Geochimica et Cosmochimica Acta, 38, 1461–1484, https://doi.org/10.1016/0016-7037(74)90099-4, 1974.

Veizer, J., Compston, W., Hoefs, J., and Nielsen, H.: Mantle buffering of the early oceans, Naturwissenschaften, 69, 173–180, https://doi.org/10.1007/BF00364890, 1982.

Veizer, J., Hoefs, J., Ridler, R., Jensen, L., and Lowe, D.: Geochemistry of Precambrian carbonates: I. Archean hydrothermal systems, Geochimica et Cosmochimica Acta, 53, 845–857, https://doi.org/10.1016/0016-7037(89)90030-6, 1989a.

Veizer, J., Hoefs, J., Lowe, D., and Thurston, P.: Geochemistry of Precambrian carbonates: II. Archean greenstone belts and Archean sea water, Geochimica et Cosmochimica Acta, 53, 859–871, https://doi.org/10.1016/0016-7037(89)90031-8, 1989b.

Veizer, J., Ala, D., Azmy, K., Bruckschen, P., Buhl, D., Bruhn, F., Carden, G. A., Diener, A., Ebneth, S., Godderis, Y., et al.: $^{87}Sr/^{86}Sr$, $\delta^{13}C$ and $\delta^{18}O$ evolution of Phanerozoic seawater, Chemical geology, 161, 59–88, https://doi.org/10.1016/S0009-2541(99)00081-9, 1999.

Viehmann, S., Reitner, J., Tepe, N., Hohl, S. V., Van Kranendonk, M., Hofmann, T., Koeberl, C., and Meister, P.: Carbonates and cherts as archives of seawater chemistry and habitability on a carbonate platform 3.35 Ga ago: Insights from Sm/Nd dating and trace element analysis from the Strelley Pool Formation, Western Australia, Precambrian Research, 344, 105742, https://doi.org/10.1016/j.precamres.2020.105742, 2020.

Von Damm, K. L.: Controls on the chemistry and temporal variability of seafloor hydrothermal fluids, Seafloor hydrothermal systems: Physical, chemical, biological, and geological interactions, 91, 222–247, https://doi.org/10.1029/GM091p0222, 1995.

Walter, M., Buick, R., and Dunlop, J.: Stromatolites 3,400–3,500 Myr old from the North Pole area, Western Australia, Nature, 284, 443–445, 1980.

Webb, G. E. and Kamber, B. S.: Rare earth elements in Holocene reefal microbialites: a new shallow seawater proxy, Geochimica et Cos- mochimica Acta, 64, 1557–1565, https://doi.org/10.1016/S0016-7037(99)00400-7, 2000.

Westall, F., Campbell, K. A., Bréhéret, J. G., Foucher, F., Gautret, P., Hubert, A., Sorieul, S., Grassineau, N., and Guido, D. M.: Archean (3.33 Ga) microbe-sediment systems were diverse and flourished in a hydrothermal context, Geology, 43, 615–618, https://doi.org/10.1130/G36646.1, 2015.

Wheat, C. G., Mottl, M. J., and Rudnicki, M.: Trace element and REE composition of a low-temperature ridge-flank hydrothermal spring, Geochimica et Cosmochimica Acta, 66, 3693–3705, https://doi.org/10.1016/S0016-7037(02)00894-3, 2002.

Willbold, M. and Jochum, K. P.: Multi-element isotope dilution sector field ICP-MS: A precise technique for the analysis of geological materials and its application to geological reference materials, Geostandards and Geoanalytical Research, 29, 63–82, https://doi.org/10.1111/j.1751-908X.2005.tb00656.x, 2005.

Yamamoto, K., Itoh, N., Matsumoto, T., Tanaka, T., and Adachi, M.: Geochemistry of Precambrian carbonate intercalated in pillows and its host basalt: implications for the REE composition of circa 3.4 Ga seawater, Precambrian Research, 135, 331–344, https://doi.org/10.1016/j.precamres.2004.09.006, 2004.

Zhang, J., Amakawa, H., and Nozaki, Y.: The comparative behaviors of yttrium and lanthanides in the seawater of the North Pacific, Geo- physical Research Letters, 21, 2677–2680, https://doi.org/10.1029/94GL02404, 1994.

Zhao, Y., Wei, W., Li, S., Yang, T., Zhang, R., Somerville, I., Santosh, M., Wei, H., Wu, J., Yang, J., et al.: Rare earth element geochemistry of carbonates as a proxy for deep-time environmental reconstruction, Palaeogeography, Palaeoclimatology, Palaeoecology, 574, 110 443, https://doi.org/10.1016/j.palaeo.2021.110443, 2021.

Zhong, S. and Mucci, A.: Partitioning of rare earth elements (REEs) between calcite and seawater solutions at 25 C and 1 atm, and high dissolved REE concentrations, Geochimica et Cosmochimica Acta, 59, 443–453, https://doi.org/10.1016/0016-7037(94)00381-U, 1995.

Appendix

1. Binary mixing model

The influence of possible detritus component can be assessed based on the binary mixing model (or two-component mixing model) using the following equation:

$$C_{mix}^{E} = C_{A}^{E} \times F + C_{B}^{E} \times (1 - F) \qquad \text{(Eq.1)}$$

where $C_{A}^{E}, C_{B}^{E}, C_{mix}^{E}$ are the concentrations of element E in component A, B and mixture, respectively, while F is a weight fraction. In this study, the binary mixing lines are calculated using the composition of fracture-filling calcite D-2-W as the seawater endmember, the mean value of EPT basalts as the basaltic endmember (Van Kranendonk and Pirajno, 2004; Yamamoto et al., 2004; Nakamura and Kato, 2004; Smithies et al., 2005; Jenner et al., 2009; Johnson et al., 2017; Nakamura et al., 2020; Tusch et al., 2021; Tympel et al., 2021; Caruso et al., 2021), and the composition of MUQ (MUd from Queensland, Kamber et al., 2005) as an endmember of the weathered upper continental crust.

For the EPT basalts, the Al and Ti contents were usually given by the contents of oxides Al_2O_3 and TiO_2, respectively. In this study, these contents were calculated using Equation 2, if they were not available:

$$C^{E} = C^{ox} \times M^{E} \times m \div M^{ox} \qquad \text{(Eq.2)}$$

where C^{E} and C^{ox} represents the concentrations of element E (here Al or Ti) and oxide E_nO_m, while M^{E} and M^{ox} represents the atomic weight of element E and the molecular weight of its oxide. The histograms of the element concentrations of EPT basalts used for estimating detritus contribution are illustrated in Fig.S2, showing the mean values of Al (7.00 wt%, N=373), Th (0.76 ppm, N =396), Sc (35.75 ppm, N=366), Ti (6216.94 ppm, N=273), Zr (73.95 ppm, N=308), total REE (without Y, 47.24 ppm, N=410) and Rb (23.43 ppm, N=395).

2. Sr isotopic evolution line

The Sr isotopic evolution lines of the Bulk Silicate Earth (BSE), Depleted Mantle (DM) and Upper Continental Crust (UCC) are calculated based on the assumptions listed below. The BSE Sr isotopic evolution line is calculated from the Basaltic Achondrite Best Initial (BABI) with an initial $^{87}Sr/^{86}Sr$ ratio of 0.69897 at 4.56 Ga (Hans et al., 2013) and a bulk Earth $^{87}Rb/^{86}Sr$ ratio of 0.085 (Taylor and McLennan, 1985). Differentiation occurred at 3.8 Ga (White, 2005; Alexander Bentley, 2006). After that, the UCC evolved highly heterogeneously in its $^{87}Sr/^{86}Sr$ ratio due to substantial Rb/Sr fractionation during igneous differentiation processes (White, 2014). Thus, this study assumes an $^{87}Rb/^{86}Sr$ of 0.26 to generate a present-day $^{87}Sr/^{86}Sr$ ratio of 0.714053 (an average present-day isotope

composition of $^{87}Sr/^{86}Sr$ ~0.715, Yokoo et al., 2004). Similarly, the present-day DM is also heterogeneous in its Sr isotope composition due to melt extraction and re-fertilization by recycled crust (White, 2014). Therefore, a present-day $^{87}Sr/^{86}Sr$ value ~0.702 to 0.703 of the global mid-ocean ridge basalts (MORB) on average (DePaolo and Wasserburg, 1977; Salters and Stracke, 2004) is considered representative for the upper depleted mantle, and accordingly an evolution line with $^{87}Rb/^{86}Sr = 0.05$ and a present-day $^{87}Sr/^{86}Sr$ ratio of 0.702603 is used in this study to indicate the DM evolution. The related decay equation is listed below with a Rb decay constant (λ ^{87}Rb) of 1.394 $\times 10^{-11}$ /a (with t in millions of years, Nebel et al., 2011):

$$(^{87}Sr/^{86}Sr)_{present} = (^{87}Sr/^{86}Sr)_{initial} + (^{87}Rb/^{86}Sr) \times (e^{\lambda t}-1) \quad \text{(Eq.3)}$$

3. Pictures and Tables

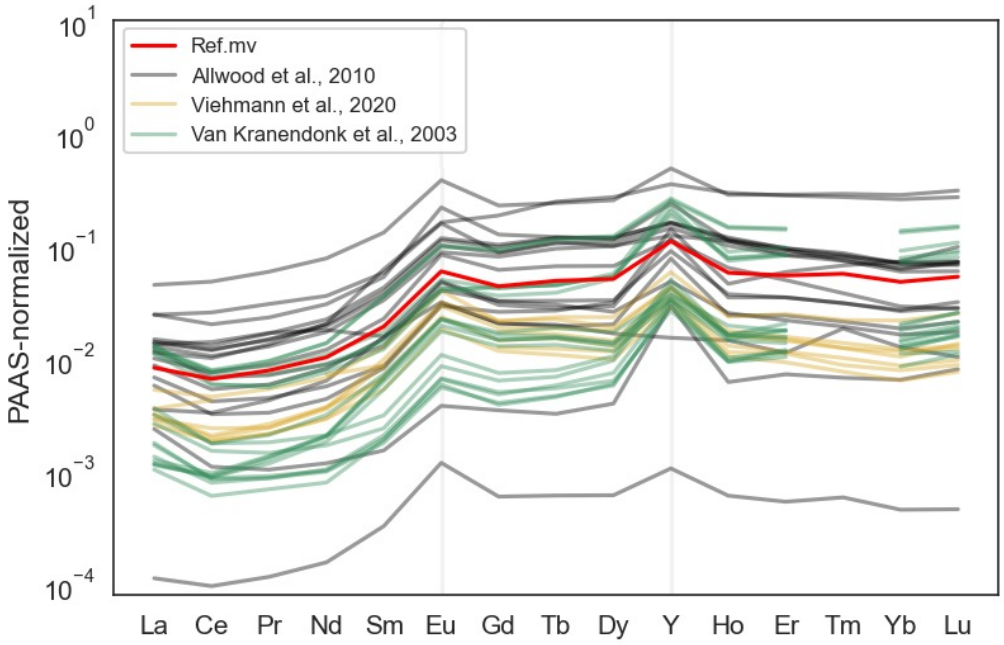

Fig.S1 The PAAS-normalized REE+Y patterns of the SPF carbonate rocks from Van Kranendonk et al., 2003; Allwood et al., 2010; Viehmann et al., 2020 that "Ref. mv" indicates the mean value.

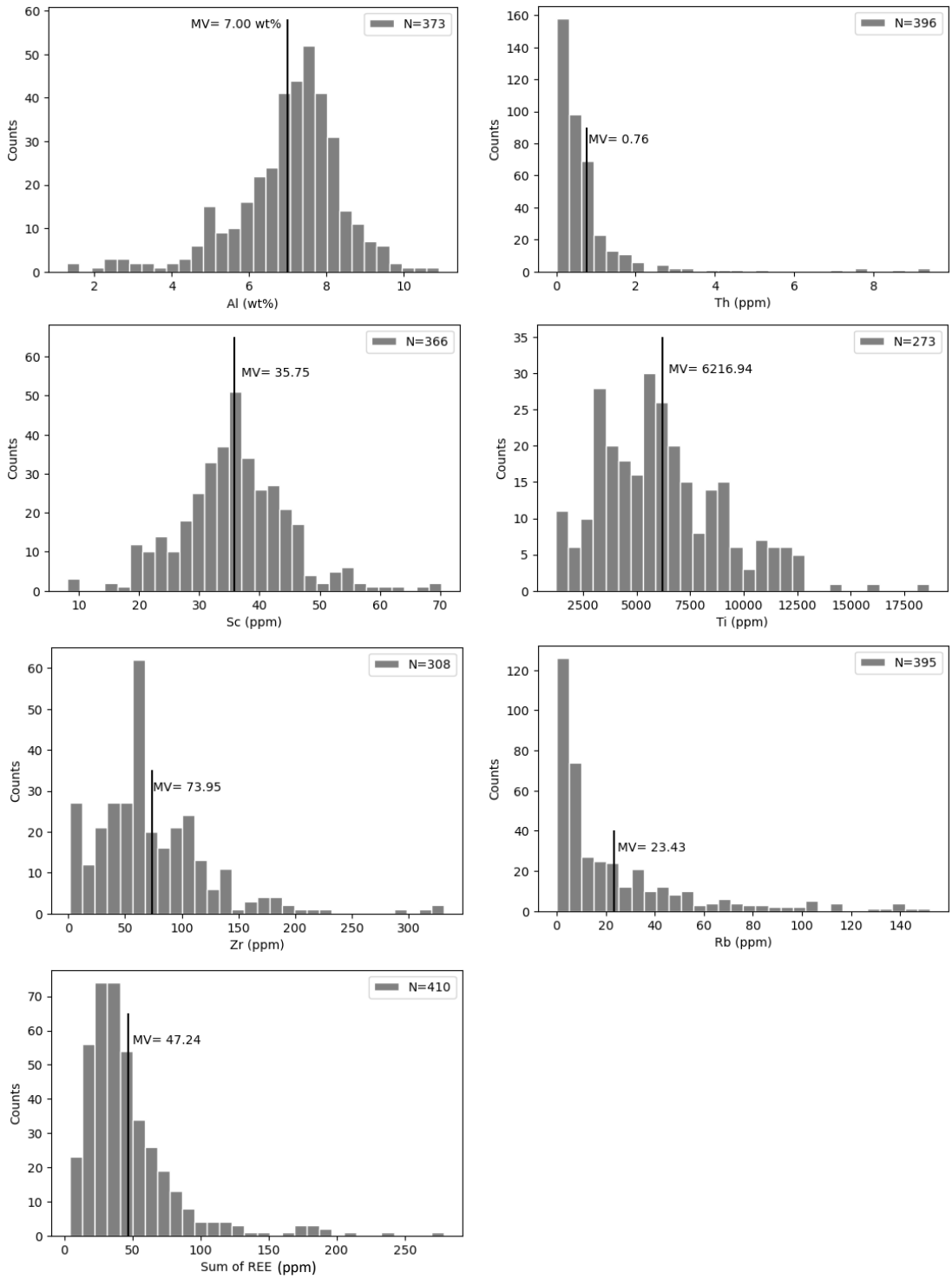

Fig.S2 The histograms about the concentrations of Al (wt%), Th, Sc, Ti, Zr, Rb and the total REE (ppm) in the EPF basalts. The mean values (MV) are shown in every image. Data come from Van Kranendonk and Pirajno, 2004; Yamamoto et al., 2004; Nakamura and Kato, 2004; Smithies et al., 2005; Jenner et al., 2009; Johnson et al., 2017; Nakamura et al., 2020; Tusch et al., 2021; Tympel et al., 2021; Caruso et al., 2021.

Table S1 The concentrations of major and trace elements of the references Cal-s, Jls-1 and JDo-1

Sample ID			Cal-s						JLs-1								Jdo-1					
Reference	Ref.a		this work				Ref.b, c		this work						Ref.b, c		this work					
	(ppm)		1st		2nd		(ppm)		1st			2nd			(ppm)		1st			2nd		
	MV (N=25)	RSD %	MV (N=2, 4*)	RSD%	MV (N=4*)	RSD%	MV (N=7)	RSD %	MV (N=2, 4*)	RSD%	Offset	MV (N=3*)	RSD%	Offset	MV (N=7)	RSD %	MV (N=4*)	RSD%	Offset	MV (N=2*)	RSD%	Offset
(wt%)																						
Al			0.015	141.4			1383.2		0.008	23.4					637		0.023	141.4				
Ca			39.499	2.6			414000		41.401	0.6					247000		24.923	4.4				
Fe	294		<0.011				106		<0.035						147		<0.028					
K			<0.509				N.A.		<1.636						N.A.		<1.314					
Mg	2358		<0.063				4400		0.220	19.1					227000		11.247	1.5				
Mn	12.076		<0.001				16.4		0.001	8.9					51		0.005	6.5				
Na			<0.414				N.A.		<1.330						N.A.		<1.068					
(ppm)																						
Sc			0.255	8.1	0.356	6.9			0.226	10.9		0.315	12.5				0.296	12.6		0.400	6.3	
Ti			1.895	11.8	1.320	0.9			0.675	8.8		0.886	6.6				1.491	5.1		2.024	1.5	
V			1.700	2.3	1.271	6.0			2.268	1.3		1.893	5.8				3.526	1.6		2.976	0.7	
Ni	5.000	100.0	N.A.	N.A.	6.860	2.3			N.A			6.572	3.4				N.A			6.160	0.8	
Zn	15.440	18.7	N.A.	N.A.	10.675	2.9			N.A			4.386	4.0				N.A			38.435	0.3	
Rb	0.897	64.5	0.085	4.8	0.055	3.5	0.114	6.0	0.055	6.3	0.483	0.062	4.5	0.545	0.140	50.6	0.032	9.0	0.230	0.035	0.4	0.247
Sr	249.000	4.4	237.880	0.5	259.295	0.9	285.000	1.7	312.369	1.0	1.096	312.823	0.7	1.098	117.000	3.4	116.658	1.1	0.997	117.737	0.4	1.006
Y	1.950	4.1	1.722	0.5	1.846	1.1	0.216	1.5	0.229	0.6	1.060	0.226	1.0	1.048	10.400	4.0	9.886	1.1	0.951	9.897	0.5	0.952
Zr	1.360	86.8	0.205	1.5	0.142	1.8	0.320	11.6	0.040	2.1	0.125	0.059	2.9	0.185	0.560	16.9	0.120	3.7	0.214	0.163	1.6	0.291
Mo	0.185	25.4	0.155	1.6	0.106	2.0			0.039	8.7		0.051	8.8				0.128	4.9		0.143	1.8	
Ba	2.260	211.5	1.207	1.3	1.313	1.5	453.000	4.1	437.858	0.8	0.967	441.142	0.3	0.974	7.000	26.4	5.640	1.6	0.806	5.754	0.2	0.822
La	0.820	8.5	0.768	1.1	0.832	0.6	0.107	1.3	0.118	1.3	1.102	0.115	1.4	1.073	7.700	3.0	7.742	0.6	1.005	7.733	0.5	1.004
Ce	0.347	28.0	0.279	1.6	0.298	1.4	0.187	2.7	0.183	1.2	0.980	0.187	0.3	0.998	2.020	2.5	1.994	0.3	0.987	1.997	0.3	0.989
Pr	0.092	17.4	0.082	1.4	0.088	0.9	0.024	0.9	0.023	0.7	0.954	0.023	2.4	0.994	1.050	3.1	0.980	0.8	0.933	0.980	0.4	0.934
Nd	0.375	19.7	0.341	0.9	0.365	1.1	0.090	0.9	0.092	2.3	1.019	0.096	3.8	1.059	4.090	2.2	4.057	0.7	0.992	4.051	0.2	0.991
Sm	0.058	43.1	0.060	2.2	0.065	1.3	0.019	1.5	0.022	1.7	1.203	0.021	1.7	1.157	0.680	2.1	0.686	1.1	1.010	0.683	0.5	1.005
^{151}Eu	0.018	44.4	0.015	3.1	0.014	1.3	0.005	5.5	0.002	51.6	0.430	0.005	10.7	1.123	0.162	2.4	0.159	1.0	0.982	0.153	0.9	0.945
^{153}Eu	0.018	44.4	0.015	3.7	0.016	3.5	0.005	5.5	0.008	8.7	1.726	0.007	28.9	1.447	0.162	2.4	0.158	1.2	0.977	0.157	0.7	0.971
Gd	0.095	22.1	0.087	1.7	0.095	7.5	0.021	1.4	0.025	5.8	1.161	0.024	6.5	1.124	0.900	2.5	0.842	1.9	0.935	0.832	0.6	0.924
Tb	0.013	23.1	0.013	1.8	0.014	3.3	0.003	0.9	0.003	6.2	1.070	0.003	2.2	1.052	0.120	2.0	0.117	1.0	0.974	0.115	0.6	0.954
Dy	0.092	21.7	0.093	2.4	0.101	0.6	0.020	1.1	0.019	2.3	0.975	0.020	3.2	1.017	0.750	2.5	0.724	0.7	0.965	0.710	0.2	0.947
Ho	0.024	12.5	0.024	2.1	0.026	1.2	0.005	1.6	0.005	3.3	1.006	0.005	2.7	1.005	0.167	2.2	0.160	0.8	0.959	0.160	0.3	0.956
Er	0.072	16.7	0.077	1.6	0.084	2.3	0.014	3.4	0.014	2.6	1.020	0.014	3.8	1.021	0.460	2.0	0.448	0.5	0.975	0.447	1.9	0.972
Tm	0.011	27.3	0.011	3.1	0.011	2.7	0.002	3.2	0.002	9.6	0.903	0.002	5.2	0.997	0.056	2.3	0.054	1.9	0.963	0.054	2.6	0.956
Yb	0.062	22.6	0.065	1.1	0.070	6.0	0.013	1.8	0.012	1.4	0.961	0.013	4.2	1.019	0.305	1.9	0.294	0.7	0.964	0.289	0.0	0.947
Lu	0.010	30.0	0.010	2.9	0.011	9.7	0.002	1.3	0.002	4.4	1.003	0.001	12.2	0.749	0.043	3.8	0.041	1.7	0.953	0.040	1.3	0.930
Hf	0.031	77.4	N.A.	N.A.	0.004	13.0	0.008	57.9	N.A		0.000	0.002	19.8	0.201	<0.03		N.A			0.005	4.3	
Th	0.022	113.6	0.020	3.4	0.018	2.3	0.016	5.2	0.016	3.4	1.007	0.018	2.0	1.107	<0.04		0.039	0.7		0.040	1.0	
U	0.727	7.3	0.734	0.6	0.770	0.4	1.830	5.6	1.569	0.5	0.857	1.540	0.4	0.841	0.880	3.4	0.756	0.7	0.859	0.733	0.8	0.833

Note:

1. The mean value is indicated by MV. RSD% represents the relative standard deviation in percent. Offset is calculated as the ratio of the mean value to the reference value.
2. The reference data of Cal-s are taken from Potts et al., 2000 (Ref.a), while the reference data of JIs-1 and JDo-1 are obtained from Schier et al., 2018 (Ref.b) for major elements, and Dulski, 2001 (Ref.c) for trace elements that the measurement number is marked with an asterisk (*) in the mean value (MV) column.

References

Alexander Bentley, R.: Strontium isotopes from the earth to the archaeological skeleton: a review, Journal of archaeological method and theory, 13, 135–187, https://doi.org/10.1007/s10816-006-9009-x, 2006.

Caruso, S., Van Kranendonk, M. J., Baumgartner, R. J., Fiorentini, M. L., and Forster, M. A.: The role of magmatic fluids in the˜ 3.48 Ga Dresser Caldera, Pilbara Craton: New insights from the geochemical investigation of hydrothermal alteration, Precambrian Research, 362, 106 299, 2021.

DePaolo, D. J. and Wasserburg, G. J.: Petrogenetic mixing models and Nd-Sr isotopic patterns, Geochimica et Cosmochimica Acta, 43, 615–627, https://doi.org/10.1016/0016-7037(79)90169-8, 1979.

Hans, U., Kleine, T., and Bourdon, B.: Rb–Sr chronology of volatile depletion in differentiated protoplanets: BABI, ADOR and ALL revisited, Earth and Planetary Science Letters, 374, 204–214, https://doi.org/10.1016/j.epsl.2013.05.029, 2013.

Jenner, F., Bennett, V., Nutman, A., Friend, C., Norman, M., and Yaxley, G.: Evidence for subduction at 3.8 Ga: geo- chemistry of arc-like metabasalts from the southern edge of the Isua Supracrustal Belt, Chemical Geology, 261, 83–98, https://doi.org/10.1016/j.chemgeo.2008.09.016, 2009.

Johnson, T. E., Brown, M., Gardiner, N. J., Kirkland, C. L., and Smithies, R. H.: Earth's first stable continents did not form by subduction, Nature, 543, 239–242, https://doi.org/10.1038/nature21383, 2017.

Kamber, B. S., Greig, A., and Collerson, K. D.: A new estimate for the composition of weathered young upper continental crust from alluvial sediments, Queensland, Australia, Geochimica et Cosmochimica Acta, 69, 1041–1058, https://doi.org/10.1016/j.gca.2004.08.020, 2005.

Nakamura, H., Sano, A., Kagami, S., Yokoyama, T., Ishikawa, A., Komiya, T., and Iwamori, H.: Compositional heterogeneity of Archean mantle estimated from Sr and Nd isotopic systematics of basaltic rocks from North Pole, Australia, and the Isua supracrustal belt, Green- land, Precambrian Research, 347, 105 803, https://doi.org/10.1016/j.precamres.2020.105803, 2020.

Nakamura, K. and Kato, Y.: Carbonatization of oceanic crust by the seafloor hydrothermal activity and its significance as a CO_2 sink in the Early Archean, Geochimica et Cosmochimica Acta, 68, 4595–4618, https://doi.org/10.1016/j.gca.2004.05.023, 2004.

Nebel, O., Scherer, E. E., and Mezger, K.: Evaluation of the 87Rb decay constant by age comparison against the U–Pb system, Earth and Planetary Science Letters, 301, 1–8, https://doi.org/10.1016/j.epsl.2010.11.004, 2011.

Salters, V. J. and Stracke, A.: Composition of the depleted mantle, Geochemistry, Geophysics, Geosystems, 5, https://doi.org/10.1029/2003GC000597, 2004.

Schier, K., Bau, M., Muenker, C., Beukes, N., and Viehmann, S.: Trace element and Nd isotope composition of shallow seawater prior to the Great Oxidation Event: Evidence from stromatolitic bioherms in the Paleoproterozoic Rooinekke and Nelani Formations, South Africa, Precambrian Research, 315, 92–102, https://doi.org/10.1016/j.precamres.2018.07.014, 2018.

Smithies, R. H., Van Kranendonk, M. J., and Champion, D. C.: It started with a plume–early Archaean basaltic proto-continental crust, Earth and Planetary Science Letters, 238, 284–297, https://doi.org/10.1016/j.epsl.2005.07.023, 2005.

Taylor, S. R. and McLennan, S. M.: The continental crust: its composition and evolution, 1985.

Tusch, J., Münker, C., Hasenstab, E., Jansen, M., Marien, C. S., Kurzweil, F., Van Kranendonk, M. J., Smithies, H., Maier, W., and Garbe- Schönberg, D.: Convective isolation of Hadean mantle reservoirs through Archean time, Proceedings of the National Academy of Sciences, 118, e2012626 118, https://doi.org/10.1073/pnas.2012626118, 2021.

Tympel, J. F., Hergt, J. M., Maas, R., Woodhead, J. D., Greig, A., Bolhar, R., and Powell, R.: Mantle-like Hf-Nd isotope signatures in ~3.5 Ga greenstones: No evidence for Hadean crust beneath the East Pilbara Craton, Chemical Geology, 576, 120273, https://doi.org/10.1016/j.chemgeo.2021.120273, 2021.

Van Kranendonk, M. J. and Pirajno, F.: Geochemistry of metabasalts and hydrothermal alteration zones associated with ca. 3.45 Ga chert and barite deposits: implications for the geological setting of the Warrawoona Group, Pilbara Craton, Australia, Geochemistry: Exploration, Environment, Analysis, 4, 253–278, https://doi.org/10.1144/1467-7873/04-205, 2004.

White, W. M.: Chapter 8: Radiogenic Isotope Geochemistry, https://www.imwa.info/geochemistry/Chapters/Chapter08.pdf, 2005.

White, W. M.: Isotope geochemistry, John Wiley Sons, ISBN 978-0-470-65670-9, 2014.

Yamamoto, K., Itoh, N., Matsumoto, T., Tanaka, T., and Adachi, M.: Geochemistry of Precambrian carbonate intercalated in pillows and its host basalt: implications for the REE composition of circa 3.4 Ga seawater, Precambrian Research, 135, 331–344, https://doi.org/10.1016/j.precamres.2004.09.006, 2004

Yokoo, Y., Nakano, T., Nishikawa, M., and Quan, H.: Mineralogical variation of Sr–Nd isotopic and elemental compositions in loess and desert sand from the central Loess Plateau in China as a provenance tracer of wet and dry deposition in the northwestern Pacific, Chemical Geology, 204, 45–62, https://doi.org/10.1016/j.chemgeo.2003.11.004, 2004.

Chapter-4 Element mobility during carbonatization of 3.46 Ga Apex Basalt and its geobiological significances

Xiang*, W., Duda, J.-P., Pack, A., Willbold, M., Bach, W., Reitner, J.

Abstract

Ocean geochemistry in the early Archean was dominantly influenced by hydrothermal fluids derived from seafloor alteration. The 3.46 Ga Apex Basalt in the East Pilbara Terrane (EPT), Western Australia, preserves putative traces of early life and a rock assemblage for studying the interaction between basaltic oceanic crust and CO_2-rich seawater. Its submarine eruption is supported by the distinct concentric structures (from core to chilled rim and interspace), including a holocrystalline core, a spherulitic zone, a variolitic zone, a glassy zone within a pillow shape, and shattered breccias in the interspace. Although the phenocrysts and primary volcanic structures are locally preserved, the replacement of protolith by a secondary mineral assemblage of chlorite+ calcite+ quartz+ anatase + pyrite ± epidote indicates that the pillow basalts experienced metamorphism of greenschist facies. However, the errorchron based on Rb-Sr isotopic compositions of different concentric domains yields an age of 3570.7 ± 144.3 Ma (n=6, MSWD= 150), comparable to the depositional age around 3460 Ma, indicative of the at-time broadly syn-depositional alteration leading to a whole-rock $^{87}Sr/^{86}Sr$ ratio of 0.706337 ± 0.000954, and the Rb-Sr system was not reset afterwards. During metamorphism, elements including Ca, Si, many bioessential elements (P, S, Fe, Mn, Mg, Ni, Zn and Co) and REE +Y (especially LREE) were leached from basalt into fluid, contributing to (1) extensive carbonatization of basaltic crust and occurrence of interstitial carbonate that played as a major carbon sink on early Earth; (2) abundance of bioessential elements in hydrothermal fluids that were nutrients or enzyme cofactors responsible for many metabolisms (sulfur/sulfate reduction, methanogenesis and anoxygenic photosynthesis, nitrogen fixation), thus paving the way for the origin and evolution of early life; (3) pervasion of Si-bearing fluids precipitated various cherts that involved in preservation of carbonaceous materials, microfossils, silicified stromatolite. Therefore, the well-preserved Apex pillow basalts are good archive for studying seafloor alteration at 3.46 Ga and its significances in global carbon cycles and adjusting ocean geochemistry to prepare Earth habitable for early life.

Keywords: Apex pillow basalt, seafloor alteration, Rb-Sr isotopic system, REE+Y, Bio-nutrients, Interstitial carbonate

Introduction

Ocean has been a significant habitat for life since its debut. Distinct from richly oxygenated modern ocean, ocean in the early Archean was anoxic, rich in trace elements

including Fe, Mn, Ni and Co and fed by hydrothermal fluids (Veizer et al., 1982, 1989; Canfield, 2005; Anbar, 2008; Poulton and Canfield, 2011; Li et al., 2013; Lyons et al., 2014; Large et al., 2014; Visscher et al., 2020). The high metal availability in environment impacted directly on incorporation of these elements into enzyme structure and subsequently the origin and evolution of early life, that Fe, Mg/Mn and Ni act as cofactors of enzymes involving the earliest metabolisms including sulfur/ sulfate reduction, methanogenesis and anoxygenic photosynthesis probably appearing between about 3.8 and 3.4 billion years ago (Anbar, 2008; Dupont et al., 2010; Moore et al., 2017). During the early Archean when exposure of continental crust was smaller (Taylor and McLennan, 1981; Arndt, 1999; Flament et al., 2008; Cawood et al., 2012), the interaction between seawater and oceanic crust, or so-called seafloor hydrothermal alteration, was not only one of major factors to control ocean chemistry (Holland, 1984; Ledevin M, 2019), but also the dominant CO_2 removal process inferred by the pervasive carbonate minerals in the Archean greenstone belts (Kitajima et al., 2001; Nakamura and Kato, 2002, 2004; Anhaeusser, 2014; Kasting, 2019; Nutman et al., 2019; Chapter-2,-3).

In three oldest Archean cratons, the 3.53-3.17 Ga East Pilbara Terrane (EPT) of the Pilbara Craton, Western Australia, appeals to many researchers for tracing early life due to the low regional metamorphism from prehnite-pumpellyite (100-250 °C) to lower greenschist facies (250-300 °C) (Hickman, 1983; Van Kranendonk et al., 2002, 2007, 2019). Since the first claim for preserving the oldest cellular microfossils on Earth (Schopf and Packer, 1987; Schopf, 1992, 1993), carbonaceous chert from 3.46 Ga Apex Basalt (informally as Apex chert) has been extensively studied, especially for testing biogenicity of the preserved microstructures. The initial interpretation of diverse trichomic cyanobacterium-like structures inferring oxygenic photosynthesis (Schopf, 1993) was later challenged by revisits of others, who argued the samples containing microstructures to be actually collected from an intrusive hydrothermal chert dike instead of sedimentary chert beds (Brasier et al., 2002, 2005; Van Kranendonk, 2006). The refuters reinterpreted the fossil-like microstructures as abiotic artifacts that carbonaceous materials were produced by Fischer-Tropsch-Type (FTT) synthesis in hydrothermal systems (Brasier et al., 2002, 2005; Wacey et al., 2016). This may cast a shadow on the alternative that the microstructures were remnants of thermophilic microbes thriving in hydrothermal systems, possibly methanogens and methanotrophs, implied by the morphospecies-correlated $\delta^{13}C$ compositions from −31‰ to −39‰ (Schopf et al., 2007, 2018), considering that such huge depletions in $\Delta^{13}C_{CO2–hydrocarbon}$ have been observed in hydrothermal experiments (McCollom and Seewald, 2006). Nonetheless, the debate on the biogenicity of the microstructures does not rule out the probability of early life in hydrothermal environments (Wacey et al., 2016). The emergence and thriving of thermophilic microbes in seafloor hydrothermal systems on early Earth are still widely supported by many researchers (Takai et al., 2004; Russell and Arndt, 2005; Brasier et al., 2006; Martin et al., 2008; Shibuya et al., 2010; Westall et al., 2015).

The pillow Apex basaltic rocks near the chert dike that preserves the controversial microfossils have been used to study seafloor hydrothermal activities in previous work (Nakamura and Kato, 2002, 2004). The protoliths of the basalt were completely replaced by a

secondary mineral assemblage of chlorite + K-mica + quartz + carbonate minerals (calcite>> ankerite and siderite) ± albite, with seawater-like $\delta^{13}C$ values of -0.3 ± 1.2 ‰ that reflect a reaction with CO_2-rich seawater (Nakamura and Kato, 2004). This interpretation was confirmed by the $\delta^{13}C$ values of diverse carbonates from the Warrawoona Group and Kelly Group, including interstitial hydrothermal carbonates and marine sedimentary carbonates, which supported the $\delta^{13}C$ values of around zero to reflect a mixture of marine and mantle carbon fluxes (Chapter 2). However, several occurrences of thermal events in the Eastern Pilbara Terrane after the epuration of Apex Basalt during the early Archean (Van Kranendonk et al., 2019) may cast doubt on the preservation of the primary chemical and isotopic characteristics of basaltic rocks and carbonate minerals. For example, the $^{87}Sr/^{86}Sr$ ratios of the primary interstitial carbonates of Apex Basalt range from 0.701796 to 0.704172, which are more radiogenic than the $^{87}Sr/^{86}Sr$ ratio of 3.5 Ga seawater (0.700596, Chapter 3), raising questions about whether the primary interstitial carbonates can truly reflect the geochemical conditions of hydrothermal fluids derived from the interaction between seawater and basaltic oceanic crust at 3.5 Ga, or from a much younger event.

Therefore, the aims of this study are: (a) to determine the metamorphic degree and age of the basaltic rocks near places preserving putative traces of early life through Rb-Sr isotopic system, (b) to find explanation of more radiogenic $^{87}Sr/^{86}Sr$ ratios of the Apex primary interstitial carbonates, and (c) to further investigate element mobility (including carbonate-forming elements, some bioessential elements and REE+Y) during alteration and metamorphism, as well as the impacts on ocean geochemistry, the origin and evolution of early life.

1. Geological setting

The 3515 to 3427 Ma Warrawoona group in the East Pilbara Terrane has been favored for studying the oldest and best-preserved Archean rocks on Earth, due to their low metamorphic degrees from prehnite-pumpellyite to greenschist facies (Terabayashi et al., 2003; Brasier et al., 2005; Van Kranendonk, 2006; Van Kranendonk et al., 2007). It is 10-15 km thick and predominantly composed of basaltic rocks intercalated with subordinate felsic volcanic rocks (tuffs and flows), with minor sedimentary rocks such as volcaniclastic rocks, cherty metasedimentary rocks (including carbonate and jasper), and hydrothermal barite and sulfide (Hickman, 1983; Van Kranendonk and Pirajno, 2004; Brasier et al., 2005; Van Kranendonk et al., 2007; Wacey et al., 2016). Displacing earlier tectonic models, including mid-ocean ridge (Ueno et al., 2001; Komiya et al., 2002; Kato and Nakamura, 2003), oceanic island arc (Komiya et al., 2002), and convergent margins involving continental magmatic arcs above subduction zones (Bickle et al., 1983, 1993; Barley et al., 1984), the tectonic model of a thick volcanic plateau is favored by recent work (Smithies et al., 2003, 2005, 2007a, b; Van Kranendonk, 2006; Van Kranendonk et al, 2007a, b, 2019; Rouillard et al., 2021), with support from the geochemistry of Archean basalts that are identical to modern oceanic plateau basalts (Barnes and Arndt, 2019).

Apex Basalt, which forms the middle section of the Warrawoona Group, overlies the

Duffer Formation that is dominated by dacite and conglomerate in the eastern part, and underlies a thick alternation of sandstone and mudstone of the Panorama Formation in the western part (Nakamura and Kato, 2004). Depositional age of Apex Basalt is regarded as between 3463 and 3454 Ma on the basis of zircon U-Pb ages of the underlying Duffer Formation (Thorpe et al., 1992; McNaughton et al., 1993) and overlying Panorama Formation (Thorpe et al., 1992). It consists mainly of pillowed tholeiitic basalts with subordinate massive komatiitic basalts (high-Mg) and intercalated bedded cherts, with indictive pillow shapes showing the stratigraphic younging direction "top to the west" (Nakamura and Kato, 2004; Brasier et al., 2005). This formation shows evidence of submarine volcanism, including chilled margins, hyaloclastic breccias, and pillow basalt textures (Brasier et al., 2005; Sforna et al., 2014). In addition, dolerite as massive lava, intrusions and dikes, is also common and locally present (Van Kranendonk and Hickman, 2000; Nakamura and Kato, 2004). The geochemical and geological relationships consistently indicated that the tholeiitic basalt units in Apex Basalt were remnants of oceanic crust, so that the hydrothermal alteration, including carbonatization and silicification of the basalts, was studied to decipher seafloor hydrothermal activities in the Early Archean (Nakamura and Kato, 2004).

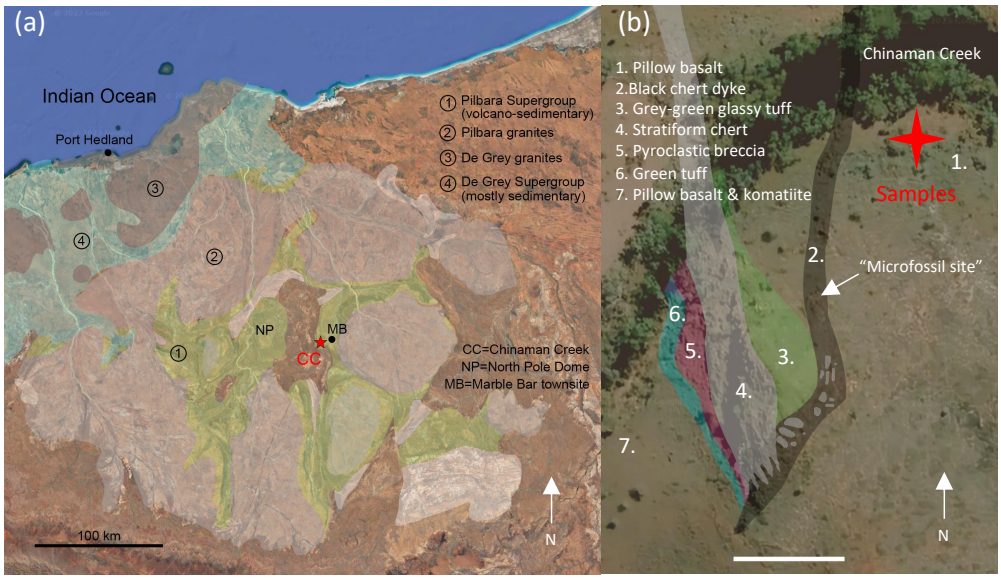

Fig. 1 Sample locality of Apex pillow basalts in this study. (a) Overview of the East Pilbara Terrane of the Pilbara Craton, Western Australia (Google Earth satellite view), showing the location of the Apex chert at Chinaman Creek (CC) (modified from Wacey et al., 2015). (b) Google Earth satellite view of the sample locality (red star) at Chinaman Creek, overlain with the geological map modified from Brasier et al. (2011). The controversial fossil site (Schopf, 1993) is indicated by white arrow.

The samples of Apex pillow basalts were collected at the Schopf's locality (Schopf, 1993) in the vicinity of Chinaman Creek, between a large black chert dike hosting controversial microstructures and stratiform chert (Fig.1). This area is located at the western end (top) of a ca. 1500m long fault, which defines the southern margin of the northern structural block (Brasier et al., 2005). Adjacent to Chinaman Creek, the basalt pillows exhibit dark chilled margins and cores with variable colors ranging from greenish, whitish to light reddish, probably reflecting the progressive alteration and weathering (Fig.2a). Abundant vesicles concentrically gather in basalt core near the margin, and the interspace between pillow basalts is filled with carbonate minerals, chert and basaltic fragments (Fig.2b). The

pillow basalts are locally cut by sharp fractures that first precipitated isopachous crystals of carbonate minerals and then white chert (Fig.2c). Overlying the pillow basalts is a wedge of grey-green tuff and ignimbrite with devitrified glass shards, interpreted as an initial volcanic eruption from the fissure now occupied by the chert dike (Brasier et al., 2005). The felsic tuffaceous materials can be observed within the overlying stratiform chert unit, informally called the "Apex chert". This unit is mainly characterized by (1) planar bedding with moderate to good local grain sorting and grain orientation, and (2) several volcanic-sedimentary subcycles that are indicated by the 1-5 m thick rhythms of tuffaceous and jaspilitic chert near the base to black and brecciated chert on the top, testifying to a primary sedimentary origin (Brasier et al., 2005).

Fig. 2 Photos of Apex Basalt at the outcrop shown in Fig.1. (a) Apex basalts consist of crystalline core and chilled margin, with the pillow-shape indicating the younging direction "top to the west" (white arrow). (b) Interspace between vesicular pillow basalts is filled with pink carbonate minerals (white arrows) and minor white chert. (c) Fracture cuts across pillow basalt and is filled first by isopachous carbonate crystals (white arrows, the brown color is caused by weathering) and then cemented by white chert.

The "microfossils" (Schopf and Packer, 1987; Schopf, 1993; Schopf et al., 2002, 2018) are preserved in the black chert dike (N1), which cuts obliquely upward through underlying pillow basalts and intersects the base of the stratiform chert (Brasier et al., 2005; Rouillard et al., 2021). The stratiform chert is incompletely penetrated by the black chert dike, and large (<1m), angular to rounded clasts of stratiform chert float in the upper part of the dike, indicating they were likely deposited around the same time, although part of the stratiform chert may predate the chert dike (Brasier et al., 2002, 2005; Van Kranendonk, 2006; Hickman-Lewis et al., 2016). Units of pyroclastic breccia and green tuff successively overlie the stratiform chert and black chert dikes. The clasts of black chert and stratiform chert within the pyroclastic breccia indicate that both were lithified prior to the commencement of the next volcanic cycle, followed by the eruption of pillow lava (Brasier et al., 2005, 2011; Hickman-Lewis et al., 2016). Numerous secondary quartz veins cut across the chert dike and stratiform chert during a later regional metamorphic overprint (Sforna et al., 2014). Van Kranendonk (2006) suggested that the stratiform Apex chert represents an extensively silicified seafloor sediment fed by swarms of black chert hydrothermal dikes. The interpretation was confirmed by the chert ^{30}Si values, that the strongly negative ^{30}Si values of black chert dikes and the slightly positive values of stratiform chert were indicative of a mixing gradient from hydrothermal fluids to seawater occurring around vents (van den Boorn et al., 2007).

2. Methods

2.1 Petrography and in-situ geochemical analysis

Petrographic thin sections (polished, ca. 60 μm thick) of Apex pillow basalts were prepared and studied using a Zeiss SteREO Discovery V12 stereomicroscope coupled to an AxioCam MRc camera. Raman spectra of ambiguous minerals were obtained using a Horiba Jobin-Yvon LabRam-HR 800 UV spectrometer with a focal length of 800 mm and an excitation wavelength of 488 nm by an Argon ion laser (Melles Griot IMA 106020B0S), calibrated using a silicon standard with a major peak at 520.4 cm^{-1}. The spectra were processed using Fityk (Wojdyr, 2010) and comparatively analyzed based on references from RRUFF database. In-situ geochemical analysis was achieved using a Bruker M4 Tornado micro-X ray fluorescence instrument equipped with a XFlash 430 Silicon Drift Detector. Measurements were performed at 50 kV voltage with a spot size of 20 μm and a chamber pressure of 20 mbar, and 400 μA for element mapping and 200 μA for point spectra, respectively. All procedures and measurements (here and following) were carried at the Geoscience center of Göttingen University.

2.2 Geochemistry via acid-digestion procedure

Three of the best-preserved sections, A22, ABAS, and A14673, were selected for studying the geochemical compositions of different basaltic lithologies. The criteria for selection included: (1) good preservation of (at least one) primary volcanic structures, including holocrystalline pillow cores, spherulitic zones, variolitic zones, glassy zones and breccia; (2) pristine facies of the neighbor interstitial carbonate on the same section, such as acicular crystal-fan calcite (Chapter 2). These criteria were used to screen out the least altered samples and to avoid ambiguity caused by samples with various degrees of alteration.

2.2.1 Sample preparation

The chips (diameter ~1 cm) of basalt core, margin and breccia were drilled from sample sections, respectively. They were ultrasonically cleaned in ethanol for three times and dried at room temperature before being crushed into small pieces. To minimize interference from interstitial carbonate, basaltic pieces were handpicked and then powdered in an agate mortar. Approximately 0.02 g of basalt was digested in 2.00 mL of concentrated HNO_3 and 1.00 mL HF for 24 hours at 90 °C, then dried down and refluxed in 5 mL 6 $mol \cdot L^{-1}$ HCl for another 24 hours at 90°C, dried, and refluxed in 1.5 mL 2.5 $mol \cdot L^{-1}$ HCl at 70 °C for 15 hours. Finally, the solutes were dried down and refluxed in 0.5 $mol \cdot L^{-1}$ HNO_3 for the next procedures. No insoluble fraction was observed during digestion. Procedure blanks and the international reference materials of basalt W-2 and JB-2 were digested in the same procedure for reproducibility and quality controls, respectively.

2.2.2 Elemental concentrations

The concentrations of major and minor elements were determined using an inductively coupled plasma-optical emission spectrometry (ICP-OES) Agilent 5100 VDV. An aliquot of digested sample solutions was diluted to 10 mL in 2 wt% HNO_3 + 0.5 wt % HCl, and the individual dilution factors were calculated gravimetrically. A blank solution and six calibration solutions of matched multi-elements were measured first for calibration. The procedural blanks were measured firstly, and the average values were subtracted element-by-element from the measured values of samples before calculating element concentrations with individual dilution factors. The two measurements of JB-2 bracketed the measurements of samples, and the standard deviations of JB-2 were used to estimate the precision of the measurement for basalt.

The measurement of trace element concentrations was carried out on ThermoFisher Scientific iCAP Q ICP-MS equipped with an apex-IR desolvating nebulizer with a PFA spray chamber, using the same procedure described in Chapter 3. Spectral overlaps of oxide formation like $^{135}Ba^{16}O^{+}$ on $^{151}Eu^{+}$, $^{141}Pr^{16}O^{+}$ on $^{157}Gd^{+}$, $^{146}Nd^{16}O^{+}$ on $^{162}Dy^{+}$, were reduced by mathematical corrections based on the measurement of two standard solutions performed with the same procedure, containing 20 ppb Ba-Nd and Pr, respectively. Oxides of Ce were lower than 0.6 %, which can be overlooked. The results of reference materials JB-2 and W-2 were shown in Table S1, after correction for matrix effects by W-2, indicating a long-term precision of REEs < 10% (RSD) and an accuracy < 10%, compared with the values reported in Dulski (2001). Afterwards, concentrations of ^{45}Sc, ^{47}Ti, ^{51}V, ^{60}Ni, ^{66}Zn, ^{85}Rb, ^{88}Sr, ^{89}Y, ^{90}Zr, ^{95}Mo, ^{137}Ba, ^{139}La, ^{140}Ce, ^{141}Pr,^{146}Nd, ^{147}Sm, ^{153}Eu, ^{157}Gd, ^{159}Tb, ^{162}Dy, ^{165}Ho, ^{166}Er, ^{169}Tm, ^{172}Yb,^{175}Lu, ^{178}Hf, ^{232}Th, and ^{238}U were used to represent the concentration of relative elements. To eliminate the herringbone-type distribution patterns due to nucleosynthesis-related differences in the abundance of elements with odd and even atomic numbers (Schmitt et al. 1963; Piper and Bau 2013) and conveniently compare, the concentrations of REE and Y are normalized to Primitive Mantle (PM, after Palme and O'Neil, 2014). Y was inserted between Dy and Ho since the ionic radius Y (+3: 1.02 Å) is similar to that of Dy (+3: 1.03 Å) and Ho (+3: 1.02 Å) (https://chemglobe.org/ptoe/), and non-normalized Y/Ho weight ratios were used to estimate the anomalous behavior of Y with respect to the REEs.

2.2.3 Radiogenic Sr isotopic composition

The aliquots of sample solutions and reference materials JB-2 were spiked with ^{87}Rb-^{84}Sr tracer solutions and purified to collect Rb and Sr solutions using BioRad AG 50 × 8 (200–400 mesh) resin and Triskem Sr-spec Resin (50–100 μm), respectively, as detailed in Chapter 3. The measurements were performed using a ThermoFisher Scientific Neptune Plus MC-ICPMS equipped with a Teledyne Cetac Aridus3 desolvation system to introduce sample solutions into the plasma. The $^{86}Sr/^{88}Sr$ ratio was normalized to 0.1194 using an exponential law. The determinations of $^{87}Sr/^{86}Sr$ ratios were obtained in static ion-collection mode, based on 100 mass scans for sample solutions and 40 scans for procedural blanks, respectively. The

sample solutions were roughly diluted to 100 ppb Sr in 0.5 mol·L^{-1} HNO_3, which was the same as the Sr concentration of an in-house reference ESI, to enable a better determination. ESI and NIST SRM 987 were run between every five samples, and the measurement concluded with reference materials and procedural blanks. Concentrations of Rb were determined using an ID-SF-ICPMS technique, as described in Willbold and Jochum (2005), on a ThermoFinnigan ELEMENT2 mass spectrometer. The current long-term, mean $^{87}Sr/^{86}Sr$ ratio of NIST SRM 987 is 0.710246 ± 0.000009 (2σ, n =48).

The initial Sr isotopic compositions of Apex pillow basalts, with an age of t= 3460 Ma, are calculated using the Rb decay constant λ of 1.397 ± 0.003 × 10^{-11} a^{-1} (Rotenberg et al., 2012), according to the following equation:

$$\left(\frac{^{87}Sr}{^{86}Sr}\right)_P = \left(\frac{^{87}Sr}{^{86}Sr}\right)_I + \frac{^{87}Rb}{^{86}Sr}\cdot(e^{\lambda t} - 1) \quad \text{(Eq.1)}$$

where $(^{87}Sr/^{86}Sr)_p$ is present-day Sr isotope ratio that is measured by mass spectrometry, and $(^{87}Sr/^{86}Sr)_I$ is the initial Sr isotope ratio. The Rb-Sr system can be used in geochronology by plotting $^{87}Sr/^{86}Sr$ (y axis) against $^{87}Rb/^{86}Sr$ (x axis), yielding a linear regression line whose intercept is the initial $(^{87}Sr/^{86}Sr)_I$ of the rock system, and slope $(e^{\lambda t} - 1)$ is used to calculate the age. The geochronology is achieved via IsoplotR (Vermeesch, 2018).

3. Result

3.1 Petrography

The studied Apex basalts exhibit a pillow-shaped structure, consisting of a crystalline core and a transition rind with shattered glassy breccia cemented by carbonate minerals in the interspace (Fig.3a). A distinct concentric structure occurs as a result of progressive crystallization at slower cooling rates toward the interior, which is subdivided into 4 main zones from core to margin based on petrological observation and in-situ geochemical analysis (Fig.3): (1) holocrystalline pillow core, (2) spherulitic zone, (3) variolitic zone, and (4) glassy zone. The shattered breccia in the interspace is labeled as (5). A zone of microcrystalline quartz and chlorite mixture with microcrystalline ankerite and calcite outside of the pillow shape is recognized to be a “migrated” zone (6), where the secondary minerals migrated from the pillow basalt to the interspace (Fig.4i). The zones (2) to (6) constitute the dark greenish transition zone distinguished at the outcrop. Secondary alteration is pervasive and spatially variable, dependent on the primitive lithology and the degree of fracturing that allows significant penetration of fluids into rock. Zones (1) to (5) are described in more details as follows:

Holocrystalline pillow core: The slower cooling rate of the interior of the pillow basalt results in a more crystalline texture, consisting of euhedral plagioclase-olivine-pyroxene

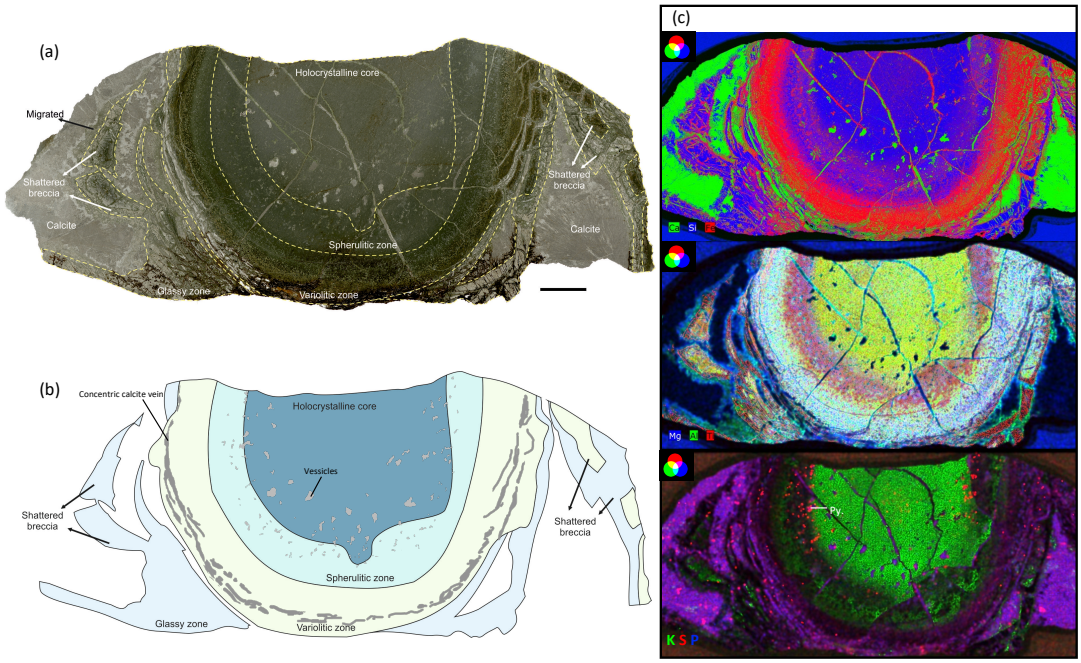

Fig.3 Photographs of the best-preserved pillow structure from Apex Basalt. (a) Scan image (transmitted light) of thin section, showing primary concentric volcanic textures from basalt core to the quenched margin consisting of holocrystalline pillow core, spherulitic zone, variolitic zone, and glassy zone. The shattered breccias are observed in the interspace cemented by interstitial calcite, of which the primary facies is acicular crystal-fan calcite. Scale bar: 1 cm. (b) Sketch of Apex pillow basalt based on (a), showing the distinctive concentric structures. (c) Elemental distributions via Micro-XRF mapping confirm the zoning defined in (a) and (b). Noteworthy, the carbonatization occurred along with Si loss from basalt. (Py.-pyrite).

crystals on a glomeroporphyritic to hyalopilitic groundmass of plagioclase microlites. The vesicles are concentrically zoned, with sizes decreasing from the interior to the margin, and are preserved as amygdules, dominantly filled by calcite and chlorite (Fig.4a). The phenocrysts and groundmass have been replaced by secondary minerals of calcite-chlorite-quartz-anatase ± pyrite (Fig.4b).

Spherulitic zone: This zone is characterized by spherulites consisting of radiating arrays of acicular chlorite-anatase crystals. The size and density of the spherulites decrease progressively towards the margin without a sharp boundary into variolitic zone (Fig.4c).

Variolitic zone: Two features are observed in this zone. One feature is the abundant occurrence of ovoid varioles commonly consisting of three layers: a thin black anatase crust, an intermediate calcite layer mixing with chlorite inwards, and a brown to dark core of calcite-anatase mixture (Fig.4d). The varioles form a dense polygonal texture on an isotropic greenish groundmass (chlorite) and outward become smaller, dispersed varioles on a brown laminated anisotropic groundmass (calcite-anatase mixture) (Fig.4e and f). The other feature is concentric cracks pervasively in the brown outer area that led to more intensive carbonatization of neighboring mafic minerals (Fig.3). The cracks are filled predominantly with blurred calcite (distinct from the later vein-filling fibrous calcite) and minor fine opaque particles of anatase as chains in the middle of calcite.

Glassy zone: This is the outermost layer of pillow basalt where it is progressively altered and thus exhibits the transition from brown mafic volcanic glass with flow structure, to a green alteration layer of chlorite-calcite-quartz, and to microcrystalline quartz with less calcite and chlorite, showing devitrification of the glassy flow structures during alteration (Fig.4g). Chlorite and anatase fill the significant crack net in this area.

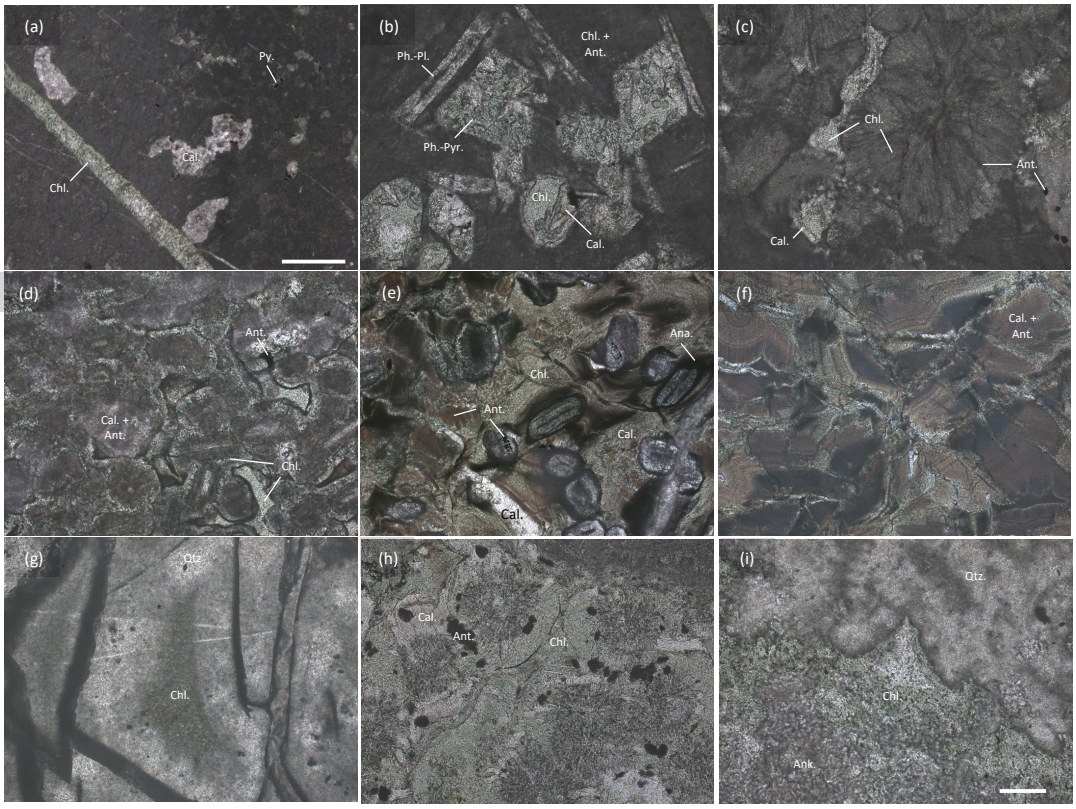

Fig.4 Photographs (PPL) on thin sections of Apex pillow basalts. (a) Holocrystalline pillow core consists of euhedral plagioclase (Pl.)-olivine-pyroxene (Pyr.) crystals and amygdules on the glomeroporphyritic to hyalopilitic groundmass, and locally cut by veins filled with chlorite (Chl.) and calcite (Cal.); (b) The phenocrysts (Ph.) and groundmass are replaced by the secondary minerals of calcite + chlorite + quartz (Qtz.) + anatase (Ant.) ± pyrite (Py.); (c) Spherulites consist of chlorite and anatase on the ground mass of chlorite and calcite; (d) to (f) belong to the variolitic zone where the sizes of anatase-calcite varioles decrease outward the rim, progressively losing the variolitic shapes; (g) microcrystalline quartz and chlorite comprise the glassy zone, showing devitrification of the glassy flow structures during alteration; (h) in basalt breccias, varioles are usually replaced by calcite laths and anatase aggregates on the isotropic chlorite matrix; (i) the secondary minerals of microcrystalline quartz+ chlorite + anatase migrated out from the pillow basalt into interspace, and mixed with ankerite. Scale bar in (a) is 2 mm, while the scale bar of 200 μm is applicable to others. (PPL: Plane-polarized light)

Shattered breccia: The shattered breccias are separated from the pillow basalt during cooling, containing angular clasts of aphyric basalt (with variolitic texture) and glassy shards. Compared with pillow basalt, basalt breccias are more susceptible to later alteration that varioles are usually replaced by calcite laths and anatase aggregates on the isotropic chlorite matrix (Fig.4h).

The entire volcanic structure of the studied Apex pillow basalts is well preserved, and in good agreement with normal tholeiitic pillow basalts from Juan de Fuca Ridge, with the ages varying from 0.8 to 3.5 Ma (Marescotti et al., 2000). However, the pseudomorphic replacement of phenocrysts and groundmass reflects the occurrence of secondary alteration, dominantly carbonatization. In the more altered samples, the primary concentric structure is eliminated, and the phenocrysts are totally replaced by anatase aggregates and epidote crystals crosscut by calcite laths on the green isotropic chlorite groundmass. The primitive structure and secondary mineral assemblage of chlorite + calcite + anatase + micro-quartz ± epidote (Fig.5) indicate the metamorphism degree of greenschist facies, consistent with previous work (Hickman, 1983; Terabayashi et al., 2003; Nakamura and Kato, 2004; Smithies et al., 2005; Van Kranendonk et al., 2002, 2019; Hickman-Lewis et al., 2019).

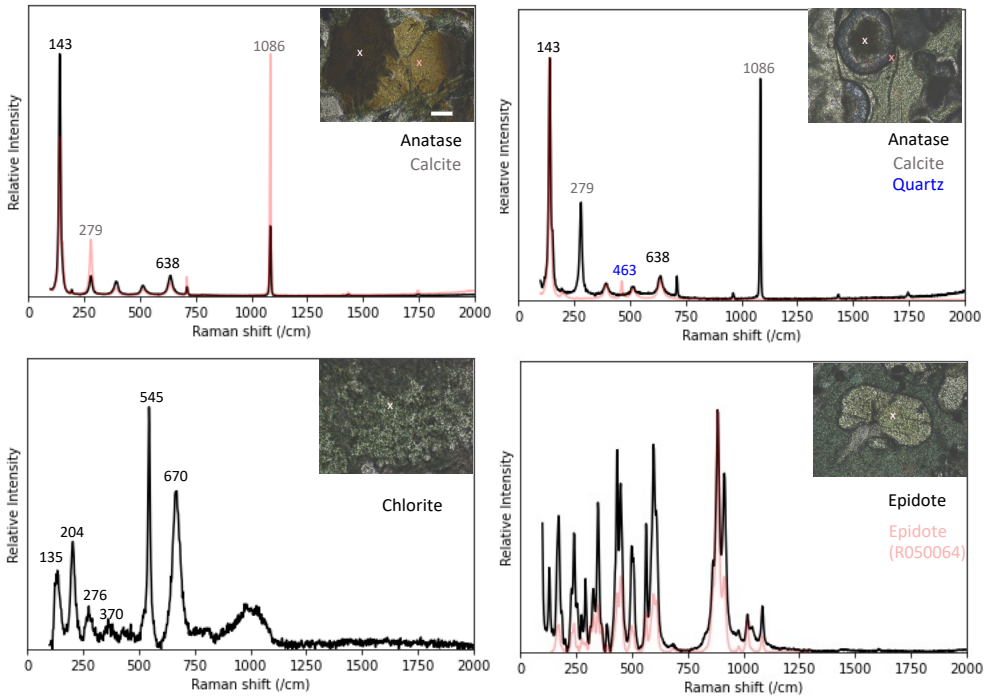

Fig.5 Raman spectroscopy analysis of minerals (crosses on the relative plane-polarized images with a scale bar of 200 μm) in Apex pillow basalts. The white and pink crosses relate to the black and pink line in Raman spectra, respectively. The numbers above the peaks indicate the diagnostic peak of minerals (color related). The mineral assemblage of calcite + chlorite + anatase + epidote + quartz indicates the metamorphism degree of greenschist facies.

3.2 Spatial-resolution geochemistry

In-situ geochemical analysis was achieved via micro-XRF and is shown in Fig.3c. The distribution of Fe, Ca and Si not only supports the distinct concentric structure of pillow basalt but also infers the loss of silica during carbonatization. Si is rich in the holocrystalline pillow core and spherulitic zone, where are the less altered interior of pillow basalt and the outermost glassy zone, respectively. However, it is lean in the variolitic zone where calcite predominantly constitutes varioles and concentric veins. The co-variation of Fe, Mg and Al corresponds to the existence of chlorite $(Mg,Fe)_3(Si,Al)_4O_{10}(OH)_2 \cdot (Mg,Fe)_3(OH)_6$, and Ti is commonly in anatase TiO_2, which is a common secondary product of Ti-bearing minerals

during low-temperature alteration of volcanic rocks. The migration of chlorite and quartz from basalt to interstitial space is identified by the distribution of the relative elements extending out of the glassy rim, while anatase is mainly fixed within the basalt. The spatial correlation of S and P with Ca or Fe infers their enrichment in carbonate facies or pyrite, where K is rich in the pillow core, spherulitic zone, and partly in breccias. To obtain better data on trace elements, the geochemistry of different concentric basalt zones was measured through acid-digestion of subsample chips drilled from three best-preserved sample sections (A14673, A22 and ABAS). The subsample locations are shown in Fig.6 and the concentrations of major, minor and trace elements are shown in Table 1.

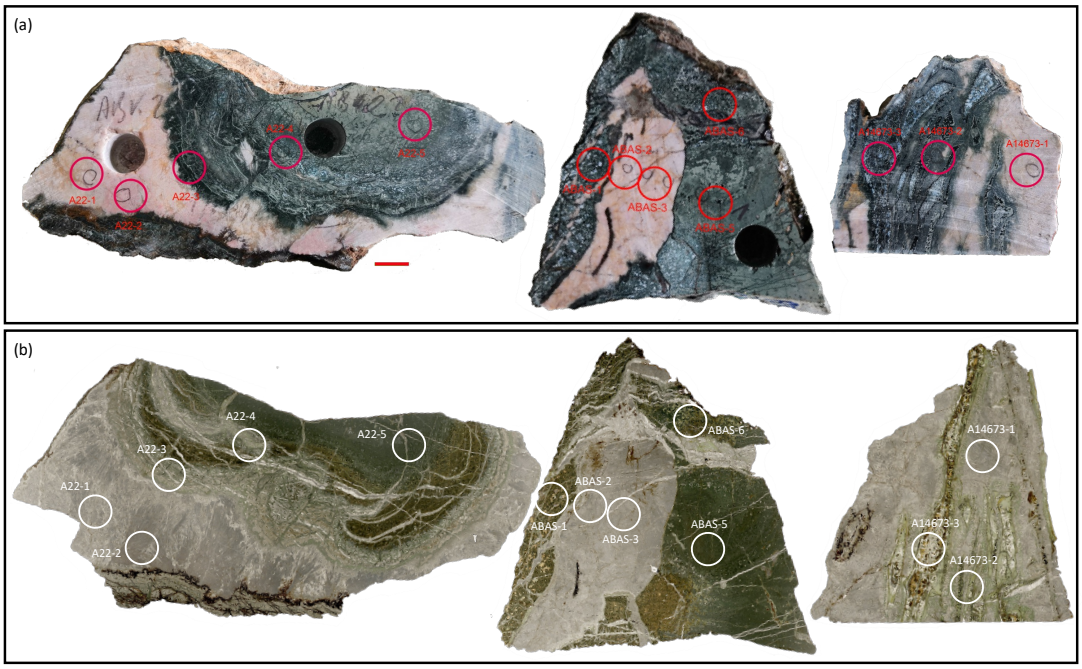

Fig.6 Photos of subsamples (columns of ca. 1 cm in diameter) drilled from (a) section A22, ABAS and A14673 (Scale bar: 1 cm). (b) Their lithologies are indicated on the relative thin sections (not completely matching; the scan images were taken under transmitted light).

3.2.1 Major, minor and trace element

The concentrations of major and minor elements acquired through acid-digestion confirm the covariations observed in the in-situ geochemical analysis (Fig.7). Fe correlates with Al and Mg, and enriches in the basalt interior and decreases from 14.18 to 5.61 wt%, while Al decreases from 8.74 to 2.99 wt% and Mg decreases from 5.57 to 2.11 wt%. Contrary to this “chlorite” distribution, Ca and Mn are rich in carbonatized parts at the margin and breccia, increasing from 2.46 to 20.01 wt% and 0.09 to 0.35 wt%, respectively. V, Ni and Zn show the same distributions with chlorite (Fe, Al, Mg), with the concentrations from 135.89 to 419.27 ppm, 45.52 to 132.25 ppm, 29.25 to 69.82 ppm, respectively, while the

Table 1 Geochemical compositions of Apex pillow basalts

SampleID	A22-3	A22-4	A22-5	ABAS-1	ABAS-5	ABAS-6	A14673-2	A14673-3
Position	(4)+(5)	(2)+(3)	(1)+(2)	(3)	(1)	(2)	(6)	(6)
(wt%)								
Al	2.99	4.67	5.18	5.26	6.24	8.74	3.44	6.67
Ca	11.84	18.00	6.14	20.01	2.46	6.67	14.68	17.70
Cu	0.01	0.03	0.00	0.01	0.01	0.07	0.01	0.04
Fe	5.61	9.82	8.74	8.60	10.01	14.18	5.97	10.93
K			0.27					
Mg	2.11	3.23	3.09	3.33	3.95	5.57	2.80	5.05
Mn	0.25	0.22	0.14	0.35	0.09	0.18	0.27	0.22
Na			0.19					
(ppm)								
Sc	19.270	41.979	28.325	46.015	32.415	48.988	16.937	47.724
Ti	1273.504	4332.824	6168.394	4750.752	5687.516	6403.443	1995.228	8829.781
V	135.894	214.533	238.690	257.894	279.777	419.271	155.987	328.748
Ni	45.519	82.208	84.986	75.677	83.798	132.253	56.763	118.273
Zn	30.790	55.991	47.019	40.105	48.847	69.819	29.253	51.024
Rb	5.365	0.955	10.806	1.248	3.152	0.543	0.074	0.048
Sr	43.152	65.089	31.703	88.154	14.651	32.237	51.080	48.832
Y	11.730	10.760	7.850	14.515	9.097	5.661	7.208	13.704
Zr	10.134	27.948	45.735	30.664	25.934	34.762	15.491	55.578
Mo	0.159	0.156	0.490	0.158	0.288	0.215	0.163	0.195
Ba	18.591	5.277	32.875	20.629	58.523	12.533	8.347	4.992
La	1.260	1.772	2.521	1.954	17.777	0.592	1.203	2.805
Ce	3.351	5.198	7.939	5.022	51.128	1.675	3.568	7.831
Pr	0.554	0.889	1.342	0.800	7.707	0.297	0.622	1.280
Nd	3.046	4.747	6.972	4.173	37.155	1.701	3.428	6.650
Sm	1.084	1.586	1.862	1.439	8.306	0.751	1.085	1.961
Eu	0.446	0.783	0.617	0.739	2.168	0.354	0.362	0.760
Gd	1.517	2.021	1.767	2.104	5.072	1.065	1.418	2.368
Tb	0.248	0.304	0.240	0.340	0.471	0.160	0.202	0.341
Dy	1.652	1.877	1.443	2.227	2.004	0.993	1.198	2.039
Ho	0.386	0.405	0.319	0.497	0.377	0.224	0.250	0.456
Er	1.185	1.198	1.005	1.507	1.023	0.709	0.694	1.367
Tm	0.189	0.184	0.164	0.230	0.145	0.118	0.096	0.202
Yb	1.304	1.302	1.169	1.626	0.935	0.898	0.617	1.444
Lu	0.215	0.214	0.188	0.267	0.143	0.153	0.101	0.246
Hf	0.286	0.867	1.489	0.971	0.843	1.068	0.524	1.832
Th	0.060	0.201	0.289	0.175	0.311	0.223	0.081	0.273
U	0.034	0.050	0.067	0.045	0.051	0.057	0.029	0.071
REY	28.168	33.241	35.399	37.441	143.508	15.352	22.054	43.456
Y/Ho	30.4	26.6	24.6	29.2	24.1	25.3	28.8	30.1

Note: The numbers of positions indicate (1) holocrystalline core, (2) spherulitic zone, (3) variolitic zone, (4) glassy zone, (5) migration zone and (6) basaltic breccia.

concentrations of P and Mo decrease from 0.07 wt% to 0 and 0.49 to 0.16 ppm, respectively. In addition, the concentrations of Ti range from 1273.50 to 8829.78 ppm, except for samples A14673-2 (breccia) and A22-3 (basalt carbonatized and glassy rim), which can be classified as high-Ti basalts (TiO_2 > 0.8 wt % and Ti > 4800 ppm). These are the most common type of tholeiitic basalts in the Pilbara Supergroup, originating from independent evolution of mantle plumes (Smithies et al. 2005). Another classification, given by Barnes and Arndt (2019), is based on La/Ti ratios normalized to PM and divides non-komatiitic basalts into low-La, intermediate-La and high-La groupings at La/Ti_{PM} values of 1.4 and 5 (differences of La and Ti concentrations between McDonough and Sun, 1995 and Palme and O'Neil, 2014 do not shift the values). Accordingly, the high-Ti Apex basalts studied in Smithies et al. (2005) are low-La to intermediate-La basalts, while most basalt samples in this work are identified as low-La basalts, with the exceptions ABAS-5 (high-La) and A22-3 (intermediate-La) (Fig.8).

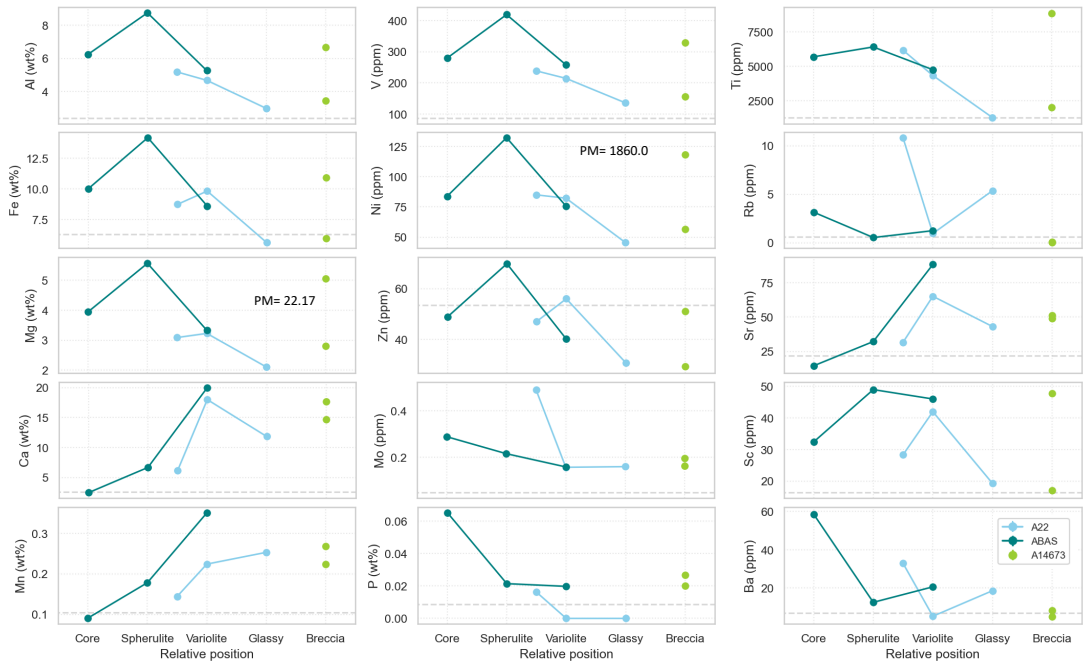

Fig.7 Elemental concentrations of various domains that are (from basalt core to rim) basalt core, spherulitic zone, variolitic zone, glassy zone and breccia. The grey dashed line indicates the elemental concentrations of Primitive Mantle (Palme and O'Neil, 2014), that the out-of-range values are given in numbers, e.g. in plots of Mg and Ni.

3.2.2 REE+Y pattern

The PM-normalized REE+Y patterns are plotted in Fig.9, sorted by Apex pillow basalts, their neighboring interstitial carbonates, and Apex basalts grouped by Ti concentrations and La/Ti_{PM} values. The least altered samples of pillow interior (ABAS-5 and A22-5) are characterized by strong LREE enrichment in line with pillow basalts of Euro Basalts (Yamamoto et al., 2004), with the closest similarity to the patterns of high-Ti and intermediate-La basalts. However, the partly carbonatized samples are prone to show similar patterns to their neighboring interstitial carbonates, consistent with those of carbonate minerals within pillow basalts from Euro Basalt (Yamamoto et al., 2004). The Y/Ho weight ratios of Apex pillow basalts range from 24.12 to 30.38, with a mean value of 27.37 ± 2.54, comparable to the chondritic value of 26 to 28 (Kamber and Webb, 2001; Pack et al., 2007;

Palme and O'Neil, 2014).

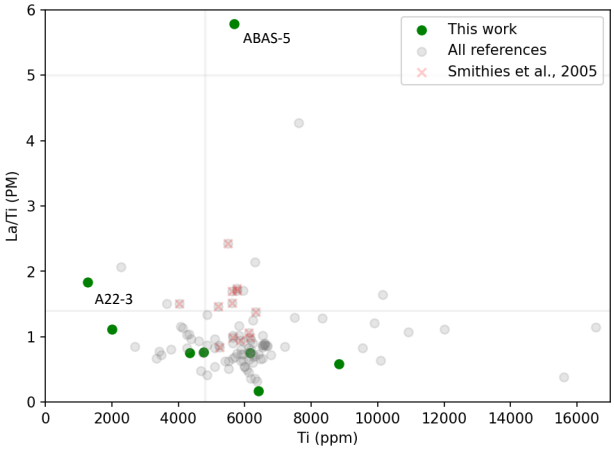

Fig.8 Classification of Apex basalts in this work and from references, based on two criteria at Ti concentration of 4800 ppm defining low- or high-Ti basalts (Smithies et al. 2005), and at the PM-normalized La/Ti values of 1.4 and 5 defining low-, intermediate- and high-La basalts (Barnes and Arndt, 2019), respectively. PM refers to Primitive Mantle with values from Palme and O'Neil (2014). Data of 'All references' are from Nakamura and Kato, 2004; Van Kranendonk and Pirajno, 2004; Smithies et al., 2005; Tusch et al., 2021; Tympel et al., 2021.

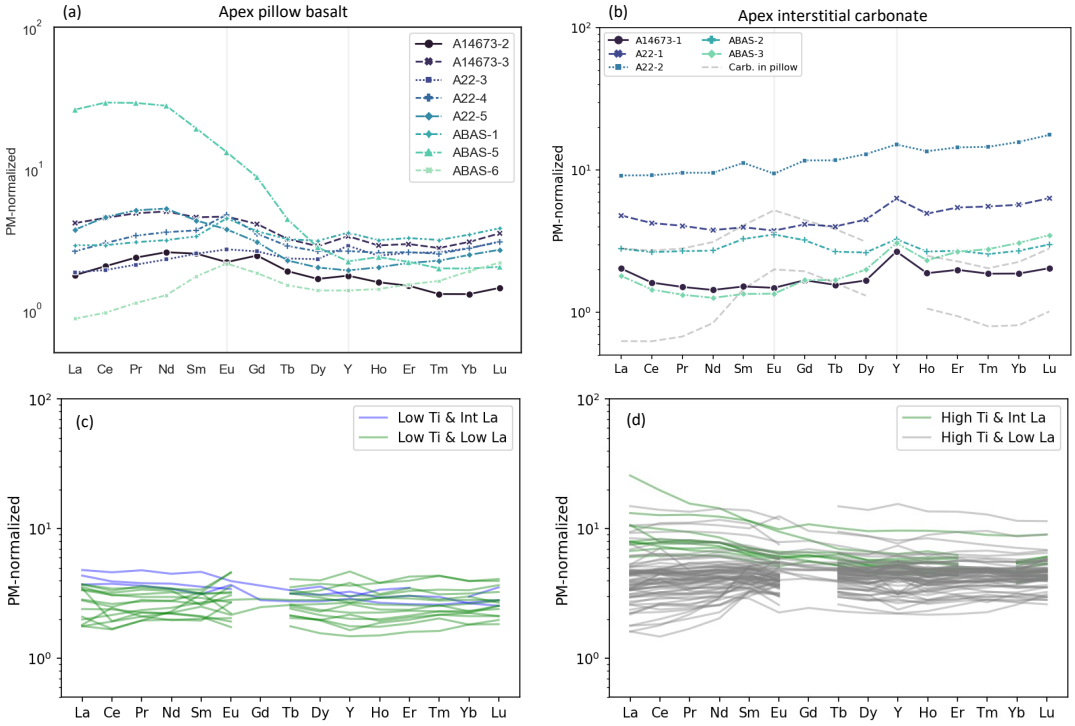

Fig.9 The PM-normalized REE+Y patterns of Apex pillow basalts (a) and (b) their neighbor interstitial carbonates where the grey dashed lines indicate carbonate minerals in the quenched margin of Euro pillow basalts (Yamamoto et al., 2004). PM refers to Primitive Mantle with values from Palme and O'Neil (2014). Reference data from Nakamura and Kato, 2004; Van Kranendonk and Pirajno, 2004; Smithies et al., 2005; Tusch et al., 2021; Tympel et al., 2021 are plotted according to four basalt types: (c) the low-Ti, low-La basalts and low-Ti, intermediate-La basalts; (d) the high-Ti, low-La basalts and high-Ti, intermediate-La basalts.

3.2.3 Rb-Sr isotopic compositions

The Rb-Sr isotopic compositions of Apex pillow basalts are listed in Table 2, and the initial $^{87}Sr/^{86}Sr$ ratios are plotted in Fig.10, together with the initial $^{87}Sr/^{86}Sr$ ratios of neighboring interstitial carbonates and fracture-filling carbonates, which were distinguished as seawater carbonate at 3.5 Ga (Chapter 3). The Sr concentrations of Apex basalts range from 12.05 to 77.98 ppm, with an average value of 41.21± 20.26 ppm, increasing from the core to margin and breccia. In contrast, the Rb concentrations commonly decline from 8.31 to 0.03 ppm, and carbonatized parts usually have relatively lower Rb and higher Sr concentrations. The initial $^{87}Sr/^{86}Sr$ ratios of Apex pillow basalt range from 0.703207 to 0.707742, with an average value of 0.705828 ± 0.001568. For individual sample section, the initial $^{87}Sr/^{86}Sr$ ratios of basalts are consistently higher than those of neighboring interstitial carbonates, showing declines in radiogenic Sr isotopic compositions from basalt to interstitial carbonate to seawater carbonate (Fig.10).

Table 2 The age-corrected radiogenic Sr isotopic compositions of Apex pillow basalts (3460 Ma)

SampleID	Sr (ppm)	Rb (ppm)	$^{87}Rb/^{86}Sr$	$^{87}Sr/^{86}Sr$	2sigma (2σ)	N	$^{87}Sr/^{86}Sr$ (i)
A14673-2	45.06	0.06	0.0037	0.706667	0.000004	97	0.706483
A14673-3	43.31	0.03	0.0021	0.703997	0.000004	96	0.703894
A22-3	37.75	4.34	0.3323	0.723341	0.000004	98	0.706605
A22-4	57.94	0.8	0.0397	0.709187	0.000004	98	0.707188
A22-5	27.27	8.31	0.8813	0.752124	0.000004	98	0.707742
ABAS-1	77.98	1.05	0.0389	0.705166	0.000004	96	0.703207
ABAS-5	12.05	2.38	0.5708	0.734342	0.000007	95	0.705601
ABAS-6	28.3	0.45	0.0462	0.708230	0.000004	97	0.705904
JB-2	166.86	5.63	0.0976	0.703710	0.000004	99	0.703711

Note:
1. $^{86}Sr/^{88}Sr$ ratio was normalized to 0.1194 using an exponential law.
2. $^{87}Sr/^{86}Sr$ ratio of NIST SRM 987 is 0.710246 ± 0.000009 (2σ, n =48).
3. $^{87}Sr/^{86}Sr$ (i) are $^{87}Sr/^{86}Sr$ ratios after correction of Rb and age.

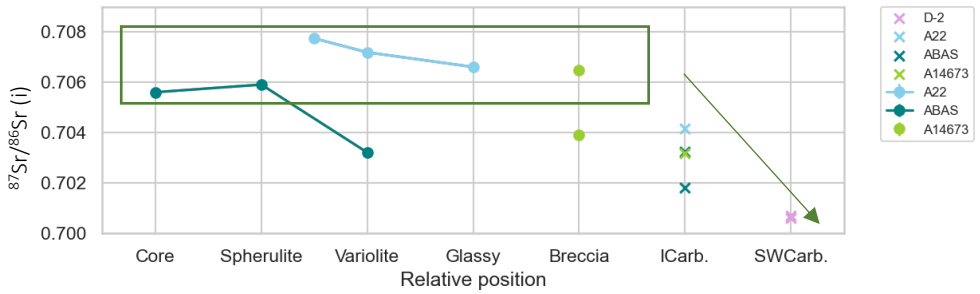

Fig.10 The initial $^{87}Sr/^{86}Sr$ ratios of Apex pillow basalts against relative positions on sample sections, the neighbor interstitial carbonates, and seawater carbonate D-2 from Dresser Formation. A decline of the initial $^{87}Sr/^{86}Sr$ ratios is observed from basalt to interstitial carbonate to seawater carbonate (green arrow).

The occurrence of secondary minerals replacing protolith indicates metamorphic events after the eruption of Apex pillow basalts. Thus, the results more likely date the metamorphic system rather than igneous crystallization. Mineral and whole-rock Rb–Sr systems may respond differently to metamorphic events corresponding to their Rb/Sr ratio, that individual minerals are open systems in which Rb and Sr redistribute during metamorphism, however, a whole-rock domain of a certain minimum size may remain an effectively closed system

during low-grade regional metamorphism (Lanphere et al., 1964; Dickin, 2018). The Rb-Sr isotope ratios of different minerals are homogenized to the whole-rock value due to metamorphism, and re-evolutions of mineral Rb-Sr systems occur afterward along a new isochron whose intercept yields the whole-rock value at the age of metamorphism that can be calculated by the slope (Compston and Pidgeon, 1962; Gebauer and Grünenfelder, 1974). The Rb–Sr isochron based on all Apex pillow basalts (n=8) yields an age of 3695.3 ± 231.1 Ma and an initial $^{87}Sr/^{86}Sr$ ratio of 0.705198 ± 0.001327 with mean squared weighted deviates (MSWD) of 440 (Fig.11a), implying the age is over-dispersed with respect to the stated analytical uncertainties. After excluding two highly carbonatized samples (A14673-3 and ABAS-1), the 6-points Rb–Sr isochron yields an age of 3570.7 ± 144.3 Ma and an initial $^{87}Sr/^{86}Sr$ ratio of 0.706337 ± 0.000954 with MSWD= 150 (Fig.11b). The large MSWD value illustrates that it is an errorchron instead of an isochron.

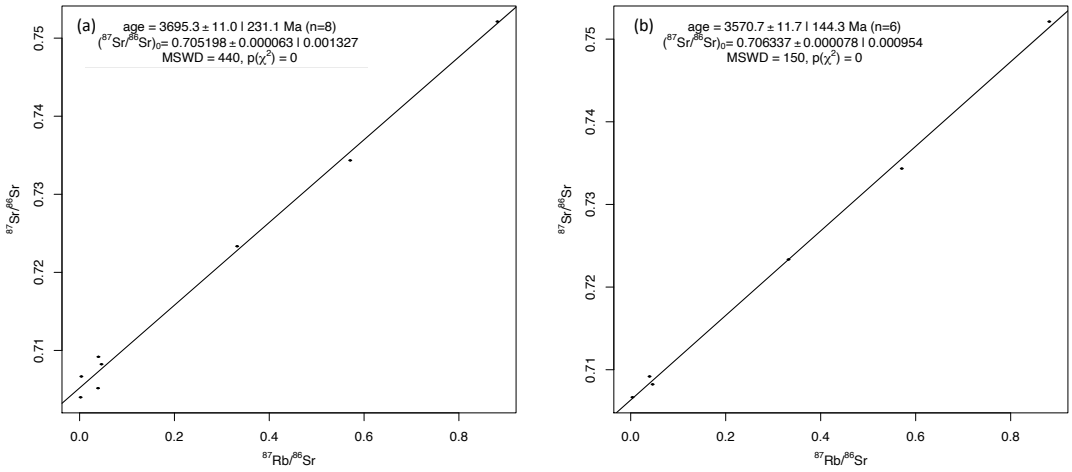

Fig.11 The Rb–Sr whole-rock isochron diagram for Apex pillow basalts, produced using IsoplotR (Vermeesch, 2018). (a) The large MSWD indicates the 8-point isochron is an errorchron. (b) After excluding two highly carbonatized subsamples, a 6-point errorchron yields an age of metamorphism identical to the depositional age (ca. 3460 Ma) of Apex Basalt.

4. Discussion

4.1 Magma source of Apex pillow basalt

The studied Apex pillow basalts belong to the lower tholeiitic basalt unit of Apex Basalt (Kato and Nakamura, 2003; Smithies et al., 2005; Brasier et al., 2005). Its origin has been intensively debated, including mid-ocean ridge basalt (Kato and Nakamura, 2003; Nakamura and Kato, 2004), island-arc and/or continental margin arc (Kitajima et al. 2001), and originally plume-derived oceanic plateau basalt (Van Kranendonk and Pirajno., 2004; Smithies et al., 2005; Van Kranendonk et al., 2007, 2010, 2015, 2019; Barnes and Arndt, 2019; Hasenstab et al., 2021; Tusch et al., 2021). Considering the elemental mobility during alteration, it is difficult to classify altered Archean basalts with the same criteria applied to fresh modern basalts like (SiO_2 vs. $Na_2O + K_2O$; (Mg-FeO-Na_2O+K_2O) (Barnes and Arndt, 2019). Instead, the concentrations of lithophile incompatible elements (Ti, Y, Zr, Nb, La, etc.)

and the REE distribution are more plausive for the relative immobility during alteration and invariant element ratios during crystal fractionation processes (Barnes et al., 2012; Caruso et al., 2021). Smithies et al. (2005) subdivided tholeiitic basalts of the Pilbara Supergroup into high-and low-Ti basalts, and as high Ti basalt Apex Basalt was derived through partial melting of a source with a composition approaching that of Primitive Mantle (PM, Condie, 2005), most likely associated with mantle plumes, in line with the presence of komatiites flows within generally basaltic sequences (Arndt et al., 1997, 2001; Arndt, 2003). A similar interpretation was suggested by the classification of Archean non-komatiitic basalts based on PM-normalized La/Ti ratios, where the low-La basalts are commonly tholeiites generated by smaller degree partial melts of the same mantle sources producing the komatiites, and the progression from low-La basalts to high-La basalts reflects progressively increasing degrees of crustal contamination and/or derivation of the more enriched samples from subduction settings (Barnes and Arndt, 2019). In this work, the PM-normalized REE+Y patterns of basalt interior parts (core to spherulitic zone) are characterized with LREE enrichment, showing the closest similarity to high-Ti and intermediate-La basalt (Fig.9), likely implying the origin of mantle plume partly contaminated by the older sialic crust basement during the extrusion (Hickman and Van Kranendonk, 2004; Van Kranendonk and Pirajno, 2004; Van Kranendonk et al., 2007, 2015; Hasenstab et al., 2021).

4.2 Metamorphic event causing carbonatization of Apex Basalt

4.2.1 Carbonatization of Apex Basalt reflects seafloor alteration

Field evidence strongly suggests that Apex pillow basalts at the “microfossil” locality have experienced strong hydrothermal alteration, including carbonatization and silicification around the chert dikes (Brasier et al., 2002; Kato and Nakamura, 2003). The best-preserved samples show distinct concentric structures of submarine volcanism, consisting of holocrystalline core, spherulitic zone, variolitic zone, glassy zone and shattered breccia (Fig.3). Nonetheless, the secondary mineral assemblage of chlorite+ calcite + anatase + micro-quartz ± epidote indicates the metamorphism of greenschist facies, which is ubiquitous in Archean greenstone belts (Hickman, 1983; Kitajima et al., 2001; Terabayashi et al., 2003; Nakamura and Kato, 2004; Smithies et al., 2005; Van Kranendonk et al., 2002, 2019; Hickman-Lewis et al., 2019). The greenschist facies assemblages are common in drilled and dredged metabasalt samples (Von Damm et al., 1985; Alt et al., 1986), which is typical in modern hydrothermally altered upper oceanic crust.

By comparing stratigraphic sequence and metamorphic facies of the greenstone complex capped by bedded cherts exposed in the North Pole (now identified as North Star Basalt) with modern oceanic crust and on-land ophiolites, Kitajima et al. (2001) interpreted it as an on-axis hydrothermal system where carbonate-bearing assemblage indicated the interaction of the Archean upper oceanic crust with CO_2-rich fluid with an estimated X_{CO_2} of 0.012-0.140. The mid–ocean ridge alteration model was supported by Terabayashi et al. (2003), however, refuted by following works that suggest the alteration of North Star Basalt underlying Dresser

Formation was supposed to occur in high temperature and acidic high-sulfidation epithermal systems (Van Kranendonk and Pirajno, 2004; Harris et al., 2009; Brown et al., 2011; Caruso et al., 2021). Van Kranendonk and Pirajno (2004) speculated extensive chlorite–carbonate alteration assemblage and the presence of barite, alunite–jarosite, and high trace metal contents in the immediate footwall of the Apex chert (Brasier et al. 2002) to be indicative of an acid-sulphate epithermal environment similar to that in the Dresser Formation. However, this interpretation cannot explain the pervasion of carbonate minerals in Apex basalt and the interspace, which were more likely precipitated in a CO_2-rich alkaline hydrothermal system, analogous to modern low-temperature off-axis hydrothermal systems (Kelley et al., 2005; Bach and Früh-Green, 2010; Coogan and Gillis et al., 2018). Westall et al. (2018) found a rapid increase in pH of artificial Hadean seawater from initially 6.24 to more alkaline (>7) within the first 3 days during the reaction with volcanic grains of East Pacific Rise basalt and komatiite, and speculated a model that slightly acidic seawater in Hadean permeates through ultramafic/mafic sediments into the crust, altering the ultramafic rocks and becoming more alkaline during these reactions.

The narrow $\delta^{13}C$ values close to zero of carbonate minerals within altered pillow basalts reflect that the carbonate carbon is derived from seawater (Nakamura and Kato, 2004; Chapter 2). In contrast to the speculation of the negligible contribution of mantle and biological carbon (Nakamura and Kato, 2004), the intermediate $\delta^{13}C$ values of most interstitial carbonates, between the more positive $\delta^{13}C$ values of marine carbonates and more negative $\delta^{13}C$ values of highly altered interstitial carbonates and carbonates in veinlets of basalt, reflect the average $\delta^{13}C$ value of zero essentially to be a hybrid signal of marine and mantle carbon (Chapter 2). Despite this divergence, it is agreed that carbonatization of Apex pillow basalts indicates the seafloor hydrothermal alteration, whereby basaltic oceanic crust reacted with circulating CO_2-rich seawater. The proportion of evolved continental crust on the early Earth was likely much lower than today (Taylor and McLennan, 1981; Cawood et al., 2012), perhaps no more than 50% of present-day volume (Dhuime et al., 2012), most of which was flooded (Arndt, 1998; Flament et al., 2008). However, the oceanic crust was more abundant, thicker (up to 20 km; Sleep and Windley, 1982), and subject to more widespread off-axis hydrothermal alteration under a lower thermal gradient (Russel and Arndt, 2005). Under such conditions, seafloor alteration may have been a significant or even dominant CO_2 removal process (Kitajima et al. 2001; Nakamura and Kato, 2002, 2004; Yamamoto et al., 2004; herein), and as part of the carbonate-silicate cycle, it plays an important role in keeping Earth habitable (Kasting, 2019). However, it may be questioned: when did the carbonatization happen? Is the altered Apex basalt truly an archive for seafloor alteration at 3.5 Ga, or later?

4.2.2 Dating carbonatization of Apex Basalt

During its long geological history, the Eastern Pilbara Terrane underwent several thermal events. For example, even in the early Archean, there were at least three times of mantle plume events at 3.53-3.42 Ga (Warrawoona event), 3.35-3.29 Ga (Kelly event), and 3.27-3.24 Ga (Sulphur Springs event), which formed a complex multistage volcanic plateau (Smithies et al., 2005; Huston et al., 2007; Van Kranendonk et al., 2002, 2006a, b, 2007b, 2015; Champion

and Smithies, 2007; Pirajno, 2007a, b). Nonetheless, the best-preserved Apex pillow basalts fortunately survived these thermal events, with evidence of a Rb-Sr errorchron age of 3570.7 ± 144.3 Ma (n=6, MSWD= 150) that is comparable to the depositional age of Apex Basalt. This also demonstrates that the Rb-Sr system of the studied Apex basalt has not been reset since the metamorphism of greenschist facies, which was syn-depositional or occurred soon after the eruption of pillow lava.

According to a comprehensive study of carbonate minerals in the basaltic basement of oceanic ridge flanks, Rausch (2012) suggested that most of these minerals were precipitated within the first 20 to 40 Myrs after the formation of the basaltic crust at mid-oceanic ridges. This is consistent with previous estimates of 10 to 15 Ma (Hart and Staudigel, 1986; Hart et al., 1994), 20 to 25 Ma (Gillis and Coogan, 2011; Coogan and Gillis, 2018), 27 to 40 Ma (Burns et al., 1992), and 40 Ma (Staudigel et al. 1989). Therefore, the validity of syn-depositional carbonatization may extend to the interstitial carbonates within the interspace, which are suggested to remain pristine conditions of their formation and thus be the best archives for reconstructing seafloor alteration in the early Archean. Meanwhile, an initial $^{87}Sr/^{86}Sr$ ratio of 0.706337 ± 0.000954 given by the errorchron can be interpreted as the homogenized whole-rock value of examined Apex pillow basalts due to the syn-depositional metamorphism of greenschist facies (Dickin, 2018).

4.3 Element mobility during metamorphism

In a closed rock system, increase or decrease in weight percent or parts per million (ppm) of an element can be used to estimate mass gain or loss of that element. However, the whole rock is an open system during metamorphism and fluid-rock reactions likely contribute to re-distribution of some elements, causing changes in the mass and/or volume of the rock. If so, the direct application of weight percent or ppm of an element in an altered rock can be problematic in reflecting the actual mass gain or loss of that element, as explained in Ague (2017). In order to avoid this problem and quantify the actual element gains and losses, relative chemical changes have been extensively adopted based on mass balance of an immobile element during metamorphism (Brimhall and Dietrich, 1987; MacLean and Barrett, 1993; Ague, 2017; Caruso et al., 2021). Considering that the EPT basaltic rocks have undergone regional metamorphism of up to greenschist facies (Nakamura and Kato, 2004; Smithies et al., 2005; Van Kranendonk et al., 2002, 2019) and the magma source of Apex basalt is derived from mantle plumes (Condie, 1997, 2001; Smithies et al., 2005; Van Kranendonk et al., 2007, 2010, 2015, 2019; Barnes and Arndt, 2019; Hasenstab et al., 2021; Tusch et al., 2021), approaching compositions of Primitive Mantle (PM, Condie, 2005), the element concentrations of the PM are used for reference (after Palme and O'Neil, 2014). Zr is utilized as the reference element due to its largely immobility during hydrothermal alteration (Finlow–Bates and Stumpfl, 1981; MacLean and Kranidiotis, 1987; Ague, 2017). The total change in rock mass Δm_i^{rm} and the fractional change Δm_i^j of element j on the basis of reference (immobile) element *i* can be calculated as follows:

$$\Delta m_i^{rm} = \left(\frac{C_i^P}{C_i^A}\right) - 1 \quad \text{(Eq.2)}$$

$$\Delta m_i^j = \left(\frac{C_i^P}{C_i^A}\right)\left(\frac{C_j^A}{C_j^P}\right) - 1 \quad \text{(Eq.3)}$$

where C with subscripts i and j are concentrations of reference element i and element of interest j, and the ^{P} and ^{A} superscripts refer to the pristine and altered states, respectively. Percentage changes are obtained by multiplying by 100 to reflect element gain or loss during alteration (gains are positive, losses negative). More details about the method can be seen in Appendix. The mass gains or losses of rock mass, major and trace elements are shown in Fig.12, and those of Si and Ca against relative positions on the basalt are plotted in Fig.13 based on point spectrum via micro-XRF (see Appendix). The Apex basalts all lost rock mass, which is attributed to volatile loss (H_2O, CO_2, Ague, 2017) as indicated by concentric vesicles at the outer part of the pillow basalts (Fig.2b).

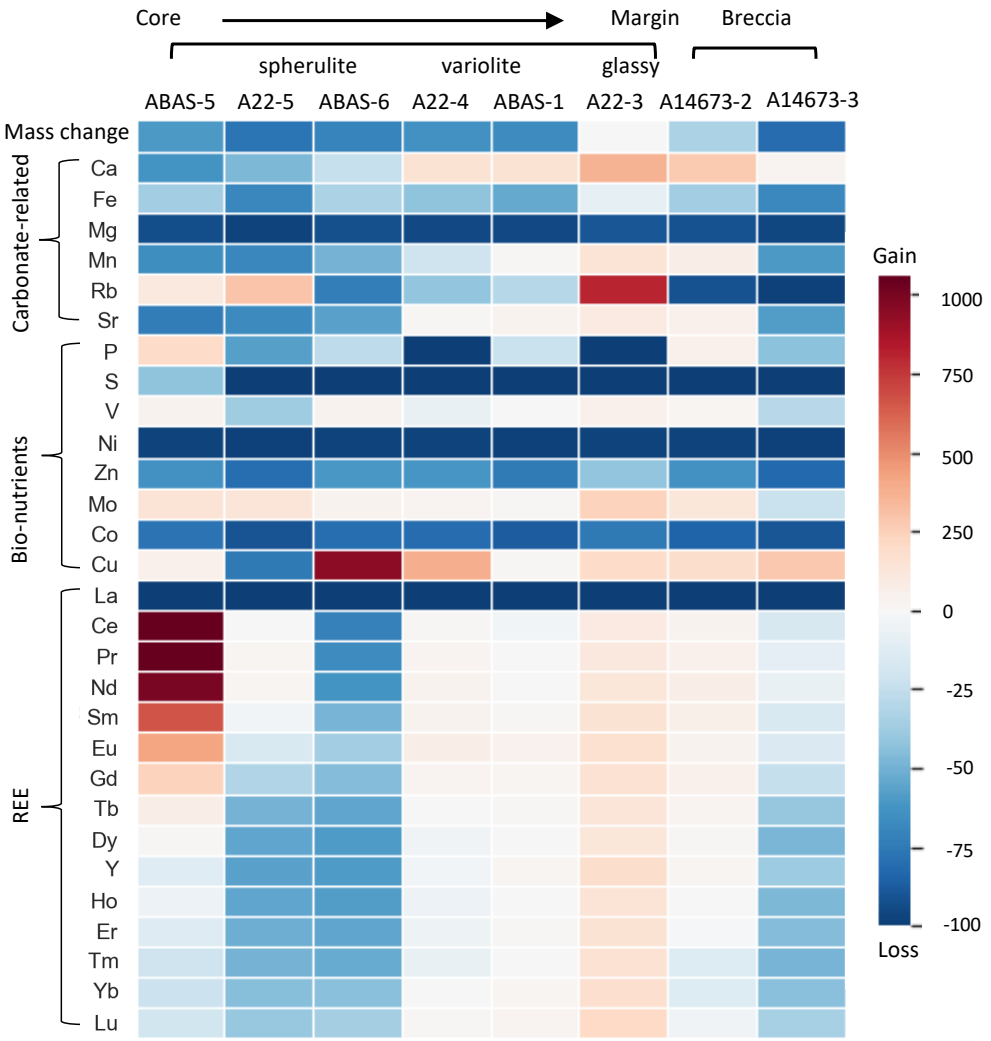

Fig.12 Heatmaps illustrating elemental mass changes of spatial-related subsamples from the core to margin and breccia of Apex pillow basalts. The warm colors indicate mass gains and the cold colors indicate mass losses.

4.3.1 Carbonate-related elements and Si

The carbonate minerals are the dominant interstitial materials between pillow basalt and are suggested to precipitate abiotically from the brine solution of high alkalinity derived from basalt-seawater interaction (Chapter 2). The basaltic origin of carbonate-related elements like Ca, Mg, Fe, Mn and Si have been well documented by bench-scale experiments within a large temperature range from 22 to 350 °C (Gudbrandsson et al., 2011; Stockmann et al., 2011; Galeczka et al., 2013a,b, 2014; McGrail et al., 2017; Menefee et al., 2018; Wolff-Boenisch and Galeczka, 2018; Xiong et al., 2018; Voigt et al., 2018), Si isotopes of chert (Van den Boorn et al., 2007), and numerical simulations (Gysi and Stefánsson, 2011). The losses of Si, Al, Fe, Mn, Mg and Ca during carbonatization of Apex basalts were observed based on the enrichment factors (>1 gain and <1 loss) using the least altered dolerite of Apex Basalt and Ti for the baseline (Nakamura and Kato, 2004). This interpretation is supported by the mass gains and losses of these carbonate-related elements in this work. Consistent with in-situ geochemical analysis (Fig.3c), the core and spherulitic zone of the pillow basalt lose Ca during the water-rock interaction, while the variolitic zone, glassy zone, and breccia, which are carbonatized, exhibit Ca gains. Fe and Mg are consistently lost from the entire basalt, while Mn and Sr show covariation with Ca being lost from the interior part, implying their preferred incorporation in carbonate. Considering the Rb-Sr isotopic system, Rb is also listed here and shows loss in the variolitic zone and breccia. Therefore, the alkaline metals that precipitate carbonate minerals within pillow basalt as secondary mineral and in the interspace as interstitial materials, are indeed derived from the breakdown of igneous minerals (olivine, pyroxene, plagioclase) during the interaction between basalt and CO_2-rich seawater.

In addition to the carbonate-related elements, the interaction between basalt and seawater produces silica-bearing fluid. The upper oceanic crust is suggested to act as a source of Ca and Si to the ocean (Alt et al., 1986; Bach et al., 2003). Except for the outermost layer consisting of microcrystalline quartz that migrated outwards from the basalt, Si is largely lost within the basalt, especially in the highly carbonatized variolitic zone (Fig.13). Ague (2017) ascribed silica loss to volatile loss (H_2O, CO_2) and speculated that most of the silica was locally transferred into adjacent vein fluid flow conduits where additional silica was precipitated. Si-bearing minerals are rare in the interspace of the best-preserved pristine rock

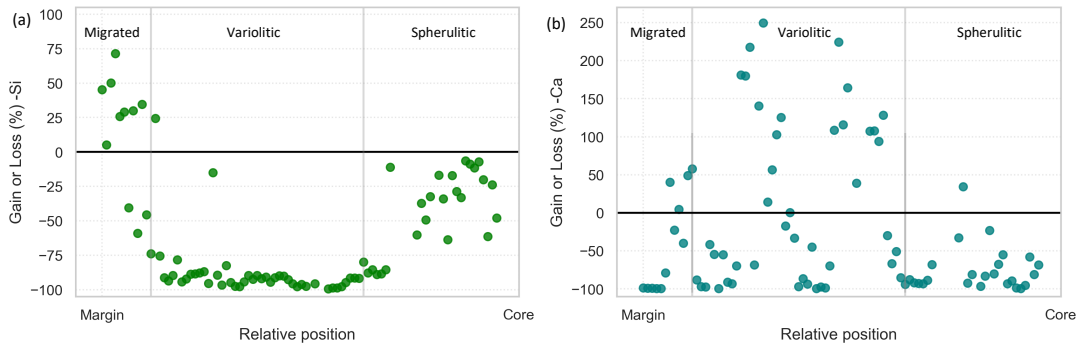

Fig.13 Mass changes of (a) Si and (b) Ca from margin to core in Apex pillow basalt A22 (Fig.6b). Data were only calculated with point spectra of non-carbonate facies via micro-XRF.

systems, only as microcrystalline quartz at the basalt margin and quartz cement on the tips of the interstitial acicular crystal-fan calcite. In contrast, vein-filling and cemented quartz or chert are common in the more altered basalt-interstitial carbonate systems, where the basalt becomes schistose and interstitial carbonate is converted to blocky or massive calcite or ankerite (Chapter 2). Therefore, silica-bearing hydrothermal fluids are consistently generated with the progressive alteration of basalts and precipitate chert during cooling, in the interspace as chert cement, in hydrothermal channels as chert dikes, at the seafloor after venting as the stratiform chert. It has been suggested that this hydrothermal chert (Van Kranendonk and Pirajno, 2004; Lindsay et al., 2005; Van Kranendonk, 2006; Van Kranendonk et al., 2008; Glikson et al., 2008; Duda et al., 2018; Hickman-Lewis et al., 2019), through rapid silicification (Gilkson et al., 2008), helps preserve remains of ancient life in both morphologies and biochemistry (Alleon et al., 2016), which has been recently supported by many researchers (Duda et al., 2018; Van Zuilen, 2019; Hickman-Lewis, 2019; Ledevin, 2019). This may explain why the most important occurrences of Archean carbonaceous materials and microfossils have been reported to be delicately preserved in chert from West Australia and South Africa (Schopf et al., 1993, 2002, 2007, 2010; Ueno et al., 2001, 2006; Tice and Lowe, 2004; Marshall et al., 2007; Oehler et al., 2009; Sugitani et al., 2010, 2013, 2015; Wacey et al., 2011, 2012; Lepot et al., 2013; Homann et al., 2016; Morag et al., 2016; Hickman-Lewis et al., 2017, 2019; Duda et al., 2018; Kozawa et al., 2019).

4.3.2 Bioessential elements

Regardless of the intensive debate on the biogenicity of carbonaceous materials and microstructures in the Apex chert dikes and stratiform chert (Scopf, 1993; Brasier et al., 2002, 2005; Scopf et al., 2018; Wacey et al., 2016; Hickman-Lewis et al., 2016; Rouillard et al., 2021), the speculation that hydrothermal systems were significant habitats for early life is not rejected by geologists and biologists (Russell and Hall, 1997; Glasby, 1998; Van Kranendonk, 2004, 2006; Brasier et al, 2006; Boussau et al., 2008; Akanuma et al., 2017; Westall et al., 2015, 2018; Garcia et al., 2017; Aoyama and Ueno, 2018). Metabolisms, including sulfur/ sulfate reduction, methanogenesis and anoxygenic photosynthesis, probably appeared between about 3.8 and 3.4 billion years ago and left clear fingerprints in the geological record (Monster et al., 1979; Rosing, 1999; Brasier et al., 2002; Strauss, 2003; Mojzsis et al., 2003; Tice and lowe, 2004, 2006; Ueno et al., 2004, 2006; Bontognali et al., 2012; McLoughlin et al., 2012; Czaja et al., 2013; Li et al., 2013; Moore et al., 2017; Aoyama and Ueno, 2018; Scopf et al., 2018). Oxygenic photosynthesis likely appeared later, around 3.0 Ga ago (Lyons et al., 2014), which was predated to 3.4 Ga by Cardona (2018).

To support the various basic biological functions, early life required many nutrients, e.g. some bio-essential elements. For instance, P is essential to biological functions as a key player in fundamental reactions involving the genetic materials (DNA and RNA), energy transfer (ATP) and membranes (phospholipids), consequently limiting primary productivity on geological timescales (Ruttenberg, 2003; Laakso and Schrag, 2018; Hao et al., 2020). S is a critical component of proteins and acts as energy source for chemoautotrophs living on either sulfur oxidation or sulfate reduction. Some transition metals act as the center cofactor of key

enzymes for foundational metabolisms, including Mg, K, Ca, Fe, Mn, and Zn involving in many biochemical reactions, and Cu, Mo, Ni, Se, and Co specific in some organismal lineages (Williams and Da Silva, 2005). However, the origin and evolution of early life is directly influenced by metal availability in environment and incorporation into enzyme structure (Dupont et al., 2010; Moore et al., 2017).

Contrary to richly oxygenated modern ocean, the early Archean ocean was suggested to be anoxic, whereby seawater was ferruginous and enriched in trace elements including Ni, Co and Mn (Canfield, 2005; Anbar, 2008; Poulton and Canfield, 2011; Li et al., 2013; Lyons et al., 2014; Large et al., 2014; Visscher et al., 2020). With the exception of Cu, Mo and V, the aforementioned nutrient elements (P, S, Ca, Fe, Mn, Mg, Ni, Zn and Co) were lost to some degree during the alteration of Apex pillow basalts. These elements were not re-distributed in secondary carbonate facies, suggesting they were likely soluble in the hydrothermal fluids and possibly exported to the ocean accessible to early life. The interstitial carbonates recorded the high concentrations of Fe, Mn, Mg, Ni in ambient hydrothermal fluids (Chapter 3), that more bioessential elements could be released with the progressive breakdown of secondary minerals (Nakamura and Kato, 2004; Caruso et al., 2021). The easy access due to the high abundances of Fe, Mg/Mn and Ni, essential for sulfur/sulfate reduction, methanogenesis and anoxygenic photosynthesis, nitrogen fixation, may explain why they were preferentially selected by early life from the various metals (Anbar, 2008; Dupont et al., 2010; Moore et al., 2017). Therefore, seafloor alteration acted as a significant source of bioessential nutrients, paving the way for origin and evolution of early life on Earth.

4.3.3 Rare earth elements

The high field strength elements (HFSE), such as Ti, Th, Zr and some REE (Ce, Y), are largely immobile and thus preserve their original magmatic concentrations during the alteration of volcanic rocks during metamorphism, hydrothermal events, and weathering (Floyd and Winchester, 1978; MacLean and Kranidiotis, 1987; MacLean and Barrett, 1993; Green et al., 2000). However, this “rule of thumb” does not always function well. HFSE mobility has been recognized during alteration (Finlow–Bates and Stumpfl, 1981; Tourpin et al., 1991; Gruau et al. 1992; Van Kranendonk and Pirajno 2004; Ague, 2017; Caruso et al., 2021), with mobility decreasing roughly in the order of REE > U > Nb > Ti > Th ~ Zr (Ague, 2017). The mobilization of REE is a strong function of the growth or breakdown of REE-bearing phases (Ague, 2017), so that REE being added, lost or redistributed during fluid-rock interaction is controlled by protolith and secondary minerals. In Section 4.1, the LREE enrichment in PM-normalized patterns of basalt core has been ascribed to the contamination of the older sialic basement, which is mirrored by gains of LREE in the samples except for La, which is largely lost. However, the carbonatized parts of basalts from the spherulitic zone to breccia show uniform REE gain or loss, inferring the redistribution of the enriched LREE during seafloor alteration. The higher mobility of LREE than HREE during alteration is supported by the more divergent LREE patterns in less altered basalt samples (Nakamura and Kato, 2004; Kranendonk and Pirajno 2004), usually showing the increasing mass losses of LREE with the progressive alteration from actinolitic assemblage to propylitic and phyllic

alteration assemblages when the contents of HREE retain (Caruso et al., 2021). Interstitial carbonates record this larger mass loss of LREE than HREE during alteration. Clearly seen in the deviations of REE+Y concentrations and PM-normalized patterns (Chapter 3), the carbonate sample of the seawater endmember (D-2-W) shows a low REE concentration and LREE depletion, whereas the Apex neighboring interstitial carbonates exhibit the higher REE concentrations and flat patterns, reflecting REE+Y (relatively more LREE) were leached from basalts during carbonatization, elevating their concentrations in the seawater-derived hydrothermal fluids. And the positive La_{PM} anomalies (~1.21) in carbonates are best explained by the large losses of La from every part of pillow basalts shown in Fig.12.

Conclusion

The pillow basalts of Apex Basalt are oceanic plateau basalts derived from mantle plumes. As a component of early Archean ocean crust, their carbonatization represents seafloor alteration with CO_2-rich seawater, significantly influencing ocean geochemistry through hydrothermal venting. Through analysis of petrographic features and geochemical compositions of elements and the Rb-Sr system, it can be concluded that:

(1) The distinct concentric volcanic structures of pillow basalt were locally preserved, from core to interspace consist of a holocrystalline core, a spherulitic zone, a variolitic zone, a glassy zone within a pillow shape, and shattered breccias in the interspace. The primary features were eliminated with progressive alteration, and phenocrysts were replaced by a secondary mineral assemblage of chlorite + calcite + quartz + anatase + pyrite ± epidote, indicating a metamorphism of greenschist facies that is typical in modern low temperature off-axis hydrothermal systems.

(2) The errorchron based on Rb-Sr isotopic compositions of different concentric domains yields an age of 3570.7 ± 144.3 Ma (n=6, MSWD= 150), which is comparable to the depositional age of 3460 Ma. This errorchron age indicates that the alteration of the studied pillow basalts occurred simultaneously with their submarine eruption, and the Rb-Sr system was not reset afterward. The whole-rock $^{87}Sr/^{86}Sr$ ratio of the examined Apex pillow basalts, given by the errorchron, is 0.706337 ± 0.000954, which was homogenized by the syn-depositional metamorphism of greenschist facies.

(3) Many elements, including Ca, Si, many bioessential elements (P, S, Fe, Mn, Mg, Ni, Zn and Co) and REE +Y (especially LREE), were leached from basalts during alteration, greatly influencing ocean geochemistry and carbon cycles in the early Archean from three aspects: (a) high concentrations of Ca, Fe, Mn, Mg in fluid caused extensive carbonatization of basaltic crust and occurrence of interstitial carbonate, playing a major role as a carbon sink; (b) hydrothermal fluids derived from the basalt-seawater reaction supplied abundant P, S, Ca, Fe, Mn, Mg, Ni, Zn and Co, which are nutrients or enzyme cofactors responsible for many metabolisms (sulfur/sulfate reduction, methanogenesis and anoxygenic photosynthesis, nitrogen fixation), paving the way for the origin and evolution of early life; (c) the Si-bearing fluid precipitated chert of various facies involving the preservation of evidence for early life,

including carbonaceous materials, microfossils, and silicified stromatolites.

Therefore, the well-preserved Apex pillow basalts are a good archive for studying seafloor alteration at 3.5 Ga, providing novel insights into ocean geochemistry, global carbon cycles, element mobility during alteration, and its biological significances to early life.

Acknowledgements

We thank Axel Hackmann and Wolfgang Dröse at the University of Göttingen for sample preliminary preparation. Dr. Dirk Hoffmann and Brigitte Dietrich at the University of Göttingen are thanked for their assistance with preparation and purification of sample solutions, Dr. Volker Karius and Nils Meßling for the assistance with geochemical data acquisition and analysis. Dr. Burkhard Schmidt is acknowledged for his assistance with the Raman spectroscopic analysis, in-situ geochemical mapping and point spectra via micro-XRF. This study was financially supported by the China Council Scholarship (CSC) and SPP1833 (DFG-Schwerpunktprogramm) "Building a Habitable Earth".

References

Ague, J. J.: Element mobility during regional metamorphism in crustal and subduction zone environments with a focus on the rare earth elements (REE), American Mineralogist: Journal of Earth and Planetary Materials, 102, 1796–1821, 2017.

Akanuma, S.: Characterization of reconstructed ancestral proteins suggests a change in temperature of the ancient biosphere, Life, 7, 33, 2017.

Alleon, J., Bernard, S., Le Guillou, C., Daval, D., Skouri-Panet, F., Pont, S., Delbes, L., and Robert, F.: Early entombment within silica minimizes the molecular degradation of microorganisms during advanced diagenesis, Chemical Geology, 437, 98–108, 2016.

Alt, J. C., Honnorez, J., Laverne, C., and Emmermann, R.: Hydrothermal alteration of a 1 km section through the upper oceanic crust, Deep Sea Drilling Project Hole 504B: Mineralogy, chemistry and evolution of seawater-basalt interactions, Journal of Geophysical Research: Solid Earth, 91, 10 309–10 335, 1986.

Anbar, A. D.: Elements and evolution, Science, 322, 1481–1483, 2008.

Anhaeusser, C. R.: Archaean greenstone belts and associated granitic rocks–a review, Journal of African Earth Sciences, 100, 684–732, 2014.

Aoyama, S. and Ueno, Y.: Multiple sulfur isotope constraints on microbial sulfate reduction below an Archean seafloor hydrothermal system, Geobiology, 16, 107–120, 2018.

Arndt, N.: Why was flood volcanism on submerged continental platforms so common in the Precambrian?, Precambrian Research, 97, 155–164, 1999.

Arndt, N.: Komatiites, kimberlites, and boninites, Journal of Geophysical Research: Solid Earth, 108, 2003.

Arndt, N. T., Kerr, A. C., and Tarney, J.: Dynamic melting in plume heads: the formation of Gorgona komatiites and basalts, Earth and Planetary Science Letters, 146, 289–301, 1997.

Arndt, N., Bruzak, G., and Reischmann, T.: The oldest continental and oceanic plateaus: Geochemistry of basalts and komatiites of the Pilbara Craton, Australia, in: Mantle plumes: their identification through time, pp. 352–359, Geological Society of America, https://doi.org/10.1130/0-8137-2352-3.359, 2001.

Bach, W., Peucker-Ehrenbrink, B., Hart, S. R., and Blusztajn, J. S.: Geochemistry of hydrothermally altered oceanic crust: DSDP/ODP Hole 504B–Implications for seawater-crust exchange budgets and Sr-and Pb-isotopic evolution of the mantle, Geochemistry, Geophysics, Geosystems, 4, 2003.

Bach, W. and Früh-Green, G. L.: Alteration of the oceanic lithosphere and implications for seafloor processes, Elements, 6, 173–178, 2010.

Barley, M., Sylvester, G., Groves, D., Borley, G., and Rogers, N.: Archaean calc-alkaline volcanism in the Pilbara Block, Western Australia, Precambrian Research, 24, 285–319, 1984.

Barnes, S. and Arndt, N.: Distribution and geochemistry of komatiites and basalts through the Archean, in: Earth's Oldest Rocks, edited by Van Kranendonk, M., Bennett, V., and Hoffmann, J., pp. 103–132, Elsevier Amsterdam, 2019.

Barnes, S. J., Van Kranendonk, M., and Sonntag, I.: Geochemistry and tectonic setting of basalts from the Eastern Goldfields Superterrane, Australian Journal of Earth Sciences, 59, 707–735, 2012.

Bickle, M., Bettenay, L., Barley, M., Chapman, H., Groves, D., Campbell, I., and De Laeter, J.: A 3500 Ma plutonic and volcanic calc-alkaline province in the Archaean East Pilbara Block, Contributions to Mineralogy and Petrology, 84, 25–35, 1983.

Bickle, M., Bettenay, L., Chapman, H. J., Groves, D., McNaughton, N., Campbell, I., and De Laeter, J.: Origin of the 3500-3300 Ma calc-alkaline rocks in the Pilbara Archaean: isotopic and geochemical constraints from the Shaw Batholith, Precambrian Research, 60, 117–149, 1993.

Bontognali, T. R., Sessions, A. L., Allwood, A. C., Fischer, W. W., Grotzinger, J. P., Summons, R. E., and Eiler, J. M.: Sulfur isotopes of organic matter preserved in 3.45-billion-year-old stromatolites reveal microbial metabolism, Proceedings of the National Academy of Sciences, 109, 15 146–15 151, 2012.

Boussau, B., Blanquart, S., Necsulea, A., Lartillot, N., and Gouy, M.: Parallel adaptations to high temperatures in the Archaean eon, Nature, 456, 942–945, 2008.

Brasier, M. D., Green, O. R., Jephcoat, A. P., Kleppe, A. K., Van Kranendonk, M. J., Lindsay, J. F., Steele, A., and Grassineau, N. V.: Questioning the evidence for Earth's oldest fossils, Nature, 416, 76–81, 2002.

Brasier, M. D., Green, O. R., Lindsay, J. F., McLoughlin, N., Steele, A., and Stoakes, C.: Critical testing of Earth's oldest putative fossil assemblage from the 3.5 Ga Apex chert, Chinaman Creek, Western Australia, Precambrian Research, 140, 55–102, 2005

Brasier, M., McLoughlin, N., Green, O., and Wacey, D.: A fresh look at the fossil evidence for early Archaean cellular life, Philosophical Transactions of the Royal Society B: Biological Sciences, 361, 887–902, 2006.

Brasier, M., Green, O., Lindsay, J., McLoughlin, N., Stoakes, C., Brasier, A., and Wacey, D.: Geology and putative microfossil assemblage of the ca. 3460 Ma 'Apex chert', Western Australia–a field and petrographic guide, Geological Survey of Western Australia, Record, 7, 60, 2011.

Brimhall, G. H. and Dietrich, W. E.: Constitutive mass balance relations between chemical composition, volume, density, porosity, and strain in metasomatic hydrochemical systems: results on weathering and pedogenesis, Geochimica et Cosmochimica Acta, 51, 567–587, 1987.

Brown, A., Cudahy, T., Walter, M., and Hickman, A.: Hyperspectral alteration mapping of early Archean hydrothermal systems in the North Pole Dome, Pilbara Craton, in: Geological Survey of Western Australia, Record 2011/15, p. 28, 2011.

Burns, S. J., Baker, P. A., and Elderfield, H.: Timing of carbonate mineral precipitation and fluid flow in sea-floor basalts, northwest Indian Ocean, Geology, 20, 255–258, 1992.

Canfield, D. E.: The early history of atmospheric oxygen: homage to Robert M. Garrels, Annual Review of Earth and Planetary Sciences., 33, 1–36, 2005.

Cardona, T.: Early Archean origin of heterodimeric Photosystem I, Heliyon, 4, e00 548, 2018.

Caruso, S., Van Kranendonk, M. J., Baumgartner, R. J., Fiorentini, M. L., and Forster, M. A.: The role of magmatic fluids in the ~3.48 Ga Dresser Caldera, Pilbara Craton: New insights from the geochemical investigation of hydrothermal alteration, Precambrian Research, 362, 106 299, 2021.

Cawood, P. A., Hawkesworth, C., and Dhuime, B.: The continental record and the generation of continental crust, Geological Society of America Bulletin, 125, 14–32, 2013.

Coggon, R. M., Teagle, D. A., Cooper, M. J., and Vanko, D. A.: Linking basement carbonate vein compositions to porewater geochemistry across the eastern flank of the Juan de Fuca Ridge, ODP Leg 168, Earth and Planetary Science Letters, 219, 111–128, 2004.

Compston, W. and Pidgeon, R.: Rubidium-strontium dating of shales by the total-rock method, Journal of Geophysical Research, 67, 3493– 3502, 1962.

Condie, K. C.: High field strength element ratios in Archean basalts: a window to evolving sources of mantle plumes?, Lithos, 79, 491–504, 2005.

Coogan, L. A. and Gillis, K. M.: Low-temperature alteration of the seafloor: impacts on ocean chemistry, Annual Review of Earth and Planetary Sciences, 46, 21–45, 2018.

Czaja, A. D., Johnson, C. M., Beard, B. L., Roden, E. E., Li, W., and Moorbath, S.: Biological Fe oxidation controlled deposition of banded iron formation in the ca. 3770 Ma Isua Supracrustal Belt (West Greenland), Earth and Planetary Science Letters, 363, 192–203, 2013.

Dhuime, B., Hawkesworth, C. J., Cawood, P. A., and Storey, C. D.: A change in the geodynamics of continental growth 3 billion years ago, Science, 335, 1334–1336, 2012.

Dickin, A. P.: Radiogenic isotope geology, Cambridge university press, 2018.

Duda, J.-P., Thiel, V., Bauersachs, T., Mißbach, H., Reinhardt, M., Schäfer, N., Van Kranendonk, M. J., and Reitner, J.: Ideas and perspectives: hydrothermally driven redistribution and sequestration of early Archaean biomass–the "hydrothermal pump hypothesis", Biogeosciences, 15, 1535–1548, 2018.

Dulski, P.: Reference materials for geochemical studies: New analytical data by ICP-MS and critical discussion of reference values, Geostandards Newsletter, 25, 87–125, 2001.

Dupont, C. L., Butcher, A., Valas, R. E., Bourne, P. E., and Caetano-Anollés, G.: History of biological metal utilization inferred through phylogenomic analysis of protein structures, Proceedings of the National Academy of Sciences, 107, 10 567–10 572, 2010.

Finlow-Bates, T. and Stumpfl, E. F.: The behaviour of so-called immobile elements in hydrothermally altered rocks associated with volcanogenic submarine-exhalative ore deposits, Mineralium Deposita, 16, 319–328, 1981.

Flament, N., Coltice, N., and Rey, P. F.: A case for late-Archaean continental emergence from thermal evolution models and hypsometry, Earth and Planetary Science Letters, 275, 326–336, 2008.

Floyd, P. and Winchester, J.: Identification and discrimination of altered and metamorphosed volcanic rocks using immobile elements, Chemical Geology, 21, 291–306, 1978.

Galeczka, I., Wolff-Boenisch, D., and Gislason, S.: Experimental studies of basalt-H_2O-CO_2 interaction with a high pressure column flow reactor: the mobility of metals, Energy Procedia, 37, 5823–5833, https://doi.org/10.1016/j.egypro.2013.06.505, 2013a.

Galeczka, I., Wolff-Boenisch, D., Jonsson, T., Sigfusson, B., Stefansson, A., and Gislason, S.: A novel high pres- sure column flow reactor for experimental studies of CO_2 mineral storage, Applied Geochemistry, 30, 91–104, https://doi.org/10.1016/j.apgeochem.2012.08.010, 2013b.

Galeczka, I., Wolff-Boenisch, D., Oelkers, E. H., and Gislason, S. R.: An experimental study of basaltic glass–H_2O–CO_2 interaction at 22 and 50 °C: Implications for subsurface storage of CO_2, Geochimica et Cosmochimica Acta, 126, 123–145, https://doi.org/10.1016/j.gca.2013.10.044, 2014.

Garcia, A. K., Schopf, J. W., Yokobori, S.-i., Akanuma, S., and Yamagishi, A.: Reconstructed ancestral enzymes suggest long-term cooling of Earth's photic zone since the Archean, Proceedings of the National Academy of Sciences, 114, 4619–4624, https://doi.org/10.1073/pnas.1702729114, 2017.

Gebauer, D. t. and Grünenfelder, M.: Rb-Sr whole-rock dating of late diagenetic to anchimetamorphic, Palaeozoic sediments in southern France (Montagne Noire), Contributions to Mineralogy and Petrology, 47, 113–130, 1974.

Gillis, K. and Coogan, L.: Secular variation in carbon uptake into the ocean crust, Earth and Planetary Science Letters, 302, 385–392, https://doi.org/10.1016/j.epsl.2010.12.030, 2011.

Glasby, G. P.: Earliest life in the Archean: rapid dispersal of CO_2-utilizing bacteria from submarine hydrothermal vents, Episodes Journal of International Geoscience, 21, 252–256,

https://doi.org/10.18814/epiiugs/1998/v21i4/007, 1998.
Glikson, M., Duck, L. J., Golding, S. D., Hofmann, A., Bolhar, R., Webb, R., Baiano, J. C., and Sly, L. I.: Microbial remains in some earliest Earth rocks: comparison with a potential modern analogue, Precambrian Research, 164, 187–200, https://doi.org/10.1016/j.precamres.2008.05.002, 2008.
Green, M. G., Sylvester, P. J., and Buick, R.: Growth and recycling of early Archaean continental crust: geochemical evidence from the Coon- terunah and Warrawoona Groups, Pilbara Craton, Australia, Tectonophysics, 322, 69–88, https://doi.org/10.1016/S0040-1951(00)00058-5, 2000.
Gruau, G., Tourpin, S., Fourcade, S., and Blais, S.: Loss of isotopic (Nd, O) and chemical (REE) memory during metamorphism of komatiites: new evidence from eastern Finland, Contributions to Mineralogy and Petrology, 112, 66–82, https://doi.org/10.1007/BF00310956, 1992.
Gudbrandsson, S., Wolff-Boenisch, D., Gislason, S. R., and Oelkers, E. H.: An experimental study of crystalline basalt dissolution from 2⩽ pH⩽ 11 and temperatures from 5 to 75 °C, Geochimica et Cosmochimica Acta, 75, 5496–5509, https://doi.org/https://doi.org/10.1016/j.gca.2011.06.035, 2011.
Gysi, A. P. and Stefánsson, A.: CO_2–water–basalt interaction. Numerical simulation of low temperature CO_2 sequestration into basalts, Geochimica et Cosmochimica Acta, 75, 4728–4751, https://doi.org/10.1016/j.gca.2011.05.037, 2011.
Hao, J., Knoll, A. H., Huang, F., Hazen, R. M., and Daniel, I.: Cycling phosphorus on the Archean Earth: Part I. Continental weathering and riverine transport of phosphorus, Geochimica et Cosmochimica Acta, 273, 70–84, https://doi.org/10.1016/j.gca.2020.01.027, 2020.
Harris, A. C., White, N. C., McPhie, J., Bull, S. W., Line, M. A., Skrzeczynski, R., Mernagh, T. P., and Tosdal, R. M.: Early Archean hot springs above epithermal veins, North Pole, Western Australia: new insights from fluid inclusion microanalysis, Economic Geology, 104, 793–814, https://doi.org/10.2113/gsecongeo.104.6.793, 2009.
Hart, S. and Staudigel, H.: Ocean crust vein mineral deposition: Rb/Sr ages, U-Th-Pb geochemistry, and duration of circulation at DSDP sites 261, 462 and 516, Geochimica et Cosmochimica Acta, 50, 2751–2761, https://doi.org/10.1016/0016-7037(86)90224-3, 1986.
Hart, S. R., Blusztajn, J., Dick, H. J., and Lawrence, J. R.: Fluid circulation in the oceanic crust: contrast between volcanic and plutonic regimes, Journal of Geophysical Research: Solid Earth, 99, 3163–3173, https://doi.org/10.1029/93JB02035, 1994.
Hasenstab, E., Tusch, J., Schnabel, C., Marien, C., Van Kranendonk, M., Smithies, H., Howard, H., Maier, W., and Münker, C.: Evolution of the early to late Archean mantle from Hf-Nd-Ce isotope systematics in basalts and komatiites from the Pilbara Craton, Earth and Planetary Science Letters, 553, 116 627, https://doi.org/10.1016/j.epsl.2020.116627, 2021.
Hickman, A. H.: Geology of the Pilbara Block and its environments, Western Australia Geological Survey, Bulletin 127, 1983.
Hickman, A. H. and Van Kranendonk, M. J.: Diapiric processes in the formation of Archaean continental crust, East Pilbara granite- greenstone terrane, Australia, in: The Precambrian Earth: tempos and events, edited by Eriksson, P.G., Altermann, W., Nelson, D.R., Mueller, W.U., Catuneau, O., vol. 12, pp. 118–139, Elsevier Amsterdam, 2004.
Hickman-Lewis, K., Garwood, R. J., Brasier, M. D., Goral, T., Jiang, H., McLoughlin, N., and Wacey, D.: Carbonaceous microstructures from sedimentary laminated chert within the 3.46 Ga Apex Basalt, Chinaman Creek locality, Pilbara, Western Australia, Precambrian Research, 278, 161–178, https://doi.org/10.1016/j.precamres.2016.03.013, 2016.

Hickman-Lewis, K., Garwood, R. J., Withers, P. J., and Wacey, D.: X-ray microtomography as a tool for investigating the petrological context of Precambrian cellular remains, Geological Society, London, Special Publications, 448, 33–56, https://doi.org/10.1144/SP448.11, 2017.

Hickman-Lewis, K., Westall, F., and Cavalazzi, B.: Trace of early life in the Barberton greenstone belt, in: Earth's Oldest Rocks, edited by Van Kranendonk, M., Bennett, V., and Hoffmann, E., pp. 1029–1058, Elsevier, https://hal.science/hal-03041208, 2019.

Holland, H. D.: The chemical evolution of the atmosphere and oceans, Princeton University Press, 2020

Homann, M., Heubeck, C., Bontognali, T. R., Bouvier, A.-S., Baumgartner, L. P., and Airo, A.: Evidence for cavity-dwelling microbial life in 3.22 Ga tidal deposits, Geology, 44, 51–54, https://doi.org/10.1130/G37272.1, 2016.

Huston, D. L., Morant, P., Pirajno, F., Cummins, B., Baker, D., and Mernagh, T. P.: Paleoarchean mineral deposits of the Pilbara Craton: genesis, tectonic environment and comparisons with younger deposits, Developments in Precambrian Geology, 15, 411–450, https://doi.org/10.1016/S0166-2635(07)15044-1, 2007.

Kamber, B. S. and Webb, G. E.: The geochemistry of late Archaean microbial carbonate: implications for ocean chemistry and continental erosion history, Geochimica et Cosmochimica Acta, 65, 2509–2525, https://doi.org/10.1016/S0016-7037(01)00613-5, 2001.

Kasting, J. F.: Early Earth Atmosphere and Oceans, in: Earth's Oldest Rocks, Van Kranendonk, M.J., B. V. H. J. (eds), pp. 49–61, Elsevier, 2019.

Kato, Y. and Nakamura, K.: Origin and global tectonic significance of Early Archean cherts from the Marble Bar greenstone belt, Pilbara Craton, Western Australia, Precambrian Research, 125, 191–243, https://doi.org/10.1016/S0301-9268(03)00043-3, 2003.

Kelley, D. S., Karson, J. A., Blackman, D. K., FruÈh-Green, G. L., Butterfield, D. A., Lilley, M. D., Olson, E. J., Schrenk, M. O., Roe, K. K., Lebon, G. T., et al.: An off-axis hydrothermal vent field near the Mid-Atlantic Ridge at 30 °N, Nature, 412, 145–149, https://doi.org/10.1038/35084000, 2001.

Kelley, D. S., Karson, J. A., Fruh-Green, G. L., Yoerger, D. R., Shank, T. M., Butterfield, D. A., Hayes, J. M., Schrenk, M. O., Ol- son, E. J., Proskurowski, G., et al.: A serpentinite-hosted ecosystem: the Lost City hydrothermal field, Science, 307, 1428–1434, https://doi.org/10.1126/science.1102556, 2005.

Kitajima, K., Maruyama, S., Utsunomiya, S., and Liou, J.: Seafloor hydrothermal alteration at an Archaean mid-ocean ridge, Journal of Metamorphic Geology, 19, 583–599, https://doi.org/10.1046/j.0263-4929.2001.00330.x, 2001.

Komiya, T., Maruyama, S., Hirata, T., and Yurimoto, H.: Petrology and geochemistry of MORB and OIB in the mid-Archean North Pole region, Pilbara craton, Western Australia: implications for the composition and temperature of the upper mantle at 3.5 Ga, International Geology Review, 44, 988–1016, https://doi.org/10.2747/0020-6814.44.11.988, 2002.

Kozawa, T., Sugitani, K., Oehler, D. Z., House, C. H., Saito, I., Watanabe, T., and Gotoh, T.: Early Archean planktonic mode of life: Implications from fluid dynamics of lenticular microfossils, Geobiology, 17, 113–126, https://doi.org/10.1111/gbi.12319, 2019.

Laakso, T. A. and Schrag, D. P.: Limitations on limitation, Global Biogeochemical Cycles, 32, 486–496, https://doi.org/10.1002/2017GB005832, 2018.

Lanphere, M., Wasserburg, G., Albee, A., and Tilton, G.: Redistribution of strontium and rubidium

isotopes during metamorphism, World Beater Complex, Panamint Range, California, in: Isotopic and Cosmic Chemistry, edited by Craig, H., Miller, S. L., and Wasserburg, G. J., pp. 269—-320, North Holland, 1964.

Large, R. R., Halpin, J. A., Danyushevsky, L. V., Maslennikov, V. V., Bull, S. W., Long, J. A., Gregory, D. D., Lounejeva, E., Lyons, T. W., Sack, P. J., et al.: Trace element content of sedimentary pyrite as a new proxy for deep-time ocean–atmosphere evolution, Earth and Planetary Science Letters, 389, 209–220, https://doi.org/10.1016/j.epsl.2013.12.020, 2014.

Ledevin, M.: Archean cherts: Formation processes and paleoenvironments, in: Earth's Oldest Rocks, edited by Van Kranendonk, M., Bennett, V., and Hoffmann, J., pp. 913–944, Elsevier, 2019.

Lepot, K., Williford, K. H., Ushikubo, T., Sugitani, K., Mimura, K., Spicuzza, M. J., and Valley, J. W.: Texture-specific isotopic compositions in 3.4 Gyr old organic matter support selective preservation in cell-like structures, Geochimica et Cosmochimica Acta, 112, 66–86, https://doi.org/10.1016/j.gca.2013.03.004, 2013.

Li, W., Czaja, A. D., Van Kranendonk, M. J., Beard, B. L., Roden, E. E., and Johnson, C. M.: An anoxic, Fe (II)-rich, U-poor ocean 3.46 billion years ago, Geochimica et Cosmochimica Acta, 120, 65–79, https://doi.org/10.1016/j.gca.2013.06.033, 2013.

Lindsay, J., Brasier, M., McLoughlin, N., Green, O., Fogel, M., Steele, A., and Mertzman, S.: The problem of deep carbon—an Archean paradox, Precambrian Research, 143, 1–22, https://doi.org/10.1016/j.precamres.2005.09.003, 2005.

Lyons, T. W., Reinhard, C. T., and Planavsky, N. J.: The rise of oxygen in Earth's early ocean and atmosphere, Nature, 506, 307–315, https://doi.org/10.1038/nature13068, 2014.

MacLean, W. and Kranidiotis, P.: Immobile elements as monitors of mass transfer in hydrothermal alteration; Phelps Dodge massive sulfide deposit, Matagami, Quebec, Economic Geology, 82, 951–962, https://doi.org/10.2113/gsecongeo.82.4.951, 1987.

MacLean, W. and Barrett, T.: Lithogeochemical techniques using immobile elements, Journal of geochemical exploration, 48, 109–133, https://doi.org/10.1016/0375-6742(93)90002-4, 1993.

Marescotti, P., Vanko, D. A., and Cabella, R.: From oxidizing to reducing alteration: Mineralogical variations in pillow basalts from the east flank, Juan de Fuca Ridge, in: Proc. Ocean Drill. Program Sci. Results, vol. 168, pp. 119–136, Ocean Drilling Program College Station, TX, 2000.

Marshall, C. P., Love, G. D., Snape, C. E., Hill, A. C., Allwood, A. C., Walter, M. R., Van Kranendonk, M. J., Bowden, S. A., Sylva, S. P., and Summons, R. E.: Structural characterization of kerogen in 3.4 Ga Archaean cherts from the Pilbara Craton, Western Australia, Precambrian Research, 155, 1–23, https://doi.org/10.1016/j.precamres.2006.12.014, 2007.

Martin, W., Baross, J., Kelley, D., and Russell, M. J.: Hydrothermal vents and the origin of life, Nature Reviews Microbiology, 6, 805–814, https://doi.org/10.1038/nrmicro1991, 2008.

Maruyama, S.: Is the Mid-Archean barite formation from the Pilbara craton, Australia under the deep-sea environment?, Eos Transactions, 72, 532, 1991.

McCollom, T. M. and Seewald, J. S.: Carbon isotope composition of organic compounds produced by abiotic synthesis under hydrothermal conditions, Earth and Planetary Science Letters, 243, 74–84, https://doi.org/10.1016/j.epsl.2006.01.027, 2006.

McDonough, W. F. and Sun, S.-S.: The composition of the Earth, Chemical geology, 120, 223–253, https://doi.org/10.1016/0009- 2541(94)00140-4, 1995.

McGrail, B. P., Schaef, H. T., Spane, F. A., Cliff, J. B., Qafoku, O., Horner, J. A., Thompson, C. J., Owen, A. T., and Sullivan, C. E.: Field validation of supercritical CO_2 reactivity with basalts,

Environmental Science & Technology Letters, 4, 6–10, https://doi.org/10.1021/acs.estlett.6b00387, 2017.

McLoughlin, N., Grosch, E., Kilburn, M., and Wacey, D.: Sulfur isotope evidence for a Paleoarchean subseafloor biosphere, Barberton, South Africa, Geology, 40, 1031–1034, https://doi.org/10.1130/G33313.1, 2012.

McNaughton, N., Compston, W., and Barley, M.: Constraints on the age of the Warrawoona Group, eastern Pilbara block, Western Australia, Precambrian Research, 60, 69–98, https://doi.org/10.1016/0301-9268(93)90045-4, 1993.

Menefee, A. H., Giammar, D. E., and Ellis, B. R.: Permanent CO_2 trapping through localized and chemical gradient-driven basalt carbonation, Environmental science & technology, 52, 8954–8964, https://doi.org/10.1021/acs.est.8b01814, 2018.

Mojzsis, S., Coath, C., Greenwood, J., McKeegan, K., and Harrison, T.: Mass-independent isotope effects in Archean (2.5 to 3.8 Ga) sedimentary sulfides determined by ion microprobe analysis, Geochimica et Cosmochimica Acta, 67, 1635–1658, https://doi.org/10.1016/S0016-7037(03)00059-0, 2003.

Monster, J., Appel, P., Thode, H., Schidlowski, M., Carmichael, C., and Bridgwater, D.: Sulfur isotope studies in early Archaean sediments from Isua, West Greenland: Implications for the antiquity of bacterial sulfate reduction, Geochimica et Cosmochimica Acta, 43, 405–413, https://doi.org/10.1016/0016-7037(79)90205-9, 1979.

Moore, E. K., Jelen, B. I., Giovannelli, D., Raanan, H., and Falkowski, P. G.: Metal availability and the expanding network of microbial metabolisms in the Archaean eon, Nature Geoscience, 10, 629–636, https://doi.org/10.1038/ngeo3006, 2017.

Morag, N., Williford, K. H., Kitajima, K., Philippot, P., Van Kranendonk, M. J., Lepot, K., Thomazo, C., and Valley, J. W.: Microstructure- specific carbon isotopic signatures of organic matter from 3.5 Ga cherts of the Pilbara Craton support a biologic origin, Precambrian Research, 275, 429–449, https://doi.org/10.1016/j.precamres.2016.01.014, 2016.

Nakamura, K. and Kato, Y.: Carbonate minerals in the Warrawoona Group, Pilbara Craton: Implications for continental crust, life, and global carbon cycle in the Early Archean, Resource Geology, 52, 91–100, https://doi.org/10.1111/j.1751-3928.2002.tb00122.x, 2002.

Nakamura, K. and Kato, Y.: Carbonatization of oceanic crust by the seafloor hydrothermal activity and its significance as a CO_2 sink in the Early Archean, Geochimica et Cosmochimica Acta, 68, 4595–4618, https://doi.org/10.1016/j.gca.2004.05.023, 2004.

Nutman, A. P., Friend, C. R., Bennett, V. C., Van Kranendonk, M., and Chivas, A. R.: Reconstruction of a 3700 Ma transgressive marine environment from Isua (Greenland): Sedimentology, stratigraphy and geochemical signatures, Lithos, 346, 105164, https://doi.org/10.1016/j.lithos.2019.105164, 2019.

Oehler, D. Z., Robert, F., Walter, M. R., Sugitani, K., Allwood, A., Meibom, A., Mostefaoui, S., Selo, M., Thomen, A., and Gibson, E. K.: NanoSIMS: insights to biogenicity and syngeneity of Archaean carbonaceous structures, Precambrian Research, 173, 70–78, https://doi.org/10.1016/j.precamres.2009.01.001, 2009.

Pack, A., Russell, S. S., Shelley, J. M. G., and Van Zuilen, M.: Geo-and cosmochemistry of the twin elements yttrium and holmium, Geochimica et Cosmochimica Acta, 71, 4592–4608, https://doi.org/10.1016/j.gca.2007.07.010, 2007.

Palme, H. and O'Neill, H.: 3.1 Cosmochemical estimates of mantle composition, in: Treatise on

Geochemistry: Oxford, pp. 1–39, Elsevier, 2nd edn., https://doi.org/http://dx.doi.org/10.1016/B978-0-08-095975-7.00201-1, 2014.

Piper, D. Z. and Bau, M.: Normalized rare earth elements in water, sediments, and wine: identifying sources and environmental redox conditions, American Journal of Analytical Chemistry, https://doi.org/10.4236/ajac.2013.410A1009, 2013.

Pirajno, F.: Ancient to modern earth: The role of mantle plumes in the making of continental crust, Developments in Precambrian Geology, 15, 1037–1064, https://doi.org/10.1016/S0166-2635(07)15083-0, 2007a.

Pirajno, F.: Mantle plumes, associated intraplate tectonomagmatic processes and ore systems, Episodes Journal of International Geoscience, 30, 6–19, https://doi.org/10.18814/epiiugs/2007/v30i1/003, 2007b.

Poulton, S. W. and Canfield, D. E.: Ferruginous conditions: a dominant feature of the ocean through Earth's history, Elements, 7, 107–112, https://doi.org/10.2113/gselements.7.2.107, 2011.

Rosing, M. T.: ^{13}C-depleted carbon microparticles in> 3700-Ma seafloor sedimentary rocks from West Greenland, Science, 283, 674–676, https://doi.org/10.1126/science.283.5402.674, 1999.

Rotenberg, E., Davis, D. W., Amelin, Y., Ghosh, S., and Bergquist, B. A.: Determination of the decay-constant of ^{87}Rb by laboratory accumulation of ^{87}Sr, Geochimica et Cosmochimica Acta, 85, 41–57, https://doi.org/10.1016/j.gca.2012.01.016, 2012.

Rouillard, J., Van Kranendonk, M. J., Lalonde, S., Gong, J., and Van Zuilen, M. A.: Correlating trace element compositions, petrology, and Raman spectroscopy data in the 3.46 Ga Apex chert, Pilbara Craton, Australia, Precambrian Research, 366, 106415, https://doi.org/10.1016/j.precamres.2021.106415, 2021.

Russell, M. J. and Hall, A.: The emergence of life from iron monosulphide bubbles at a submarine hydrothermal redox and pH front, Journal of the Geological Society, 154, 377–402, https://doi.org/10.1144/gsjgs.154.3.0377, 1997.

Russell, M. and Arndt, N.: Geodynamic and metabolic cycles in the Hadean, Biogeosciences, 2, 97–111, https://doi.org/10.5194/bg-2-97- 2005, 2005.

Ruttenberg, K.: The global phosphorus cycle, Treatise on geochemistry, 8, 682, https://doi.org/10.1016/B0-08-043751-6/08153-6, 2003.

Schmitt, R., Smith, R., Lasch, J., Mosen, A., Olehy, D., and Vasilevskis, J.: Abundances of the fourteen rare-earth elements, scandium, and yttrium in meteoritic and terrestrial matter, Geochimica et Cosmochimica Acta, 27, 577–622, https://doi.org/10.1016/0016-7037(63)90014-0, 1963.

Schopf, J.: Paleobiology of Archean, The Proterozoic Biosphere. A Multidisciplinary Approach, pp. 25–39, 1992.

Schopf, J. W.: Microfossils of the Early Archean Apex chert: new evidence of the antiquity of life, Science, 260, 640–646, https://doi.org/10.1126/science.260.5108.640, 1993.

Schopf, J. W. and Packer, B. M.: Early Archean (3.3-billion to 3.5-billion-year-old) microfossils from Warrawoona Group, Australia, Science, 237, 70–73, https://doi.org/10.1126/science.11539686, 1987.

Schopf, J. W., Kudryavtsev, A. B., Agresti, D. G., Wdowiak, T. J., and Czaja, A. D.: Laser–Raman imagery of Earth's earliest fossils, Nature, 416, 73–76, https://doi.org/10.1038/416073a, 2002.

Schopf, J. W., Kudryavtsev, A. B., Czaja, A. D., and Tripathi, A. B.: Evidence of Archean life: stromatolites and microfossils, Precambrian Research, 158, 141–155, https://doi.org/10.1016/j.precamres.2007.04.009, 2007.

Schopf, J. W., Kudryavtsev, A. B., Sugitani, K., and Walter, M. R.: Precambrian microbe-like pseudofossils: A promising solution to the problem, Precambrian Research, 179, 191–205, https://doi.org/10.1016/j.precamres.2010.03.003, 2010.

Schopf, J. W., Kitajima, K., Spicuzza, M. J., Kudryavtsev, A. B., and Valley, J. W.: SIMS analyses of the oldest known assemblage of microfossils document their taxon-correlated carbon isotope compositions, Proceedings of the National Academy of Sciences, 115, 53– 58, https://doi.org/10.1073/pnas.1718063115, 2018.

Sforna, M.-C., Van Zuilen, M., and Philippot, P.: Structural characterization by Raman hyperspectral mapping of organic carbon in the 3.46 billion-year-old Apex chert, Western Australia, Geochimica et Cosmochimica Acta, 124, 18–33, https://doi.org/10.1016/j.gca.2013.09.031, 2014.

Shibuya, T., Komiya, T., Nakamura, K., Takai, K., and Maruyama, S.: Highly alkaline, high-temperature hydrothermal fluids in the early Archean ocean, Precambrian Research, 182, 230–238, https://doi.org/10.1016/j.precamres.2010.08.011, 2010.

Sleep, N. H. and Windley, B. F.: Archean plate tectonics: constraints and inferences, The Journal of Geology, 90, 363–379, 1982.

Smithies, R., Champion, D., and Cassidy, K.: Formation of Earth's early Archaean continental crust, Precambrian Research, 127, 89–101, https://doi.org/10.1016/S0301-9268(03)00182-7, 2003.

Smithies, R. H., Van Kranendonk, M. J., and Champion, D. C.: It started with a plume–early Archaean basaltic proto-continental crust, Earth and Planetary Science Letters, 238, 284–297, https://doi.org/10.1016/j.epsl.2005.07.023, 2005.

Smithies, R., Champion, D., Van Kranendonk, M., and Hickman, A.: Geochemistry of volcanic rocks of the northern Pilbara Craton, Western Australia, Geological Survey of Western Australia Report, 104, 1–47, 2007a.

Smithies, R. H., Champion, D. C., and Van Kranendonk, M. J.: The oldest well-preserved felsic volcanic rocks on Earth: Geochemical clues to the early evolution of the Pilbara Supergroup and implications for the growth of a Paleoarchean protocontinent, in: Earth's Oldest Rocks, edited by Van Kranendonk, M., Smithies, R., and Bennett, V., vol. Developments in Precambrian Geology 15, pp. 339–367, Elsevier, Amsterdam, https://doi.org/10.1016/S0166-2635(07)15042-8, 2007b.

Staudigel, H., Hart, S. R., Schmincke, H.-U., and Smith, B. M.: Cretaceous ocean crust at DSDP Sites 417 and 418: Carbon uptake from weathering versus loss by magmatic outgassing, Geochimica et Cosmochimica Acta, 53, 3091–3094, https://doi.org/10.1016/0016- 7037(89)90189-0, 1989.

Stockmann, G. J., Wolff-Boenisch, D., Gislason, S. R., and Oelkers, E. H.: Do carbonate precipitates affect dissolution kinetics? 1: Basaltic glass, Chemical Geology, 284, 306–316, https://doi.org/10.1016/j.chemgeo.2011.03.010, 2011.

Strauss, H.: Sulphur isotopes and the early Archaean sulphur cycle, Precambrian Research, 126, 349–361, https://doi.org/10.1016/S0301- 9268(03)00104-9, 2003.

Sugitani, K., Lepot, K., Nagaoka, T., Mimura, K., Van Kranendonk, M., Oehler, D. Z., and Walter, M. R.: Biogenicity of morphologically di- verse carbonaceous microstructures from the ca. 3400 Ma Strelley Pool Formation, in the Pilbara Craton, Western Australia, Astrobiology, 10, 899–920, https://doi.org/10.1089/ast.2010.0513, 2010.

Sugitani, K., Mimura, K., Nagaoka, T., Lepot, K., and Takeuchi, M.: Microfossil assemblage from the 3400 Ma Strelley Pool Formation in the Pilbara Craton, Western Australia: results form a new locality, Precambrian Research, 226, 59–74, https://doi.org/10.1016/j.precamres.2012.11.005, 2013.

Sugitani, K., Mimura, K., Takeuchi, M., Yamaguchi, T., Suzuki, K., Senda, R., Asahara, Y., Wallis, S., and Van Kranendonk, M.: A Pale- oArchean coastal hydrothermal field inhabited by diverse microbial communities: the Strelley Pool Formation, Pilbara Craton, Western Australia, Geobiology, 13, 522–545, https://doi.org/10.1111/gbi.12150, 2015.

Takai, K., Gamo, T., Tsunogai, U., Nakayama, N., Hirayama, H., Nealson, K. H., and Horikoshi, K.: Geochemical and microbiological evidence for a hydrogen-based, hyperthermophilic subsurface lithoautotrophic microbial ecosystem (HyperSLiME) beneath an active deep-sea hydrothermal field, Extremophiles, 8, 269–282, https://doi.org/10.1007/s00792-004-0386-3, 2004.

Taylor, S. R. and McLennan, S.: The composition and evolution of the continental crust: rare earth element evidence from sedimentary rocks, Philosophical Transactions of the Royal Society of London. Series A, Mathematical and Physical Sciences, 301, 381–399, https://doi.org/10.1098/rsta.1981.0119, 1981.

Taylor, S. R. and McLennan, S.: The continental crust: its composition and evolution, 1985.

Terabayashi, M., Masada, Y., and Ozawa, H.: Archean ocean-floor metamorphism in the North Pole area, Pilbara Craton, western Australia, Precambrian Research, 127, 167–180, https://doi.org/10.1016/S0301-9268(03)00186-4, 2003.

Thorpe, R., Hickman, A., Davis, D., Mortensen, J., and Trendall, A.: U-Pb zircon geochronology of Archaean felsic units in the Marble Bar region, Pilbara Craton, Western Australia, Precambrian Research, 56, 169–189, https://doi.org/10.1016/0301-9268(92)90100-3, 1992.

Tice, M. M. and Lowe, D. R.: Photosynthetic microbial mats in the 3,416-Myr-old ocean, Nature, 431, 549–552, https://doi.org/10.1038/nature02888, 2004.

Tice, M. M. and Lowe, D. R.: The origin of carbonaceous matter in pre-3.0 Ga greenstone terrains: A review and new evidence from the 3.42 Ga Buck Reef Chert, Earth-Science Reviews, 76, 259–300, https://doi.org/10.1016/j.earscirev.2006.03.003, 2006.

Tourpin, S., Gruau, G., Blais, S., and Fourcade, S.: Resetting of REE, and Nd and Sr isotopes during carbonitization of a komatiite flow from Finland, Chemical geology, 90, 15–29, https://doi.org/10.1016/0009-2541(91)90030-U, 1991.

Tusch, J., Münker, C., Hasenstab, E., Jansen, M., Marien, C. S., Kurzweil, F., Van Kranendonk, M. J., Smithies, H., Maier, W., and Garbe- Schönberg, D.: Convective isolation of Hadean mantle reservoirs through Archean time, Proceedings of the National Academy of Sciences, 118, e2012626 118, https://doi.org/10.1073/pnas.2012626118, 2021.

Ueno, Y., Isozaki, Y., Yurimoto, H., and Maruyama, S.: Carbon isotopic signatures of individual Archean microfossils (?) from Western Australia, International Geology Review, 43, 196–212, https://doi.org/10.1080/00206810109465008, 2001.

Ueno, Y., Yoshioka, H., Maruyama, S., and Isozaki, Y.: Carbon isotopes and petrography of kerogens in 3.5-Ga hydrothermal silica dikes in the North Pole area, Western Australia, Geochimica et Cosmochimica Acta, 68, 573–589, https://doi.org/10.1016/S0016-7037(03)00462- 9, 2004.

Ueno, Y., Yamada, K., Yoshida, N., Maruyama, S., and Isozaki, Y.: Evidence from fluid inclusions for microbial methanogenesis in the early Archaean era, Nature, 440, 516–519, https://doi.org/10.1038/nature04584, 2006.

van den Boorn, S. H., van Bergen, M. J., Nijman, W., and Vroon, P. Z.: Dual role of seawater and hydrothermal fluids in Early Archean chert formation: evidence from silicon isotopes, Geology, 35, 939–942, https://doi.org/10.1130/G24096A.1, 2007.

Van Kranendonk, M. J.: Volcanic degassing, hydrothermal circulation and the flourishing of early life

on Earth: A review of the evi- dence from ca. 3490-3240 Ma rocks of the Pilbara Supergroup, Pilbara Craton, Western Australia, Earth-Science Reviews, 74, 197–240, https://doi.org/10.1016/j.earscirev.2005.09.005, 2006.

Van Kranendonk, M. J.: A review of the evidence for putative Paleoarchean life in the Pilbara Craton, Western Australia, Developments in Precambrian Geology, 15, 855–877, https://doi.org/10.1016/S0166-2635(07)15072-6, 2007.

Van Kranendonk, M. J. and Hickman, A. H.: Archaean Geology of the North Shaw Region, East Pilbara Granite-Greenstone Terrane, Western Australia: A Field Guide, Geological Survey of Western Australia, Record 2000/5, 2000.

Van Kranendonk, M. J. and Pirajno, F.: Geochemistry of metabasalts and hydrothermal alteration zones associated with ca. 3.45 Ga chert and barite deposits: implications for the geological setting of the Warrawoona Group, Pilbara Craton, Australia, Geochemistry: Exploration, Environment, Analysis, 4, 253–278, https://doi.org/10.1144/1467-7873/04-205, 2004.

Van Kranendonk, M. J., Hickman, A. H., Smithies, R. H., Nelson, D. R., and Pike, G.: Geology and tectonic evolution of the Archean North Pilbara terrain, Pilbara Craton, Western Australia, Economic Geology, 97, 695–732, https://doi.org/10.2113/gsecongeo.97.4.695, 2002.

Van Kranendonk, M. J., Hugh Smithies, R., Hickman, A. H., and Champion, D.: Secular tectonic evolution of Archean continental crust: interplay between horizontal and vertical processes in the formation of the Pilbara Craton, Australia, Terra Nova, 19, 1–38, https://doi.org/10.1111/j.1365-3121.2006.00723.x, 2007a.

Van Kranendonk, M. J., Smithies, R. H., Hickman, A. H., and Champion, D. C.: Paleoarchean development of a continental nu- cleus: the East Pilbara terrane of the Pilbara craton, Western Australia, Developments in Precambrian geology, 15, 307–337, https://doi.org/10.1016/S0166-2635(07)15041-6, 2007b.

Van Kranendonk, M. J., Philippot, P., Lepot, K., Bodorkos, S., and Pirajno, F.: Geological setting of Earth's oldest fossils in the ca. 3.5 Ga Dresser formation, Pilbara Craton, Western Australia, Precambrian Research, 167, 93–124, https://doi.org/10.1016/j.precamres.2008.07.003, 2008.

Van Kranendonk, M. J., Smithies, R. H., Griffin, W. L., Huston, D. L., Hickman, A. H., Champion, D. C., Anhaeusser, C. R., and Pirajno, F.: Making it thick: a volcanic plateau origin of Palaeoarchean continental lithosphere of the Pilbara and Kaapvaal cratons, Geological Society, London, Special Publications, 389, 83–111, https://doi.org/10.1144/SP389.12, 2015.

Van Kranendonk, M. J., Smithies, R. H., Hickman, A. H., and Champion, D. C.: Paleoarchean development of a continental nucleus: the East Pilbara Terrane of the Pilbara Craton, Western Australia, in: Earth's Oldest Rocks, edited by Van Kranendonk, M., Bennett, V., and Hoffmann, J., pp. 437–462, Elsevier, 2019.

van Zuilen, M.: The Significance of Carbonaceous Matter to Understanding Life Processes on Early Earth. In: Van Kranendonk, M.J., Bennett, V.C., Hoffmann, J.E. (Eds.), in: Earth's Oldest Rocks. Elsevier, 945–963, 2019.

Veizer, J., Compston, W., Hoefs, J., and Nielsen, H.: Mantle buffering of the early oceans, Naturwissenschaften, 69, 173–180, https://doi.org/10.1007/BF00364890, 1982.

Veizer, J., Hoefs, J., Ridler, R., Jensen, L., and Lowe, D.: Geochemistry of Precambrian carbonates: I. Archean hydrothermal systems, Geochimica et Cosmochimica Acta, 53, 845–857, https://doi.org/10.1016/0016-7037(89)90030-6, 1989.

Vermeesch, P.: IsoplotR: a free and open toolbox for geochronology, Geoscience Frontiers, 9, 1479-

1493, https://doi.org/10.1016/j.gsf.2018.04.001, 2018.

Visscher, P. T., Gallagher, K. L., Bouton, A., Farias, M. E., Kurth, D., Sancho-Tomás, M., Philippot, P., Somogyi, A., Medjoubi, K., Vennin, E., et al.: Modern arsenotrophic microbial mats provide an analogue for life in the anoxic Archean, Communications Earth & Environment, 1, 24, https://doi.org/10.1038/s43247-020-00025-2, 2020.

Voigt, M., Pearce, C. R., Baldermann, A., and Oelkers, E. H.: Stable and radiogenic strontium isotope fractionation during hydrothermal seawater-basalt interaction, Geochimica et Cosmochimica Acta, 240, 131–151, https://doi.org/10.1016/j.gca.2018.08.018, 2018.

Von Damm, K. L.: Controls on the chemistry and temporal variability of seafloor hydrothermal fluids, Seafloor hydrothermal systems: Physical, chemical, biological, and geological interactions, 91, 222–247, https://doi.org/10.1029/GM091p0222, 1995.

Wacey, D., Kilburn, M. R., Saunders, M., Cliff, J., and Brasier, M. D.: Microfossils of sulphur-metabolizing cells in 3.4-billion-year-old rocks of Western Australia, Nature Geoscience, 4, 698–702, https://doi.org/10.1038/ngeo1238, 2011.

Wacey, D., Menon, S., Green, L., Gerstmann, D., Kong, C., Mcloughlin, N., Saunders, M., and Brasier, M.: Taphonomy of very ancient microfossils from the 3400 Ma Strelley Pool Formation and 1900 Ma Gunflint Formation: New insights using a focused ion beam, Precambrian Research, 220, 234–250, https://doi.org/10.1016/j.precamres.2012.08.005, 2012.

Wacey, D., Saunders, M., Kong, C., Brasier, A., and Brasier, M.: 3.46 Ga Apex chert 'microfossils' reinterpreted as mineral artefacts produced during phyllosilicate exfoliation, Gondwana Research, 36, 296–313, https://doi.org/10.1016/j.gr.2015.07.010, 2016.

Westall, F., Campbell, K. A., Bréhéret, J. G., Foucher, F., Gautret, P., Hubert, A., Sorieul, S., Grassineau, N., and Guido, D. M.: Archean (3.33 Ga) microbe-sediment systems were diverse and flourished in a hydrothermal context, Geology, 43, 615–618, https://doi.org/10.1130/G36646.1, 2015.

Westall, F., Hickman-Lewis, K., Hinman, N., Gautret, P., Campbell, K. A., Bréhéret, J.-G., Foucher, F., Hubert, A., Sorieul, S., Dass, A. V., et al.: A hydrothermal-sedimentary context for the origin of life, Astrobiology, 18, 259–293, https://doi.org/10.1089/ast.2017.1680, 2018.

Willbold, M. and Jochum, K. P.: Multi-element isotope dilution sector field ICP-MS: A precise technique for the analysis of geological materials and its application to geological reference materials, Geostandards and Geoanalytical Research, 29, 63–82, https://doi.org/10.1111/j.1751-908X.2005.tb00656.x, 2005.

Williams, R. J. P. and Da Silva, J. F.: The chemistry of evolution: the development of our ecosystem, Elsevier, 2005.

Wojdyr, M.: Fityk: a general-purpose peak fitting program, Journal of Applied Crystallography, 43, 1126–1128, https://doi.org/10.1107/S0021889810030499, 2010.

Wolff-Boenisch, D. and Galeczka, I.: Flow-through reactor experiments on basalt-(sea) water-CO_2 reactions at 90 °C and neutral pH. What happens to the basalt pore space under post-injection conditions?, International Journal of Greenhouse Gas Control, 68, 176–190, https://doi.org/10.1016/j.ijggc.2017.11.013, 2018.

Xiong, W., Wells, R. K., Horner, J. A., Schaef, H. T., Skemer, P. A., and Giammar, D. E.: CO_2 mineral sequestration in naturally porous basalt, Environmental Science & Technology Letters, 5, 142–147, https://doi.org/10.1021/acs.estlett.8b00047, 2018.

Yamamoto, K., Itoh, N., Matsumoto, T., Tanaka, T., and Adachi, M.: Geochemistry of Precambrian

carbonate intercalated in pillows and its host basalt: implications for the REE composition of circa 3.4 Ga seawater, Precambrian Research, 135, 331–344, https://doi.org/10.1016/j.precamres.2004.09.006, 2004.

Appendix

1. Quantification of element gains and losses

The mass change of a mobile element can be generally quantified using the mass balance equations with a relatively immobile element during alteration as the geochemical reference (MacLean and Kranidiotis, 1987; Ague et al., 2017). The detailed discussion about the method can be found in Ague et al. (2017), and it is briefly described here.

The basic mass balance expression is:

$$V^{P}\,\rho^{P}C_i^{P} = V^{A}\rho^{A}C_i^{A} \qquad \text{(Eq.1)}$$

Where V is rock volume (including pore space), ρ is rock density, C_i is the concentration of a reference (immobile) species i, and the ^{P} and ^{A} superscripts refer to the pristine and altered states. The volume change is given by:

$$\Delta V = \frac{V^A}{V^P} - 1 \qquad \text{(Eq.2)}$$

Substitution of Equation 2 into Equation 1 and rearranging for volume change of reference element i yields:

$$\Delta V_i = \left(\frac{C_i^P}{C_i^A}\right)\left(\frac{\rho^P}{\rho^A}\right) - 1 \qquad \text{(Eq.3)}$$

The fractional change in mass (Δm_j) for some mobile constituent j is given by:

$$\Delta m_j = \frac{V^A\rho^A C_j^A}{V^P\rho^P C_j^P} - 1 \qquad \text{(Eq.4)}$$

Noting (2), substitution yields:

$$\Delta m_j = \frac{\rho^A C_j^A}{\rho^P C_j^P}(\Delta V_i + 1) - 1 \qquad \text{(Eq.5)}$$

providing a quantitative relationship between changes in rock chemical and physical properties. This expression may be simplified further by substituting explicitly for volume change:

$$\Delta m_i^j = \left(\frac{C_i^P}{C_i^A}\right)\left(\frac{C_j^A}{C_j^P}\right) - 1 \qquad \text{(Eq.6)}$$

The total change in rock mass Δm_i^{rm} on the basis of reference element *i* is:

$$\Delta m_i^{rm} = \left(\frac{C_i^P}{C_i^A}\right) - 1 \quad \text{(Eq.7)}$$

Equations 3, 6, and 7 give fractional changes; percentage changes are obtained by multiplying by 100 (gains are positive, losses negative).

In this work, Zr is utilized as the reference element for its largely immobility during hydrothermal alteration (Finlow–Bates and Stumpfl, 1981; MacLean and Kranidiotis, 1987; Ague, 2017), and the element concentrations of Primitive Mantle (PM, Palme and O'Neil, 2014) are used as the precursor composition.

2. Si gain or loss against relative position

The concentrations of Si, Ca and Zr used to estimate the gain or loss of Si from the spherulitic zone to migration zone (in the interspace) consisting of microcrystalline quartz, were measured through point spectrum of micro-XRF. The results are listed in Table S1, and increasing of the numbers in the Sample ID indicate approaching the basalt core. To be noted, the values calculated in this way can only indicate the gain or loss of Si and Ca qualitatively, due to uncertainties in the measurements (lack of standards and reference materials for reproducibility and quality control).

References

Ague, J. J.: Element mobility during regional metamorphism in crustal and subduction zone environments with a focus on the rare earth elements (REE), American Mineralogist: Journal of Earth and Planetary Materials, 102, 1796–1821, 2017.

Finlow-Bates, T. and Stumpfl, E. F.: The behaviour of so-called immobile elements in hydrothermally altered rocks associated with volcanogenic submarine-exhalative ore deposits, Mineralium Deposita, 16, 319–328, 1981.

MacLean, W. and Kranidiotis, P.: Immobile elements as monitors of mass transfer in hydrothermal alteration; Phelps Dodge massive sulfide deposit, Matagami, Quebec, Economic Geology, 82, 951–962, https://doi.org/10.2113/gsecongeo.82.4.951, 1987.

Palme, H. and O'Neill, H.: 3.1 Cosmochemical estimates of mantle composition, in: Treatise on Geochemistry: Oxford, pp. 1–39, Elsevier, 2nd edn., https://doi.org/http://dx.doi.org/10.1016/B978-0-08-095975-7.00201-1, 2014.

Table S1 The concentrations of Zr (ppm), Si and Ca (wt%) acquired from point spectra of micro-XRF, and mass gain-loss of Ca and Si (%).

		Concentration			Gain or Loss	
SampleID	Position	Zr (ppm)	Si (wt%)	Ca (wt%)	Si (%)	Ca (%)
A22_blt_line_ 006	6	10.87	32.52	0.03	45.24	-98.73
A22_blt_line_ 007	7	14.82	32.11	0.03	5.18	-99.10
A22_blt_line_ 008	8	10.55	32.64	0.02	50.13	-99.19
A22_blt_line_ 009	9	9.21	32.55	0.02	71.46	-99.25
A22_blt_line_ 010	10	12.54	32.52	0.03	25.88	-99.21
A22_blt_line_ 011	11	11.43	30.37	0.61	28.94	-78.88
A22_blt_line_ 012	12	20.56	25.20	7.31	-40.50	40.40
A22_blt_line_ 013	13	11.41	30.58	2.23	30.07	-22.83
A22_blt_line_ 014	14	25.75	21.70	6.82	-59.10	4.44
A22_blt_line_ 015	15	10.96	30.39	1.67	34.65	-39.68
A22_blt_line_ 016	16	22.06	24.70	8.32	-45.66	48.88
A22_blt_line_ 017	17	30.89	16.62	12.34	-73.89	57.71
A22_blt_line_ 018	18	11.90	30.50	0.36	24.45	-87.95
A22_blt_line_ 019	19	32.64	16.40	0.24	-75.62	-97.10
A22_blt_line_ 020	20	54.07	9.74	0.38	-91.26	-97.19
A22_blt_line_ 021	21	58.21	7.56	8.60	-93.70	-41.67
A22_blt_line_ 022	22	44.28	9.40	5.09	-89.70	-54.65
A22_blt_line_ 023	23	37.15	16.62	0.04	-78.28	-99.57
A22_blt_line_ 024	24	95.18	11.09	10.87	-94.34	-54.91
A22_blt_line_ 025	25	56.45	9.07	1.25	-92.20	-91.23
A22_blt_line_ 026	26	43.99	10.14	0.77	-88.81	-93.05
A22_blt_line_ 027	27	46.26	10.98	3.58	-88.48	-69.46
A22_blt_line_ 028	28	40.37	10.21	28.77	-87.72	181.24
A22_blt_line_ 029	29	40.06	10.85	28.44	-86.85	180.11
A22_blt_line_ 030	30	47.70	4.42	38.38	-95.50	217.54
A22_blt_line_ 031	31	16.12	28.25	1.29	-14.92	-68.45
A22_blt_line_ 032	32	44.08	9.60	26.87	-89.43	140.54
A22_blt_line_ 033	33	46.65	3.20	41.32	-96.67	249.59
A22_blt_line_ 034	34	40.30	14.57	11.69	-82.45	14.44
A22_blt_line_ 035	35	54.68	5.98	21.73	-94.69	56.81
A22_blt_line_ 036	36	64.67	3.28	33.20	-97.54	102.59
A22_blt_line_ 037	37	58.25	2.68	33.24	-97.77	125.20
A22_blt_line_ 038	38	58.36	6.80	12.26	-94.34	-17.06
A22_blt_line_ 039	39	56.08	12.03	14.27	-89.59	0.41
A22_blt_line_ 040	40	50.12	7.89	8.50	-92.36	-33.08

(to be continued)

		Concentration			Gain or Loss	
SampleID	Position	Zr (ppm)	Si (wt%)	Ca (wt%)	Si (%)	Ca (%)
A22_blt_line_ 041	41	46.70	10.05	0.35	-89.55	-97.06
A22_blt_line_ 042	42	55.12	9.19	1.88	-91.91	-86.56
A22_blt_line_ 043	43	53.13	9.98	0.88	-90.88	-93.45
A22_blt_line_ 044	44	60.35	6.80	8.44	-94.53	-44.79
A22_blt_line_ 045	45	53.44	9.64	0.05	-91.24	-99.61
A22_blt_line_ 046	46	49.58	10.24	0.35	-89.97	-97.25
A22_blt_line_ 047	47	50.98	10.31	0.18	-90.19	-98.64
A22_blt_line_ 048	48	55.58	8.39	4.30	-92.68	-69.44
A22_blt_line_ 049	49	46.10	4.07	24.38	-95.71	108.67
A22_blt_line_ 050	50	50.72	2.27	41.69	-97.83	224.35
A22_blt_line_ 051	51	50.73	4.03	27.75	-96.14	115.85
A22_blt_line_ 052	52	58.07	3.04	38.90	-97.46	164.34
A22_blt_line_ 054	54	56.11	5.06	19.77	-95.62	39.07
A22_blt_line_ 057	57	80.55	0.97	42.31	-99.41	107.31
A22_blt_line_ 058	58	73.26	1.86	38.55	-98.77	107.66
A22_blt_line_ 059	59	65.05	1.89	31.98	-98.59	93.98
A22_blt_line_ 061	60	63.16	3.00	36.52	-97.70	128.17
A22_blt_line_ 063	61	63.16	6.93	11.26	-94.68	-29.62
A22_blt_line_ 064	62	50.59	8.79	4.29	-91.57	-66.50
A22_blt_line_ 065	63	50.19	8.80	6.24	-91.49	-50.90
A22_blt_line_ 066	64	61.89	10.46	2.33	-91.80	-85.16
A22_blt_line_ 067	65	38.59	15.99	0.57	-79.89	-94.13
A22_blt_line_ 068	66	45.65	11.42	1.41	-87.86	-87.83
A22_blt_line_ 069	67	46.60	13.84	0.95	-85.58	-91.92
A22_blt_line_ 070	68	47.71	10.85	0.88	-88.96	-92.71
A22_blt_line_ 071	69	41.25	9.75	0.74	-88.53	-92.95
A22_blt_line_ 072	70	43.74	13.15	1.28	-85.41	-88.49
A22_blt_line_ 073	71	15.30	28.05	1.24	-11.02	-67.89
A22_blt_line_ 079	77	28.26	23.17	4.80	-60.20	-32.93
A22_blt_line_ 080	78	19.97	25.85	6.80	-37.19	34.30
A22_blt_line_ 081	79	22.66	23.67	0.45	-49.31	-92.09
A22_blt_line_ 082	80	19.68	27.39	0.94	-32.42	-81.15
A22_blt_line_ 084	82	17.09	29.31	0.15	-16.75	-96.55
A22_blt_line_ 085	83	19.96	27.17	0.86	-33.93	-82.96
A22_blt_line_ 086	84	27.79	20.84	5.41	-63.60	-23.23
A22_blt_line_ 087	85	16.81	28.74	0.85	-17.03	-80.16
A22_blt_line_ 088	86	18.76	27.52	1.55	-28.79	-67.45
A22_blt_line_ 089	87	19.54	26.98	2.23	-33.01	-55.00
A22_blt_line_ 090	88	15.35	29.62	0.26	-6.36	-93.23
A22_blt_line_ 091	89	15.80	29.67	0.42	-8.81	-89.45
A22_blt_line_ 092	90	15.99	29.18	0.06	-11.42	-98.60
A22_blt_line_ 093	91	15.56	29.81	0.03	-7.04	-99.23
A22_blt_line_ 094	92	16.32	26.83	0.20	-20.21	-95.11
A22_blt_line_ 095	93	28.16	22.42	3.01	-61.35	-57.86
A22_blt_line_ 096	94	17.03	26.74	0.83	-23.82	-80.79
A22_blt_line_ 097	95	21.67	23.29	1.73	-47.81	-68.50

Fig.S1 Photographs of one altered sample labelled as 'Apex' from Apex Basalt. (a) Scan image (transmitted light) of thin section, showing primary concentric volcanic textures that were lost during alteration, as well as recrystallization of interstitial calcite (yellow circles). Two sets of vein systems were developed, of which constituents were dominated by quartz and calcite, respectively. The rough localities of the close-up photos (PPL) (b) to (e) are marked in (a). (b) to (d) show that the secondary minerals found in the well-preserved samples are transformed to epidote (Eq.) + calcite (Cal.) + chlorite (Chl.) and aggregates of anatase (An.) particles. (e) Chlorite migrates displacively outward along intracrystalline joints of blocky interstitial calcite. Scale bar of 200 µm applies to pictures (b) to (e). (PPL: Plane-polarized light)

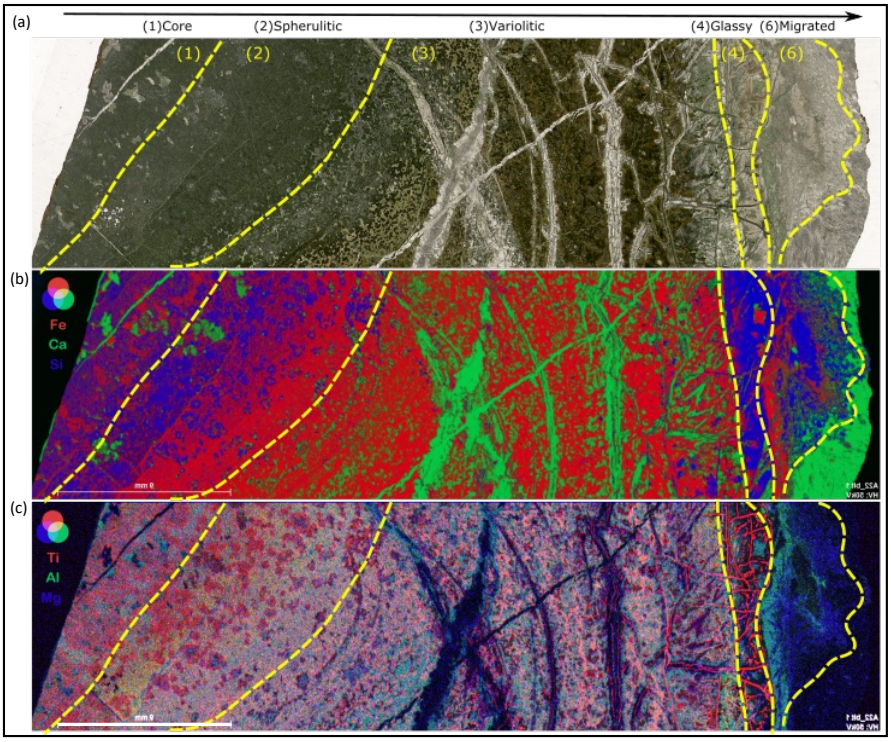

Fig.S2 Images of a well-preserved sample labeled as 'A22' from Apex Basalt. (A) A close-up view of the thin section (scan image under transmitted light) shown in Fig.5b near the subsample A22-5, showing primary concentric volcanic textures from the basalt core to the quenched margin consisting of holocrystalline pillow core, spherulitic zone, variolitic zone, glassy zone and migrated zone. The elemental distributions via micro-XRF mapping, shown in false-color overlaps (b) and (c), confirm the zoning defined in (a). Note that carbonatization occurred along with Si loss from the basalt, mainly in the variolitic zone. Scale bar in the left bottom of (c) is 9 mm, applicable to other images.

Chapter-5 Application: Reconstructing environment conditions in the early Archean

In this chapter, the geochemical compositions of the carbonates (Chapter 3) and Apex pillow basalts (Chapter 4) from the Eastern Pilbara Terrane, Western Australia (EPT) are utilized to reconstruct the fluid conditions under which the EPT carbonates precipitated, and to identify the factors that triggered depositional alteration, such as recrystallization and dolomitization. To be specific, (1) the oxygen isotopic compositions of the least altered carbonates are used to calculate fluid temperatures; (2) the temperature-dependent distribution coefficients and carbonate Sr/Ca ratios are used to reconstruct fluid Sr/Ca ratios; (3) the fluid Sr/Ca ratios and Ca concentrations from fluid inclusions are used to calculate fluid Sr concentrations; and (4) numerical models are employed to quantitatively study the water-rock interaction during carbonate diagenesis using fluid Sr concentrations and $^{87}Sr/^{86}Sr$ ratios based on mass balance principle.

1. Temperature of the early Archean ocean

The $\delta^{18}O$ values of marine carbonates depend on the isotopic composition of fluids from which the carbonates are precipitated, and the temperature-dependent fractionation during initial precipitation and possible recrystallization. Generally, lower temperatures result in larger isotopic fractionations, that enable the $^{18}O/^{16}O$ ratio of well-preserved marine authigenic minerals to determine the approximate temperature of formation, if the isotopic composition of seawater is known. This method is widely used in studying modern marine carbonates. However, there is controversy surrounding its application in estimating the temperature of the Archean ocean.

More depleted $\delta^{18}O$ values of carbonates, chert and phosphates on early Earth than today have been reported and invoked a long-standing debate for the cause (Veizer and Hoefs, 1976; Shemesh et al., 1988; Veizer et al., 1999; Shields and Veizer, 2002; Knauth and Lowe, 2003; Robert and Chaussidon, 2006; Blake et al., 2010), with three scenarios, including a hot Archean ocean (Knauth and Lowe, 2003; Robert and Chaussidon, 2006; Tartèse et al. 2017), low $\delta^{18}O$ Archean seawater (Perry, 1967; Perry and Lefticariu, 2003; Kasting et al., 2006; Jaffrés et al., 2007; Galili et al., 2019; Vérard and Veizer, 2019) and diagenesis (Degens and Epstein, 1962; Marin-Carbonne et al., 2012, 2014; Sengupta et al., 2020). One school of thought suggests seawater $\delta^{18}O$ remains fixed throughout Earth's history (Gregory, 1991; Muehlenbachs, 1998; Tartèse et al. 2017), whereas the others insist it changes through time (Veizer et al., 2000; Kasting et al., 2006; Jaffrés et al., 2007). Based on the assumption of the invariable seawater $\delta^{18}O$ at ~0 ± 1‰ (modern seawater, Hoefs, 2018), higher ocean temperatures during the Archean have been calculated using the $\delta^{18}O$ values of chert (~70 °C) and carbonate (~100 °C), the former within the range of 60 to 80 °C given by the research of chert $\delta^{30}Si$ (Robert and Chaussidon, 2006; Jaffrés et al. 2007). Recently, triple oxygen isotopic studies of Archean chert also illustrated a hot Archean ocean > 77 °C with similar

$\delta^{18}O$ values to that of today around -1 ‰ (67 °C assuming -2‰ ocean) up to 100 °C (McGunnigle et al., 2022), although the same data of Archean chert from the Pilbara craton was first interpreted as chert initially precipitated in the 10~60 °C ocean and then altered by high-temperature fluids of higher $^{18}O/^{16}O$ ratio (Sengupta et al., 2020). However, the most reported Archean chert units were suggested to be of hydrothermal origin or mixed hydrothermal-seawater origin (van den Boorn et al., 2007; Rouillard et al., 2021), whereby the seawater temperatures were likely overestimated. In contrast, marine carbonates are less ambiguous than cherts in terms of their depositional environment and possible hydrothermal overprint that can be recognized with comprehensive Sr and C isotope studies on the same samples (Shields, 2019).

In this work, two sets of pristine carbonates are demonstrated in the previous chapters: shallow marine carbonates from the 3.48 Ga Dresser Formation and the interstitial carbonates from the 3.46 Ga Apex Basalt that precipitated from seawater-derived low-temperature hydrothermal fluid. They are consequently used to calculate the temperatures of seawater and hydrothermal fluid, respectively. In this case, deviation by later diagenesis can be negligible, and the only factor impacting the temperature is seawater $\delta^{18}O$ in the early Archean. Five scenarios of Archean seawater $\delta^{18}O$ are considered, ranging from -13.3‰ (Jaffrés et al., 2007), -10 ‰, -5 ‰ (Herwartz et al., 2021), -1.2‰ (Shackleton and Kennett, 1975), 0 ‰ (Hoefs, 2018), and 3.3 ‰ (Johnson and Wing, 2020). The paleotemperature equations based on oxygen isotopes were given by Shackleton and Kennett, 1975 (eq.1), Hays and Grossman, 1991 (eq.2), and Anderson and Arthur, 1983 (eq.3) and are tested here before more calculations, where $\delta^{18}O_{CaCO3}$ data are versus PDB, and $\delta^{18}O_w$ is the $\delta^{18}O$ of seawater versus VSMOW:

$$T\,(°C) = 16.9 - 4.38(\,\delta^{18}O_{CaCO3} - \delta^{18}O_w) + 0.1\,(\,\delta^{18}O_{CaCO3} - \delta^{18}O_w)^2 \qquad \text{(Eq.1)}$$

$$T\,(°C) = 15.7 - 4.36(\,\delta^{18}O_{CaCO3} - \delta^{18}O_w) + 0.12\,(\,\delta^{18}O_{CaCO3} - \delta^{18}O_w)^2 \qquad \text{(Eq.2)}$$

$$T\,(°C) = 16.0 - 4.14(\,\delta^{18}O_{CaCO3} - \delta^{18}O_w) + 0.13\,(\,\delta^{18}O_{CaCO3} - \delta^{18}O_w)^2 \qquad \text{(Eq.3)}$$

When assumed the seawater $\delta^{18}O$ value of -1.2‰ (Shackleton and Kennett, 1975), the temperatures calculated from the seawater endmember D-2-W are 82.7, 84.1, and 83.2 °C, respectively, showing little deviation caused by different paleotemperature equations. Considering the seawater $\delta^{18}O$ value of -1.2‰ from Shackleton and Kennett, 1975, the eq.1 is applied in this work to roughly estimate the potential formation temperature of carbonates. The results are listed in Table 1 and plotted in Fig.1. With the increasing seawater $\delta^{18}O$ values from -13.3‰ to 3.3 ‰, the calculated temperatures of seawater increase from 15.7 °C to 112.5 °C. The temperature of 15.7 °C, calculated with the very depleted Archean seawater $\delta^{18}O$ of −13.3 ‰ (Jaffrés et al., 2007), indicates a modern-like Archean ocean. Likewise, more temperate to even cold conditions (< 40 °C) during the Archean are inferred from studies in the Barberton Greenstone Belt (Hofmann, 2005; Hren et al., 2009; Blake et al., 2010; de Wit and Furnes, 2016). The relatively moderate temperatures of Archean climate are supported by modeling in Charnay et al. (2017) (8~30 °C) and Krissansen-Totton et al. (2018) (0 ~50 °C),

Table 1 Temperatures calculated with the $\delta^{18}O_{PDB}$ values (‰) of the seawater endmember and primary interstitial calcites, and various seawater $\delta^{18}O_{SMOW}$ values (‰).

SampleID	Lithology	Formation	Age (Ma)	Carbonate $\delta^{18}O$ (PDB, ‰)	Temperature (°C) calculated via seawater $\delta^{18}O$ (SMOW, ‰)					
					-13.3 (a)	-10	-5 (b)	-1.2 (c)	0 (d)	3 (e)
A14673-1	Interstitial calcite	Apex Basalt	3460	-16.74	33.2	51.0	82.1	109.1	118.3	142.3
A22-1				-17.29	35.9	54.1	85.8	113.2	122.5	146.9
A22-2				-16.72	33.0	50.8	81.9	108.9	118.1	142.1
ABAS-2				-16.97	34.3	52.3	83.7	110.9	120.0	144.3
ABAS-3				-15.79	28.4	45.6	75.8	102.1	111.0	134.5
D-2-W	Seawater calcite	Dresser Formation	3480	-13.03	15.7	31.1	58.5	82.7	91.0	112.8

Reference: a. Jaffrés et al., 2007, b.Herwartz et al., 2021, c. Shackleton and Kennett, 1975, d.Hoefs, 2018, and e.Johnson and Wing, 2020.

due to the combined negative feedbacks of continental and seafloor weathering. Meanwhile, a marine temperature above 80 °C would not be plausible for the flourishing of early life. An analysis of ribosomal RNAs by Boussau et al. (2008) proposed the hypothesis of two environmental-temperature-related phases during the evolutionary history of the tree of life, in which thermotolerance increased from a mesophilic (optimal growth temperature, briefly OGT < 50 °C) LUCA (the last universal common ancestor) to thermophilic (OGT 50–80 °C) ancestors of Bacteria and of Archaea–Eukaryota and then decreased, leading to the ancestors of Bacteria and Archaea–Eukaryota convergently adapted to high temperatures possibly in response to a climate change of the early Earth, and/or aided by the transition from an RNA genome in the LUCA to organisms with more thermostable DNA genomes. Additionally, the thermostability of ancestral enzymes reconstructed from photic-zone cyanobacteria and land plants indicates a cooling of Earth's surface temperature from ~75 °C in the Archean (~3,000 Ma) to ~35 °C in the Devonian (~420 Ma) (Garcia et al., 2017), consistent with the previous geological and biological results. If the biological evidence is valid, some ancestral organisms were indeed thermophilic, and then the model of a hot Archean ocean (60°C to 80 °C) may not be the best option but can be acceptable. The heat flux was probably offered by a relatively efficient escape of internal heat through abundant volcanoes and associated hydrothermal activity in the absence of plate tectonics and linear spreading centers (Camprubí et al., 2019). Hence, the temperatures based on seawater $\delta^{18}O$ values of 0 ‰ (Hoefs, 2018), and 3.3 ‰ (Johnson and Wing, 2020) are precluded from the following discussion and calculations.

On the other hand, the average temperatures of hydrothermal fluids from which the primary Apex interstitial carbonates precipitated range from 33.0 ± 2.8 to 108.9 ± 4.1 °C, with seawater $\delta^{18}O$ values from -13.3 ‰ to -1.2 ‰, indicating the low-temperature hydrothermal circulations through the upper oceanic crust. A paradox seems to appear when considering the pillow basalts, which are commonly at greenschist metamorphic facies, implying a metamorphic temperature between 300–450 °C. However, they are not the same case, and the discrepancy can be explained by the fact that carbonate is a low-temperature alteration product precipitated from the cooled hydrothermal fluids during the latest stage of the seafloor alteration, as observed in carbonate veins hosted in ultramafic basement drilled in the ODP Leg 209 (Bach et al., 2011). The heat loss from the oceanic lithosphere via hydrothermal circulation, either in the form of warm (20–65 °C), altered seawater or as cooler, much more subtly chemically altered water, continues in the modern oceanic crust from 0 to 65 million years in age after its formation (Stein et al., 1995; Mottl, 2003; Nielsen et al., 2006). It is

concluded that temperatures of the seawater-derived hydrothermal fluids that formed Apex interstitial carbonates were 17.3 to 26.1 °C higher than that of the contemporary seawater, and

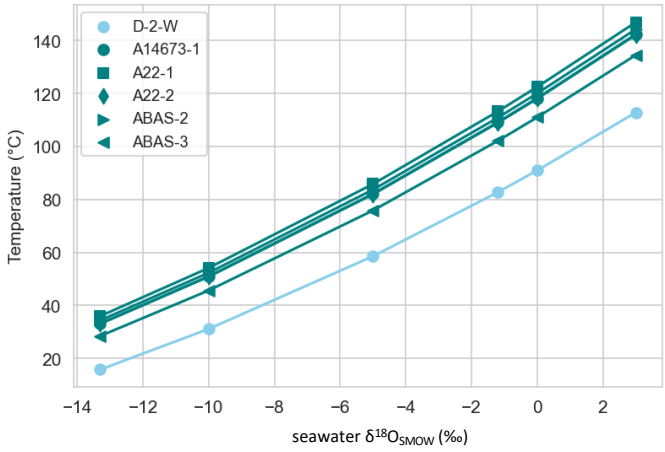

Fig.1 Temperatures of the seawater and seawater-derived hydrothermal fluid in the early Archean, based on the $\delta^{18}O_{PDB}$ values (‰) of the seawater endmember and primary interstitial calcites that are from Dresser Formation and Apex Basalt, respectively, against seawater $\delta^{18}O_{SMOW}$ values of −13.3‰ (Jaffrés et al., 2007), −10 ‰, -5 ‰ (Herwartz et al., 2021), −1.2‰ (Shackleton and Kennett, 1975), 0 ‰ (Hoefs, 2018), and 3.3 ‰ (Johnson and Wing, 2020).

the heat was from the cooling of Apex pillow basalts.

2. Reconstruct the fluid Sr/Ca ratio and Sr concentration

According to modern drilling cores, carbonate minerals in the oceanic crust are predominantly calcite (Alt and Teagle, 1999; Bach et al., 2001, 2011). Rausch (2012) found 90% of the examined samples of 23 DSDP and ODP drill cores from the Atlantic and Pacific consist of calcite, whereas only minor amounts of aragonite and dolomite occur. The carbonates in the cores occur in carbonate veins, vugs and vesicles as well as carbonate matrices of breccias (Rausch, 2012), analogous to our interstitial carbonates. The compositions of these carbonates provide records for the chemistry of the basement and temperature at which the carbonates formed (Coggon et al., 2004, 2010; Rausch, 2012; herein). Fluid Sr/Ca ratios exert a fundamental control on the Sr concentration of diagenetic carbonates and vary widely in natural fluids, making them diagnostic of a given type or source of fluid when used in conjunction with other parameters, such as $^{87}Sr/^{86}Sr$ ratios (Banner et al., 1994; Banner, 1995). Recently, they have been widely used in studies of paleoceanography, marine sediment diagenesis, hydrothermal alteration of the oceanic crust, and the evolving influence of life (Lear et al., 2003; Tripati et al., 2009; Elderfield, 2010; Coggon et al., 2010; Sosdian et al., 2012; Gothmann et al., 2015). In this work, the well-preserved EPT carbonates provide the opportunity to study the Sr/Ca ratios and Sr concentrations of the contemporaneous seawater and seawater-derived hydrothermal fluids, for better understanding the hydrothermal contribution to the early Archean ocean.

2.1 Method

Theoretical and experimental works on the trace element behavior of Sr in carbonate-fluid systems have assumed that the only significant mechanism to be solid-solution substitution of Sr into Ca^{2+} structural sites (McIntire, 1963; Amiel et al., 1973; Sun and Hanson, 1975; Zachara et al., 1991; Pingitore et al., 1992; Banner, 1995). This apparent restriction of Sr to Ca structural sites simplifies a quantitative approach to estimating the Sr geochemical behavior in carbonate-fluid systems through carbonate-fluid distribution coefficient (or partition coefficient), K_{Sr}, which is expressed as follows (Banner and Hanson, 1990; Banner, 1995):

$$K_{Sr} = \frac{(Sr/Ca)_{carbonate}}{(Sr/Ca)_{fluid}} \quad \text{(Eq.4)}$$

where the Sr/Ca concentration ratios can be either a weight or molar basis, that the latter is more popular and used in this work. laboratory studies suggest that Sr incorporation into calcite is strongly dependent on the mineral precipitation rate (Lorens, 1981; Tesoriero and Pankow, 1996; Gabitov and Watson, 2006; Tang et al., 2008), and the equilibrium K values can be determined from these laboratory studies and models. In this work, an empirical temperature-dependent equation of the equilibrium K_{Sr} values for the temperature range 0–200 °C is performed on the seawater endmember and Apex pristine hydrothermal carbonates with the expression below from Zhang and DePaolo (2020):

$$K_{Sr}^{eq}(T) = 0.025\exp\left(\frac{\Delta G_{r,0}}{R}\left(\frac{1}{298.15} - \frac{1}{T}\right)\right) \quad \text{(Eq.5)}$$

where $\Delta G_{r,0}$ is the free energy change associated with the exchange reaction, with the recommended value of 1.2 kcal/mol (5.0 kJ/mol), the molar gas constant R is 8.31 J/(mol*K) and temperature is in Kelvin ([K] = [°C] + 273.15). Based on discussion of the temperature of the Paleoarchean ocean in Section 1, two scenarios of the Paleoarchean ocean $\delta^{18}O$ value are used to reconstruct temperatures: -1.2‰ (Shackleton and Kennett, 1975) as the upper limit and −13.3‰ (Jaffrés et al., 2007) as the lower limit. There temperatures are further used in the Eq.5 to calculate K_{Sr} values and fluid Sr/Ca ratios. As a presupposition for the next section about water-rock reactions, all the EPT carbonates are used to reconstruct fluid Sr concentrations. The fluid Sr concentrations are calculated using different distribution coefficients, carbonate Sr/Ca ratios (data from Chapter 3), and different fluid Ca concentrations provided by the study of quartz-bearing fluid inclusion of Ironstone Pods (3.23 Ga, the Barberton greenstone belt, South Africa) (De Ronde et al., 1997). Specifically, the hydrothermal Ca concentration of 42.6 mmol/L is applied to the interstitial carbonates and one sedimentary carbonate DB for their hydrothermal origin, while the seawater Ca concentration of 232 mmol/L is applied to fracture-filling calcite, marine sedimentary carbonates and the SPF stromatolite for their seawater origin.

2.2 Results

The carbonate Sr/Ca molar ratio, temperature, the relative distribution coefficient K, the fluid Sr/Ca ratio and Sr concentration are calculated based on the EPT carbonates and shown in Table 2. The fracture-filling calcite has the highest carbonate Sr/Ca ratio of 0.00194, whereas the sedimentary carbonate and the SPF stromatolite have the lowest ratios with a mean value of 0.00010. The primary interstitial calcite has carbonate Sr/Ca molar ratios ranging from 0.00012 to 0.00017 with an average value of 0.00014 ± 0.00002, while the altered interstitial calcite has a similar mean value of 0.00010 ± 0.00003. However, the carbonate Sr/Ca ratios of interstitial dolomite range from 0.00006 to 0.00039 with a mean value of 0.00027 ± 0.00015, which is intermediate between the primary interstitial calcite and fracture-filling calcite due to its Sr-enriched calcite overgrowth.

Table 2 The reconstruction of fluid Sr/Ca molar ratios and Sr concentrations based on the EPT carbonates

Lithology	SampleID	Carb. Sr/Ca (μmol/mol)	$\delta^{18}O$ sw = −1.2‰ (a)				$\delta^{18}O$ sw = −13.3 ‰ (b)			
			Temperature (°C)	K	Fluid Sr/Ca	Fluid Sr (mmol/L)	Temperature (°C)	K	Fluid Sr/Ca	Fluid Sr (mmol/L)
Interstitial Cal.(P)	A14673-1	125	109.1	0.039	0.0032	0.136	33.2	0.026	0.0047	0.201
	A22-1	116	113.2	0.040	0.0029	0.125	35.9	0.027	0.0043	0.184
	A22-2	132	108.9	0.039	0.0034	0.144	33.0	0.026	0.0050	0.213
	ABAS-2	168	110.9	0.039	0.0043	0.182	34.3	0.027	0.0063	0.269
	ABAS-3	150	102.1	0.038	0.0040	0.169	28.4	0.026	0.0059	0.250
Interstitial Cal.(A)	E-1	111	128.4	0.042	0.0026	0.113	46.4	0.029	0.0039	0.166
	E-2	76	130.7	0.042	0.0018	0.076	48.0	0.029	0.0026	0.112
	E-3	53	129.0	0.042	0.0013	0.054	46.9	0.029	0.0018	0.079
	Apex1	135	115.5	0.040	0.0034	0.144	37.5	0.027	0.0050	0.212
	Apex2	131	116.4	0.040	0.0033	0.139	38.1	0.027	0.0048	0.206
	Apex3	127	113.9	0.040	0.0032	0.136	36.4	0.027	0.0047	0.201
	D-3	87	133.0	0.043	0.0020	0.086	49.6	0.029	0.0030	0.127
	CP-1	81	127.9	0.042	0.0019	0.083	46.1	0.029	0.0029	0.121
Interstitial Dol.	A-1-C	308	119.8	0.041	0.0076	0.323	40.4	0.028	0.0112	0.475
	A-1-E	323	123.1	0.041	0.0078	0.334	42.7	0.028	0.0115	0.492
	A-2	388	104.0	0.038	0.0102	0.433	29.7	0.026	0.0150	0.641
	CP-2	56	91.7	0.036	0.0015	0.066	21.6	0.024	0.0023	0.097
Fracture Carb.	D-2-R	1300	117.3	0.040	0.0323	7.489	38.7	0.027	0.0476	11.042
	D-2-W	1939	82.7	0.035	0.0559	12.974	15.7	0.023	0.0828	19.202
Sedimentary Carb.	D-1	102	103.3	0.038	0.0027	0.620	29.2	0.026	0.0040	0.917
	PDP	224	80.4	0.034	0.0065	1.513	14.3	0.023	0.0096	2.238
	DB	83	50.6	0.029	0.0028	0.121	-3.9	0.020	0.0041	0.176
	TSU	81	93.9	0.037	0.0022	0.512	23.0	0.025	0.0033	0.759
	E-4	44	97.8	0.037	0.0012	0.275	25.5	0.025	0.0018	0.406
SPF Stromatolite	Strelley	97	83.6	0.035	0.0028	0.643	16.3	0.024	0.0041	0.952

Note:
1. K is the temperature-dependent distribution coefficient calculated by the method described by Zhang and DePaolo, 2020.
2. $\delta^{18}O$ sw values are assumed $\delta^{18}O$ value of Paleoarchean seawater based on references: (a) Shackleton and Kennett, 1975; (b) Jaffrés et al., 2007
3. Abbreviations: Cal. –calcite; ; P-primary; A-altered; Dol.- dolomite; Carb. –carbonate; SPF-the Strelley Pool Formation

The distribution coefficient K is temperature-dependent, corresponding synchronously to the variance of the carbonate $\delta^{18}O$ value and assumed seawater $\delta^{18}O$ value. With a seawater $\delta^{18}O$ value of – 1.2 ‰, the K values of the EPT carbonates range from 0.029 to 0.043 with an average value of 0.039 ± 0.003, comparable with the empirical K values for low-temperature diagenetic calcite and dolomite that form at slow growth rates (Carpenter and Lohmann, 1992; Banner, 1995). In this scenario, the fluid Sr/Ca ratios of fracture-filling calcites are up to 0.0559. The primary interstitial calcites have an average fluid Sr/Ca ratio of 0.0036 ± 0.0006, which is slightly higher than that of the altered interstitial calcites 0.0024 ± 0.0008. The interstitial dolomites and sedimentary carbonates have more varied fluid Sr/Ca ratios of

0.0068 ± 0.0037 and 0.0031 ± 0.0020, respectively, on average. The SPF stromatolite has a value of 0.0028. Accordingly, the fracture-filling calcite has the maximum fluid Sr concentration of 12.974 mmol/L. The primary interstitial calcite has an average Sr concentration of 0.151 ± 0.024 mmol/L and the altered interstitial calcite of 0.122 ± 0.038 mmol/L, while the interstitial dolomite has 0.289 ± 0.157 mmol/L. The sedimentary carbonates and stromatolite have a mean value of 0.614 ± 0.485 mmol/L. If the seawater $\delta^{18}O$ value were -13.3 ‰, the K values of the EPT carbonates would range from 0.020 to 0.029 with an average value of 0.026 ±0.002, lower than the results based on the scenario of -1.2 ‰, leading to higher fluid Sr/Ca ratios and Sr concentrations. The highest fluid Sr/Ca ratios of fracture-filling calcites move to 0.0828. The average fluid Sr/Ca ratio of interstitial calcites is 0.0042 ± 0.0013 and that of interstitial dolomite 0.0100 ± 0.0054, while the sedimentary carbonate and stromatolite have an average value of 0.0045 ± 0.0027. The fluid Sr concentrations of the primary and altered interstitial calcites are 0.223 ± 0.035 mmol/L and 0.153 ± 0.050 mmol/L, respectively. The interstitial dolomite has a mean fluid Sr concentration of 0.426 ± 0.232 mmol/L, while the sedimentary carbonate and stromatolite have a mean value of 0.908 ± 0.719 mmol/L.

2.3 Discussion

As the temperature-dependent K values of the pristine EPT carbonates are controlled by the Paleoarchean $\delta^{18}Osw$, that invokes a long-standing debate over an invariable seawater $\delta^{18}O$ (Gregory, 1991; Muehlenbachs, 1998; Tartèse et al. 2017) and variable, low $\delta^{18}O$ Archean seawater (Perry, 1967; Perry and Lefticariu, 2003; Kasting et al., 2006; Jaffrés et al., 2007; Galili et al., 2019; Vérard and Veizer, 2019), the low K values calculated with low $\delta^{18}Osw$ values accordingly cause the high fluid Sr/Ca ratios (Table 2). In this work, the seawater endmember exhibited a fluid Sr/Ca ratio of 0.05592 ($\delta^{18}Osw$ = -1.2 ‰) or 0.08277 ($\delta^{18}Osw$ = -13.3 ‰), higher than the 3.23 Ga seawater endmember of 0.01948 given by the study of quartz-bearing fluid inclusion from Ironstone Pods of the Barberton greenstone belt (De Ronde et al., 1997). They are much higher than that of the bottom seawater around the Lost City venting (0.00885) (Seyfried et al., 2015), when the mean values of seawater from 0.008269 to 0.008404 vertically in different depth intervals on a global scale (Lebrato et al., 2020). The low-temperature hydrothermal fluids based on the EPT primary interstitial calcite have an average Sr/Ca ratio of 0.00355 ±0.00056 ($\delta^{18}Osw$ = -1.2 ‰), identical to the fluid Sr/Ca ratios of the 3.23 Ga hydrothermal fluid endmember (0.00352, De Ronde et al., 1997) and the modern counterpart from Lost City venting field (~0.00383, Seyfried et al., 2015). However, a higher average Sr/Ca ratio of 0.00525 ±0.00083 is observed when calculated with $\delta^{18}Osw$ of -13.3 ‰. Nonetheless, it can be concluded that the low-temperature hydrothermal fluids have likely consistently had lower Sr/Ca molar ratios than contemporaneous seawater since the early Archean.

The Sr concentration of fluid can be easily calculated using the fluid Sr/Ca ratio and Ca concentration. Due to the much higher carbonate Sr concentration (1789.259 ppm) in the seawater endmember and the high Ca concentration of the assumed seawater (232 mmol/L), changes in the Paleoarchean $\delta^{18}Osw$ value greatly influence the seawater Sr concentration but

do not affect the Sr concentration of the low-temperature fluid (Fig.2). The unequal decreases in Ca and Sr concentrations, with Sr decreasing faster than Ca (141: 22, respectively), explain the decline in seawater Sr/Ca ratios from 3.48 Ga to the present. If so, what could be responsive for the unequal decreases in seawater Ca and Sr concentrations? The answer may lie in changes in input and output. Hydrothermal fluid is usually considered an important source of Ca and Sr for the ocean. However, the consistent Sr concentrations of low-temperature hydrothermal fluids since the early Archean (0.15 mmol/L) raise questions about estimating the secular change of the low-temperature hydrothermal flux. Gillis and Coogan (2011) attributed changing reaction kinetics and higher Ca concentrations in seawater to higher bottom water temperatures during the Cretaceous, a view concurred by Rausch (2012). Hence, the progressively cooling bottom water due to attenuated hydrothermal activities since the early Archean may provide a good explanation for the decreasing Ca and Sr inputs to the ocean. On the other hand, the interstitial dolomites are suggested to have precipitated from high-temperature hydrothermal fluids, resulting in a slightly higher average Sr concentration of 0.29 ± 0.16 mmol/L, although still much lower than the contemporary seawater Sr concentration (12.97 mmol/L). Therefore, the input of high Sr concentrations needs to be considered, either through subaerial or submarine weathering of Sr-rich continental crust. The study of low-temperature and high-temperature hydrothermal fluxes in the early Archean is encouraged to provide a better estimate or even qualification the relative contributions to the ocean geochemical cycles.

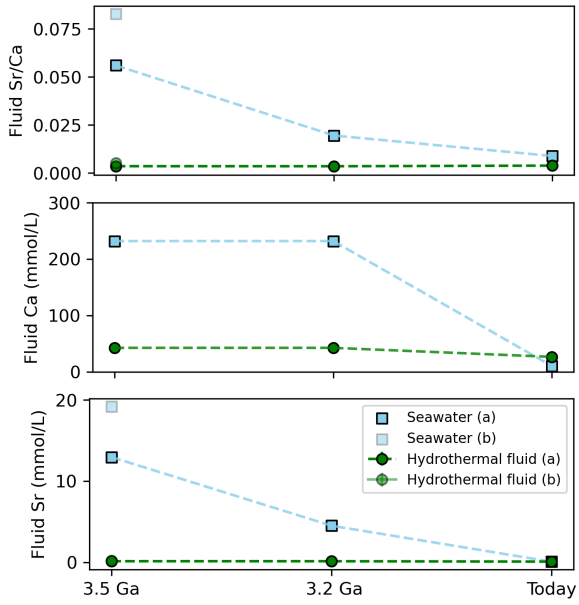

Fig. 2 The fluid Sr/Ca molar ratios, Ca and Sr concentrations (mmol/L) of seawater and (low-temperature) hydrothermal fluid at 3.5 Ga, 3.2 Ga and present-day. (a) in labels means the values are calculated with δ^{18}Osw of -1.2 ‰ (Shackleton and Kennett, 1975), while (b) δ^{18}Osw of -13.3 ‰ (Jaffrés et al., 2007). Data of 3.2 Ga are from the quartz-bearing fluid inclusion of Ironstone Pods (3.23 Ga, the Barberton greenstone belt, South Africa) (De Ronde et al., 1997), while the present-day data are from Lost City hydrothermal venting (Seyfried et al., 2015).

3. Quantification on fluid-rock reaction during carbonate diagenesis

The fluid Sr concentration may be useful in identifying diagenetic fluid. A comprehensive study of $\delta^{13}C$ and $\delta^{18}O$ values, carbonate Sr concentrations and $^{87}Sr/^{86}Sr$ ratios (Fig.3a-c), as well as Eu anomalies (Chapter 3), can qualitatively assess whether there is later diagenesis and which fluid may be responsible for it. This is supported in the space of $^{87}Sr/^{86}Sr$ ratios vs. fluid Sr concentrations (Fig.3d and e, noting the trends independent of seawater $\delta^{18}O$ values), where the sedimentary carbonates and SPF stromatolite are located closer to the interstitial dolomites, which are interpreted to be precipitated in a marine environment and then influenced more by high-temperature hydrothermal alteration. Meanwhile, the primary interstitial calcites and their altered counterparts are precipitated and altered by low-temperature hydrothermal fluids. In this section, numerical modeling based on mass balance principle is adopted to quantify the fluid-rock reaction during carbonate diagenesis.

3.1 Mass balance model

The mass balance model was developed to quantify the variations in Sr concentration and isotopic composition during fluid-rock interaction, assuming elemental isotopic mass balance upon homogeneous equilibration in a closed system (Banner and Hanson, 1990; Banner, 1995). The repetition (iteration) of the equations in the closed system can be used to represent open-system fluid-rock interaction (Land, 1980; Banner, 1995). However, in this work, only the scenario of the reaction under equilibrium in a closed system is considered. It is assumed that Sr in the modified fluid is from the rock and the fluid entering this closed system prior to reaction. Hence, the Sr concentration of the modified fluid (C_f^{Sr}) can be expressed in the same way as Eq.6:

$$C_f^{Sr} = C_{f,0}^{Sr} \times F + C_{r,0}^{Sr} \times (1 - F) \quad \text{(Eq.6)}$$

where $C_{f,0}^{Sr}$ and $C_{r,0}^{Sr}$ are the Sr concentrations in fluid (f) and rock (r) before interaction, respectively, while F is a weight fraction for fluid and the water-rock ratio W/R equals to F/(1-F). This equation can be further expressed with the $^{87}Sr/^{86}Sr$ ratios and the ^{86}Sr concentrations [^{86}Sr] as:

$$(^{87}Sr/^{86}Sr)_f \times [^{86}Sr]_f = (^{87}Sr/^{86}Sr)_{f,0} \times [^{86}Sr]_{f,0} \times F + (^{87}Sr/^{86}Sr)_{r,0} \times [^{86}Sr]_{r,0} \times (1 - F) \quad \text{(Eq.7)}$$

where [^{86}Sr] can be approximated by total Sr without introducing significant errors when ^{88}Sr makes up the bulk of strontium in most rocks, such as carbonate and basalt (Dickin, 2018). Therefore, a mass-balance expression for the Sr isotopic composition of water-rock system upon equilibration is:

$$(^{87}Sr/^{86}Sr)_f = \{ (^{87}Sr/^{86}Sr)_{f,0} \times [Sr]_{f,0} \times F + (^{87}Sr/^{86}Sr)_{r,0} \times [Sr]_{r,0} \times (1 - F) \}$$

$$/\ \{[\mathrm{Sr}]_{f,0} \times F + \ [\mathrm{Sr}]_{r,0} \times (1-F)\} \qquad \text{(Eq.8)}$$

3.2 Discussion and conclusion

According to the previous chapters, this fluid-rock model matches the recrystallization of interstitial calcites triggered by seawater or low temperature hydrothermal-fluid. Therefore, the average carbonate Sr concentration and $^{87}Sr/^{86}Sr$ ratio of the four pristine Apex interstitial calcites (A14673-1, A22-2, ABAS-2, ABAS-3) are regarded as the rock endmember. For the fluid endmember, two scenarios are considered: the fluid Sr concentration and $^{87}Sr/^{86}Sr$ ratio of D-2-W as seawater endmember, while the diagenetic fluid is assumed here to have the fluid Sr concentration of E-3 and the whole-rock $^{87}Sr/^{86}Sr$ ratio of 0.706337 from Apex pillow basalts (Chapter 3 and 4). The parameters of various endmembers are listed in Table 3 and the quantitative modeling is shown in Fig.4. According to the results, the recrystallized Apex interstitial calcites fit the model well, occurring under small fluid-rock ratios from 10 to 15. The fracture-filling calcite D-2-R, an interstitial calcite altered by seawater, also matches well under fluid-rock ratio of 1 to 2. However, other interstitial calcites located outside of the area, indicating different diagenetic fluids apart from the one in Apex Basalt system, although the close $^{87}Sr/^{86}Sr$ ratios of two interstitial calcites from Euro Basalt to the whole-rock $^{87}Sr/^{86}Sr$ ratio of 0.706337 from Apex pillow basalts may infer a similar hydrothermal system to Apex Basalt. The depleted $\delta^{18}O$ sw value of -13.3 ‰ rarely influences the fluid-rock ratio (still 1~2) in recrystallization triggered by seawater, and slightly decreases the fluid-rock ratios (6~10) in low-temperature hydrothermal alteration. It can be speculated that the fluid-rock model functions better in the same rock setting and the fluid-rock ratio during the recrystallization is small (<15).

Table 3 Parameters of various endmembers used in the numerical models.

Endmember	SampleID	$^{87}Sr/^{86}Sr$	Fluid Sr conc. (a)	Fluid Sr conc. (b)	Carbonate Sr conc.
Seawater	D-2-W	0.700596	1136.79	1682.49	
LT hydrothermal fluid	Ave. Apex ical	0.703094	13.84	20.45	111.17
LT hydrothermal fluid (A)	E-3	0.706337	4.69	6.89	
HT hydrothermal fluid	A-2	0.712832	37.96	56.15	

Note:
1. LT hydrothermal fluid (A) means the low-temperarure (LT) hydrothermal fluid triggering post-depositional alteration (A), i.e. recrystallization of interstital calcites, whereas HT hydrothermal fluid caused the dolomitization of interstitial calcites.
2. Ave. Apex ical in SampleID indicates data are the average values calculated from the Apex primary interstitial calcites.
3. conc.- concentration in ppm.
4. Calculation are based on the seawater $\delta^{18}O$ value of (a) −1.2‰ (Shackleton and Kennett, 1975) and (b) -13.3 ‰ (Jaffrés et al., 2007).

And assuming that all of the aforementioned parameters and equations can be applied to dolomite, a three-component mixing model is proposed to estimate the degree of hydrothermal alteration by high-temperature (HT) hydrothermal fluids. First, it is suggested that the EPT interstitial dolomites, marine sedimentary carbonates and the SPF stromatolite were precipitated from a mixture of seawater and low-temperature hydrothermal fluid that produced and/or altered the Apex pristine interstitial calcite, respectively. Second, they were later altered by high-temperature hydrothermal fluid, triggering dolomitization. The fluid Sr concentration and $^{87}Sr/^{86}Sr$ ratio of A-2 are used as the endmembers of high-temperature hydrothermal flui1d, as it is an interstitial carbonate sample from the deep carbonate vein of Mount Ada Basalt, that likely has closer composition to the alteration fluid. The results are

illustrated in Fig.5 where numbers in the plot indicate the fractions of one component during two-component mixing, F (0<F<1). Except for DB, the formation and diagenesis of other carbonates can be explained by this model. However, the Sr concentrations and $^{87}Sr/^{86}Sr$ ratios of most carbonates are largely overprinted (>60%) by HT hydrothermal fluids, although some marine sedimentary carbonates and stromatolite still retain a tiny fraction of seawater signals (0.05~0.2). CP-2 is located on the mixing line of seawater and low temperature-hydrothermal fluid (altered) (Fig.5c and d), inferring it was precipitated from this fluid rather than HT hydrothermal fluid, consistent with its REE+Y pattern which is closer to interstitial calcite.

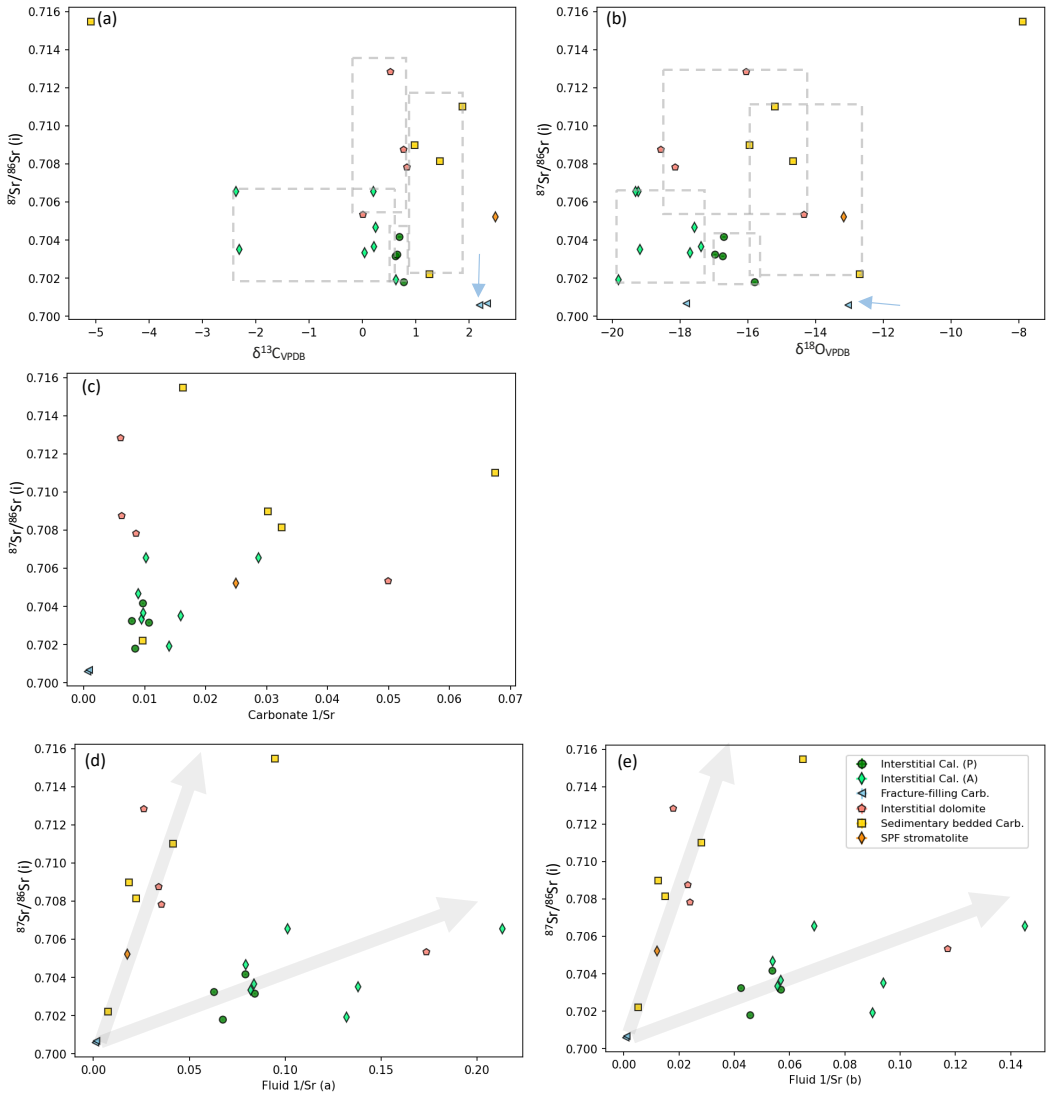

Fig. 3 The cross-plots of the age-corrected $^{87}Sr/^{86}Sr$ ratios of the EPT carbonates against their (a) $\delta^{13}C_{VPDB}$ values, (b) $\delta^{18}O_{VPDB}$ values, the reciprocal of Sr concentrations as 1/Sr (ppm^{-1}) of (c) carbonate and (d) fluid precipitating the carbonate based on the seawater $\delta^{18}O$ value of −1.2‰ (Shackleton and Kennett, 1975) and (e) -13.3 ‰ (Jaffrés et al., 2007). The seawater endmember is indicated by the greyblue arrows in (a) and (b). The grey lines with arrow in (d) indicates there might be two types of hydrothermal fluids involved in the precipitation and post-depositional alteration of the EPT carbonates. (Abbreviations: Cal. –calcite; P-primary; A-altered; Carb. –carbonate; SPF- Strelley Pool Formation)

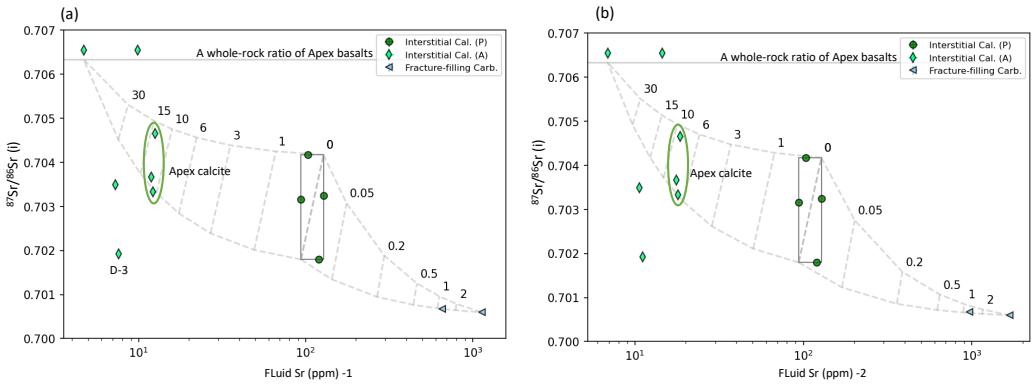

Fig.4 Numerical models for quantitively estimating fluid-rock reactions during diagenesis of the hydrothermal EPT calcites. Numbers in plots indicate water-rock ratios. This model fits the interstitial calcites of Apex Basalt and Dresser Formation well, however, does not match other cases possibly due to their different parent fluids from the assumed endmembers. The fluid Sr concentrations calculated with seawater $\delta^{18}O$ value of (a) −1.2‰ (Shackleton and Kennett, 1975) and (b) -13.3 ‰ (Jaffrés et al., 2007). Similarities between (a) and (b) indicate the choice of seawater $\delta^{18}O$ value does not largely influence the interpretation.

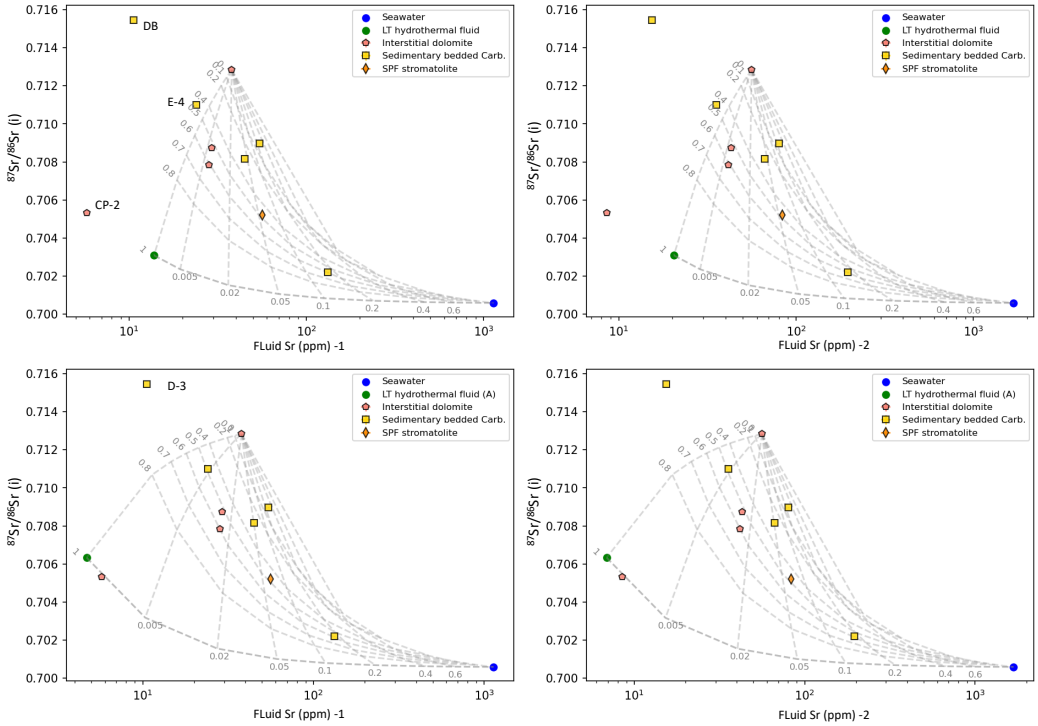

Fig.5 Numerical models based on the two-component mixing model and mass balance principle, proposed for quantitively estimating the Sr overprint during dolomitization. Numbers in plots indicate one component fraction F. The endmember of low-temperature (LT) hydrothermal fluid in (a) and (b) is calculated with data of the Apex primary interstitial calcites (on average), while it is changed with the assumed one labelled as LT hydrothermal fluid (A) in (c) and (d) (Table 3). The fluid Sr concentrations are calculated with seawater $\delta^{18}O$ value of −1.2‰ (Shackleton and Kennett, 1975) in (a) and (c), whereas -13.3 ‰ (Jaffrés et al., 2007) in (b) and (d). It is noted that the $^{87}Sr/^{86}Sr$ ratios and fluid Sr concentrations of most EPT dolomites are overprinted by high-temperature hydrothermal fluid, while some partly retain seawater signals to support their origins of seawater or seawater-derived fluids. Similarities between (a) and (b), (c) and (d), indicate the choice of seawater $\delta^{18}O$ value does not largely influence the interpretation.

In summary, the application of fluid Sr concentration and $^{87}Sr/^{86}Sr$ ratio for quantitively estimating fluid-rock reaction during carbonate diagenesis can be expected, although this work is still in progress due to uncertainties of parameters used in calculations. Our pristine carbonate samples are good archives for reconstructing environment conditions and are plausible candidates for future geochemical and modeling works.

Summary

This chapter attempts to use the EPT carbonates to reconstruct environmental conditions, including the temperature of the depositional fluid, Sr/Ca and Sr concentration of seawater and hydrothermal fluids originating from low-temperature seafloor alteration, and water-rock reactions during diagenesis. Considering the debates and uncertainties over some key parameters, such as the ~3.5 Ga seawater $\delta^{18}O$ values, different scenarios are discussed. Only unambiguous conclusions are listed as follows: (1) The temperatures of the seawater-derived hydrothermal fluids that form Apex interstitial carbonates were 17.3 to 26.1 °C higher than the temperature of the contemporary seawater, and the heat was from the cooling of Apex pillow basalts; (2) The low-temperature hydrothermal fluids likely have had consistently lower Sr/Ca molar ratios than contemporaneous seawater since the early Archean; (3) The fluid Sr concentration (calculated from carbonate $\delta^{18}O$ value and Sr/Ca ratio, and parent fluid Ca concentration) and $^{87}Sr/^{86}Sr$ ratio can be applied to quantify the fluid-rock reaction during carbonate diagenesis.

Acknowledgements

This chapter has greatly benefited from invaluable discussions with Dr. Jakub Surma and Oliver Jäger, who provided insights on triple oxygen isotopes and modeling. We would like to express our gratitude to Prof. Andreas Pack and Prof. em. Dr. Jochen Hoefs for their advice on calculating temperatures using carbonate oxygen isotopes. We also acknowledge Prof. Dr. Wolfgang Bach at the University of Bremen for reconstructing fluid compositions, and Prof. Dr. Matthias Willbold for his suggestions on modeling.

References

Alt, J. C. and Teagle, D. A.: The uptake of carbon during alteration of ocean crust, Geochimica et Cosmochimica Acta, 63, 1527–1535, 1999.

Amiel, A. J., Friedman, G. M., and Miller, D. S.: Distribution and nature of incorporation of trace elements in modern aragonitic corals, Sedimentology, 20, 47–64, https://doi.org/10.1111/j.1365-3091.1973.tb01606.x, 1973.

Anderson, T. F. and Arthur, M. A.: Stable isotopes of oxygen and carbon and their application to sedimentologic and paleoenvironmental problems, https://doi.org/10.2110/scn.83.01.0000, 1983.

Bach, W., Alt, J. C., Niu, Y., Humphris, S. E., Erzinger, J., and Dick, H. J.: The geochemical consequences of late-stage low-grade alteration of lower ocean crust at the SW Indian Ridge: Results from ODP Hole 735B (Leg 176), Geochimica et Cosmochimica Acta, 65, 3267–3287, 2001.

Bach, W., Rosner, M., Jöns, N., Rausch, S., Robinson, L. F., Paulick, H., and Erzinger, J.: Carbonate veins trace seawater circulation during exhumation and uplift of mantle rock: Results from ODP Leg 209, Earth and Planetary Science Letters, 311, 242–252, 2011.

Banner, J. L., Musgrove, M., and Capo, R.: Tracing ground-water evolution in a limestone aquifer using Sr isotopes: Ef- fects of multiple sources of dissolved ions and mineral-solution reactions, Geology, 22, 687–690, https://doi.org/10.1130/0091- 7613(1994)022<0687:TGWEIA>2.3.CO;2, 1994.

Banner, J. L.: Application of the trace element and isotope geochemistry of strontium to studies of carbonate diagenesis, Sedimentology, 42, 805–824, https://doi.org/10.1111/j.1365-3091.1995.tb00410.x, 1995.

Banner, J. L. and Hanson, G. N.: Calculation of simultaneous isotopic and trace element variations during water-rock interaction with applications to carbonate diagenesis, Geochimica et Cosmochimica Acta, 54, 3123–3137, 1990.

Blake, R. E., Chang, S. J., and Lepland, A.: Phosphate oxygen isotopic evidence for a temperate and biologically active Archaean ocean, Nature, 464, 1029–1032, https://doi.org/10.1038/nature08952, 2010.

Boussau, B., Blanquart, S., Necsulea, A., Lartillot, N., and Gouy, M.: Parallel adaptations to high temperatures in the Archaean eon, Nature, 456, 942–945, 2008.

Burns, S. J., Baker, P. A., and Elderfield, H.: Timing of carbonate mineral precipitation and fluid flow in sea-floor basalts, northwest Indian Ocean, Geology, 20, 255–258, 1992.

Camprubí, E., De Leeuw, J., House, C., Raulin, F., Russell, M., Spang, A., Tirumalai, M., and Westall, F.: The emergence of life, Space Science Reviews, 215, 1–53, https://doi.org/10.1007/s11214-019-0624-8, 2019.

Carpenter, S. J. and Lohmann, K. C.: SrMg ratios of modern marine calcite: Empirical indicators of ocean chemistry and precipitation rate, Geochimica et Cosmochimica Acta, 56, 1837–1849, 1992.

Charnay, B., Le Hir, G., Fluteau, F., Forget, F., and Catling, D. C.: A warm or a cold early Earth? New insights from a 3-D climate-carbon model, Earth and Planetary Science Letters, 474, 97–109, https://doi.org/10.1016/j.epsl.2017.06.029, 2017.

Coggon, R. M., Teagle, D. A., Cooper, M. J., and Vanko, D. A.: Linking basement carbonate vein compositions to porewater geochemistry across the eastern flank of the Juan de Fuca Ridge, ODP Leg 168, Earth and Planetary Science Letters, 219, 111–128, 2004.

Coggon, R. M., Teagle, D. A., Smith-Duque, C. E., Alt, J. C., and Cooper, M. J.: Reconstructing past seawater Mg/Ca and Sr/Ca from mid-ocean ridge flank calcium carbonate veins, Science, 327, 1114–1117, https://doi.org/10.1126/science.1182252, 2010.

De Ronde, C. E., Channer, D. M. d., Faure, K., Bray, C. J., and Spooner, E. T.: Fluid chemistry of Archean seafloor hydrothermal vents: Implications for the composition of circa 3.2 Ga seawater, Geochimica et Cosmochimica Acta, 61, 4025–4042, https://doi.org/10.1016/S0016-7037(97)00205-6, 1997.

de Wit, M. J. and Furnes, H.: 3.5-Ga hydrothermal fields and diamictites in the Barberton Greenstone Belt—Paleoarchean crust in cold environments, Science advances, 2, e1500 368, https://doi.org/10.1126/sciadv.1500368, 2016.

Degens, E. T. and Epstein, S.: Relationship between O^{18}/O^{16} ratios in coexisting carbonates, cherts, and diatomites, AAPG Bulletin, 46, 534–542, https://doi.org/10.1306/BC743841-16BE-11D7-8645000102C1865D, 1962.

Dickin, A. P.: Radiogenic isotope geology, Cambridge university press, 2018.

Elderfield, H.: Seawater Chemistry and Climate, Science, 327, 1092-1093. doi:10.1126/science.1186769, 2010.

Gabitov, R. I. and Watson, E. B.: Partitioning of strontium between calcite and fluid, Geochemistry, Geophysics, Geosystems, 7, https://doi.org/10.1029/2005GC001216, 2006.

Galili, N., Shemesh, A., Yam, R., Brailovsky, I., Sela-Adler, M., Schuster, E. M., Collom, C., Bekker, A., Planavsky, N., Mac- donald, F. A., et al.: The geologic history of seawater oxygen isotopes from marine iron oxides, Science, 365, 469–473, https://doi.org/10.1126/science.aaw9247, 2019.

Garcia, A. K., Schopf, J. W., Yokobori, S.-i., Akanuma, S., and Yamagishi, A.: Reconstructed ancestral enzymes suggest long-term cooling of Earth's photic zone since the Archean, Proceedings of the National Academy of Sciences, 114, 4619–4624, https://doi.org/10.1073/pnas.1702729114, 2017.

Gillis, K. and Coogan, L.: Secular variation in carbon uptake into the ocean crust, Earth and Planetary Science Letters, 302, 385–392, https://doi.org/10.1016/j.epsl.2010.12.030, 2011.

Gothmann, A. M., Stolarski, J., Adkins, J. F., Schoene, B., Dennis, K. J., Schrag, D. P., Mazur, M., and Bender, M. L.: Fossil corals as an archive of secular variations in seawater chemistry since the Mesozoic, Geochimica et Cosmochimica Acta, 160, 188–208, https://doi.org/10.1016/j.gca.2015.03.018, 2015.

Gregory, R.: Oxygen isotope history of seawater revised: timescales for boundary event changes in the oxygen isotope composition of seawater, Stable isotope geochemistry: A tribute to Samuel Epstein, 3, 65–76, 1991.

Hart, S. and Staudigel, H.: Ocean crust vein mineral deposition: Rb/Sr ages, U-Th-Pb geochemistry, and duration of circulation at DSDP sites 261, 462 and 516, Geochimica et Cosmochimica Acta, 50, 2751–2761, https://doi.org/10.1016/0016-7037(86)90224-3, 1986.

Hays, P. D. and Grossman, E. L.: Oxygen isotopes in meteoric calcite cements as indicators of continental paleoclimate, Geology, 19, 441–444, https://doi.org/10.1130/0091-7613(1991)019<0441:OIIMCC>2.3.CO;2, 1991.

Herwartz, D., Pack, A., and Nagel, T. J.: A CO_2 greenhouse efficiently warmed the early Earth and decreased seawater $^{18}O/^{16}O$ before the onset of plate tectonics, Proceedings of the National Academy of Sciences, 118, e2023617 118, https://doi.org/10.1073/pnas.2023617118, 2021.

Hoefs, J.: Stable isotope geochemistry, Springer International Publishing AG, part of Springer Nature, 8th ed., 2018.

Hofmann, A.: The geochemistry of sedimentary rocks from the Fig Tree Group, Barberton greenstone belt: Implications for tectonic, hydrothermal and surface processes during mid-Archaean times, Precambrian Research, 143, 23–49, https://doi.org/10.1016/j.precamres.2005.09.005, 2005.

Hren, M., Tice, M., and Chamberlain, C.: Oxygen and hydrogen isotope evidence for a temperate climate 3.42 billion years ago, Nature, 462, 205–208, https://doi.org/10.1038/nature08518, 2009.

Jaffrés, J. B., Shields, G. A., and Wallmann, K.: The oxygen isotope evolution of seawater: A critical review of a long-standing controversy and an improved geological water cycle model for the past 3.4 billion years, Earth-Science Reviews, 83, 83–122, https://doi.org/10.1016/j.earscirev.2007.04.002, 2007.

Johnson, B. W. and Wing, B. A.: Limited Archaean continental emergence reflected in an early Archaean ^{18}O-enriched ocean, Nature Geoscience, 13, 243–248, https://doi.org/10.1038/s41561-020-0538-9, 2020.

Kasting, J. F., Howard, M. T., Wallmann, K., Veizer, J., Shields, G., and Jaffrés, J.: Paleoclimates, ocean depth, and the oxygen isotopic composition of seawater, Earth and Planetary Science Letters, 252, 82–93, https://doi.org/10.1016/j.epsl.2006.09.029, 2006.

Knauth, L. P. and Lowe, D. R.: High Archean climatic temperature inferred from oxygen isotope geochemistry of cherts in the 3.5 Ga Swaziland Supergroup, South Africa, Geological Society of America Bulletin, 115, 566–580, https://doi.org/10.1130/0016-7606(2003)115<0566:HACTIF>2.0.CO;2, 2003.

Krissansen-Totton, J., Arney, G. N., and Catling, D. C.: Constraining the climate and ocean pH of the early Earth with a geological carbon cycle model, Proceedings of the National Academy of Sciences, 115, 4105–4110, https://doi.org/10.1073/pnas.1721296115, 2018.

Land, L. S.:The isotopic and trace element geochemistry of dolomite: the state of the art. In: Ed. by D. H. Zenger, J. B. Dunham and R. L. Ethington, Special Publications of SEPM, 28, 87-110, 1980.

Lear, C. H., Elderfield, H., and Wilson, P.: A Cenozoic seawater Sr/Ca record from benthic foraminiferal calcite and its application in determining global weathering fluxes, Earth and Planetary Science Letters, 208, 69–84, https://doi.org/10.1016/S0012-821X(02)01156-1, 2003.

Lebrato, M., Garbe-Schönberg, D., Müller, M. N., Blanco-Ameijeiras, S., Feely, R. A., Lorenzoni, L., Molinero, J.-C., Bremer, K., Jones, D. O., Iglesias-Rodriguez, D., et al.: Global variability in seawater Mg: Ca and Sr: Ca ratios in the modern ocean, Proceedings of the National Academy of Sciences, 117, 22 281–22 292, https://doi.org/10.1073/pnas.1918943117, 2020.

Lorens, R. B.: Sr, Cd, Mn and Co distribution coefficients in calcite as a function of calcite precipitation rate, Geochimica et Cosmochimica Acta, 45, 553–561, https://doi.org/10.1016/0016-7037(81)90188-5, 1981.

Marin-Carbonne, J., Chaussidon, M., and Robert, F.: Micrometer-scale chemical and isotopic criteria (O and Si) on the origin and history of Precambrian cherts: implications for paleo-temperature reconstructions, Geochimica et Cosmochimica Acta, 92, 129–147, https://doi.org/10.1016/j.gca.2012.05.040, 2012.

Marin-Carbonne, J., Robert, F., and Chaussidon, M.: The silicon and oxygen isotope compositions of Precambrian cherts: A record of oceanic paleotemperatures?, Precambrian Research, 247, 223–234, https://doi.org/10.1016/j.precamres.2014.03.016, 2014.

McGunnigle, J., Cano, E., Sharp, Z., Muehlenbachs, K., Cole, D., Hardman, M., Stachel, T., and Pearson, D.: Triple oxygen isotope evidence for a hot Archean ocean, Geology, 50, 991–995, https://doi.org/10.1130/G50230.1, 2022.

McIntire, W.: Trace element partition coefficients—a review of theory and applications to geology, Geochimica et Cosmochimica Acta, 27, 1209–1264, https://doi.org/10.1016/0016-7037(63)90049-8, 1963.

Mottl, M.: Partitioning of energy and mass fluxes between mid-ocean ridge axes and flanks at high and low temperature, in: Energy and mass transfer in marine hydrothermal systems, edited by Halbach, P. E., Tunnicliffe, V., and Hein, J. R., pp. 271–286, Berlin: Dahlem University Press, 2003.

Muehlenbachs, K.: The oxygen isotopic composition of the oceans, sediments and the seafloor, Chemical Geology, 145(3-4), 263-273, 1998.

Nielsen, S. G., Rehkämper, M., Teagle, D. A., Butterfield, D. A., Alt, J. C., and Halliday, A. N.: Hydrothermal fluid fluxes calculated from the isotopic mass balance of thallium in the ocean crust, Earth and Planetary Science Letters, 251, 120–133, https://doi.org/10.1016/j.epsl.2006.09.002, 2006.

Perry, Jr. E. C.: The oxygen isotope chemistry of ancient cherts[J]. Earth and Planetary Science Letters, 3, 62-66, 1967.

Perry Jr, E. C. and Lefticariu, L.: Formation and geochemistry of Precambrian cherts, vol. 7, 2003.

Pingitore Jr, N. E., Lytle, F. W., Davies, B. M., Eastman, M. P., Eller, P. G., and Larson, E. M.: Mode of incorporation of Sr^{2+} in cal- cite: Determination by X-ray absorption spectroscopy, Geochimica et Cosmochimica Acta, 56, 1531–1538, https://doi.org/10.1016/0016- 7037(92)90222-5, 1992.

Rausch, S.: Carbonate veins as recorders of seawater evolution, CO_2 uptake by the ocean crust, and seawater-crust interaction during low- temperature alteration, Ph.D. thesis, Universität Bremen, 2012.

Robert, F. and Chaussidon, M.: A palaeotemperature curve for the Precambrian oceans based on silicon isotopes in cherts, Nature, 443, 969–972, https://doi.org/10.1038/nature05239, 2006.

Rouillard, J., Van Kranendonk, M. J., Lalonde, S., Gong, J., and Van Zuilen, M. A.: Correlating trace element compositions, petrology, and Raman spectroscopy data in the 3.46 Ga Apex chert, Pilbara Craton, Australia, Precambrian Research, 366, 106415, https://doi.org/10.1016/j.precamres.2021.106415, 2021.

Sengupta, S., Peters, S. T., Reitner, J., Duda, J.-P., and Pack, A.: Triple oxygen isotopes of cherts through time, Chemical Geology, 554, 119 789, https://doi.org/10.1016/j.chemgeo.2020.119789, 2020.

Seyfried Jr, W., Pester, N. J., Tutolo, B. M., and Ding, K.: The Lost City hydrothermal system: Constraints imposed by vent fluid chemistry and reaction path models on subseafloor heat and mass transfer processes, Geochimica et Cosmochimica Acta, 163, 59–79, https://doi.org/10.1016/j.gca.2015.04.040, 2015.

Shackleton, N. J. and Kennett, J. P.: Paleotemperature history of the Cenozoic and the initiation of Antarctic glaciation: oxygen and carbon isotope analyses in DSDP Sites 277, 279, and 281, Initial Reports Deep Sea Drilling Project, 29, 743–755, 1975.

Shemesh, A., Kolodny, Y., and Luz, B.: Isotope geochemistry of oxygen and carbon in phosphate and carbonate of phosphorite francolite, Geochimica et Cosmochimica Acta, 52, 2565–2572, https://doi.org/10.1016/0016-7037(88)90027-0, 1988.

Shields, G. A.: Implications of Carbonate and Chert Isotope Records for the Early Earth, in: Earth's Oldest Rocks, edited by Van Kranendonk, M., Bennett, V., and Hoffmann, J., pp. 901–912, Elsevier, 2019.

Shields, G. and Veizer, J.: Precambrian marine carbonate isotope database: Version 1.1, Geochemistry, Geophysics, Geosystems, 3, 1–of, https://doi.org/10.1029/2001GC000266, 2002.

Sosdian, S. M., Lear, C. H., Tao, K., Grossman, E. L., O'Dea, A., and Rosenthal, Y.: Cenozoic seawater Sr/Ca evolution, Geochemistry, Geophysics, Geosystems, 13, https://doi.org/10.1029/2012GC004240, 2012.

Stein, C. A., Stein, S., and Pelayo, A. M.: Heat flow and hydrothermal circulation, in: Seafloor Hydrothermal Systems: Physical, Chemical, Biological, and Geological Interactions, Geophysical Monograph Series, edited by Humphris, S. E., Zierenberg, R. A., Mullineaux, L. S., and Thomson, R. E., vol. 91, pp. 425–445, Washington, DC: American Geophysical Union, 1995.

Sun, S. S. and Hanson, G. N.: Origin of Ross Island basanitoids and limitations upon the heterogeneity of mantle sources for alkali basalts and nephelinites, Contributions to Mineralogy and Petrology, 52, 77–106, https://doi.org/10.1007/BF00395006, 1975.

Tang, J., Dietzel, M., Böhm, F., Köhler, S. J., and Eisenhauer, A.: Sr^{2+}/Ca^{2+} and $^{44}Ca/^{40}Ca$ fractionation during inorganic calcite formation: II. Ca isotopes, Geochimica et Cosmochimica Acta, 72, 3733–3745, https://doi.org/10.1016/j.gca.2008.05.033, 2008.

Tartèse, R., Chaussidon, M., Gurenko, A., Delarue, F., and Robert, F.: Warm Archean oceans reconstructed from oxygen isotope composition of early-life remnants, Geochemical Perspectives Letters, 3, 55–65, 2017.

Tesoriero, A. J. and Pankow, J. F.: Solid solution partitioning of Sr^{2+}, Ba^{2+}, and Cd^{2+} to calcite, Geochimica et Cosmochimica Acta, 60, 1053–1063, https://doi.org/10.1016/0016-7037(95)00449-1, 1996.

Tripati, A. K., Allmon, W. D., and Sampson, D. E.: Possible evidence for a large decrease in seawater strontium/calcium ratios and strontium concentrations during the Cenozoic, Earth and Planetary Science Letters, 282, 122–130, https://doi.org/10.1016/j.epsl.2009.03.020, 2009.

van den Boorn, S. H., van Bergen, M. J., Nijman, W., and Vroon, P. Z.: Dual role of seawater and hydrothermal fluids in Early Archean chert formation: evidence from silicon isotopes, Geology, 35, 939–942, https://doi.org/10.1130/G24096A.1, 2007.

Veizer, J. and Hoefs, J.: The nature of O^{18}/O^{16} and C^{13}/C^{12} secular trends in sedimentary carbonate rocks, Geochimica et Cosmochimica Acta, 40, 1387–1395, https://doi.org/10.1016/0016-7037(76)90129-0, 1976.

Veizer, J., Ala, D., Azmy, K., Bruckschen, P., Buhl, D., Bruhn, F., Carden, G. A., Diener, A., Ebneth, S., Godderis, Y., et al.: $^{87}Sr/^{86}Sr$, $\delta^{13}C$ and $\delta^{18}O$ evolution of Phanerozoic seawater, Chemical geology, 161, 59–88, https://doi.org/10.1016/S0009-2541(99)00081-9, 1999.

Veizer, J., Godderis, Y., and François, L. M.: Evidence for decoupling of atmospheric CO_2 and global climate during the Phanerozoic eon, Nature, 408, 698–701, https://doi.org/10.1038/35047044, 2000.

Vérard, C. and Veizer, J.: On plate tectonics and ocean temperatures, Geology, 47, 881–885, https://doi.org/10.1130/G46376.1, 2019.

Zachara, J., Cowan, C., and Resch, C.: Sorption of divalent metals on calcite, Geochimica et cosmochimica acta, 55, 1549–1562, https://doi.org/10.1016/0016-7037(91)90127-Q, 1991.

Chapter-6 Case study: Stromatolite? Comprehensive investigation on carbonates from 4.0 -3.6 Ga Isua Supracrustal Belt, West Greenland

1. Introduction

When was debut of life on Earth? The oldest evidence comes from carbonaceous inclusions within apatite with the depleted $\delta^{13}C$ values, which have a weighted mean of -30 ± 3 ‰ from ~3800 Ma banded iron formation in the lsua Supracrustal Belt, West Greenland, and a weighted mean of -37 ± 3‰ from a similar formation in the nearby Akilia island that is possibly older than 3850 Ma (Mojzsis et al., 1996). However, it has been intensively debated on the age and protolith of the rocks (Whitehouse et al., 1999, 2005, 2009; Mojzsis and Harrison, 2002; Nutman et al., 1996, 2002; Fedo and Whitehouse, 2002), and the preservation (Lepland et al. 2005, 2011; McKeegan et al., 2007) and biogenicity (Rosing, 1999; Ueno et al., 2002; van Zuilen et al., 2002, 2003, 2007; Ohtomo et al., 2014; van Zuilen, 2019) of graphite inclusions. For example, a sedimentary origin (Mojzsis and Harrison, 2002; Mojzsis et al., 2003; Dauphas et al., 2004, 2007) of rocks (identified as BIF) in Akilia island (Fig.1), was rejected by others who argued to be a strongly metasomatized ultramafic rock (Fedo and Whitehouse, 2002; Whitehouse et al., 2005, 2009). Similarly, various rocks in the Isua Supracrustal Belt (ISB) are suggested to be of metasomatic origin (van Zuilen, 2019) rather than a sedimentary origin (Nutman et al., 1984), that fluid circulation during multiple metamorphic events created talc-rich alteration zones and secondary carbonate veins around mafic/ultramafic rocks (Rose et al., 1996; Rosing et al., 1996; van Zuilen, 2019).

On the other hand, Nutman et al. (2016) reported 3.7 Ga metacarbonate rocks in the ISB that contain 1–4 cm thick conical and domical stromatolites deposited in a shallow marine environment, with evidence of seawater-like REE+Y patterns and the occurrence of interlayered detrital sedimentary rocks with cross-lamination and storm-wave generated breccias. However, in contrast to the stromatolites in the Strelley Pool Formation, whose biogenicity has been well-documented in the past years (Lowe, 1983; Van Kranendonk, 2006; Westall, 2008; Allwood et al., 2006, 2007, 2009, 2010; Wacey, 2010; Bontognali et al, 2012;

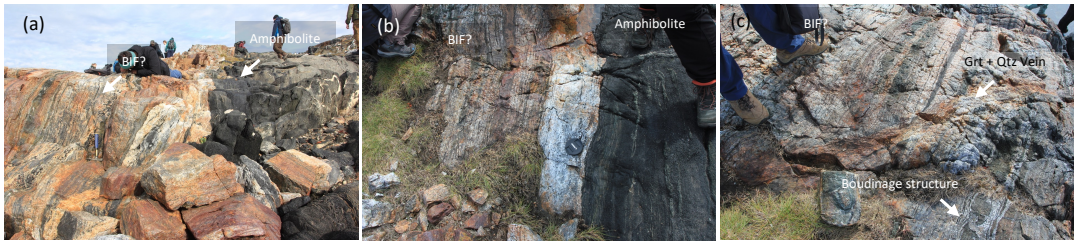

Fig.1 The outcrop photos of the controversial banded iron formation (BIF) in Akilia island, Greenland. (a) The weathered surficial photo of the BIF. The eastern side is a vein consisting of black amphibolite. (b) A narrow white quartz vein separates the BIF and amphibolite. (c) The BIF is cut by a ca. 2.7 Ga vein consisting of garnet (Grt) and quartz (Qtz). Boundinage structure indicates the rock was influenced by the extension caused by tectonic deformation.

Flannery et al., 2018), the biogenicity of this oldest stromatolite has stirred up a controversy over whether it is truly stromatolite (Nutman et al., 2016, 2019a, b) or just a deformation artifact (Allwood et al., 2018; Zawaski et al, 2020, 2021). Nevertheless, those authors did not preclude the possibility that life played some role at some time in the original formation of these rocks (Zawaski et al, 2020). Under this situation, the comprehensive research was conducted on a stromatolite-like carbonate sample and a nearby metasomatic carbonate-talc sample, to investigate the origin of stromatolite-like carbonate and estimate possible diagenesis, using the method of petrographic observation, stable carbon and oxygen isotopes described in Chapter 2, and geochemical compositions plus $^{87}Sr/^{86}Sr$ in Chapter 3.

2. Sampling site

Samples were collected by Mark van Zuilen (2018) in the vicinity of the controversial stromatolite site A described in Nutman et al. (2016) and Allwood et al. (2018). It was later defined in field research to be in the Sandstone and Dolostone Member of Snowpatch Formation, which was deposited unconformably on the ~3710 Ma Solvang Volcanic Formation of picrites, basalts and basaltic-andesites with arc-like geochemical signatures (Nutman et al., 2019a). The age of the Sandstone and Dolostone Member is ca. 3700 Ma, restricted by the underlying Conglomerate Member containing detrital zircons, the youngest of which are ~3710 Ma, and the overlying ~3695 Ma BIF Member (Nutman et al., 2019a). Based on the detailed field and geochemical evidence, such as a positive correlation between Fe/Mg and Pr/Yb* in the Snowpatch Formation dolostones and BIF, Nutman et al. (2019a) indicated that the dolomitic lithologies developed in a shallow water setting with clastic sedimentation, during a marine transgression over a weathered ~3710 Ma volcanic arc basement when the stromatolite developed, followed by BIF deposition in deeper water.

3. Debates on the ISB stromatolite-like carbonate

In Nutman et al. (2016), the biogenicity of the ISB stromatolite was supported by several lines of evidence: (1) diverse morphologies with sharp, steep-sided walls matching the SPF stromatolites; (2) the presence of low-temperature dolomite (inferred from carbon and oxygen isotopes) requiring microbial activity for precipitation; (3) seawater-like REE+Y pattens of dolomite (via LA-ICP-MS); (4) convex-upwards internal lamination. However, they were rejected one-by-one by Allwood et al. (2018): (1) the 3D geometry of triangular structures (interpretated to be a cross-sectional view of conical stromatolite in Nutman et al. (2016)) showed orientation-dependent, contrasting fabrics that were inconsistent with sedimentary process and substantially lengthened in an orthogonal direction, indicative of typical deformation fabrics rather than elongated stromatolite cones; (2) the microbial role in producing low-temperature dolomite was equivocal, and the secondary origins of dolomite could not be precluded; (3) the REE+Y pattens of dolomite (via acid digestion) were interpreted to have originally been deposited in a marine environment, followed by secondary carbonate alteration any time between early diagenesis and late carbonate metasomatism; (4) the convex-up and convex-down features occurred in one layer, and the latter was inconsistent

with the upward growth of structures from a palaeo-seafloor, again, interpretated as deformational features. In Nutman et al., (2019b), it was argued that: (1) sedimentary and volcanic features could partly survive in the other two dimensions in the fold core/hinge region, regardless of deformation; (2) the dolomite was an early facies, whereas tremolite was a late facies; (3) the REE+Y pattens of pure dolomites, via single-spot analyses that were distinctive to carbonate veins and mica-bearing layers, supported the marine origin of dolomites; (4) the convex-down feature was actually a disrupted layer within a stromatolite cut on both sides by the secondary carbonate. In subsequent works, the marine origin of the stromatolites has been acknowledged, and the debate has shifted towards their 3D geometry, whether it is compelling to demonstrate the presence of stromatolite rather than the deformation of layered rocks (Zawaski et al, 2020, 2021; Nutman et al., 2021).

4. Results

From a visual inspection of the hand specimen, the stromatolite-like carbonate exhibits wavy-crinkled geometries characterized by irregularly undulated stromatolite-like layers

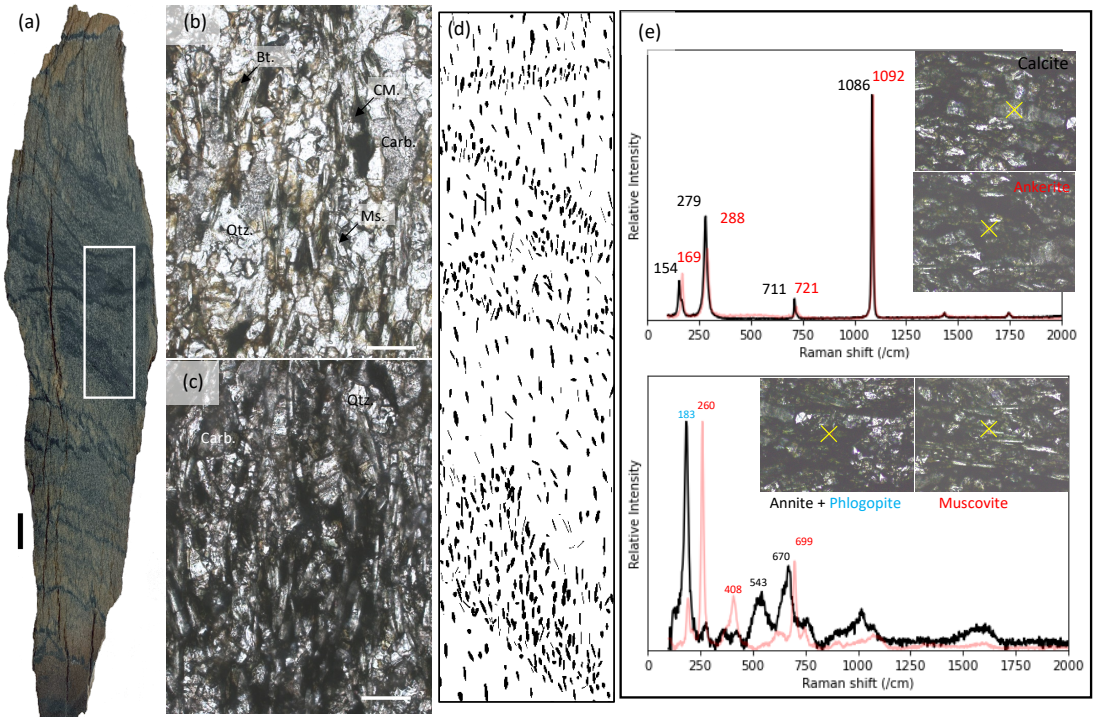

Fig.2 Photographs of the stromatolite-like carbonate from the Isua Supracrustal Belt, Greenland. (a) Cross-section of the hand specimen (scale bar: 1 cm). The close-up images (PPL) of laminae: (b) The lighter lamina consists of more transparent minerals like carbonate (Carb.), muscovite (Ms.), whereas (c) the darker lamina mainly consists of dark minerals like biotite (Bt.) and carbonaceous matter (CM). Crystals of muscovite and biotite exhibit the subparallel arrangement, inferring the extrusion stress during the deformation. (d) Sketch of the laminae in the rectangle area in (a), consisting of parallel-oriented dark minerals and CM that are nearly perpendicular to the laminae orientation. (e) Raman spectroscopic spot analysis verified the minerals of calcite+ ankerite+ biotite + muscovite shown in (b) and (c). PPL: Plane-polarized light. Scale bar: 200 μm.

Table 1 Geochemical compositions of the ISB metasomatic and stromatolite-like carbonates

SampleID	IS-1	IS-2
Age (Ma)	3700?	3700?
Rock Type	Metasomatic Carb.	Stromatolite-like Carb.
Dissolved fraction(wt%)	94.1	28.5
(wt%)		
Al	0.004	2.440
Ca	22.136	23.295
Cu	0.001	0.000
Fe	3.259	13.613
K	bd	2.475
Mg	11.593	7.273
Mn	0.680	1.194
(ppm)		
Sc	4.313	9.740
Ti	0.029	765.437
V	0.493	52.915
Rb	0.097	90.288
Sr	55.680	61.950
Y	5.810	12.202
Zr	0.000	0.968
Mo	0.193	0.288
Ba	0.854	1739.072
La	0.474	10.667
Ce	1.723	16.349
Pr	0.310	2.006
Nd	1.622	7.770
Sm	0.517	1.605
Eu	0.109	0.658
Gd	0.752	1.858
Tb	0.138	0.257
Dy	0.970	1.579
Ho	0.224	0.341
Er	0.688	1.033
Tm	0.107	0.158
Yb	0.799	1.142
Lu	0.137	0.182
Th	0.017	0.326
U	0.014	0.113
REY	14.382	57.808
Y/Ho	25.99	35.78
Ce/Ce*	0.95	0.85
Pr/Pr*	0.97	1.00
La/La*	2.23	1.36
Gd/Gd*	0.98	1.10
Eu/Eu* new	0.94	2.17
Y/Y*	2.74	2.51
$\delta^{13}C_{VPDB}$ (‰)	-2.03	0.99
$\delta^{18}O_{VPDB}$ (‰)	-18.96	-11.66
87Sr/86Sr (i)	0.711960	0.913835

Note:
1. Anomalies were calculated based on PAAS-normalized values (after Pourmand et al., 2012) :
$Ce/Ce^* = Ce_{SN}/(0.5Pr_{SN} + 0.5La_{SN})$ and $Pr/Pr^* = Pr_{SN}/(0.5Ce_{SN} + 0.5Nd_{SN})$ (after Bau and Dulski, 1996)
$La/La^* = La_{SN}/(3Pr_{SN} - 2Nd_{SN})$ and $Gd/Gd^* = Gd_{SN}/(2Tb_{SN} - Dy_{SN})$ (after Alexander et al., 2008)
$Eu/Eu^* = Eu_{SN}/(Sm_{SN}^2 * Tb_{SN})^{1/3}$ and $Y/Y^* = Y_{SN}/(0.5Er_{SN} \times 0.5Ho_{SN})$ (after Lawrence et al. 2006)
2. bd: below the limits of detection

(Fig.2 a). Under microscopic examination, the laminae consist of leucocratic minerals including calcite, ankerite, quartz, muscovite, and melanocratic minerals, including annite and phlogopite (potentially biotite), as well as carbonaceous matter. These observations were further confirmed by Raman spectroscopic analysis (Fig.2b, c and e). The mineral assemblage is consistent with the work of Nutman et al. (2016), which infers amphibolite metamorphism at temperatures ranging from 500 to 550°C. However, the parallel orientation of micas, almost perpendicular to the laminae orientation, makes its origin equivocal, whether the material is an altered and deformed biogenic stromatolite, or just an abiotic product of deformation (Fig.2d). Previous works have reported that the mineral orientation and layer-parallel foliation are typical deformation fabrics (Nutman et al., 2016; Allwood et al., 2018; Zawaski et al., 2020).

The geochemical compositions of the ISB metasomatic and stromatolite-like carbonate rocks are listed in Table 1. The dissolved fraction of the metasomatic carbonate is high, at 94.1 wt%, whereas that of the stromatolite-like carbonate is low, at 28.5 wt%, reflecting a small fraction of carbonate minerals in the stromatolite-like carbonate, consistent with the petrological observation (Fig.2b and c). The concentrations (wt%) of Ca, Mg, Fe and Mn are 22.136, 11.593, 3.259 and 0.680, respectively, and the molar ratios (%) of Ca, Mg, and Fe+Mn are 49.99, 43.64, and 6.38, respectively, indicating that the metasomatic carbonate is dolomite in geochemistry. In contrast, the concentrations (wt%) of Ca, Mg, Fe and Mn are 23.295, 7.273, 13.613 and 1.194, respectively, and the molar ratios (%) of Ca, Mg, and Fe+Mn are 50.63, 26.35, 23.02, respectively, indicating that the stromatolite-like carbonate is predominantly ankerite. The low concentration of Al, Sc, Ti, Th, Rb, Zr in the metasomatic carbonate and their high abundance in the stromatolite-like carbonate demonstrate that the metasomatic carbonate has no detritus component, whereas the stromatolite-like carbonate suffered detritus contamination. Similarly, the stromatolite-like carbonate contains much higher concentrations of elements like V and Ba, which are identified to be of basaltic origin, inferring it likely experienced heavy hydrothermal alteration, supporting the amphibolite metamorphism recognized in the petrological

observation.

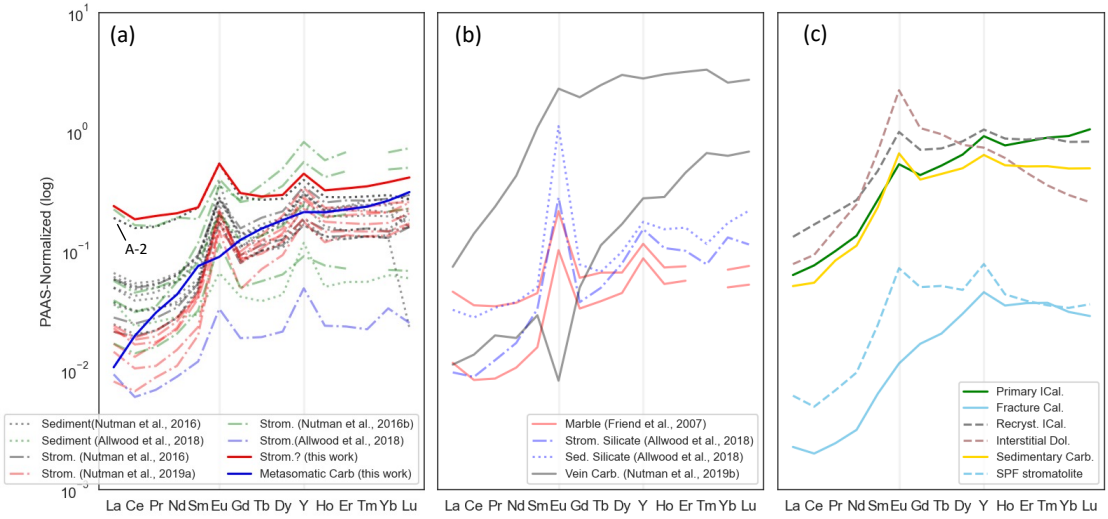

Fig.3 The REE+Y patterns of the ISB and EPT Archean carbonates are shown, normalized to Post-Archean Australian Shale (PAAS, after Pourmand et al., 2012). The PAAS-normalized REE+Y patterns of (a) the ISB carbonates in this work and from references, (b) the marble, vein carbonates and silicates from references, and (c) different lithologies from the EPT, including the primary interstitial calcite (Primary ICal.), the altered recrystallized interstitial calcite (Recryst. ICal.), the interstitial dolomite (Dol.) and fracture-filling calcite (Fracture Cal.) and (b) sedimentary carbonates (Carb.) and the Strelley Pool (SPF) stromatolites (details in Chapter 3). The REE+Y pattern of the studied ISB stromatolite-like carbonate in this work is consistent with the most Ti-Al-rich "marly" layer (A-2, black dotted line) (Nutman et al., 2016), which was interpreted as a degeneration of seawater-like signature. The most reported ISB stromatolites showing the seawater-like REE+Y features are actually not distinctive from the EPT marine sedimentary carbonates and hydrothermal interstitial calcites. However, they are distinctive from those of the nearby metasomatic and vein carbonate. With the exception of strong Eu anomalies, the REE+Y patterns of silicates (Allwood et al., 2018) cannot be differentiated from carbonates.

The PAAS-normalized REE+Y pattern of the stromatolite-like sample is in good accordance with the most Ti-Al-rich "marly" layer (A-2) (Nutman et al., 2016), which was interpreted to be degeneration of a seawater-like signature (Fig.3a). In additional to the REE+Y pattern, other REE+Y signatures are all within the range of the EPT interstitial calcites and marine sedimentary carbonates, showing a near-chondritic Y/Ho ratio, no Ce and Gd anomaly, slightly positive La, and positive Eu and Y anomalies. The PAAS-normalized REE+Y patterns of the ISB marble, sediments and stromatolites (Friend et al., 2007; Nutman et al., 2016, 2019a, b) show many similarities with the EPT marine sedimentary carbonates and the SPF stromatolite (Fig.3c), suggesting similar depositional and burial conditions. With the exception of strong Eu anomalies, the REE+Y patterns of silicates (Allwood et al., 2018) cannot actually be differentiated from carbonates (Fig.3b). However, the metasomatic carbonate shows a totally different REE+Y pattern of a smooth increase from La to Lu without any anomaly (Fig.3a), and the vein carbonates show more various REE+Y patterns (Fig.3b), which are both far apart from the ISB stromatolitic and sedimentary carbonates, implying the REE+Y signatures of the ISB stromatolitic and sedimentary carbonates were not greatly overprinted by later fluid circulations.

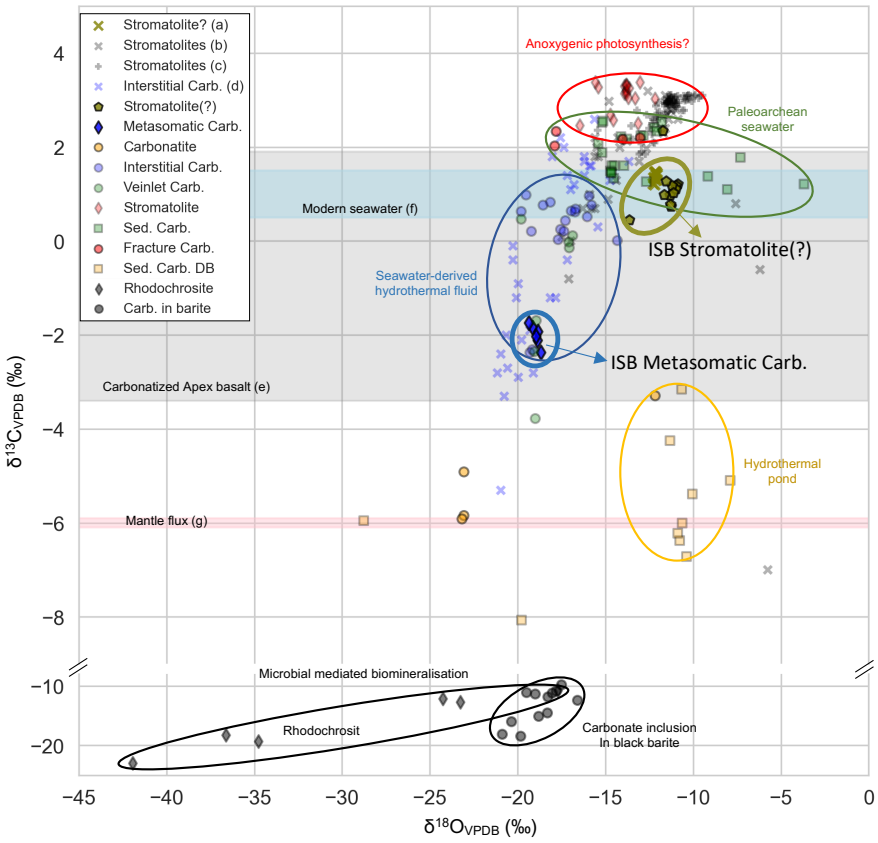

Fig.4 The $\delta^{13}C$ and $\delta^{18}O$ values of the early Archean carbonates. It is noted that the controversial ISB stromatolite-like carbonates have the values within the range of the EPT marine sedimentary carbonates rather than the SPF stromatolites, while the ISB metasomatic carbonates have the values within the range of the more altered EPT interstitial carbonates. The lightblue area is restricted by the $\delta^{13}C$ values of modern seawater (Kroopnick, 1980; Tan, 1988), the grey one is restricted by the $\delta^{13}C$ values of carbonatized basalt from Apex Basalt (Nakamura & Kato, 2004), and the red area is restricted by the mantle $\delta^{13}C$ values of -6 ± 0.5 ‰ (Hayes and Waldbauer, 2006). (Abbreviation in labels: Carb.-carbonate; Sed.- sedimentary. The question mark in labels refers to the controversial origin. Data are in Table 1, Chapter 2. Reference list: a.Nutman et al., 2016, b. Lindsay et al., 2005, c. Flannery et al., 2018, d. Shibuya et al., 2012, e. Nakamura and Kato, 2004, f. Kroopnick, 1980 and Tan, 1988; g. Hayes and Waldbauer, 2006.)

The carbon and oxygen isotopic compositions of the metasomatic and stromatolite-like carbonates are shown in Chapter 2 and replotted in Fig.4 with data from the EPT carbonates. Only the values from the same subsamples studied here are listed in Table 2. The $\delta^{13}C$ values of the stromatolite-like carbonates range from 0.45 to 2.35 ‰ with an average value of 1.10 ± 0.46 ‰, while their $\delta^{18}O_{VPDB}$ values range from -13.64 to -10.88 ‰ (a mean value of -11.47 ± 0.73 ‰), within the range of the EPT sedimentary carbonates. Therefore, the interpretation of low-temperature dolomite formed through microbial activities (Nutman et al., 2016) is not convincing, considering the EPT sedimentary carbonates as organominerals (Chapter 2). On the other hand, the average $\delta^{13}C$ and $\delta^{18}O_{VPDB}$ values of the metasomatic carbonates are -2.00 ± 0.22 ‰ and -18.98 ± 0.25 ‰, respectively, showing the similarities to the more altered EPT interstitial carbonates, distinct from the ISB stromatolite-like carbonates. The age-corrected $^{87}Sr/^{86}Sr$ ratio of the stromatolite-like carbonate is extremely high, 0.913835, possibly

impacted by the hydrothermal overprint during alteration of some surrounding felsic rocks or the unsuitable spiked ratio during the measurement due to its high Rb concentration of 90.288 ppm (unusual in carbonate). The age-corrected $^{87}Sr/^{86}Sr$ ratio of the metasomatic carbonates is 0.711960, within the range of the EPT sedimentary carbonates and interstitial dolomites.

5. Conclusion

The comprehensive research on the ISB stromatolite-like carbonates and metasomatic carbonates, compared with the EPT carbonates, can assist in recognizing the protolith and possible influence by depositional alteration. Several conclusions can be made: (1) The mineral assemblage and the parallel orientation of micas in the investigated stromatolite-like carbonate indicate it experienced the metamorphism of amphibolite facies and deformation; (2) During alteration, some vulnerable components including the abundances of mobile elements and $^{87}Sr/^{86}Sr$ ratio were largely deviated, whereas some relatively robust components like REE+Y and carbon isotopes were retained, supporting a marine origin of the stromatolite-like carbonates, consistent with previous work (Nutman et al., 2016, 2019a, b; Allwood et al., 2018; Zawaski et al, 2020); (3) The geochemical compositions surviving from alteration cannot support an interpretation of stromatolite, which instead requires more geological, sedimentological survey and research on the field, as well as support from 3D macroscopic and microscopic structures, as seen in the research used on the Dresser and SPF stromatolites (van Zuilen, 2018; this work). In fact, whether the 3D geometry of the structures reflects the elongated conical stromatolite or deformation is a bone of contention (Nutman et al., 2016, 2019b, 2021; Allwood et al., 2018; van Zuilen, 2018; Zawaski et al, 2020, 2021), instead of the marine origin. The geochemical compositions of the stromatolite-like carbonates infer that the protolith is likely a marine sedimentary carbonate formed through organomineralization, and the stromatolite-like structures were possibly caused by deformation during tectonic events, as described in Zawaski et al. (2020).

Acknowledgements

I express my gratitude to Dr. Mark van Zuilen at the CNRS-UMR6538 Laboratoire Geo-Ocean for providing sample materials and significant insights into the formation of the two types of carbonates. Dr. Burkhard Schmidt is thanked for his assistance with the Raman spectroscopic analysis. Dr. Tommaso Di Rocco, Dennis Kohl and Thierry Wasselin are acknowledged for the measurement of stable carbon and oxygen isotopes. The fieldtrip in Greenland is organized by Prof. Dr. Carsten Münker and Dr. Daniela Hülle at the University of Cologne, and funded by SPP1833 (DFG-Schwerpunktprogramm) "Building a Habitable Earth". This study was financially supported by the China Council Scholarship (CSC).

Appendix

Table S1 Geochemical compositions of the ISB carbonates and silicates from references.

SampleID	Reference	Rock type	La	Ce	Pr	Nd	Sm	Eu	Gd	Tb	Dy	Y	Ho	Er	Tm	Yb	Lu
G05/54b	Friend et al., 2007	Marble	2.041	3.111	0.351	1.378	0.307	0.263	0.362	0.059	0.353	3.15	0.077	0.230		0.211	0.033
G05/55b			0.517	0.736	0.087	0.395	0.108	0.124	0.200	0.034	0.238	2.38	0.056	0.174		0.150	0.023
G11/63a	Nutman et al., 2016	Dolostone	2.20	3.40	0.41	1.60	0.40	0.46	0.66	0.11	0.66	6.6	0.17	0.46	0.07	0.46	0.09
track-2 a		Dirty A-2	8.47	13.80	1.63	7.03	1.60	0.66	1.71	0.24	1.47	10.8	0.30	0.87	0.13	0.89	0.12
G12/93-1		Sediment (below)	2.72	4.49	0.54	2.35	0.61	0.34	0.83	0.14	1.00	8.27	0.23	0.72	0.11	0.73	0.12
G12/93-2			8.47	13.80	1.63	7.03	1.60	0.66	1.71	0.24	1.47	10.82	0.30	0.87	0.13	0.89	0.12
G12/93-3			2.93	4.76	0.57	2.44	0.63	0.33	0.84	0.15	1.01	8.61	0.24	0.74	0.11	0.77	0.07
G12/93-4			1.59	2.76	0.33	1.41	0.38	0.22	0.51	0.09	0.57	4.59	0.13	0.39	0.06	0.41	0.10
G12/93-5			1.09	1.78	0.22	1.04	0.34	0.25	0.65	0.13	0.95	8.16	0.23	0.68	0.10	0.64	0.07
G12/93-6			1.67	2.80	0.34	1.34	0.36	0.30	0.50	0.09	0.62	4.88	0.14	0.39	0.06	0.39	0.01
G12/93-7			2.21	3.73	0.46	2.09	0.58	0.33	0.80	0.14	0.91	7.05	0.21	0.60	0.09	0.59	0.08
G12/93-11		Sediment (above)	2.58	4.22	0.50	2.07	0.51	0.26	0.67	0.12	0.90	8.31	0.23	0.73	0.12	0.82	0.13
G12/93-8		Strom.	1.24	2.18	0.28	1.26	0.37	0.25	0.56	0.10	0.67	5.09	0.16	0.46	0.07	0.44	0.07
G12/93-9			0.94	1.71	0.22	1.03	0.32	0.21	0.48	0.09	0.60	4.51	0.14	0.41	0.06	0.39	0.07
G12/93-10			2.60	4.37	0.53	2.35	0.64	0.34	0.94	0.17	1.15	9.52	0.27	0.82	0.12	0.83	0.13
G12/93-7s	Nutman et al., 2019a	Strom.	1.061	1.670	0.218	1.040	0.283	0.257	0.520	0.085	0.640	5.2	0.153	0.454	0.066	0.443	0.075
G12/93-12			1.010	1.460	0.176	0.821	0.276	0.179	0.600	0.121	1.060	9.3	0.244	0.709	0.106	0.763	0.113
G12/93-14			0.951	1.600	0.196	0.964	0.306	0.268	0.525	0.104	0.722	6.17	0.186	0.529	0.076	0.521	0.091
G12/93-22			0.746	1.150	0.170	0.851	0.316	0.235	0.557	0.110	0.823	7.71	0.220	0.681	0.097	0.633	0.112
G12/93-dol		Strom-dol (spot)	0.361	0.592	0.089	0.409	0.136	0.179	0.289	0.063	0.495	4.83	0.125	0.419	0.060	0.407	0.072
G12/93-dol2			0.640	0.919	0.111	0.557	0.160	0.211	0.486	0.094	0.754	7.44	0.204	0.615	0.093	0.640	0.100
G11/71D (1)	Nutman et al., 2019b	Strom.	2.52	3.97	0.50	2.16	0.81	0.43	1.62	0.32	2.63	22.5	0.61	2.08		2.03	0.32
G11/71D (2)			0.75	1.23	0.16	0.76	0.22	0.14	0.30	0.05	0.34	2.48	0.08	0.22		0.21	0.03
G11/71B (3)			1.73	2.73	0.35	2.07	0.55	0.25	0.75	0.12	0.87	6.77	0.20	0.63		0.65	0.10
G11/71B (4)			10.00	14.59	1.65	7.15	1.28	0.49	1.56	0.25	1.88	15.3	0.44	1.44		1.46	0.22
G17/32		Vein Carb.	0.50	1.20	0.20	0.70	0.20	0.01	0.30	0.10	0.90	7.58	0.30	1.40	0.30	1.90	0.30
G17/64			3.30	12.40	2.40	16.00	7.50	2.80	11.80	2.20	16.00	76.6	3.20	9.80	1.50	7.80	1.20
C3C	Allwood et al., 2018	Strom. Carb.	0.414	0.530	0.070	0.332	0.082	0.040	0.113	0.017	0.113	1.335	0.025	0.072	0.010	0.100	0.011
M3C		Sed. Carb.	1.670	2.080	0.260	1.047	0.203	0.080	0.252	0.034	0.230	3.209	0.053	0.170	0.025	0.190	0.026
C3M		Strom. Si	0.430	0.781	0.124	0.636	0.226	0.343	0.226	0.044	0.421	4.182	0.112	0.310	0.035	0.393	0.050
M3M		Sed. Si	1.438	2.456	0.341	1.398	0.344	1.358	0.468	0.060	0.528	4.812	0.161	0.485	0.052	0.519	0.096

*Abbreviation: Carb.- carbonate; Strom.-stromatolite; Sed.-sedimentary; Si-silicates.
** (spot) indicates the spot analyses of pure dolomite crystal.

References

Allwood, A. C., Walter, M. R., Kamber, B. S., Marshall, C. P., and Burch, I. W.: Stromatolite reef from the Early Archaean era of Australia, Nature, 441, 714–718, 2006.

Allwood, A. C., Walter, M. R., Burch, I. W., and Kamber, B. S.: 3.43 billion-year-old stromatolite reef from the Pilbara Craton of Western Australia: ecosystem-scale insights to early life on Earth, Precambrian Research, 158, 198–227, 2007.

Allwood, A. C., Grotzinger, J. P., Knoll, A. H., Burch, I. W., Anderson, M. S., Coleman, M. L., and Kanik, I.: Controls on development and diversity of Early Archean stromatolites, Proceedings of the National Academy of Sciences, 106, 9548–9555, 2009.

Allwood, A. C., Kamber, B. S., Walter, M. R., Burch, I. W., and Kanik, I.: Trace elements record depositional history of an Early Archean stromatolitic carbonate platform, Chemical Geology, 270, 148–163, 2010.

Allwood, A. C., Rosing, M. T., Flannery, D. T., Hurowitz, J. A., and Heirwegh, C. M.: Reassessing evidence of life in 3,700-million-year-old rocks of Greenland, Nature, 563, 241–244, 2018.

Bontognali, T. R., Sessions, A. L., Allwood, A. C., Fischer, W. W., Grotzinger, J. P., Summons, R. E., and Eiler, J. M.: Sulfur isotopes of organic matter preserved in 3.45-billion-year-old stromatolites reveal microbial metabolism, Proceedings of the National Academy of Sciences, 109, 15 146–15 151, 2012.

Dauphas, N., Van Zuilen, M., Wadhwa, M., Davis, A. M., Marty, B., and Janney, P. E.: Clues from Fe isotope variations on the origin of early Archean BIFs from Greenland, Science, 306, 2077–2080, 2004.

Dauphas, N., van Zuilen, M., Busigny, V., Lepland, A., Wadhwa, M., and Janney, P. E.: Iron isotope, major and trace element characterization of early Archean supracrustal rocks from SW Greenland: protolith identification and metamorphic overprint, Geochimica et Cosmochimica Acta, 71, 4745–4770, https://doi.org/10.1016/j.gca.2007.07.019, 2007.

Fedo, C. M. and Whitehouse, M. J.: Metasomatic origin of quartz-pyroxene rock, Akilia, Greenland, and implications for Earth's earliest life, Science, 296, 1448–1452, https://doi.org/10.1126/science.1070336, 2002.

Flannery, D. T., Allwood, A. C., Summons, R. E., Williford, K. H., Abbey, W., Matys, E. D., and Ferralis, N.: Spatially-resolved isotopic study of carbon trapped in 3.43 Ga Strelley Pool Formation stromatolites, Geochimica et Cosmochimica Acta, 223, 21–35, 2018.

Lepland, A., van Zuilen, M. A., Arrhenius, G., Whitehouse, M. J., and Fedo, C. M.: Questioning the evidence for Earth's earliest life—Akilia revisited, Geology, 33, 77–79, https://doi.org/10.1130/G20890.1, 2005.

Lepland, A., van Zuilen, M., and Philippot, P.: Fluid-deposited graphite and its geobiological implications in early Archean gneiss from Akilia, Greenland, Geobiology, 9, 2–9, https://doi.org/10.1111/j.1472-4669.2010.00261.x, 2011.

Lowe, D. R.: Restricted shallow-water sedimentation of Early Archean stromatolitic and evaporitic strata of the Strelley Pool Chert, Pilbara Block, Western Australia, Precambrian Research, 19, 239–283, https://doi.org/10.1016/0301-9268(83)90016-5, 1983.

McKeegan, K. D., Kudryavtsev, A. B., and Schopf, J. W.: Raman and ion microscopic imagery of graphitic inclusions in apatite from older than 3830 Ma Akilia supracrustal rocks, west Greenland, Geology, 35, 591–594, https://doi.org/10.1130/G23465A.1, 2007.

Mojzsis, S. and Harrison, T.: Origin and significance of Archean quartzose rocks at Akilia, Greenland, Science, 298, 917–917, 2002.

Mojzsis, S. J., Arrhenius, G., McKeegan, K., Harrison, T., Nutman, A., and Friend, C.: Evidence for life on Earth before 3,800 million years ago, Nature, 384, 55–59, https://doi.org/10.1038/384055a0, 1996.

Mojzsis, S., Coath, C., Greenwood, J., McKeegan, K., and Harrison, T.: Mass-independent isotope effects in Archean (2.5 to 3.8 Ga) sedimentary sulfides determined by ion microprobe analysis, Geochimica et Cosmochimica Acta, 67, 1635–1658, https://doi.org/10.1016/S0016-7037(03)00059-0, 2003.

Nutman, A. P., Allaart, J. H., Bridgwater, D., Dimroth, E., and Rosing, M.: Stratigraphic and geochemical evidence for the depositional environment of the early Archaean Isua supracrustal belt, southern West Greenland, Precambrian Research, 25, 365–396, https://doi.org/10.1016/0301-9268(84)90010-X, 1984.

Nutman, A. P., McGregor, V. R., Friend, C. R., Bennett, V. C., and Kinny, P. D.: The Itsaq Gneiss Complex of southern West Greenland; the world's most extensive record of early crustal evolution (3900-3600 Ma), Precambrian Research, 78, 1–39, https://doi.org/10.1016/0301- 9268(95)00066-6, 1996.

Nutman, A. P., McGregor, V. R., Shiraishi, K., Friend, C. R., Bennett, V. C., and Kinny, P. D.: ⩾ 3850 Ma BIF and mafic inclusions in the early Archaean Itsaq Gneiss Complex around Akilia, southern West Greenland? The difficulties of precise dating of zircon-free protoliths in migmatites, Precambrian Research, 117, 185–224, https://doi.org/10.1016/S0301-9268(02)00045-1, 2002.

Nutman, A. P., Bennett, V. C., Friend, C. R., Van Kranendonk, M. J., and Chivas, A. R.: Rapid emergence of life shown by discovery of 3,700-million-year-old microbial structures, Nature, 537, 535–538, https://doi.org/10.1038/nature19355, 2016.

Nutman, A. P., Friend, C. R., Bennett, V. C., Van Kranendonk, M., and Chivas, A. R.: Reconstruction of a 3700 Ma transgressive marine environment from Isua (Greenland): Sedimentology, stratigraphy and geochemical signatures, Lithos, 346, 105164, https://doi.org/10.1016/j.lithos.2019.105164, 2019a.

Nutman, A. P., Bennett, V. C., Friend, C. R., Van Kranendonk, M. J., Rothacker, L., and Chivas, A. R.: Cross-examining Earth's oldest stromatolites: Seeing through the effects of heterogeneous deformation, metamorphism and metasomatism affecting Isua (Greenland) 3700 Ma sedimentary rocks, Precambrian Research, 331, 105 347, https://doi.org/10.1016/j.precamres.2019.105347, 2019b.

Nutman, A. P., Bennett, V. C., Friend, C. R., and Van Kranendonk, M. J.: In support of rare relict 3700 Ma stromatolites from Isua (Greenland), Earth and Planetary Science Letters, 562, 116 850, https://doi.org/10.1016/j.epsl.2021.116850, 2021.

Ohtomo, Y., Kakegawa, T., Ishida, A., Nagase, T., and Rosing, M. T.: Evidence for biogenic graphite in early Archaean Isua metasedimentary rocks, Nature Geoscience, 7, 25–28, https://doi.org/10.1038/ngeo2025, 2014.

Rose, N. M., Rosing, M. T., and Bridgwater, D.: The origin of metacarbonate rocks in the Archaean Isua supra-crustal belt, West Greenland, American Journal of Science, 296, 1004–1044, https://doi.org/10.2475/ajs.296.9.1004, 1996.

Rosing, M. T.: ^{13}C-depleted carbon microparticles in> 3700-Ma seafloor sedimentary rocks from West Greenland, Science, 283, 674–676, https://doi.org/10.1126/science.283.5402.674, 1999.

Rosing, M. T., Rose, N. M., Bridgwater, D., and Thomsen, H. S.: Earliest part of Earth's stratigraphic record: a reappraisal of the> 3.7 Ga Isua (Greenland) supracrustal sequence, Geology, 24, 43–46, https://doi.org/10.1130/0091-7613(1996)024<0043:EPOESS>2.3.CO;2, 1996.

Ueno, Y., Yurimoto, H., Yoshioka, H., Komiya, T., and Maruyama, S.: Ion microprobe analysis of graphite from ca. 3.8 Ga metasediments, Isua supracrustal belt, West Greenland: relationship between metamorphism and carbon isotopic composition, Geochimica et Cosmochimica Acta, 66, 1257–1268, https://doi.org/10.1016/S0016-7037(01)00840-7, 2002.

Van Kranendonk, M. J.: Volcanic degassing, hydrothermal circulation and the flourishing of early life on Earth: A review of the evidence from ca. 3490-3240 Ma rocks of the Pilbara Supergroup, Pilbara Craton, Western Australia, Earth-Science Reviews, 74, 197–240, https://doi.org/10.1016/j.earscirev.2005.09.005, 2006.

van Zuilen, M. A.: Proposed early signs of life not set in stone, Nature, pp. 190–191, https://doi.org/10.1038/d41586-018-06994-x, 2018.

van Zuilen, M.: The Significance of Carbonaceous Matter to Understanding Life Processes on Early Earth. In: Van Kranendonk, M.J., Bennett, V.C., Hoffmann, J.E. (Eds.), in: Earth's Oldest Rocks. Elsevier, 945–963, 2019.

van Zuilen, M. A., Lepland, A., and Arrhenius, G.: Reassessing the evidence for the earliest traces of life, Nature, 418, 627–630, https://doi.org/10.1038/nature00934, 2002.

van Zuilen, M. A., Lepland, A., Teranes, J., Finarelli, J., Wahlen, M., and Arrhenius, G.: Graphite and carbonates in the 3.8 Ga old Isua supracrustal belt, southern West Greenland, Precambrian Research, 126, 331–348, https://doi.org/10.1016/S0301-9268(03)00103-7, 2003.

van Zuilen, M. A., Chaussidon, M., Rollion-Bard, C., and Marty, B.: Carbonaceous cherts of the Barberton Greenstone Belt, South Africa: Isotopic, chemical and structural characteristics of individual microstructures, Geochimica et Cosmochimica Acta, 71, 655–669, https://doi.org/10.1016/j.gca.2006.09.029, 2007.

Wacey, D.: Stromatolites in the 3400 Ma Strelley Pool Formation, Western Australia: examining biogenicity from the macro-to the nano- scale, Astrobiology, 10, 381–395, https://doi.org/10.1089/ast.2009.0423, 2010.

Westall, F.: Morphological biosignatures in early terrestrial and extraterrestrial materials, Space Science Reviews, 135, 95–114, https://doi.org/10.1007/s11214-008-9354-z, 2008.

Whitehouse, M. J., Kamber, B. S., and Moorbath, S.: Age significance of U–Th–Pb zircon data from early Archaean rocks of west Greenland—a reassessment based on combined ion-microprobe and imaging studies, Chemical geology, 160, 201–224, https://doi.org/10.1016/S0009-2541(99)00066-2, 1999.

Whitehouse, M. J., Kamber, B. S., Fedo, C. M., and Lepland, A.: Integrated Pb-and S-isotope investigation of sulphide minerals from the early Archaean of southwest Greenland, Chemical Geology, 222, 112–131, https://doi.org/10.1016/j.chemgeo.2005.06.004, 2005.

Whitehouse, M. J., Myers, J. S., and Fedo, C. M.: The Akilia Controversy: field, structural and geochronological evidence questions interpretations of > 3.8 Ga life in SW Greenland, Journal of the Geological Society, 166, 335–348, https://doi.org/10.1144/0016-76492008-070, 2009.

Zawaski, M. J., Kelly, N. M., Orlandini, O. F., Nichols, C. I., Allwood, A. C., and Mojzsis, S. J.: Reappraisal of purported ca. 3.7 Ga stromatolites from the Isua Supracrustal Belt (West Greenland) from detailed chemical and structural analysis, Earth and Planetary Science Letters, 545, 116 409, https://doi.org/10.1016/j.epsl.2020.116409, 2020.

Zawaski, M. J., Kelly, N. M., Orlandini, O. F., Nichols, C. I., Allwood, A. C., and Mojzsis, S. J.: Reply: The Isua (Greenland)" relict stromatolites" cannot be confidently interpreted as original sedimentary structures, Earth and Planetary Science Letters, 562, 116 851, https://doi.org/10.1016/j.epsl.2021.116851, 2021.

Chapter-7 Summary and Outlook

1. Summary

The research within the framework of this dissertation aims to fill the gap in the early Archean carbonate rocks. Carbonate rocks, which are widespread in diverse environments, have proven to be reliable material for reconstructing ancient environmental conditions that trigger carbonate precipitation and post-depositional alteration. From the oldest dolomitic stromatolites in the early Archean to the various present-day carbonate buildups involving calcifying organisms, carbonate has linked ecosystems and biogeochemical cycles, such as the global carbon cycle over long geological time, reflecting the co-evolution of life and Earth. Decades after the preliminary 'mud mound' carbonate factory (carbonate production system, Reitner et al. 1995; Reitner and Neuweiler, 1995), the notion of carbonate factory has been rapidly developed and characterized by several key aspects of depositional settings, mineralogies and pathways through which carbonates are precipitated (Schlager, 2000, 2003; Reijmer, 2021; Wang et al., 2023). It is now extensively applied in describing carbonate systems after Precambrian, however, rarely in the ancient carbonate systems, especially for the early Archean carbonates.

Sample scarcity is one cause for the vacuum in this field. The reported less metamorphosed Archean rocks are preserved in three places, namely the 4.0-3.6 Ga Isua supracrustal belt (ISB) of southern West Greenland, the 3.53-3.17 Ga East Pilbara Terrane (EPT) of the Pilbara Craton, Western Australia, and 3.55- 3.2 Ga Barberton Greenstone belt (BGB) of southern Africa, which are not so easily accessible. On the other hand, pristine carbonate is rare due to its vulnerability to diagenesis and post-depositional alteration, which commonly erases the original information in every regard. Additionally, stromatolites, microbial-induced carbonate buildup, are the cynosure of all eyes, however, the biogeochemical significance of the more pervasive silicified sedimentary carbonate and "hydrothermal" carbonate (the carbonates associated with greenstones, Veizer, 1989) has been long underestimated. Benefiting from the abundance in relative carbonate samples that were collected by Joachim Reitner, I delve into the research on the early Archean carbonates from the three greenstone belts, mainly from the EPT, that are sorted into three carbonate types based on sedimentology, including interstitial carbonate (within the interspace between pillow basalts), bedded sedimentary carbonate, and stromatolite.

Microfacies analysis is the foundation and thus the start of my research. Hundreds of thin sections were examined, and only the representative samples were selected to study in-situ geochemistry (micro-XRF) and carbon-oxygen isotopes (Chapter 2). Consequently, three carbonate factories are recognized, as major carbon sinks in the infancy of subaerial silicate weathering, namely oceanic crust factory, organo-carbonate factory, microbial factory. To be specific, the oceanic crust factory is charactered by the prevalence of interstitial carbonates in the interspace between carbonatized pillow basalts, precipitated inorganically on the seafloor from CO_2-rich seawater or seawater-derived hydrothermal fluids of high alkalinity. The

organo-carbonate factory occurs in diverse environments from the ocean to terrestrial hydrothermal ponds, intermittently fed by hydrothermal inputs, and is characterized by abundant organic materials, organomicrite and graded carbonates forming through taphonomy-controlled organo-mieralization, with organic macromolecules acting as nucleation sites independent of their origins (either biotic or abiotic). The microbial factory is characterized by various stromatolites and microbial buildups formed through microbial EPS-controlled mineralization (possibly anoxygenic photosynthesis), resulting in their common occurrence in the photic, relatively restricted, shallow marine environments like lagoon on slope or platform, with minor detritus and hydrothermal inputs.

Hydrothermal fluids play significant roles in constructing three carbonate factories. They not only export substantial alkaline metals and organic materials to promote carbonate precipitation, but also provide sufficient soluble silica that precipitated as chert matrices. Chert of this origin assists in delicately preserving the primary sedimentary textures, carbonaceous materials, and some of the degraded structures, hinting at traces of early life. In addition, as an abiotic product of the interaction between the basaltic seafloor and seawater, the geochemical composition of interstitial carbonates can be utilized as a baseline for the early Archean ocean in future studies. This helps to illustrate the co-evolution of geological processes and infantile life on early Earth, which are possibly recorded in the bio-induced mineralization of sedimentary carbonate and stromatolites.

With the desire to have more precise and accurate geochemical data and trace the parent and alteration fluids, I measured the elemental concentration (ICP-OES, ICP-MS) and radiogenic strontium isotopic compositions (MC-ICP-MS) of distinctive carbonates via micro-drilling and acid-digestion to separate carbonate and silicate components (Chapter 3). The most exciting findings are two pristine interstitial carbonates that inorganically precipitated from ~3.5 Ga seawater and seawater-derived low-temperature hydrothermal fluid, respectively. These two fluid endmembers share some REE+Y features of near-chondritic Y/Ho weight-ratios, and the PAAS(shale)-normalized REE+Y patterns (subscript SN) characterized by LREE depletion, no Ce_{SN} yet positive La_{SN} and Y_{SN} anomalies. However, the seawater endmember exhibits the higher Sr concentration of 1789 ppm and lower REE+Y concentration, no Eu_{SN} anomaly, the diagnostic shallow seawater-like $\delta^{13}C$ value of +2.20 ‰, and the age-corrected $^{87}Sr/^{86}Sr$ ratio of 0.700596. In contrast, the hydrothermal endmember has the lower Sr concentration (119 ± 17 ppm) and higher REE+Y concentration, positive Eu_{SN} anomaly, the hybrid $\delta^{13}C$ value (+ 0.63 ± 0.12 ‰), and the age-corrected $^{87}Sr/^{86}Sr$ ratio (0.703094 ± 0.000979), both of which are intermediate between seawater and basalt. In addition, the multi-element behaviors during post-depositional alterations have been identified to be source-dependent. Recrystallization is commonly induced by low-temperature hydrothermal fluid or seawater, slightly deviating the original geochemical compositions but having less impact on the REE+Y pattern and the $\delta^{13}C$ value. However, dolomitization is triggered by high-temperature hydrothermal fluids, usually leading to dissolution and neomorphism, thus showing greatly increased elemental abundances of basaltic origin, variant normalized REE+Y patterns with MREE enrichment, plus a strong positive Eu_{SN} anomaly, and largely elevated $^{87}Sr/^{86}Sr$ ratios, yet consistent $\delta^{13}C$

values. Therefore, this work not only provides the pristine geochemical compositions of seawater and low-temperature hydrothermal fluid at 3.5 Ga, but also assists in recognizing the origin of ancient carbonate rocks, i.e sedimentary carbonate and stromatolite, and estimating the geochemical influence of possible post-depositional alteration. It is also demonstrated that the EPT carbonates are important archives for reconstructing environments on Early Earth.

However, the work in Chapter 3 raises several new questions. For example, the more radiogenic $^{87}Sr/^{86}Sr$ ratios of the primary interstitial carbonates of Apex Basalt than those of the contemporary seawater raise the question of whether the primary interstitial carbonates can truly reflect the geochemical conditions of hydrothermal fluids derived from the seawater-basalt reaction at 3.5 Ga, or much younger one? In other words, when did the greenschist metamorphism occur? Whether and how did it influence ocean chemistry?

To answer these questions, I conducted further studies on pillow basalt components from the same section as the primary interstitial calcite (Chapter 4). Its submarine eruption was supported by the distinct concentric structures (from core to chilled rim and interspace), including a holocrystalline core, a spherulitic zone, a variolitic zone, a glassy zone within a pillow shape, and shattered breccias in the interspace. Despite experiencing metamorphism of greenschist facies, the pillow basalts preserved distinct concentric structures and secondary mineral assemblages (chlorite+ calcite+ quartz+ anatase + pyrite ± epidote). They indicate broadly syn-depositional alteration, which is supported by the errorchron based on Rb-Sr isotopic compositions of different concentric domains yields an age of 3570.7 ± 144.3 Ma (n=6, MSWD= 150), comparable to the depositional age around 3460 Ma, yielding a whole-rock $^{87}Sr/^{86}Sr$ ratio of 0.706337 ± 0.000954. This errorchron age implies that the Rb-Sr system was not largely reset afterwards. During this alteration, various elements and bioessential elements (Ca, Si, P, S, Fe, Mn, Mg, Ni, Zn, Co, REE +Y) were leached from the basalt into fluid, leading to extensive carbonatization of the basaltic crust, the occurrence of interstitial carbonate, and the abundance of bioessential elements in hydrothermal fluids. These fluids provided nutrients or enzyme cofactors that were responsible for many metabolisms and played a significant role in paving the way for the origin and evolution of early life. Furthermore, the pervasion of Si-bearing fluids that precipitated various cherts involved in the preservation of carbonaceous materials, microfossils and stromatolites. Therefore, the well-preserved Apex pillow basalts are an excellent archive for studying seafloor alteration at 3.46 Ga and its significances in global carbon cycles and adjusting ocean geochemistry to prepare Earth habitable for early life.

Finally, I provided some practical applications based on the study of the EPT carbonates. The first is to reconstruct fluid conditions from which the EPT carbonates were precipitated and that triggered depositional alteration (Chapter 5), including temperature, fluid Sr/Ca ratio and fluid Sr concentration, as well as numerical models for quantitively studying the water-rock interaction during carbonate diagenesis, performed based on mass balance using fluid Sr concentrations and $^{87}Sr/^{86}Sr$ ratios. Considering debates and uncertainties over some key parameters, i.e. various ~3.5 Ga seawater $\delta^{18}O$ values, different scenarios are discussed, and only unambiguous conclusions are listed as follows: (1) temperatures of the seawater-derived

hydrothermal fluids forming Apex interstitial carbonates were 17.3 to 26.1 °C higher than that of the contemporary seawater, and the heat was from the cooling of Apex pillow basalts; (2) the low-temperature hydrothermal fluids likely have consistently had lower Sr/Ca molar ratios than contemporaneous seawater since the early Archean; (3) fluid Sr concentration and $^{87}Sr/^{86}Sr$ ratio can be applied in quantifying the fluid-rock reaction during carbonate diagenesis.

On the other hand, the findings are used to recognize the protolith and possible influence by depositional alteration on the controversial ISB stromatolite-like carbonates, testing the validity of the interpretation that they are stromatolites rather than deformation artifacts (Chapter 6). The ISB stromatolite-like carbonates indeed experienced metamorphism of amphibolite facies and deformation evidenced by the mineral assemblage and parallel orientation of micas, which changed some vulnerable components, such as the abundances of mobile elements and the $^{87}Sr/^{86}Sr$ ratio. However, some relatively robust components like REE+Y and carbon isotopes were retained, supporting a marine origin of the stromatolite-like carbonates. Nonetheless, the geochemical compositions surviving from alteration cannot support an interpretation of stromatolite, which instead requires more geological and sedimentological survey and research on the field, as well as support from the 3D macroscopic and microscopic structures, as used in the research on the Dresser and SPF stromatolites, which are a bone of contention instead of marine origin (Nutman et al., 2016, 2019, 2021; Allwood et al., 2018; van Zuilen, 2018; Zawaski et al, 2020, 2021). And the geochemical compositions of the stromatolite-like carbonates infer the protolith is likely marine sedimentary carbonate formed through organomineralization, and the stromatolite-like structures are possibly caused by deformation during tectonic events, as described in Zawaski et al, (2020). As long as this possibility cannot be precluded, the stromatolite origin may not be extensively approved.

2. Outlook

This dissertation has introduced the sedimentology, microfacies and geochemistry of early Archean carbonates of various facies. It has proposed three carbonate factories on the juvenile Earth and their roles in biogeochemical cycles, such as major carbon sinks in the global carbon cycle, confirming that carbonate can be a reliable archive for reconstructing environment conditions. However, several problems cannot be solved in the scope of this dissertation.

Carbonate can only record information of ambient fluids, and accordingly, it is at most representative of the regional water column. Hence, more caution should be paid when extrapolating the geochemical compositions of some samples to the global scale. The differences of the REE+Y patterns and carbon isotopic compositions of the EPT carbonates demonstrate the diverse depositional environments, where inputs and outputs can greatly determine the geochemical compositions of the local water. Additionally, although D-2-W is regarded as the seawater endmember at 3.5 Ga in this dissertation, it is more plausive to reflect a shallow marine environment where anoxygenic photosynthesis likely flourished

during the interval of volcanic and hydrothermal activities. Whether it can be applicable to the other two greenstone belts is still unknown. Hence, more research on ancient carbonates of various facies and potential depositional environments is encouraged, especially those associated with other Archean rocks.

In cases of application, uncertainties of key parameters greatly impact the interpretations and conclusions. For example, uncertainty in the $\delta^{18}O$ value of the Archean ocean causes a large deviation of ocean temperatures in calculation. It invokes a long debate on a hot or modern-like Archean ocean, and raise questions about the origin of early life. In addition to the seawater $\delta^{18}O$ values, the empirical equation used to calculate the temperature for dolomite is void possibly due to difficulties in its experimental synthesis and the recognition of dolomite as a secondary product. However, the texture and geochemistry of EPT sedimentary carbonates suggest that dolomite is likely a primary facies in some environments fed by hydrothermal fluids. Nevertheless, this interpretation requires more convincing studies to demonstrate its validity. If this is the case, some empirical key parameters for dolomite will be necessary for reconstructing certain environmental conditions.

The seafloor alteration and associated secular hydrothermal inputs to the ocean have become new hotspots. More and more researchers have recognized the significant contributions of low-temperature hydrothermal alteration within the oceanic crust in controlling ocean geochemistry and acting as a carbon sink (Bach et al., 2001, 2011; Coggon et al., 2004, 2010; Gillis and Coogan, 2011; Rausch, 2012; Coogan and Gillis, 2013, 2018; Coogan and Dosso, 2015). However, research in this field is still limited to ancient rocks and extremely rare in the early Archean rocks, which cannot provide insight into secular changes. Additionally, geochemical analysis of inclusions is urgently required as a direct record of seawater and hydrothermal fluids in the early Archean to estimate the hydrothermal flux to the ocean and reconstruct some diagnostic proxies, such as fluid Sr concentrations that can be used to quantify fluid-rock reactions combined with $^{87}Sr/^{86}Sr$ ratios.

Acknowledgements

We would like to express our heartfelt gratitude to the individuals and institutions who have made invaluable contributions and provided unwavering support throughout this research. While many of them have been acknowledged in the respective chapters, we would like to extend our thanks to the following:

- Prof. Dr. Martin Van Kranendonk from the University of New South Wales, Australia, and Dr. Arthur Hickman from the Geological Survey of Western Australia for their indispensable logistical assistance in the field and their invaluable guidance in unraveling the intricate geological aspects of the Pilbara region.

- Prof. Dr. Axel Hofmann from the University of Johannesburg, South Africa, for his substantial support in working with the Barberton drill cores and for imparting a comprehensive understanding of the geology of the Barberton Greenstone Belt.

- Faye and Geoffrey Myers, the caretakers of the old North Pole Gold Mine, whose gracious hospitality and exceptional assistance in locating suitable outcrops have played a pivotal role in our research. We are deeply grateful for their generosity and the warm atmosphere they have created. Without their invaluable help, numerous aspects of this study would not have been possible. Faye and Geoffrey Myers epitomize the great Mimi spirit in the outback.

- The core library of the Geological Survey of Western Australia, for granting us the necessary permission to sample drill core materials from the Pilbara region (approval for P954, 1014, 1091).

- Prof. Graham Shields, for his expertise and efforts in conducting the measurement of strontium isotopic compositions of barites from the Dresser Formation.

- We would like to extend our sincere appreciation to the Göttingen Academy of Sciences and Humanities of Lower Saxony for the financial and scientific support, which has been instrumental in the successful execution of this research project.

We are deeply thankful to all the individuals and institutions mentioned above for their invaluable contributions and unwavering support throughout this study.

References

Allwood, A. C., Rosing, M. T., Flannery, D. T., Hurowitz, J. A., and Heirwegh, C. M.: Reassessing evidence of life in 3,700-million-year-old rocks of Greenland, Nature, 563, 241–244, 2018.

Bach, W., Alt, J. C., Niu, Y., Humphris, S. E., Erzinger, J., and Dick, H. J.: The geochemical consequences of late-stage low-grade alteration of lower ocean crust at the SW Indian Ridge: Results from ODP Hole 735B (Leg 176), Geochimica et Cosmochimica Acta, 65, 3267–3287, 2001.

Bach, W., Rosner, M., Jöns, N., Rausch, S., Robinson, L. F., Paulick, H., and Erzinger, J.: Carbonate veins trace seawater circulation during exhumation and uplift of mantle rock: Results from ODP Leg 209, Earth and Planetary Science Letters, 311, 242–252, 2011.

Coggon, R. M., Teagle, D. A., Cooper, M. J., and Vanko, D. A.: Linking basement carbonate vein compositions to porewater geochemistry across the eastern flank of the Juan de Fuca Ridge, ODP Leg 168, Earth and Planetary Science Letters, 219, 111–128, 2004.

Coggon, R. M., Teagle, D. A., Smith-Duque, C. E., Alt, J. C., and Cooper, M. J.: Reconstructing past seawater Mg/Ca and Sr/Ca from mid-ocean ridge flank calcium carbonate veins, Science, 327, 1114–1117, https://doi.org/10.1126/science.1182252, 2010.

Coogan, L. A. and Gillis, K. M.: Evidence that low-temperature oceanic hydrothermal systems play an important role in the silicate-carbonate weathering cycle and long-term climate regulation, Geochemistry, Geophysics, Geosystems, 14, 1771–1786, 2013.

Coogan, L. A. and Dosso, S. E.: Alteration of ocean crust provides a strong temperature dependent feedback on the geological carbon cycle and is a primary driver of the Sr-isotopic composition of seawater, Earth and Planetary Science Letters, 415, 38–46, 2015.

Coogan, L. A. and Gillis, K. M.: Low-temperature alteration of the seafloor: impacts on ocean chemistry, Annual Review of Earth and Planetary Sciences, 46, 21–45, 2018.

Gillis, K. and Coogan, L.: Secular variation in carbon uptake into the ocean crust, Earth and Planetary Science Letters, 302, 385–392, https://doi.org/10.1016/j.epsl.2010.12.030, 2011.

Nutman, A. P., Bennett, V. C., Friend, C. R., Van Kranendonk, M. J., and Chivas, A. R.: Rapid emergence of life shown by discovery of 3,700-million-year-old microbial structures, Nature, 537, 535–538, https://doi.org/10.1038/nature19355, 2016.

Nutman, A. P., Bennett, V. C., Friend, C. R., Van Kranendonk, M. J., Rothacker, L., and Chivas, A. R.: Cross-examining Earth's oldest stro- matolites: Seeing through the effects of heterogeneous deformation, metamorphism and metasomatism affecting Isua (Greenland) 3700 Ma sedimentary rocks, Precambrian Research, 331, 105 347, https://doi.org/10.1016/j.precamres.2019.105347, 2019.

Nutman, A. P., Bennett, V. C., Friend, C. R., and Van Kranendonk, M. J.: In support of rare relict 3700 Ma stromatolites from Isua (Green- land), Earth and Planetary Science Letters, 562, 116 850, https://doi.org/10.1016/j.epsl.2021.116850, 2021.

Rausch, S.: Carbonate veins as recorders of seawater evolution, CO_2 uptake by the ocean crust, and seawater-crust interaction during low-temperature alteration, Universität Bremen, 2012.

Reijmer, J. J.: Marine carbonate factories: review and update, Sedimentology, 68, 1729–1796, https://doi.org/10.1111/sed.12878, 2021.

Reitner, J. and Neuweiler, F.: Part I Mud mounds: recognizing a polygenetic spectrum of fine-grained carbonate buildups, in: Mud mounds: a polygenetic spectrum of fine-grained carbonate buildups,

edited by Reitner, J. and Neuweiler, F., pp. 2–4, 1995.
Reitner, J., Wilmsen, M., and Neuweiler, F.: Cenomanian/Turonian sponge microbialite deep-water hardground community (Liencres, Northern Spain), Facies, 32, 203–212, https://doi.org/10.1007/BF02536869, 1995.
Schlager, W.: Sedimentation rates and growth potential of tropical, cool-water and mud-mound carbonate systems, Geological Society, London, Special Publications, 178, 217–227, https://doi.org/10.1144/GSL.SP.2000.178.01.14, 2000.
Schlager, W.: Benthic carbonate factories of the Phanerozoic, International Journal of Earth Sciences, 92, 445–464, https://doi.org/10.1007/s00531-003-0327-x, 2003.
van Zuilen, M. A.: Proposed early signs of life not set in stone, Nature, pp. 190–191, https://doi.org/10.1038/d41586-018-06994-x, 2018.
Veizer, J., Hoefs, J., Ridler, R., Jensen, L., and Lowe, D.: Geochemistry of Precambrian carbonates: I. Archean hydrothermal systems, Geochimica et Cosmochimica Acta, 53, 845–857, https://doi.org/10.1016/0016-7037(89)90030-6, 1989.
Wang, J., Tarhan, L. G., Jacobson, A. D., Oehlert, A. M., and Planavsky, N. J.: The evolution of the marine carbonate factory, Nature, pp. 1–5, https://doi.org/10.1038/s41586-022-05654-5, 2023.
Zawaski, M. J., Kelly, N. M., Orlandini, O. F., Nichols, C. I., Allwood, A. C., and Mojzsis, S. J.: Reappraisal of purported ca. 3.7 Ga stromatolites from the Isua Supracrustal Belt (West Greenland) from detailed chemical and structural analysis, Earth and Planetary Science Letters, 545, 116 409, https://doi.org/10.1016/j.epsl.2020.116409, 2020.
Zawaski, M. J., Kelly, N. M., Orlandini, O. F., Nichols, C. I., Allwood, A. C., and Mojzsis, S. J.: Reply: The Isua (Greenland)" relict stromatolites" cannot be confidently interpreted as original sedimentary structures, Earth and Planetary Science Letters, 562, 116 851, https://doi.org/10.1016/j.epsl.2021.116851, 2021.

Personal acknowledgements

As the song goes, "time rolls by, the clock doesn't stop", and I have spent more than four years in Germany. Over the past few years, I have attended many farewell parties, but now it's my turn to have one. Doctoral studies are never easy or relaxing, and I couldn't have made it this far without the kindness of others. So, if you could spare me a few more minutes, I would like to express my gratitude to the people who have been there for me throughout my journey.

First and foremost, I would like to thank my first supervisor, Prof. Dr. Joachim Reitner. He is erudite and friendly, always willing to lend a hand whenever I encounter difficulties. He participated in every aspect of my research, from introducing sample information (his collections) and background to estimating research plans, guiding me to find solutions, and inspiring me when I struggled with data interpretation. Discussing my work with him is always a pleasure, even when we have intense debates. However, these debates ultimately lead to a better understanding of the issue at hand, and I'm grateful for that. This is what science is all about. He helped me to enjoy the long, painful journey of being a PhD student. Beyond the scientific realm, I've also learned a lot from him about daily life. We share hobbies like wine, food, and travel, and he always helps me plan my trips, including transportation, accommodations, local cuisine, wine, beer, tourist sites, and museums. He's also a source of solutions for my daily problems. Therefore, he is not only a responsible supervisor but also a wonderful friend to me.

The second person I would like to thank is also my supervisor, Prof. Dr. Jan-Peter Duda. I am constantly impressed by his intelligence and wit. He has an exceptional ability to find clues amidst chaos and helps me clear my mind, making significant contributions to the writing of our manuscripts. In his personal life, he has a great sense of humor. Before I came to Germany, I attended a summer course at my university, which was taught by Prof. Reitner and Prof. Duda. His performance during the course shattered my preconceived notions of "serious and stereotypical Germans." Compared to him, I felt like a boring person. This experience planted a seed in my mind, which sprouted when I decided to study abroad. As a result, I ultimately chose to become their student.

Next, I would like to express my gratitude to Prof. Dr. Andreas Pack and his group members. Prof. Pack provided guidance on stable carbon and oxygen isotopes, which were significant in interpreting my data. Dr. Tommaso Di Rocco and Dr. Dingsu Feng kindly provided me with laboratory space, equipment, and materials for sample preparation. They are both my close friends and appear in my daily life outside of work. I would also like to thank the technical assistants, Dennis Kohl and Thierry Wasselin, for their laboratory work in measuring the stable isotopes and analysis. I had the pleasure of working with Dr. Jakub Surma and Oliver Jäger on early Archean carbonates. We held small meetings to discuss recent data and freely share opinions, and their professional support was invaluable.

Additionally, I would like to express my sincere gratitude to Prof. Dr. Matthias Willbold

and his team, who have patiently taught me and supported me throughout my experiments measuring rare earth elements and radiogenic strontium isotopic compositions. I was a complete novice in this area, but with their guidance, I was able to learn a great deal. Dr. Dirk Hoffmann also deserves special thanks for teaching me how to prepare carbonate samples and work safely and efficiently in the clean lab. Whenever I encountered problems during my experiments, he was the first person I thought of, and he always came to my aid with kindness and immediacy. Brigitte Dietrich, a retired technical assistant, taught me spike and purification procedures, as well as how to prepare silicate samples. The lab was always kept prepared and clean thanks to the hard work of technical assistant Erwin Schiffczyk. Nils Meßling was also incredibly helpful, always willing to lend a hand with various measurements and teaching me how to handle raw data, despite being a busy PhD student himself. Matthias was involved in every aspect of my work, from preparation to data processing and interpretation. I am grateful for the support I received during my two-year experiment in their lab, especially during the harsh and difficult pandemic period. I know I was a burden on their time, as I made mistakes that were harmful to instruments and caused delays in their normal work schedule. Working with them has taught me the importance of everyone's efforts in making a lab function smoothly, and will undoubtedly benefit me in my future career.

In order to test my ideas, I used multiple methods that required technical support. Petrological observation was the foundation of my research, and all thin sections were prepared by Axel Hackmann, who also provided rock slabs and drilling columns for my further geochemistry work. Wolfgang Dröse assisted with sample preparation and ordered necessary chemical reagents. Prof. Dr. Gernot Arp provided the microscopes for my examination of thin sections, and fixed technical problems in a timely manner. Dr. Burkhard Schmidt provided guidance for Raman spectroscopic analysis and in-situ geochemical mapping via micro-XRF. Dr. Volker Karius helped with measuring major element concentration with ICP-OES and processing raw data. Whenever I had questions about rare earth elements and strontium isotopes, I turned to Prof. Dr. Wolfgang Bach at Bremen University, an expert in this field. He also provided some carbonates within modern oceanic crust collected from drilling projects, which served as supplementary materials for the Archean counterparts. Lastly, I am grateful to Dr. Nadine Schäfer and our secretary Jennifer Schelling for their help with office computer maintenance and documents, respectively.

While academic study is an important part of my life, I've also had many wonderful and impressive experiences with my colleagues and friends in my spare time. I'm someone who enjoys staying at home, so my friends are usually my colleagues, like Yu Pei, Dingsu Feng, Liuyi Lu, Tommaso Di Rocco, Lingqi Zeng, and their friends. Yu Pei was the first person I met in Göttingen, and I'll never forget when she and Lingqi came to pick me up in the cold midnight. Even though she's a bad cook, her terrible cooking warmed me up that night because of the care that went into it. I enjoy being with her because she's simple, easygoing, and insensitive, which means I can always relax around her without worrying about behaving properly. Yu Pei has many friends, and some of them have become my friends as well. Similarly, Dingsu is also a social butterfly. She regularly organizes gatherings, including

meetings, dinners, BBQs, and other fun activities to bring together friends. Through these events, I have had the pleasure of meeting many interesting people and forming friendships with them. Dingsu is not only a great friend but also my travel companion, and together we have shared many interesting experiences and created wonderful memories. Thanks to the two amazing women, I have never felt lonely in the past years. Liuyi Lu is a talented person who always surprises me with her newly developed hobbies, and she's my tennis teacher. She's also the only person in Göttingen who I can discuss Anime & Manga with, even though most of the time we complain that certain authors are out of their minds. Tommaso is a zealous Italian who used to be my office roommate. Our friendship developed from sharing mandarin and videos of Ziqi Li, and deepened during our snack and food sharing sessions, which is a very typical Chinese style! Lingqi Zeng is my fellow-townsman, and we're both working hard to promote Leshan cuisine to the outside world. As I mentioned before, I have many friends who are friends of my friends, such as Shuang Liu (my gym partner), Jinjin He (my Wein partner), Ranling Zhang, Yin Yu, and more, who are friends of Yu Pei, while Julien Delhez, Yilin Jiang, Xinglin Li, Hui Hui, Lele Jin are friends of Dingsu.

Of course, I also have my own friends, such as Dorothea Hause-Reitner, Dingliu Yang, Guantao Chen, Yinyin Huang, and Mengyi Wang. Dorothea is a great friend with whom I can discuss arts, culture, experiences, and our opinions on the world around us. Dingliu is an artist with great talent. She was my best friend in primary school, but we parted ways when we went to different schools. Fortunately, we met again in Germany, and whenever I see her, I feel like I'm back in our carefree childhood days. Time rolls by. Guantao, Yinyin, Mengyi and I were classmates in a German course in China that prepared us for our lives in Germany. We were surprised to learn that we would all be studying at Göttingen University for our PhDs, even though we came from different places. Mengyi is my close friend, a woman who is as free-spirited as the wind. Her perspectives on life and the world often amaze me, and her wisdom is so captivating that it always heals my weary mind. If the insensitivity of Yu is one ability I wish to have, Mengyi's liberality must be another. I want to thank my friends in China too, because despite the distance, we stay in touch often, and it feels like I am still with them. I am looking forward to meeting them soon.

Most importantly, I want to express my gratitude to my family, who selflessly provided me with spiritual and material support. In the past four years, I have not been able to go home once due to the pandemic and various restrictions, and it has made me feel homesick. However, the care and concern from my parents and relatives almost brought me to tears, especially when I contracted Covid in Greenland and felt extremely uncomfortable in the hotel. In addition to my family, I am grateful for the financial support that enabled me to focus on my academic studies and research. This includes the precious four-year scholarship from China Scholarship Council, the project funding from the Department of Geobiology at the Geoscience Centre, University of Göttingen, and the SPP 1833 “Building a Habitable Earth”. I would also like to express my gratitude for the three-month emergency financial support from GAUSS.

Lastly, I would like to extend my heartfelt appreciation to everyone who has played a

role in my academic journey, both those I have mentioned and those I have not. They are like beautiful flowers that have bloomed along my long and challenging path, adding color to my life and keeping me from giving up. And thank you, this self who never gave up in times of hesitation and pain.